Numerical Assessment of Cardio- and Neurovascular Pathologies: Modeling Variability, Flow Transition and Treatment Planning

Dissertation
zur Erlangung des akademischen Grades

Doktoringenieurin (Dr.-Ing.)

von M-Sc. Jana Korte-Bektaş, geb. Korte
geb. am 24.06.1993 in Köln

genehmigt durch die Fakultät für Verfahrens- und Systemtechnik der Otto-von-Guericke-Universität Magdeburg

Promotionskommission:

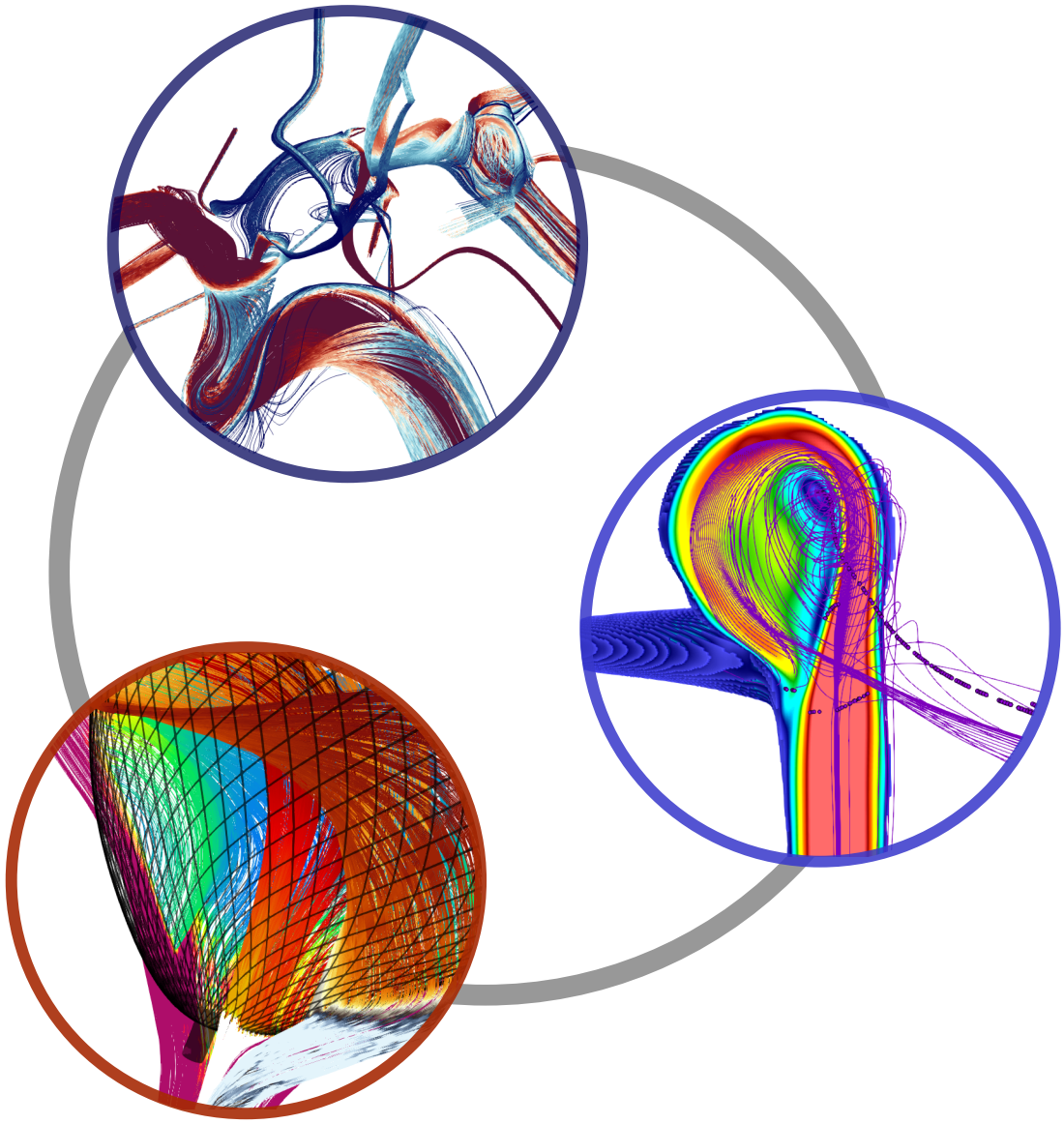
Prof. Dominique Thévenin (Vorsitz)
Prof. Gábor Janiga (Gutachter)
Prof. Daniel Behme (Gutachter)
Prof. Melissa Brindise (Gutachterin)
PD Dr.-Ing. Philipp Berg (Mitglied)

eingereicht am: 04.03.2025
Promotionskolloquium am: 20.06.2025

Jana Korte-Bektaş: Numerical Assessment of Cardio- and Neurovascular Pathologies: Modeling Variability, Flow Transition and Treatment Planning

Dissertation
Jana Korte-Bektaş

Numerical Assessment of Cardio- and Neurovascular Pathologies: Modeling Variability, Flow Transition and Treatment Planning



Abstract

Various vascular pathologies can arise in the human cardio- and neurovascular systems, impacting human health. This thesis primarily focuses on the neurovascular pathology of intracranial aneurysms (IAs) and secondarily on the cardiovascular pathology of mitral valve insufficiency. Technical advancements in medical imaging over the past years have enabled the capture of vascular lumen geometry, which serves as a basis for numerical fluid dynamic simulations to determine hemodynamics and assess the associated risk status of these pathologies. Furthermore, treatment procedures can be virtually simulated, and medical devices tested for their efficacy. Since the patient-specific input in these simulations is limited to the vascular geometry, numerous assumptions must be made, which can lead to unrealistic hemodynamic results if not appropriately defined. The impact of these variabilities remains insufficiently understood, necessitating further research to enhance patient-specific numerical simulations.

In this thesis, five variabilities in hemodynamic modeling are evaluated for their impact on vascular pathology hemodynamics. These include the vasculature complexity incorporated in the model, the segmentation method used to define the vessel lumen, the choice of outlet boundary condition in the simulation, the physiological state of the human heart cycle (resting vs. exercise conditions), and the selected numerical solver. Additionally, based on the impact analysis, a novel treatment device for IAs, the Contour Neurovascular System, is virtually tested through an in silico workflow, utilizing both phantom-specific in vitro data and patient-specific in vivo data.

The inclusion of complex vasculature demonstrates notable variations in hemodynamic results, influencing the classification of IAs as ruptured or unruptured. Similar variability is observed with different segmentation methods. The choice of boundary condition reveals a clear trend in the magnitude of hemodynamic results, with this effect reducing when more

accurate segmentation is applied and disappearing with the inclusion of complex vasculature. Simulations incorporating exercise conditions show increased intraventricular kinetic energy and, in the context of aneurysmal flow, the occurrence of high-frequency flow fluctuations. These fluctuations, however, can only be detected with high-resolution numerical solvers. Finally, the novel treatment device was successfully evaluated in silico through a virtual mimicking process, demonstrating efficient flow reduction into the IA.

The findings of this thesis highlight the importance of accounting for modeling assumptions in numerical hemodynamic simulations to improve patient-specific accuracy. The incorporation of exercise conditions should be further considered to derive the physiological flow behavior. Furthermore, in silico treatment analysis has proven to be efficient. Automated treatment planning through systematic in silico analyses could optimize the efficacy testing of novel medical devices in the future.

Zusammenfassung

Im menschlichen kardiovaskulären und neurovaskulären System können verschiedene vaskuläre Pathologien auftreten, die sich auf die Gesundheit des Menschen auswirken. Diese Dissertation konzentriert sich primär auf die neurovaskuläre Pathologie intrakranieller Aneurysmen (IAs) und sekundär auf die kardiovaskuläre Pathologie der Mitralklappeninsuffizienz. Der technische Fortschritt in der medizinischen Bildgebung hat in den letzten Jahren die Erfassung der Geometrie des Gefäßlumens ermöglicht, die als Grundlage für numerische fluiddynamische Simulationen zur Bestimmung der Hämodynamik und zur Bewertung des damit verbundenen Risikostatus dieser Pathologien dient. Außerdem können Behandlungsverfahren virtuell simuliert und medizinische Implantate auf ihre Wirksamkeit getestet werden. Da sich die patientenspezifischen Daten in diesen Simulationen auf die Gefäßgeometrie beschränken, müssen zahlreiche Annahmen getroffen werden, die bei unzureichender Definition zu unrealistischen hämodynamischen Ergebnissen führen können. Die Auswirkungen dieser Schwankungen sind nach wie vor unzureichend bekannt, so dass weitere Forschungsarbeiten zur Verbesserung der patientenspezifischen numerischen Simulationen erforderlich sind.

In dieser Arbeit werden fünf Variabilitäten in der hämodynamischen Modellierung auf ihre Auswirkungen auf die Hämodynamik in der Gefäßpathologie untersucht. Dazu gehören die Komplexität der Gefäßstruktur, die zur Definition des Gefäßlumens verwendete Segmentierungsmethode, die Wahl der Auslassrandbedingung in der Simulation, der physiologische Zustand des menschlichen Herzzyklus (Ruhezustand vs. Belastungszustand) und der gewählte numerische Solver. Darüber hinaus wird auf der Grundlage der Auswirkungsanalyse ein neuartiges Implantat für intrakranielle Aneurysmen, das Contour Neurovascular System, durch einen in-silico-Arbeitsablauf virtuell getestet, wobei sowohl phantomspezifische in-vitro-Daten als auch patientenspezifische in-vivo-Daten verwendet werden.

Die Einbeziehung komplexer Gefäßstrukturen führt zu Abweichungen bei den hämodynamischen Ergebnissen, die sich auf die Klassifizierung von IAs als rupturiert oder nicht rupturiert auswirken. Eine ähnliche Variabilität wird bei verschiedenen Segmentierungsmethoden beobachtet. Die Wahl der Randbedingung zeigt einen klaren Trend in der Größenordnung der hämodynamischen Ergebnisse, wobei dieser Effekt abnimmt, wenn eine genauere Segmentierung angewandt wird, und verschwindet, wenn komplexe Gefäße einbezogen werden. Simulationen, die Belastungsbedingungen einbeziehen, zeigen eine erhöhte intraventrikuläre kinetische Energie und, im Zusammenhang mit neurovaskulärem Fluss, das Auftreten von hochfrequenten Flussfluktuationen in Aneurysmen. Diese Fluktuationen können jedoch nur mit hochaufgelösten numerischen Solvern erkannt werden. Schließlich wurde die neuartige Behandlungsvorrichtung erfolgreich in-silico durch ein virtuelles Nachahmungsverfahren-Verfahren evaluiert, wobei eine effiziente Reduzierung des Flusses in die Aneurysmen nachgewiesen werden konnte.

Die Ergebnisse dieser Arbeit zeigen, wie wichtig die Berücksichtigung akkurater Modellierungsannahmen in numerischen hämodynamischen Simulationen ist, um die patientenspezifische Genauigkeit zu verbessern. Die Einbeziehung von Belastungsbedingungen sllte zukünfitg in Betracht gezogen werden, um ein realistisches physiologisches Flussverhalten abzuleiten. Darüber hinaus hat sich die in-silico-Behandlungsanalyse als effizient erwiesen. Eine automatisierte Behandlungsplanung durch systematische in-silico-Analysen könnte die Bewertung und Wirksamkeitsprüfung neuartiger medizinischer Geräte in Zukunft optimieren.

Contents

Abstract iii

Zusammenfassung v

Table of Contents vii

Acronyms xi

Nomenclature xv

List of Figures xvii

List of Tables xxiii

1 Introduction 1
- 1.1 Motivation . . . 2
- 1.2 Contribution and structure . . . 3

2 Background 5
- 2.1 Anatomy of the cardio- and neurovascular system . . . 6
- 2.2 Intracranial aneurysms . . . 7
- 2.3 Medical imaging . . . 11
- 2.4 Computational Fluid Dynamics . . . 12
- 2.5 Hemodynamic parameters . . . 14
- 2.6 Fluid dynamics in medical applications . . . 16
  - 2.6.1 Evolution of CFD in intracranial aneurysms . . . 16
  - 2.6.2 Current status of CFD in intracranial aneurysms . . . 16
  - 2.6.3 Hemodynamic instabilities and transitional features in the flow . . . 19
  - 2.6.4 CFD to evaluate endovascular treatment . . . 20
  - 2.6.5 Validation of numerical vascular flow assessment . . . 22

3 Part 1: Impact of segmentation, vasculature complexity, and outlet boundary condition in image-based blood flow simulations of intracranial aneurysms 25
- 3.1 Variabilities in image-based blood flow simulations of intracranial aneurysms . . . 27
- 3.2 Contribution . . . 32

3.3 Methodology . . . 34
3.3.1 Patient cohort . . . 34
3.3.2 Variabilities in hemodynamic modeling . . . 36
3.3.3 Numerical investigation . . . 39
3.4 Impact of variability in segmentation, vasculature complexity, and outlet boundary condition . . . 41
3.4.1 Vasculature complexity . . . 41
3.4.2 Segmentation . . . 43
3.4.3 Outlet boundary condition . . . 44
3.5 Interaction between segmentation, vasculature complexity, and outlet boundary condition . . . 49
3.5.1 Boundary condition effects and segmentation . . . 49
3.5.2 Boundary condition effects and vasculature complexity 53
3.6 Limitations . . . 56
3.7 Conclusions . . . 56

4 Part 2: Influence of rest and exercise conditions on flow parameters in vascular pathologies 59
4.1 Analysis of rest and exercise conditions in vascular flows . . . 61
4.2 Modeling requirements to assess the impact of rest and exercise on vascular flow conditions . . . 65
4.3 Mitral valve insufficiency . . . 67
4.4 Contribution . . . 68
4.5 Methodology . . . 70
4.5.1 Patient cohort . . . 70
4.5.2 Integration of rest and exercise conditions . . . 70
4.5.3 Ventricular wall movement from ultrasound . . . 72
4.5.4 Intra-aneurysmal flow validation with volumetric particle tracking velocimetry . . . 74
4.5.5 Hemodynamic investigation: Moving mesh, direct numerical and low resolution simulation . . . 77
4.5.6 Post-processing . . . 79
4.6 Impact of rest and exercise on cardiac hemodynamics . . . 80
4.6.1 Implementation of ventricular wall movement and resulting transient kinetic energy . . . 80
4.6.2 Intraventricular pathological flow behavior under rest and exercise . . . 82
4.6.3 Limitations . . . 83

4.7 Appearance of transitional flow in an intracranial aneurysm during rest and exercise . . . 84
4.7.1 Validation of aneurysmal flow under rest and exercise using volumetric particle tracking velocimetry . . . 84
4.7.2 Occurrence of high-frequency fluctuations under rest and exercise conditions . . . 89
4.7.3 Limitations . . . 94
4.8 Conclusion . . . 95

5 Part 3: In silico assessment of aneurysmal hemodynamics after deployment of the Contour Neurvascular System 99
5.1 A long-term effective device to treat wide-necked bifurcation aneurysms . . . 101
5.2 Efficacy of the Contour Neurovascular System compared to other treatment devices . . . 104
5.3 Contribution . . . 107
5.4 Methodology . . . 109
5.4.1 Patient cohort . . . 110
5.4.2 In vitro and in vivo imaging . . . 111
5.4.3 Aneurysm dome stitching . . . 113
5.4.4 Contour digitalization . . . 113
5.4.5 Virtual Contour deployment . . . 113
5.4.6 Hemodynamic investigation . . . 114
5.5 Reliability of the Contour processing workflow . . . 116
5.5.1 Contour fitting . . . 116
5.5.2 Geometric and fluid modeling . . . 117
5.5.3 Comparison to in vitro measurements . . . 119
5.6 Advantages of the Contour Neurovascular System . . . 121
5.6.1 Short-term treatment outcome . . . 122
5.6.2 Systematic evaluation of Contour placement impact on hemodynamics . . . 126
5.6.3 Longitudinal Contour displacement and its impact on hemodynamics . . . 128
5.7 Limitations . . . 134
5.8 Conclusion . . . 135

6 Final Conclusion **137**
6.1 Summary 138
6.2 Future Work 140

References **143**

List of own Publications **167**

Acronyms

ACA	anterior communicating artery
BA	basilar artery
BBMRI	black blood magnetic resonance imaging
BC	boundary condition
bpm	beats per minute
CFD	computational fluid dynamics
Contour	Contour Neurovascular System
CoW	circle of Willis
CTA	computed tomography angiography
DNS	direct numerical simulation
DSA	digital subtraction angiography
ESV	end-systolic volume
FDS	flow-diverter stent
FIA	fusiform intracranial aneurysm
FSI	fluid-structure interaction
FU	follow up
HFpEF	heart failure with preserved ejection fraction
IA	intracranial aneurysm
ICA	internal carotid artery
ICI	inflow concentration index
KE	kinetic energy

KER kinetic energy ratio

LES large eddy simulation

LRNS low-resolution numerical simulations

LSA low shear area

LV left ventricle

MCA middle cerebal artery

MI mitral valve insufficiency

MRI magnetic resonance imaging

NIR neck inflow rate

nTAWSS normalized time-averaged wall shear stress

OSI oscillatory shear index

OVI oscillatory velocity index

PC-MRI phase-contrast magnetic resonance imaging

PCA posterior communicating artery

PDMS polydimethylsiloxane

PIV particle image velocimetry

PSD power spectral densities

PTV particle tracking velocimetry

RA rotational angiography

RMS root mean square

SD standard deviation

SIA saccular intracranial aneurysm

STB shake-the-box

STL standard triangle language

TA time-averaged

TE treatment effect

TOF time-of flight

TOT aneurysm turnover time

VA vertebral artery

WEB WovenEndoBridge embolization device

WNBA wide-necked bifurcation aneurysm

WSS wall shear stress

Nomenclature

α	node correlation factor
β	node correlation factor
η	dynamic viscosity
λ	wave length
μ	micro
ν	kinematic viscosity
ω	vorticity
ρ	density
c	time instance over cardiac cycle
C_i	cell node
kg	kilogram
m	meter
n	exponent
P_1	vertice on triangular surface
Pa	Pascal
R	Radius
r	radial distance
s	second
V_{x}	x-velocity component
V_{y}	y-velocity component
V_{z}	z-velocity component

v_{mean} mean inlet velocity

v_{rad} radial velocity

List of Figures

2.1 Representation of the cardio- and neurovascular system comprising the heart-brain connection (top left), the heart (mid bottom), and the Circle of Willis (top right). Within the heart-brain connection, the aortic arch is marked with a black circle to visualize the connection to the heart. Moreover, the Circle of Willis is marked as well with a black circle, which is shown in detail on the right [122, 239]. 7
2.2 Three types of intracranial aneurysms separated by shape: Wide-necked bifurcation aneurysm (left), fusiform aneurysm (middle), and saccular aneurysm (right). 8
2.3 Visualization of the three treatment options of coil embolization (Coil - Left) [302], flow-diverter stents (Flow Diverter - middle), and flow disrupter (right). 10
2.4 Patient specific and generalized flow curves by Jansen et al. [135] 18
2.5 Turbulent kinetic energy (TKE) of representative intracranial aneurysm cases. Figure adapted form [297] 19
2.6 Visualization of velocity streamlines through an intracranial aneurysm treated with a Coil. Figure adapted from [61]. 20
2.7 Visualization of velocity streamlines in a saccular intracranial aneurysm (IA) treated with a flow diverter stent. Figure adapted form [155] 21
2.8 Visualization of velocity streamlines in a saccular intracranial aneurysm (IA) treated with a Woven EndoBridge device (WEB). Figure adapted form [7] 22

3.1 Underlying workflow of pathological Circle of Willis (CoW) model creation: Cropping the complex (red) and trimmed (blue) CoW model at the two locations for the IA implementation. Additional cropping of the peri-aneurysmal models by excluding dome and parent vessel from the domain. Stitching of the patient-specific IAs onto the complex and trimmed physiological CoW model. 35
3.2 Top: Patient-specific peri-aneurysmal models 1-3 with the five aneurysms in total (peri-aneurysmal model 1: IA A & B, peri-aneurysmal model 2: IA C & D, peri-aneurysmal model 3: IA E). Black arrowheads depict the inlets, colored arrows the outlets. Bottom: Zoom on each IA (A-E), including the visualization of the parent vessel (blue) and ostium surface area (brown). Note that IA A and C were used for stitching on the CoW vasculature. 35
3.3 Presentation of the 24 variations in segmentation of peri-aneurysmal model 3 including IA E. Again, black arrowheads depict the inlet and colored arrows the outlets. 26 groups participated in providing segmentations of the peri-aneurysmal model, while 2 groups needed to be excluded from the data analysis. 38
3.4 Inflow boundary condition (BC)s for the three inlets basilar artery (BA), left internal carotid artery (ICA), and right ICA from phase-contrast magnetic resonance imaging (PC-MRI) measurements for the CoW inlets and inflow curve data derived from literature for the vessel model inlets (1-3). Note, that the literature data were additionally scaled to be used for the CoW model inlets when comparing the intra-aneurysmal hemodynamics of IA A and IA C within the vessel models and within the trimmed CoW vasculature. 40
3.5 Qualitative representation of the hemodynamic parameters time-averaged wall shear stress (TAWSS), oscillatory shear index (OSI), and velocity (v) inside the dome of IA A and IA C within the complex and trimmed CoW vasculature model. Hemodynamic parameters are normalized by their mean value. 41

3.6 Representation of the neck inflow rate (NIR), average wall shear stress (WSS), and maximum (max) WSS over one cardiac cycle for IA A and IA C within the complex and trimmed model. Additionally, the mean values inside the IA dome of velocity, OSI and TAWSS are presented below. 42
3.7 Qualitative and quantitative hemodynamics within IA E based on the 24 varying segmentations and BC2. The oscillatory velocity index (OVI) and time-averaged wall shear stress (TAWSS) are shown qualitatively, while the mean inside the IA dome of TAWSS is as well presented quantitatively together with the mean TA velocity (v). 44
3.8 Qualitative illustration of the five IAs analyzed with the varying boundary condition (BC)s (BCs). The IA models are presented for one chosen segmentation. Time averaged wall shear stress (TAWSS) and kinetic energy (KE) are shown over all five BCs. 46
3.9 Plots of the resulting hemodynamic parameters mean time averaged (TA v) velocity, kinetic energy ratio (KER), mean TA wall shear stress (TAWSS), and low shear area (LSA) inside the five aneurysm models with the chosen segmentation. The results are presented over the five boundary condition (BC)s (BC1-5). 47
3.10 Left: Qualitative illustration of the time-averaged (TA) velocity on five chosen planes inside the trimmed Circle of Willis vasculature. Plane locations are shown on the top. Middle: Temporally averaged flow rates at each plane over all five BCs. Right: Time resolved flow rates at each plane over all five BCs. 48
3.11 Resulting flow splitting distribution from the five boundary condition (BC)s (BC1-BC5) for each outlet (O1-O3) of vessel model 3 (IA E). 50
3.12 Visualization of the differences in hemodynamics based on varying segmentations and boundary conditions (BCs). The varying boundary condition (BC)s are shown coloumnwise and the different segmenations row-wise. Left: Time-averaged wall shear stress (TAWSS) of IA E over the 24 segmentations and five boundary condition (BC)s. Right: Isosurface of the TA velocity (v) of IA E over the 24 segmentations and five BCs. 51
3.13 Plots of the mean values inside the dome of IA E of the time-averaged (TA) wall shear stress (TAWSS) and TA velocity. X-axis is depicting the segmentations, while the boundary condition (BC)s (BCs) are presented each with a unique color. Small circles are the groups defined as outliers. 52
3.14 Boxplots presenting the distribution of the hemodynamic parameters mean velocity, kinetic energy ratio (KER), mean vorticity (ω), mean time-averaged (TA) wall shear stress (TAWSS), normalized TAWSS (nAWSS), and low shear area (LSA) over all segmentations. Blue boxes represent the distribution over segmentations with outliers (marked with a) and red boxes the distribution without outliers (marked with b). 53
3.15 Qualitative hemodynamics of IA A and IA C within the trimmed CoW vasculature. Time-averaged wall shear stress and time-averaged (TA) kinetic energy are presented over the five boundary condition (BC)s (BCs). 54
3.16 Plots of the temporally and spatially averaged parameters velocity, time-averaged wall shear stress (TAWSS), kinetic energy ratio (KER), and low shear area (LSA) within the two IAs A and C over the five outlet boundary conditions (BCs). Note that the y-axis, depicts values of low ranges (TAv: 0.01-0.04 $\mathrm{m\,s^{-1}}$; TAWSS: 0.1-0.7 Pa; KER: 5-12$\cdot 10^{-3}$; LSA: 98.8-99.6) 55

4.1 Representation of the incorporation of exercise into medical imaging processes. Figure adapted from [18, 1, 194]. 62
4.2 Visualization of the mitral valve once in healthy condition (left) and with regurgitation (right) namely mitral valve insufficiency (MI). Figure adapted from [293]. 67
4.3 Visualization of the patient cohort of this chapter. a) For each patient the end-systolic geometry of the ventricle is shown for the rest (re) and exercise (ex) condition. The stage of the mitral valve insufficiency (MI) is shown in brackets for each case. b) The processed aneurysm model used for simulations is presented. For both, a) and b) the inlet and outlets are marked with blue (inlet) and orange (outlet) arrows. 71
4.4 Mean time-averaged (TA) velocity magnitude inside the ventricle over six mesh base sizes included in the sensitivity analysis. 73
4.5 Visualization of the node relation between the initial mesh (points P_1, P_2, and P_3) and the meshed surface (point C) and the according calculation of α and β. 74

4.6 Representation of the processing steps of the neurovascular analysis in this chapter, starting with the phantom model creation (a). This model was used in the experimental particle tracking velocimetry (PTV) setup (b). Moreover, the model was used to establish the virtual model for the simulations (c-e). Inflow and outlet pressure curves measured during the experiments were provided to CFD (f). 75

4.7 Root mean square (RMS) of the velocity components at four representative probes inside the vascular domain obtained from three different meshes. 78

4.8 Qualitative visualization of the kinetic energy distribution in the systolic and diastolic state of each patient during rest and exercise. The resulting transient intra-ventricular kinetic energy (KE) normalized by the end diastolic volume (EDV) are shown in red below each visualization together with the change in volume (V) over time in green. 81

4.9 Qualitative distribution on plane 1 (left) and plane 2 (right) of the time-averaged (TA) velocity magnitude normalized by each plane's spatial mean value. DNS - direct numerical simulation; LRNS - low-resolution numerical simulation; PTV - particle tracking velocimetry. 85

4.10 Violin plots of time-averaged (TA) velocity magnitude (v mag) normalized by each plane's spatial mean value. Violins are shown for each heart rate (HR) 1-3 for the experiments (shake-the-box - STB), direct numerical simulation (DNS), low-resolution numerical simulation (LRNS), whereas the results of the two simulation approaches were further voxelized (vox) to match the STB grid size. 86

4.11 Qualitative distribution on plane 1 (left) and plane 2 (right) of the time-averaged (TA) vorticity magnitude normalized by each plane's spatial mean value. DNS - direct numerical simulation; LRNS - low-resolution numerical simulation; PTV - particle tracking velocimetry. 87

4.12 Violin plots of time-averaged (TA) vorticity magnitude (ω mag) normalized by each plane's spatial mean value. Violins are shown for each heart rate (HR) 1-3 for the experiments (shake-the-box - STB), direct numerical simulation (DNS), low-resolution numerical simulation (LRNS), whereas the results of the two simulation approaches were further voxelized (vox) to match the STB grid size. 88

4.13 Root mean square (RMS) of the velocity magnitude (v) and vorticity magnitude (ω) of chosen probes inside the intracranial aneurysm model. The RMS are shown for the two numerical solvers (direct numerical simulation - DNS; low-resolution numerical simulation (LRNS)) over the three heart rates (HR) 1-3. The probes are separated by location, depicting a loop around the aneurysm dome, the middle of the dome, the bifurcation area (left and right) and the inlet area. 90

4.14 Transient velocity magnitude over one cardiac cycle of six chosen probes for the two numerical solvers direct numerical simulation (DNS) and low-resolution numerical simulation (LRNS). 92

4.15 Transient vorticity magnitude of chosen probes for the two numerical solvers direct numerical simulation (DNS) and low-resolution numerical simulation (LRNS). 93

4.16 Power spectral density (PDS) of chosen probes for the two numerical solvers direct numerical simulation (DNS) and low-resolution numerical simulation (LRNS). 94

5.1 Visualization of the Contour Neurovascular System (Contour) pulled out of catether but not fully extracted on the left. The shape memory induces the recovery of the umbrella-like shape. On the right, the Contour is shown during deployment into a wide-necked bifurcation aneurysm. Figure adapted from [65]. 101

5.2 Visualization of the conventional flow-diverter stent (FDS) extracted and during deployment in an IA with a catheder. Figure adapted from [219]. 104

5.3 Visualization of the WovenEndoBridge embolization device (WEB) device extracted and during deployment in an IA with a catheder. Figure adapted from [74]. 106

5.4 The underlying complex methodology pipeline used in this chapter. The pipeline is structured into six subitems marked with a-f. a) Representation of the database from intervention including two follow up (FU)s (patient-specific data) and from experiments (phantom model data). b) Medical imaging of the two datasets including the imaging of the Contour. c) Workflow to extract the true aneurysm dome from the pre-state to be stitched on the post-interventional and FU states of the patient-specific data. d) Processing pipeline to digitalize the Contour from medical imaging for the use in the numerical simulations. e) Workflow to achieve the correct placement of the Contours inside the virtual phantom models. f/g) Performance of hemodynamic simulation based on in vivo (f) and in vitro (g) based data. 109

5.5 Visualization of the four phantom models M1-M4 used in this chapter. 110

5.6 Flow (mL) and pressure (Pa) curves for the phantom models. At the inlet a massflow was set (shown in red on left y-axis) and at the outlet a pressure curve (shown in blue on the right y-axis). For each model without (M1-M4) and with (C1-C10) Contour the resulting curves are presented. On the bottom, the phantom model is shown depicting the inlet and outlets. Additionally, the flow curve based on the literature, which was used for the patient-specific data is presented. 112

5.7 The ostium extraction for the patient-specific and phantom data is shown on the top (a). On the bottom (b), the data analysis of the patient-specific data regarding the morphological interaction between ostium surface and Contour is presented. 115

5.8 Qualitative comparison of the scanned (purple) and virtually mimicked (green) Contour for four representative cases, including a configuration from each phantom model size (M1 C1, M2 C3, M3 C6, and M4 C10). 117

5.9 Resulting qualitative variations due to method adjustments necessary to implement the virtual analysis of the treatment outcome due to Contour and the related comparison to in vitro investigations. 118

5.10 Comparison of resulting velocity distribution from phase-contrast magnetic resonance imaging (PC-MRI) and CFD, captured on three planes through the aneurysm model (transverse, saggital, and coronal) presented for all cases without Contour and for one example per IA size with deployed Contour (C1, C3, C6, and C10). Due to metal artifacts, the flow around the Contour could not be captured after treatment (marked with black arrows). 119

5.11 Distribution of velocity magnitude captured with phase-contrast magnetic resonance imaging (PC-MRI) and CFD, presented for all cases without Contour (M1-M4). Dashed vertical lines depict the median values. 120

5.12 Time-dependent pressure curves at the IA tip measured with phase-contrast magnetic resonance imaging (PC-MRI) and CFD, presented for all cases without Contour and for one example per IA size with deployed Contour (C1, C3, C6, and C10). 121

5.13 Modeled (M1-M4) and patient-specific (P1-P8) aneurysm cases before (left) and after (right) Contour deployment. Once shown with transparent wall to visualize the aneurysm shape and Contour position, once with the vessel wall colored with time-averaged (TA) wall shear stress (TAWSS). 123

5.14 Post-interventional treatment effect (TE) in % of all cases for the hemodynamic parameters neck inflow rate (NIR), time-averaged (TA) wall shear stress (TAWSS), velocity (v), kinetic energy (KE), inflow concentration index (ICI), and oscillatory shear index (OSI). 125

5.15 Outflow diversion into the two side branches of the phantom models. The proportion of the total outflow is shown on the left and the treatment effect (TE) comparing the case with and without Contour on the right. 127

5.16 Qualitative visualization of the time-averaged (TA) velocity (v) distribution on the ostium surfaces of the six patient-specific cases including follow-up analysis. The according vessel model in pre-state is shown on the left with the ostium colored in blue. Additionally, the circular distances from the Contour crossing the ostium surface to ostium neck curve are shown as pie charts below each ostium. 129

5.17 Longitudinal flow diversion into left and right vessel branch of the six patients including a follow-up investigation. For each time point (post-interventional (post), first follow-up (FU1) and second follow-up (FU2)) the treatment effect (TE) is shown in %. 131

5.18 Longitudinal representation of the spatially averaged values of uncovered ostium area (UOA) by the Contour, the Contour coverage (CC) by the aneurysm dome, the mean neck inflow rate (NIR) and inflow concentration index (ICI), the mean velocity (v) inside the IA dome, and the time-averaged (TA) wall shear stress on the aneurysm dome wall (TAWSS) for the six cases (P1, P2, P5, P6, P7, P8). The x-axis depicts the months passed after intervention. 132

List of Tables

2.1 Overview over the medical imaging approaches including their radiation, highest possible resolution, and clinical application. . . . 11

3.1 Representative studies analyzing segmentation variability in regard of segmentation routine (varying research groups), segmentation software (Commercial: Mimics, Materialise; Open Source: 3D Slicer, The Slicer Community), and segmentation algorithm (Region Growing Threshold, Chan-Vese model, Threshold-Based Level Set). . . . 28
3.2 Representative studies investigating the circle of Willis (CoW) including varying outlet counts and pathologies. . . . 29
3.3 Inlet area of the circle of Willis (CoW) models at each of the three inlet branches, respectively (left and right internal carotid artery (ICA) and basilar artery (BA)). Shown together with the outlet count and sum over all outlet cross-sectional areas for the complex and reduced model. . . . 37
3.4 Overview of the simulations conducted for this chapter, classified using model basis, source (PC-MRI or literature (Lit.)) of inflow boundary condition (BC), chosen outlet boundary condition (BC) and resulting simulation (Sim.) count. . . . 39
3.5 Splitting values of the five aneurysm cases with IA A & B and IA C & D being located at the same vessel. The percentage deviation of each splitting value to its counterpart calculated with BC5 is shown in brackets. . . . 45
3.6 Splitting values of the five BCs of the trimmed CoW model. The percentage deviation of each splitting value to its counterpart calculated with BC5 is shown in brackets. . . . 45
3.7 Averaged deviation from mean value before and after exclusion of segmentation outliers in % over the five boundary condition (BC)s (BCs) (top rows) and before and after exclusion of BC1 and 3 in % over the five BCs (bottom row). The subsequent reduction is shown in brackets after each value pair. Chosen hemodynamic parameters: Vorticity (ω), kinetic energy ratio (KER), low shear area (LSA), normalized time-averaged (TA) wall shear stress (nAWSS). . . . 52

4.1 Patient data of ventricular pathologies used in this chapter including the mitral valve insufficiency (MI) state from I-III and one clipped (cl) case, the captured time instances (n), the heart rate (HR), the end systolic volume (ESV), the end diastolic volume (EDV), and the ejection fraction (EF). All data are presented during rest and exercise conditions. 72
4.2 Chosen heart rates and resulting inflow conditions comprising the mean inflow velocity and Reynolds number (Re) for the aneurysm investigation under rest and exercise. . . . 72
4.3 Detailed key settings of the two simulation approaches for the neurovascular flow simulation to resolve high-frequency fluctuations, Low resolution numerical simulation (LRNS) and direct numerical simulation (DNS). . . . 79
4.4 Resulting hemodynamics inside the patient data under rest (re) and exercise (ex). The p-value describes the statistical comparison between rest and exercise per parameter. Kinetic energy (KE); end-diastolic volume (EDV); velocity (VEL); vorticity (ω); maximum systolic (max sys); maximum diastolic (max dias); standard deviation (SD). . . . 82
4.5 Resulting hemodynamics inside the ventricles averaged over patients 1-5 and patients 6-10 to compare the effect of the MI stages. Kinetic energy (KE); end-diastolic volume (EDV); velocity (VEL); maximum systolic (max sys); maximum diastolic (max dias); standard deviation (SD). . . . 83

4.6 Mean normalized time-averaged (TA) velocity magnitude (v) values at planes 1 and 2. . 85
4.7 Mean normalized time-averaged (TA) vorticity magnitude (ω) values at planes 1 and 2. . 89

5.1 Contour size deployment guideline. 102
5.2 In vivo analyses conducted to assess the performance of the Contour Neurovascular System. For each study the count of included patients, the highest occlusion rate at last follow up in months (m) and complications that occurred are listed. 103
5.3 In vivo analyses conducted to assess the performance of the flow diverter stents. For each study the count of included cases, the highest occlusion rate at last follow up in months (m) and complications that occurred are listed. 105
5.4 In vivo analyses conducted to assess the performance of the WovenEndoBridge (WEB) device. For each study the count of included cases, the highest occlusion rate at last follow up (FU) in months (m) or years (y) and complications that occurred are listed. 107
5.5 Overview over the model basis of the in vitro based data. For each case M the implanted Contour variations (C) and sizes are presented, together with the aneurysm sizing parameters intracranial aneurysm (IA) height, neck diameter (D), and dome diameter (D). . . . 110
5.6 Overview over the patient-specific in vivo data including the medical imaging applications digital subtraction angiographic (DSA) or computed tomographic angiography (CTA). The months after intervention are shown in brackets behind the imaging for FU1 and FU2 caes. Additionally, the employed Contour size as well as the aneurysm specific parameters sac volume (V) and ostium area (OA) for the pre-interventional state are demonstrated. Pre-interventional (pre), post-interventional (pos), first follow-up (FU1), second follow-up (FU2). 111
5.7 Overview over the simulations conducted for the content of this chapter, divided by medical imaging basis and the states after intervention. First follow-up (FU1), second follow-up (FU2). 115
5.8 Comparison of mean strut thickness, mean diameter and total area of the segmented (µCT) and fitted (CAD) Contour for the three in vitro Contour sizes 5 mm, 11 mm, and 14 mm. Parameters are averaged over each Contour size. 117
5.9 Overall mean value of spatially and temporally averaged parameters without Contour (pre-interventional) and with Contour (post-interventional) presented for the cases based on in vitro data (left) and on in vivo data (right). Mean values and standard deviations (SD) are shown together with the according p-value. Significant parameters reduced by the placement of the Contour for the cases analyzed are marked with a '*'. 124
5.10 Mean values of the months, proportion of uncovered ostium area (UOA) and Contour coverage (CC) in % over all patient cases per time instant. For the hemodynamic parameters velocity, time-averaged (TA) wall shear stress (TAWSS), neck inflow rate (NIR), and inflow concentration index (IC) the mean values of the treatment effect are presented in %. Statistical comparison of hemodynamic parameters with UOA showed significant relation (marked with *). 133

Chapter 1

Introduction

Outline

In this chapter the need for improvement of image-based blood flow simulations is stated and the related aspects explained. The structure of the thesis and the aim of each project conducted are presented.

The human heart pumps approximately 10,000 liters of blood per day through the arterial and venous vessel network, ensuring the delivery of oxygen and nutrients essential for sustaining life [266]. Blood flow through this network plays a critical role in maintaining physiological function. Consequently, vascular diseases that disrupt this blood flow can severely impact human health by compromising oxygen and nutrient supply. These conditions can affect any vessel in the body, manifesting, for example, as widenings, such as aneurysms, or narrowings, such as stenosis. Additionally, diseases affecting the complex structure and function of the heart can further exacerbate the risks associated with impaired blood flow. Studying vascular diseases is therefore crucial for understanding their formation, progression, and potential for complications such as rupture. Furthermore, such research plays an essential role in improving risk assessment and optimizing treatment planning to mitigate their impact on patient health.

Beyond in vivo investigations using medical imaging and clinical practices, in silico studies of blood flow dynamics in arterial vessels have become a significant area of research over the past four decades. Computational hemodynamic analysis based on computational fluid dynamics (CFD) offers valuable insights into the formation, growth, and risk of vascular diseases, supplementing clinical investigations. CFD studies are particularly beneficial for treatment planning, as computer-aided models enable us to evaluate the effectiveness of treatment devices without posing risks to patients. This approach not only enhances understanding of vascular pathologies but also contributes to safer and more effective clinical management strategies. Highly severe pathologies with life-threatening risk can occur in the neuro- and cardiovascular system. In case of an intracranial aneurysm (IA), which is a disease occuring in the neurovascular vessels, these investigations can give insights especially in the assessment of rupture risks. IAs are localized widenings of cerebral blood vessels with a prevalence of approximately 3.5 % in the general population [325]. IAs are typically detected through medical imaging of cerebral arteries, however, as IAs often remain asymptomatic, they may go undetected for long periods or even throughout a person's lifetime unless discovered incidentally. In some cases, patients experience symptoms such as headaches, prompting medical imaging scans that lead to diagnosis. While the annual risk of rupture for an IA is relatively low, approximately 0.006 %, rupture events can result in life-threatening complications, such as subarachnoid hemorrhage [76].

1.1 Motivation

The investigation of arterial neuro- and cardiovascular vessel hemodynamics using CFD has become a widely adopted approach in biomedical research due to its ability to provide detailed insights into complex flow dynamics within the vasculature. Despite its growing popularity and potential, CFD is not yet routinely applied in clinical settings, primarily because of limitations in replicating realistic blood flow conditions. These limitations arise from the necessary and often unavoidable assumptions inherent in CFD simulations, including simplified boundary condition (BC)s, inadequate representation of vessel wall properties, and the lack of patient-specific flow data. CFD simulations are typically derived from medical imaging data, which is predominantly captured under resting conditions. Consequently, exercise-induced hemodynamic changes which are critical for understanding physiological and pathological variations are rarely incorporated. This lack of dynamic representation may result in incomplete or inaccurate predictions of blood flow behavior under physiologically relevant conditions, limiting the clinical relevance of the simulations.

The continuous development of new medical devices poses additional challenges. Tailored in silico methodologies are required to evaluate their effectiveness and optimize their designs, particularly when patient-specific conditions are considered. CFD modeling has the potential

to play a critical role in assessing the performance of a device before clinical implementation, reducing the risks associated with invasive procedures and enabling patient-specific treatment optimization. Moreover, the lack of robust validation against experimental or clinical data remains a significant barrier to the clinical adoption of CFD. Validation using large-scale clinical datasets, post-treatment follow-up data, or in vitro experimental data is essential to build confidence in the predictive accuracy of these models. Despite these challenges, the clinical application of CFD is both feasible and valuable. Addressing current limitations through incorporating dynamic conditions, improved patient-specific modeling, and rigorous validation could unlock its full potential. Such advancements would enhance diagnostic precision, improve treatment planning, and provide a safer, more efficient pathway for evaluating novel medical devices. Ultimately, CFD offers the potential to bridge the gap between computational research and clinical practice, advancing vascular healthcare and patient outcomes, and providing insights into the most impactful modeling choices for improving the accuracy, reliability, and applicability of CFD simulations in vascular diagnostics and treatment planning.

1.2 Contribution and structure

The primary objective of this thesis is to refine and adapt CFD methodologies for medical applications, with a particular focus on identifying key factors that enhance the clinical applicability of CFD simulations. To achieve this, the study systematically evaluates critical modeling parameters that influence the accuracy and reliability of simulations in a clinical setting. A major emphasis is placed on the segmentation of medical imaging data, the extent of vasculature included in the analysis, and the selection of outlet BCs, particularly in the context of IA simulations. By assessing the impact of these factors on hemodynamic predictions, this study aims to establish best practices for improving the fidelity of CFD models in cerebrovascular research. Furthermore, the scope of this work extends to investigating the effects of rest and exercise conditions on vascular hemodynamics, with a particular focus on cardiac function. Since exercise-induced variations in blood flow dynamics are often overlooked in CFD studies, incorporating these physiological conditions is essential for achieving more realistic simulations that can better support clinical decision-making.

Beyond optimizing CFD applications, this thesis also explores a novel treatment approach for IAs by developing an in silico methodology based on in vitro investigations. This integrated approach enables the validation of computational simulations and facilitates an extensive examination of the proposed treatment strategy using patient-specific data. By combining experimental and computational techniques, this study aims to assess the effectiveness of the intervention, providing a comprehensive evaluation of its hemodynamic impact and clinical feasibility. Ultimately, the findings of this work seek to advance the development of innovative, patient-specific treatment options for intracranial aneurysms.

As a basis, the background information will be first explained including the medical and technical background information (Chapter 2). The main body of this thesis is then separated into three parts, starting with the improvement of image-based blood flow simulations for IAs focussing on the segmentation, chosen vasculature, and outlet BC in Chapter 3. The second part (Chapter 4) comprises the investigation of rest and exercise condition on the neuro- and cardiovascular hemodynamics, including the use case of a cardiovascular pathology (mitral valve insufficiency (MI)) and a neurovascular pathology (IA). The third part of this thesis deals with establishing a realistic workflow to investigate the efficacy of a novel endovascular treatment device for IAs and further the examination of the according efficacy of the device based on patient-specific data in Chapter 5. Each chapter starts with a short review that is specific to the

chapter's topic, followed by the outline of the contribution and the research questions asked. The methodology is then explained, followed by the results and discussion. The concluding findings for each part are summarized at the end of each chapter and the limitations are listed. Finally, the overall summary of the main findings and the future work will be proposed to conclude the thesis.

Chapter 2

Background

Outline

This chapter provides the theoretical foundation for this thesis, beginning with an overview of the medical background of the cardiovascular and neurovascular systems, as well as the pathology of IA. Additionally, it presents a summary of medical imaging modalities used to capture both healthy and pathological vascular structures and discusses the application of CFD for resolving hemodynamics in these vessels. The chapter concludes with a review of recent advancements in the application of fluid dynamics in the medical field, highlighting the most commonly used methodological approaches and underlying assumptions.

The first part of the background describes the medical basis of this thesis. Focus was set on the cardio- and neurovascular system and the mainly investigated pathology. The IA occurs in the human neurovascular artery system, which comprises the brain supplying arteries and the arteries inside the brain, therefore representing a localized dilation or bulge in the arterial wall caused by structural weakness. They pose a significant risk of rupture that can lead to life-threatening subarachnoid hemorrhage and other severe neurological complications. This section first explains the anatomy of the underlying geometrical circumferences of the heart-brain-connection, the circle of Willis (CoW) and the pathology of IAs. Further, the classification and occurence as well as the rupture risk of IAs are addressed. Lastly, it explains the current treatment opportunities as well as the basis of medical imaging options to scan the anatomy and pathology.

2.1 Anatomy of the cardio- and neurovascular system

The heart is the pump of the human body, supporting the arterial system with oxygenated blood. The heart consists of four parts, two ventricles (left and right ventricle) and two according atria (left and right) as shown in Figure 2.1 on the bottom. The right atrium receives the deoxygenated blood from the venous system, which is carried on to the right ventricle. The right ventricle then pumps the deoxygenated blood further through the pulmonary artery into the lungs. In the lungs the blood is oxygenated and further transported through the pulmonary vein to the left atrium.

The heart comprises four heart valves separating the ventricles from the atria, and from the artery and vein. Namely the tricuspid valve, separating the right atrium from the right ventricle and the pulmonary valve, separating the right ventricle from the pulmonary artery. The mitral valve, separating the left atrium from the left ventricle and the aortic valve, separating the left ventricle from the aorta [267]. From the left atrium the oxygenated blood is carried on to the left ventricle. The left ventricle then supplies the arterial system with the oxygenated blood. The oxygenated blood is pumped from the left ventricle into the aortic arch, where it is separated into the different arteries supplying the human body with oxygen. The circulation completes with the oxygenated blood moving through the arterial into the venous system and then back to the right atrium [267]. In Figure 2.1 heart-brain-connection is shown comprising the aortic arch, the brain-supplying arteries, and the CoW.

When looking at the neurovascular system, for each human being, the neurovascular arterial system is individual and, consequently, different structures appear. In general, if the structure is fully developed, which occurs in approximately 20 % of the population, four arteries originating from the aortic arch supply the brain [35], namely the left and right internal carotid and the left and right vertebral arteries. These are presented in Figure 2.1, together with the remaining arteries leaving the aortic arch to different body parts. The four brain-supplying arteries form into a circular system through the left and right cerebral hemisphere leading into the cerebral veins [303]. This circular system is the so called CoW, with the circular structure helping to ensure the oxygenated blood supply if arterial pathologies occur [303, 312]. Describing in flow direction, first the vertebral arteries combine to the basilar artery from which the posterior and anterior inferior arteries branch off.

The basilaris then splits into the left and right posterior communicating arteries, which branch into the left and right middle cerebal artery (MCA), as shown in detail in Figure 2.1 on the top right. The left and right internal carotid arteries split into the left and right arterior commu-

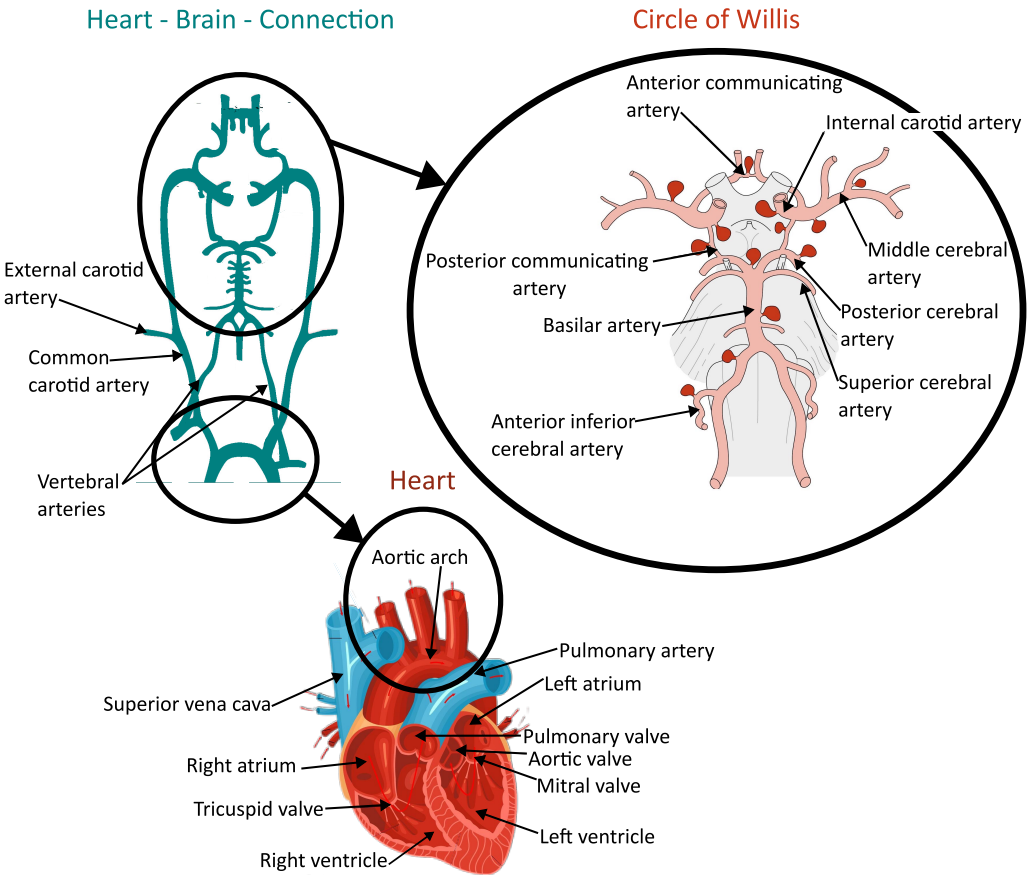


Figure 2.1: Representation of the cardio- and neurovascular system comprising the heart-brain connection (top left), the heart (mid bottom), and the Circle of Willis (top right). Within the heart-brain connection, the aortic arch is marked with a black circle to visualize the connection to the heart. Moreover, the Circle of Willis is marked as well with a black circle, which is shown in detail on the right [122, 239].

nicating arteries and the left and right MCAs. With 80 %, a majority of the population does not comprise a fully developed CoW. Options which can occur here are missing connections and an earlier or later branching [312]. Moreover, the size of the arteries vary specifically for each person, ranging between 0.5-3 mm for the posterior communicating artery (PCA) and 2-4 mm for the basilar artery.

Various pathologies can affect the cerebral arteries, for instance an IA, an artery stenosis or an arterial malformation [212]. All these may remain asymptomatic or undetected, without showing an immediate danger [110]. Arterial stenosis is the narrowing of an artery due to plaque buildup and can lead to ischemic stroke by reducing the blood supply to the brain. Arteriovenous malformations are tangled blood vessels that can cause chronic compression of brain tissue, in severe cases leading to cerebral hemorrhage [197]. IAs occur when the arterial wall weakens and expands at specific locations, which may cause a subarachnoid hemorrhage if the IA ruptures. In many cases, this rupture can result in severe neurological disease or even death [251].

2.2 Intracranial aneurysms

The main focus in this thesis is set on studying IAs investigating hemodynamics and relating it to clinical outcomes and decision making. Especially due to high risk factors, early detection and prevention of IAs is important, however, detecting IAs is often challenging since medical

imaging is required, which is costly and not routinely performed, unless there are specific symptoms or risk indicators [212].

Occurence

IAs occur with an estimated prevalence of 2-5% in the population [325]. This variation can be explained by differences in study populations and screening methods. Moreover, occurence depends on specific population subgroups and age demographics [289]. Some studies found a relation between genetics and the occurence of IAs [210], additionally, a higher number of IAs is found in women than men, but no reasoning was found for this up to today. Regarding the geographical spread, more IAs are found in Finnish and Japanese population than North American and European population. Higher risks of IA occurence and rupture appear also based on factors such as hypertension or smoking [103]. Since many IAs remain asymptomatic, the actual number of cases might be higher than detected through routine medical procedures. The risk of rupture, however, is influenced by factors such as aneurysm size, location, and patient health.

Classification

IAs can be classified in different structures and systems, inlcuding size and growth potential, location, morphology and rupture status, of which the latter three are most important for this thesis. Regarding location, IAs can develop anywhere in the cerebral vasculature, but common locations in the anterior and posterior circulation exist. Most IAs occur in the anterior circulation, especially the anterior communicating artery (ACA), internal carotid artery (ICA) and MCA. Fewer IAs develop in the posterior circulation, namely the vertebral artery (VA) and basilar artery (BA) [161]. Typical IA locations are demonstrated in Figure 2.1 in the detailed CoW visualization (top right). They build particularly in the bifurcation of arteries (so called bifurcation aneurysms) and less commonly at the side of a straight vessel wall (side wall aneurysm). In Figure 2.2, a bifurcation aneurysm is shown on the left and a side wall aneurysm on the right. The black circle depicts the expanded vessel wall. For the WNBA (left) the ostium is exemplarily shown in green. The ostium is the separating surface between the IA dome and the non-pathological parent vessel.

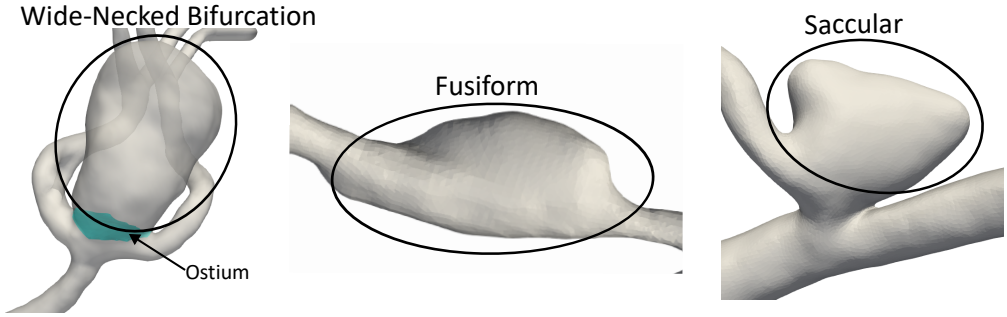


Figure 2.2: Three types of intracranial aneurysms separated by shape: Wide-necked bifurcation aneurysm (left), fusiform aneurysm (middle), and saccular aneurysm (right).

IA morphology can be intensively studied by analyzing distances and circumferences [71]. IAs can be classified in these general morphologies: saccular intracranial aneurysm (SIA), fusiform intracranial aneurysm (FIA), and wide-necked bifurcation aneurysm (WNBA). WNBAs can be recognized by their typical wide neck, which is defined by a dome-to-neck ratio of less than 2 [191]. They mostly occur at bifurcations as shown in Figure 2.2 on the left. FIAs have a circumferential shape evenly spread around the vessel as shown in Figure 2.2 in the middle.

SIA have a bulb shape with a recognizable neck and make up 80-90% of all IAs as shown in Figure 2.2 on the right. Additionally, dissecting IAs can occur, which develop inside the arterial wall when blood is collected between the arterial wall layers due to a ripped part of the wall [301].

Rupture

IA rupture appears when the aneurysmal wall breaks and the blood leaks into the surrounding tissues [161]. Approximately 8-10 out of 100,000 IAs rupture annually [325]. The probability of IA rupture varies with its morphology and location. For instance, IAs occuring in the posterior circulation are associated with a higher rupture risk than in the anterior circulation [301]. Moreover, larger IAs are more likely to rupture than smaller ones [161]. Rupture can lead to subarachnoid hemorrhage, which can have fatal consequences like neurological damage, coma, or death if not treated immediately.

Rupture risk assessment

To assess the rupture risk of an IA several factors play a role in defining and estimating. These factors can be divided in two categories: 1) accessible patient data (e.g. age, gender etc.), 2) accessible aneurysmal data (e.g. IA size, shape, location etc.) and 3) mathematically assessed data (e.g. hemodynamics).

- **PHASES Score:** The first category is determined as the so called PHASES-Score [32]. This score includes the aspects **P**opulation, **H**ypertension, **A**ge, **S**ize of IA, **E**arlier SAH from another aneurysm, **S**ite of aneurysm. As this is mainly patient data and data easily accessible by medical imaging, the PHASES-Score is currently partly used by physicians to estimate IA rupture risk. Additionally, the IA growth rate can be accessed by longitudinal medical imaging. A growth of an IA is as well associated with higher risk of rupture [300].

- **Morphology:** To measure the morphological parameters, the three-dimensional shape of the IA including surrounding vasculature has to be extracted. For this, medical imaging is needed to scan the arterial shape of the patient. The medical imaging scans are then used to establish three-dimensional geometries, which can further be analyzed morphologically and serve as a basis for hemodynamic simulations. Regarding morphological parameters, especially the nonsphericity index, the undulation index, elongation and flatness, ellipticity index, sphericity and aspect ratio show relation to rupture [71]. To analyze the patient-specific IA data numerically, further conditions for the boundaries and fluid modeling are needed.

- **Hemodynamic parameters:** For the estimation of hemodynamic parameters, numerical models and simulations are applied and, using statistical tests, the relation to rupture and the according rupture risk is assessed. Recent studies show that these numerical models can improve the prediction of rupture risk [180]. When looking at hemodynamic parameters, high and low wall shear stress (WSS), as well as low shear area (LSA) were associated to higher rupture risk. This also comprises a higher inflow angle and changes in flow pattern [180]. Moreover, flow instabilities feature a relation to rupture [142]. Nevertheless, in this field research is still needed to quantify the influence of each parameter.

Treatment options

If an IA is detected and the rupture prediction suggests a high risk or the patient declares themself in favor, IA treatment can be performed. Treatment can be divided into invasive and minimally invasive options. Within invasive treatment techniques, the IA is completely exposed by craniotomy and surgery performed on the open skull. The surgical techniques comprise clipping an IA, implementing a bypass or occluding the artery temporarily [332]. For minimally-invasive treatment methods, a catheter is placed using the transfemoral (at the thigh) or alternatively the transradial (at the wrist) access [311], which is then led to the cerebrovascular arteries. For this so-called endovascular treatment, different devices were developed in the past years to prevent rupture risk and/or help the IA heal [168].

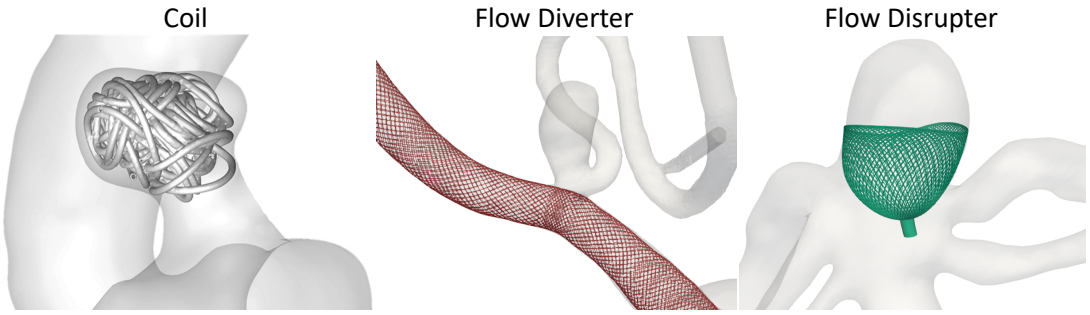


Figure 2.3: Visualization of the three treatment options of coil embolization (Coil - Left) [302], flow-diverter stents (Flow Diverter - middle), and flow disrupter (right).

- **Coiling:** Coiling is a wide-spread technique to treat IAs by placing the catheter directly into the sac and inserting a long coil wire to fill the sac with. This aims to isolate the sac from the active circulation by achieving dense packing and causing a blood clot to form quickly inside the aneurysmal sac, leading to IA occlusion. A sample case of a coil is presented in Figure 2.3 on the left. When a simple coiling method is not applicable, due to the wire reaching out of the sac, assisted coiling is employed. Here, a temporarily inflated balloon can be placed to block the IA neck (Balloon-Assisted Coiling). Alternatively, a stent is used for this block (Stent-Assisted Coiling) [309]. Coiling has its advantages against surgical techniques, however, it is limited in regard to efficacy in wide necked and large IAs or FIAs.

- **Flow Diverter:** In Figure 2.3 (middle) a flow-diverter stent (FDS) is shown, which is intended to treat IAs by recanalizing the IA sac and separating it from the circulation [332]. This aims to cause thrombosis formation in the IA sac and subsequent occlusion of the IA. These FDS can be either stents built by a braided mesh or are fully covered, with the latter being also important for dissecting aneurysms [331]. With FDS being especially advantageous in FIAs or wide necked IAs, drawbacks exist when deploying in bifurcation IAs due to occlusion of nearby vessels.

- **Intrasaccular Flow Disruption:** Intrasaccular Flow Disrupters are novel devices invented to overcome the drawback of FDS nearby vessel occlusion. They are especially invented to treat wide necked IAs and therefore also overcome limitations of coiling. Moreover, intrasaccular flow disruption is advantageous to coiling when looking at occlusion

rates [139]. The first intrasaccular flow disrupter is the WovenEndoBridge embolization device (WEB) (Sequent Medical, Aliso Viejo, California). It is placed directly inside the IA sac and was invented to cause immediate thrombosis [330]. The WEB shows a promising outcome for wide necked IAs and is additionally useful to treat ruptured IAs. Nevertheless, the WEB is restricted to a specific IA height and showed some complications during deployment [91]. To overcome these restrictions, the novel Contour Neurovascular System (Contour) (Stryker, USA) was developed and investigated within the last years (see Figure 2.3 (right)). The Contour is inserted into the IA neck, where it unfolds and clamps to reduce blood flow into the IA sac and cause blood stasis, leading to thrombosis [8]. Compared to the WEB the Contour can be employed independently from IA height and less interventional complications as well as higher occlusion rates occur [91]. Moreover, Contour shows promising outcome when applied in ruptured IAs [69].

2.3 Medical imaging

Due to technical improvements within the last decades, a wide range of medical imaging techniques exist to scan neurovascular arteries. These differ in clincial applicability, minimally accessible resolution and impairment of the patient. Four possible technical applications will be presented in this thesis: computed tomography angiography (CTA), digital subtraction angiography (DSA), magnetic resonance imaging (MRI), and ultrasound. Table 2.1 lists the four modalities and summarizes important facts.

Table 2.1: Overview over the medical imaging approaches including their radiation, highest possible resolution, and clinical application.

		Resolution		
Modality	Radiation	Spatial	Temporal	Clinical Application
CTA	Moderate ionizing	0.3 mm	250–500 ms	Vascular diseases, cardiac, pulmonary embolism
DSA	High ionizing	0.08–0.2 mm	Real-time	Vascular interventions
MRI	Non ionizing	0.5-5 mm	10-120 ms	Soft tissues, brain, oncology, functional studies
Ultrasound	Non ionizing	0.2–0.3 mm	Real-time	Obstetrics, cardiology, vascular flow studies

- **Computed Tomography Angiography:** CTA scanners use X-rays to create cross-sectional image slices of the human body. The scanner rotates around the patient and provides detailed images of the bones, blood vessels and soft tissues (brain, muscles, etc.). In general, CTA is used to detect tumors, infections and especially, important for this thesis, vascular diseases. X-rays carry a high ionizing radiation, which has been tried to reduce in the past years but is still a limitation regarding patient risk [10]. Details on resolution (spatial and temporal) are listed in Table 2.1.

- **Digital Subtraction Angiography:** With DSA, the arterial and venous vessels in the human body can be captured. The DSA scanner consists of a tube (the so called CT arm), which rotates around the patient who is lying on a carrier in the center. Two separate X-ray images are taken, one before and one after the injection of a contrast agent into the blood flow circulation of the patient. By subtracting the two scans (before and after injection), a clear view of the vessel is made possible without any background interference [136]. DSA is, like CTA, an imaging technique which implies ionizing radiation. Nevertheless, it features higher spatial resolution with a voxel size of down to 0.08 mm [85].

- **Magnetic Resonance Imaging:** MRI is a non-invasive imaging technique, which is based on strong magnetic fields and radio waves. These can generate detailed insights into the human organs and tissues without using ionizing radiation [29]. MRI scanners are operated sequences, determining the pulse strength and frequency, which are applied through software applications. Several different sequences exist to image brain and muscle tissue, bones, or flowing blood parameters, which can be applied depending on the application. MRI comes with a spatial resolution of 0.5-5 mm, decreasing with a rising temporal resolution (10-120 ms) [213]. One part of MRI is phase-contrast magnetic resonance imaging (PC-MRI), with uniquely combines morphological imaging and velocity data in a single scan [87]. Recent advancements, such as 4D PC-MRI, enable time-resolved, three-dimensional imaging with three-directional velocity encoding, allowing comprehensive analysis of human hemodynamics and retrospective flow evaluation. Its ability to study flow-related vessel wall parameters highlights its potential as a diagnostic tool in preemptive medicine, supported by improvements in computing power, data acquisition, and image processing. An additional option of tissue contrast within MRI comprises black blood magnetic resonance imaging (BBMRI), where the moving blood is suppressed and the vessel wall is highlighted within the imaging [116].

- **Ultrasound:** High-frequency sound waves are passed through human tissues to produce images of the internal organs and blood flow [314]. The real-time analysis makes it possible to monitor the blood flow velocity within a vessel as well as evaluate movements.Ultrasound does not involve any radiation and since this makes it to one of the safest medical imaging techniques, it is widely used in prenatal and pediatric care. Depending on the frequency applied, the spatial resolution in ultrasound ranges from 0.2 mm voxel size (high-frequency 7-15 MHz) to 3 mm (low frequency 2-5 Mhz). Regarding the temporal resolution, ultrasound comprises a real-time imaging, whereas typically 20 to 100 frames per second are captured and saved, depending on the scanner and captured structure [160].

Geometric modeling

Based on medical imaging, patient-specific data can be used to reconstruct the anatomy of the neurovascular vessels. The resulting three-dimensional models serve as input for the numerical simulations [282]. This aims to simulate the realistic fluid dynamics inside the complex neurovasculature. For this, medical images need to be segmented into 3D shaped geometries. Segmentation means that the 2D imaging slices will be converted into discrete nodes forming the shape of the wall of the neurovascular anatomy or pathology. Several tools can be accessed, wheras the basis for the segmentations conducted for this thesis was MEVISLab (Fraunhofer MEVIS, Bremen, Germany). Following the segmentation, the resulting 3D-models need further geometrical adjustments. These include smoothing the aneurysmal wall, removing holes and artifacts, and cutting the inlet and outlets perpendicular to the flow stream. These steps were performed in the modeling tool Blender (Blender Foundation, NL) in this thesis.

2.4 Computational Fluid Dynamics

CFD is a branch of numerical fluid mechanics dealing with the simulation of fluid flows using numerical methods. This applies to both liquid and gaseous fluids, such as blood in the vasculature or air in the respiratory tract. By integrating mathematical and numerical models with geometric representations derived from medical imaging, CFD plays a crucial role in medical

research, particularly in the analysis of neurovascular arteries and veins. To solve a numerical problem, an appropriate mathematical model must first be defined based on the specific application. These model specifications include, among other factors, the dimensionality, fluid flow characteristics, viscosity, and compressibility [81]. In this thesis, three-dimensional models are employed, and blood is assumed to be an incompressible fluid. The viscosity is considered either constant or variable, depending on the case study. Fluid flow can be analyzed using either a Lagrangian or Eulerian framework. In the Lagrangian approach, individual fluid particles are tracked over time, with their positions determined as a function of their initial location and time. Conversely, the Eulerian framework describes flow properties from a fixed spatial perspective, treating fluid properties as functions of spatial coordinates and time. The Eulerian approach is predominantly used in numerical and experimental flow studies.

Governing equations and numerical methods

The numerical simulation of fluid flow is based on fundamental fluid dynamic principles, which are expressed as partial differential equations. The most significant among these are the Navier-Stokes equations, which describe the conservation of momentum for a viscous fluid. These equations govern the flow behavior within control volumes represented in Cartesian coordinates, with fluid entering and exiting through the control volumes' boundaries. The conservation laws of mass, momentum, and energy collectively form a system of second-order nonlinear partial differential equations known as the Navier-Stokes equations. Since human blood is assumed to maintain a constant temperature over time, the energy conservation equation can be neglected in the simulations conducted in this thesis [269]. The derivation of these governing equations, along with the foundations of numerical modeling, has been extensively discussed in previous research [305, 269] and will not be elaborated further.

Due to the complexity of the Navier-Stokes equations, numerical methods are required for their solution, as analytical approaches are only feasible for highly simplified cases. The discretization process converts the continuous equations into algebraic equations by dividing the physical domain into small elements or control volumes. The most commonly used discretization techniques are the Finite Difference Method, Finite Volume Method, and Finite Element Method [119]. The discretization technique used here is the Finite Volume Method, which is widely applied in CFD as it formulates the conservation equations in their integral form and applies them to a finite number of control volumes within the domain. The flow variables are computed at the center of each control volume, and interpolation techniques are used to determine values at the volume surfaces. Unlike the Finite Difference Method, which is primarily suited for structured grids, FVM can be applied to any grid type due to its subdivision into control volumes. This makes it particularly advantageous for handling complex geometries, provided that all volume surfaces serve as boundaries between adjacent control volumes.

Direct numerical simulation and solver implementation

A high-fidelity computational approach employed in this thesis is direct numerical simulation (DNS), which directly resolves all turbulent scales by solving the full Navier-Stokes equations without any turbulence modeling. This method requires extremely fine spatial and temporal resolution, resulting in a substantial computational cost. The specific DNS methodology applied is detailed in section 4.5.5. The solvers used to solve the Navier-Stokes equations in this thesis are STAR-CCM+ and ANSYS Fluent, both of which are commercial CFD solvers with comparable performance. For DNS simulations, the in-house solver DINO was used, which was developed at the Laboratory of Fluid Dynamics and Technical Flows, University of Magdeburg [5, 2].

2.5 Hemodynamic parameters

Based on the performance of the CFD simulations, various hemodynamic parameters can be calculated to evaluate both the qualitative and quantitative behavior of fluid flow in cerebral vessels. Recent research has employed a wide range of parameters to assess the hemodynamics within IAs. However, there is no standardized framework or general consensus for categorizing and interpreting these parameters in relation to aneurysmal status. By incorporating hemodynamic parameters into the analysis, the role of blood flow dynamics in the development, progression, and treatment of neuro- and cardiovascular diseases can be more comprehensively understood. In addition to analyzing absolute parameter values, normalization plays a critical role in assessing vascular hemodynamics, particularly in studies involving IAs [247]. Normalization ensures comparability across varying patient data, enabling a more consistent evaluation of clinical outcomes. Given the inherent variability in CFD simulations of vascular pathologies, normalization can address absolute differences in parameters and relate results to their relative variations, facilitating more meaningful comparisons.

This thesis focuses on key hemodynamic parameters previously linked to vascular pathologies, especially the rupture risk of IAs. These parameters are derived from fundamental equations that provide the velocity components and tangential frictional forces along the vessel wall, specifically the WSS. This section outlines hemodynamic parameters, which form the foundation of the analysis in this thesis and is structured in two categories: flow-related parameters and wall-related parameters.

Flow-related parameters

Blood flow velocity describes the speed of blood flow through the vessels. Abnormal velocities can indicate stenosis, IAs, or flow disturbances. Vortex patterns are formations of swirling flow patterns, which can indicate pathological changes. Unstable or stagnant flow can lead to clot formation or vessel wall weakening [53, 45, 173]. Residence time refers to the time blood stays within a specific vascular region. Prolonged residence times can promote thrombosis or plaque formation [123].

The flow rate depicts the volume of fluid that passes through a given cross-sectional area per unit of time. In this regard, the neck inflow rate (NIR) describes the flow rate through the aneurysm neck plane. The area of the aneurysm neck is thereby the A_{ostium} and the area that is flowed through the $A_{flowedostium}$. The inflow concentration index (ICI) is the ratio of flow into the IA sac (Q_{IA}) related to the flow through the parent vessel ($Q_{parentvessel}$), see Equation (2.1).

$$ICI = \frac{\frac{Q_{IA}}{Q_{parent\ vessel}}}{\frac{A_{flowed\ ostium}}{A_{ostium}}} \tag{2.1}$$

Vorticity represents the rotation of fluid elements around their own axe and is represented by its three components of each coordinate direction x, y, z, using the velocity components v_x, v_y, v_z see (2.4).

$$\zeta_x = \frac{\partial v_z}{\partial_y} - \frac{\partial v_y}{\partial_z} \tag{2.2}$$

$$\zeta_y = \frac{\partial v_x}{\partial_z} - \frac{\partial v_z}{\partial_x} \tag{2.3}$$

$$\zeta_z = \frac{\partial v_y}{\partial_x} - \frac{\partial v_x}{\partial_y}. \tag{2.4}$$

The kinetic energy (KE) quantifies the motion-related energy within the aneurysm volume [70]. KE is the velocity squared and multiplied with the density as described in Equation (2.5). The related kinetic energy ratio (KER) is the relationship between the KE in the aneurysm and in the parentvessel (see Equation (2.6)).

$$KE = 0.5 \cdot \rho v^2 \tag{2.5}$$

$$KER = \frac{KE_{Aneurysm}}{KE_{Parentvessel}} \tag{2.6}$$

Moreover, the oscillating velocity inside the vessel can be described with the parameter oscillatory velocity index (OVI) as shown in Equation (2.7). The OVI is used to describe temporal velocity fluctuations and vortex formation within the flow field. It ranged from 0 (steady flow) to 0.5 (high temporal and spatial variation) [261]. The parameters are obtained through transient CFD simulations with one cardiac cycle describing a time period T. Temporal averaging is thus performed over one cardiac cycle.

$$OVI = 0.5 \times \left(1 - \frac{\left|\int_0^T v\, dt\right|}{\int_0^T |v|\, dt}\right). \tag{2.7}$$

Wall-related parameters

WSS measures the frictional force exerted by blood flow on the vessel walls. Low WSS is often associated with aneurysm formation, while high or oscillatory WSS can lead to vessel wall degradation [178]. The WSS is often averaged over one cardiac cycle (time-averaged wall shear stress: TAWSS), as shown in Equation (2.8).

$$TAWSS = \frac{1}{T}\int_0^T WSS\, dt. \tag{2.8}$$

The LSA represents the area of the aneurysm wall exposed to time-averaged (TA)WSS values lower than the TAWSS of the parent vessel wall, minus its standard deviation (SD) (Equation (2.10)) [52]. This area was normalized relative to the total aneurysm surface area.

$$TAWSS_{boundary} = TAWSS_{Parentvessel} - SD(TAWSS_{Parentvessel}) \tag{2.9}$$

$$LSA = \frac{Area_{Aneurysm(TAWSS<TAWSS_{boundary})}}{Area_{Aneurysm}} \tag{2.10}$$

For comparative analysis across different aneurysms, TAWSS was normalized by calculating the ratio of shear stress on the aneurysm wall to that on the parent vessel wall (normalized time-averaged wall shear stress (nTAWSS)) [318] (Equation (2.11)).

$$nTAWSS = \frac{TAWSS_{Aneurysm}}{TAWSS_{Parentvessel}} \tag{2.11}$$

The oscillatory shear index (OSI) is defined by the temporal shear fluctuations on the aneurysmal wall. As the OVI, the OSI ranges between 0 and 0.5. The OSI quantifies the change in flow direction and is used to assess disturbed flow patterns. High OSI is associated with regions prone to atherosclerosis or aneurysm development. As for the flow-related parameters, T is also the total length of the investigated cardiac cycle [292]:

$$OSI = 0.5 \times \left(1 - \frac{\left|\int_0^T WSS\, dt\right|}{\int_0^T |WSS|\ dt}\right). \tag{2.12}$$

2.6 Fluid dynamics in medical applications

CFD simulations are a vital tool in modern medicine, improving diagnoses and treatment by modeling blood flow in the human body. Moreover, it helps enhance diagnostic accuracy and optimize therapy. By using patient-specific data like IAs these simulations can provide personalized analyses and help clinicians with diagnosis and therapy planning. In recent studies, fluid dynamics were used for medical applications, investigating intra-aneurysmal hemodynamics and treatment outcome. The optimization of these methods is important for future clinical prediction and treatment planning.

2.6.1 Evolution of CFD in intracranial aneurysms

Starting in the early 1970s, first in vitro analysis was carried out and the first parameter which was found to play a role in IA research was estimated: the WSS [80]. Moreover, within these first studies transition to turbulence was already found in IAs and related to IA growth. In further studies during the 1980s and 1990s, using in vitro experiments, WSS was again found to be important [99].

Starting from the early 2000s, with computational possibilities rising, first numerical analyses of IAs were carried out [112] and CFD emerged as a key tool for studying IAs. Focus was set on mechanisms of growth, rupture, and the influence of hemodynamic forces on aneurysm walls [275]. CFD was already used to explore vascular remodeling, evaluate endovascular treatments, and validate new devices [111]. Despite these advancements in understanding vascular pathologies, crucial knowledge gaps remain in IA research due to the complex nature of blood flow and controversies over factors inducing rupture, such as high or low wall shear stress and appropriate viscosity models. Addressing these issues is crucial for improving IA research methodologies.

2.6.2 Current status of CFD in intracranial aneurysms

CFD simulations to assess intra-aneurysmal hemodynamics comprise specific assumptions in regard of *Viscosity modeling*, *Boundary conditions*, and *Flow regime*, which are examined in this section.

Viscosity modeling

In conventional CFD methods, the viscosity model is assumed to be Newtonian, even if blood exhibits a Non-Newtonian behavior [275, 58]. Several studies have highlighted the impact of using different blood viscosity models in CFD simulations of IAs. Hippelheuser et al. compared Newtonian and non-Newtonian (Carreau) models in 26 patient-specific aneurysms, finding differences in TAWSS, which could affect rupture predictions [118]. But flow patterns were found to be similar and only neglegible dependencies on the chosen blood model exist. Similarly, Otani et al. demonstrated that using a non-Newtonian (Carreau-Yasuda) model produced distinct flow structures and hemodynamic parameters compared to the Newtonian model, particularly underestimating low shear-rate regions, which could impact thrombus formation [222]. Nevertheless, Morales et al. investigated the influence of the two models in coiled IAs, stating that the the use of a Newtonian model can be safely assumed in hemodynamic CFD simulations [200].

In contrary, a study by Xiang et al. confirmed that different viscosity models result in significant variations in predicted aneurysm hemodynamics, emphasizing the importance of accurately modeling blood viscosity for CFD analyses [319]. However, Liu et al. showed in their analysis of intracranial stenosis that difference due to the fluid modeling are negligible when looking at intra-vessel flow parameters and at WSS in higher diameter areas of the vessel (no stenosis) [176]. In summary, assuming blood to be Newtonian is the conventional modeling approach used by the majority of published studies and justified with similarities in flow patterns and reduced computational effort. Modeling blood as Non-Newtonian has proven to be more sophisticated in CFD within the last years and should be implemented as default in the future. Nevertheless, for the present study choosing a constant viscosity seems appropriate.

Boundary conditions

The BC can be set steady or unsteady, whereas steady flow BCs are often employed in CFD to qualitatively analyze aneurysm flow and wall patterns only [93]. Up to the year 2018, the majority of CFD simulations (69%) according to [262] included steady BCs. However, even when applied to patient-specific geometries, these conditions are idealized and overlook important hemodynamic phenomena, thus limiting the clinical accuracy and relevance of the CFD models [227]. Thus, recent studies increasingly use unsteady conditions. Setting these unsteady BCs in hemodynamic simulations accurately is challenging due to the complexity of modeling blood circulation as a closed-loop system that begins and ends at the heart. Simulations mostly focus on a small pathological segment of the vasculature, isolated from the complete circulatory system, since a full domain simulation would exceed the computational ressources and time. However, this separation results in uncertainties regarding the inlet and outlet BCs, particularly in terms of vascular compliance and resistance [190].

In some cases, patient-specific data, such as flow rates obtained through transcranial Doppler ultrasound or MRI, have been incorporated to improve the accuracy of BCs compared to generalized flow waveforms [135, 58]. Jansen et al. captured patient-specific flow curves with PC-MRI and compared the results to generalized flow curves as shown in Figure 2.4 [135]. Experiment-specific BCs are mostly used, when hemodynamic simulations are compared to in vitro measurements. Namely, the experimentally measured waveforms are applied to the simulations to ensure a comparable basis. This is possible e.g. if MRI measurements [233] or PIV experiments [84] are performed and if the flow can be directly captured using MRI itself or suitable flow meters. However, PIV can not be used in patients, while MRI can not yet fully show the detailed flow behavior due to artifacts in the measurements [38].

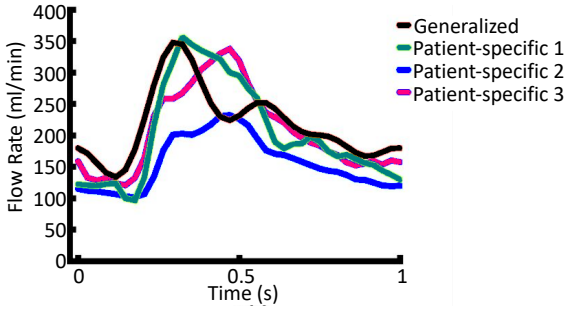


Figure 2.4: Patient specific and generalized flow curves by Jansen et al. [135]

Najafi et al. compared patient-specific waveforms measured with 2D MRI to one representative waveform scaled by the mean flow rate based on the inlet crosssection as BC for hemodynamic simulations [211]. The study concluded that the averaged flow rate has a higher impact on the hemodynamic outcome than the waveform. Li et al. also compared the influence of patient-specific and idealized inflow conditions to the hemodynamic results in CFD simulations [171]. A significant difference in the results was found, depending on the chosen inflow curve. Nevertheless, when compared to the rupture status of the IA, this difference did not change the relation of hemodynamic results to the estimated rupture status.

In scenarios where patient-specific data is unavailable, scaling laws like Da Vinci's rule and Murray's law are frequently used to estimate flow rates based on inlet and outlet cross-sectional areas. Da Vinci's rule, which scales flow according to the square of the diameter, has been found to yield more consistent results in simulating hemodynamic patterns [63]. Campo-Deaño et al. explained the waveform development by using mathematical formulas for the Womersley flow and developed profiles [49]. These can be used to estimate the inflow conditions, based on known velocities in the corresponding arteries. The use of given flow rates, scaled by the crosssectional area of the fluid domain, however, is a more common approach in IA hemodynamics research. Additionally, the extension of the inlet is common to ensure a developed inflow profile. In conventional CFD this has a similar impact as applying a developed inflow profile [25]. Studies have shown that variations in estimated flow rates using different inlet BC strategies can be substantial, with differences reaching up to 70% [62].

Regarding the outlet BC, a commonly employed approach is the zero-pressure boundary, which assumes that the pressure at the outlet is atmospheric, simplifying the simulation. For systems with multiple branches, flow distribution at the exits is typically managed by specifying traction-free conditions at all outlets, ensuring that the simulated flow naturally divides according to the vascular geometry. The error induced by these approximations is, however, still not completely clear.

Flow regime

Regarding the chosen viscosity, most studies assume the blood flow in neurovascular pathologies to be laminar [58]. This is related to the low Reynolds number occuring in the human arteries and the tube like shapes. Yang et al. approximated the internal vessel flow in an ICA to be around 270 ml/min, which results with a mean diameter of 0.5 cm in a Reynolds number less than 850, leading to use laminar flow conditions [326]. This assumption will be revisited later in this thesis.

2.6.3 Hemodynamic instabilities and transitional features in the flow

Recent DNS studies have provided detailed insights into the hemodynamics of cerebral aneurysms using Newtonian viscosity assumptions [297, 299, 143]. These studies revealed that blood flow in aneurysms exhibits turbulent-like structures and subcritical transitional behavior, as indicated by the analysis of velocity power spectrum analysis in patient-specific models. DNS showed that solution methods significantly impact WSS and OSI.

Valen-Sendstad et al. estimated the fluctuations in IAs using high-resolution simulations and visualized aneurysms with occurrence of fluctuations with the turbulent kinetic energy [297]. In Figure 2.5, six exemplary cases from their study are presented, with the volume rendering of the turbulent kinetic energy. Their results revealed higher fluctuations in some cases depending on the aneurysm location (sidewall or bifurcation).

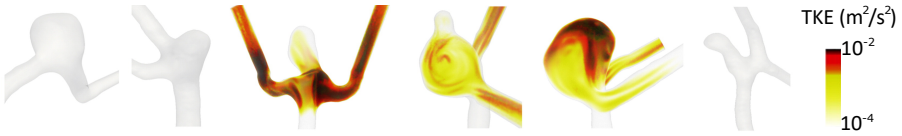


Figure 2.5: Turbulent kinetic energy (TKE) of representative intracranial aneurysm cases. Figure adapted form [297]

DNS offers solutions to the Navier-Stokes equations of highest resolution in space and time [202]. Despite high computational costs, this makes it the most accurate method for studying complex vascular flows. Previous studies have worked effectively on validating DNS in pipe flows and over a backward facing step as well [167]. Unlike standard CFD solvers that resolve only laminar scales and inherently impose simplified physics in their solutions, DNS captures the full range of flow dynamics. This is crucial given the complex pulsatile nature of blood flow and vascular geometry that promote instability. To capture the in-depth flow structures, the grid size of the fluid domain must be smaller than the smallest existing vortex structure [313].

The mechanisms governing the transition to turbulence in viscous, incompressible flows, especially in simple geometries like straight pipes or under shear conditions remain not fully understood. Research on turbulence transition in pulsatile pipe did not reach a uniform statement up to now [125]. Furthermore, most studies have focused on monoharmonic pulsatile pipe flow [320] and less studies include physiological conditions (multiharmonic) into pipe flow analysis [42].

In IAs, blood flow dynamics are influenced by complex vascular geometries, including the shape and orientation of the parent and daughter vessels, as well as the size and location of the aneurysm. Moreover, the complexity in studying IA hemodynamics is supplemented by distinct flow features such as shear stress, vortices, and regions of recirculation and flow separation [83]. These flow phenomena differ from those in pulsatile pipe flows, making classical laminar-to-turbulence transition criteria unsuitable for characterizing IA hemodynamics [321]. Consequently, there is a need for fundamental fluid dynamics research to accurately describe the transition to turbulence in aneurysmal blood flow.

However, these refinements of CFD and accurately solving the fluid domain spatially and temporally, results in an excessively high need of computational hours. Low-fidelity CFD continues

to play a crucial role in current research, particularly for scenarios requiring rapid simulations [25, 141]. This approach demands fewer computational resources and offers simpler implementation, making it well-suited for quick analysis. In cases involving complex geometries, low-fidelity CFD facilitates grid generation and model setup, allowing for a larger number of cases to be simulated in a shorter time frame. DNS, while more accurate, impose stringent requirements on grid resolution and mesh quality, which become increasingly challenging to meet as the complexity of the geometry increases.

This limitation is especially relevant in the context of endovascular treatment planning and virtual interventions, where modeling stented geometries presents crucial challenges [155, 54]. The intricate mesh requirements and computational cost associated with high-fidelity simulations make their clinical application currently impractical. Therefore, low-fidelity CFD remains a more feasible and efficient option for clinical use, providing a balance between computational efficiency and the ability to handle complex vascular geometries in treatment planning.

2.6.4 CFD to evaluate endovascular treatment

Surgical clipping is a traditional method for managing cerebrovascular pathologies such as IAs. In this approach, a metal clip is placed at the aneurysm neck to exclude it from circulation, thereby reducing the risk of rupture [40]. Postoperative studies have demonstrated that clipping can significantly increase blood velocity and WSS in the parent vessels while lowering intra-aneurysmal pressure. However, clipping is an invasive procedure that requires open surgery, which carries inherent risks and longer recovery times [277]. In recent years, minimally invasive endovascular treatments, such as coiling, flow diversion, and flow disruption, have emerged as safer and more patient-friendly alternatives to surgical clipping [229].

Coiling

Early studies of coil embolization implemented the coil as a sphere inside the IA [47]. Mitsos et al. firstly simulated aneurysm coiling by applying a porous medium approach, and using medical images of a ruptured IA. The simulations revealed that the introduction of coils led to a reduction in vortical blood flow within the IA sac and a decrease in wall pressure at the aneurysm's fundus [196]. Morales et al. analyzed coiling virtually using a novel coiling technique and found a decrease in WSS and velocity as well [201].

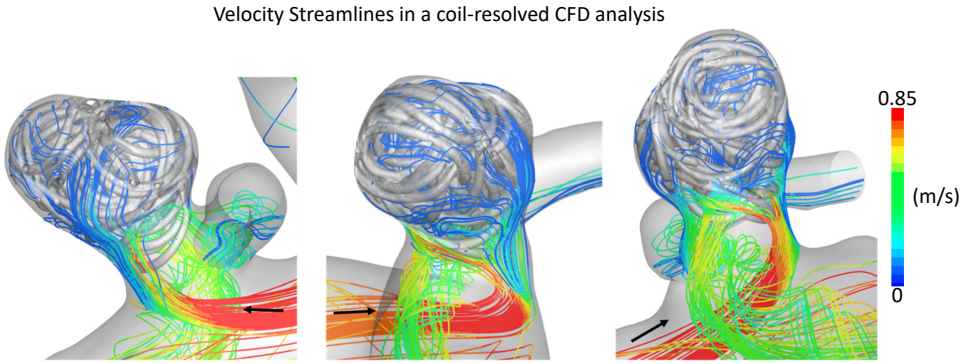


Figure 2.6: Visualization of velocity streamlines through an intracranial aneurysm treated with a Coil. Figure adapted from [61].

A first CFD studies showing the possibility to use CFD for optimization of coil design was published by Babiker et al. [14]. It performed post-treatment simulations in an idealized aneurysm

model, incorporating virtual coil placements and analyzed the influence of coil parameters on aneurysmal hemodynamics. Chivukula et al. treated phantom models of IAs with endovascular coils and captured medical images of the coiled models with microtomography [61]. They performed hemodynamic simulations of untreated and treated states, with the coil being segmented from microtomography and the aneurysm dome being modeled as porous medium. The results revealed that the porous medium approach overestimated the hemodynamics. With the coil-resolved approach, the positive treatment outcome due to coil embolization was shown as presented in Figure 2.6.

Flow diversion

Cebral et al. extracted the shape angiography of the flow diverter and aneurysm from post-interventional 3D rotational angiography and compared pre- and post-interventional hemodynamics [54]. Reduction in velocity and WSS was found after treatment. A virtual stenting tool, earlier proposed by Mut et al. was applied in this study [206]. With the stenting tool, the user is able to easily interchange different stent designs in one aneurysm model in order to perform fast comparative characterizations.

Fast virtual stenting approaches were established by Larrabide et al. in order to serve as a basis for clinical decision making [165]. The tool calculates approximated positioning and deformation of the flow diverter after implementation into the aneurysm geometry. Ma et al. presented a method to simulate the mechanical flow diverter deployment based on finite-element analysis [182]. Janiga et al. developed a fast virtual stenting algorithm, based on the centerline of the vessel and an iterative approximation of the stent boundaries towards the vessel wall [134].

In Figure 2.7, a representative saccular side-wall aneurysm case is shown in its treated state using a FDS. The streamlines accurately show the flow diversion, leading the flow through the parent vessel and the subsequent reduction of flow into the IA. Additionally, the streamlines represent the disadvantage of using a FDS, since a subsequent flow reduction is also visible in the adjacent vessel leaving the aneurysm dome.

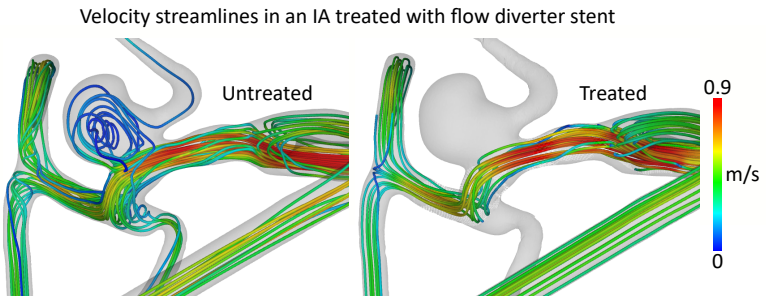


Figure 2.7: Visualization of velocity streamlines in a saccular intracranial aneurysm (IA) treated with a flow diverter stent. Figure adapted form [155]

In the study conducted prior to this thesis, six aneurysm cases including three abnormally shaped FIAs and three SIAs were comparatively investigated with endovascular flow diversion treatment [155]. To derive the preferable treatment outcome, the pre-pathological states were manually created and analyzed with CFD as well. The results revealed a clear intrasaccular velocity reduction from pre- to post-treatment state for all cases. Still, higher reduction was found in saccular compared to fusiform cases, which can be related to a reduction in porosity due to a higher stent expansion in FIAs. The study showed that the choice of the device has to be accurately conducted based on the aneurysm shape.

In general, the existing studies comparing pre- and post-treatment with flow diverter stents of IAs showed a significant reduction of flow into the aneurysm dome and of wall shear parameters on the aneurysmal wall.

Flow disruption

For specific shapes of IAs, clipping would be the most suitable method to treat the pathology. Nevertheless, as already mentioned, clipping is an interventional method, which includes opening the patient's skull and thus comes with a high risk and harming of the patient [40]. Therefore, in recent research novel devices to disrupt the flow on a minimally invasive endovascular basis were developed to achieve a clipping-similar outcome, by closing the aneurysm neck and subsequently disrupting the flow [229].

The first flow disrupting device was developed in the early 2010s, by the company Temuro Neuro, called WEB. This device is implanted using a catheder placing a cylindrically shaped wired web into the aneurysm dome. The WEB was studied in vivo showing a positive treatment outcome in IAs [73]. Aghli et al. compared the hemodynamics in an IA with and without the placement of a WEB. The resulting velocity streamlines are presented in Figure 2.8, indicating the flow reduction into the aneurysm after treatment. Further studies analyzed the efficacy of the device in vivo and in silico, all showing a generally good treatment outcome [159]. Due to the cylindrical shape of the WEB, the device choice is dependent on the aneurysm's height.

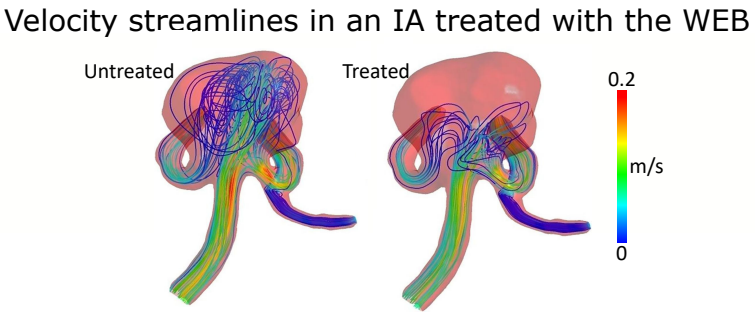


Figure 2.8: Visualization of velocity streamlines in a saccular intracranial aneurysm (IA) treated with a Woven EndoBridge device (WEB). Figure adapted form [7]

In the late 2010s, a novel device called Contour was developed, which is implanted using a catheter and placed in the aneurysm neck as well. The Contour features the shape of an umbrella out of a wired web. Preliminary in vivo analyses showed a positive treatment outcome when a Contour was employed [174, 105, 114]. Due to the novelty of the device, only a few studies have been performed up to now, especially in silico investigations, to derive the treatment effect and clinical applicability. An in-depth analysis of the Contour performance is conducted in Chapter 5.

2.6.5 Validation of numerical vascular flow assessment

Validating numerical hemodynamic blood flow simulations is crucial to ensure their accuracy and reliability. A robust validation framework can be established using in vivo data, in vitro experiments, and theoretical solutions. These approaches can be combined strategically to address various aspects of blood flow, ranging from simplified benchmark cases to complex, patient-specific scenarios. When experimental or clinical imaging data are unavailable, a wide array of

previously conducted experiments and studies can serve as reference points to support validation efforts.

In vivo data validation

Numerical results can be compared to data obtained from in vivo clinical imaging of blood flow data. The modality of MRI, with specialized sequences comprising PC-MRI or BBMRI can serve as a basis in this regard. For example, Rayz et al. compared velocity fields calculated with CFD simulations based on the geometrical and inflow BC information from MRI data to the MRI velocity fields [246]. The results revealed a good agreement between measured and calculated data and the study suggests using patient-specific measured BC whenever possible. Cebral et al. reconstructed 3D geometry data of IAs from 3D rotational angiography (RA) and simulated the contrast agent inflow measured with the in vivo medical imaging [56]. Here, a good alignment was found between the two datasets as well.

Regarding the comparison of hemodynamics resulting from CFD simulations and MRI scans, a study was conducted prior to this thesis analyzing PC-MRI data for six patients with pathological aortic arches [151]. Numerical simulations were performed based on MRI resolution and compared to PC-MRI data, focusing on velocity and WSS in the aortic arch at three cardiac cycle phases. High-resolution data showed good velocity agreement but overestimated WSS during peak systole, while moderate and low-resolution data exhibited discrepancies in velocity magnitudes. The study suggested that while low-resolution PC-MRI can qualitatively evaluate flow patterns, a higher resolution is essential for accurate quantitative analysis.

As explained in section 2.3, ultrasound imaging has the capability to capture real-time flow dynamics as well. Although the spatial resolution is lower than with MRI, the easy applicability is highly valuable especially considering pedriatric patients. Nevertheless, ultrasound can be mainly used for cardiac imaging, as, for example, Quaini et al. compared CFD simulations with Doppler velocity measurements finding a consistency in their investigations [240].

In vitro data validation

Regarding in vitro validation, similar imaging techniques as explained for in vivo validation can be used. These are then applied to phantom models instead of the living organism. Moreover, particle image velocimetry (PIV) or particle tracking velocimetry (PTV) are established methods to analyze flow conditions experimentally. Phantom models were mostly created out of glass, until 3D printing enabled faster, cheaper and easier processing [327]. For example, Roloff et al. investigated flow dynamics in IAs using PIV and CFD and found a good agreement between the experimental and simulated data [254]. Further studies have been performed in the past showing this alignement between experimental and simulated data [84].

Regarding the comparison of measured MRI data and CFD simulations, further studies were performed prior to this thesis to investigate the relationship between luminal enhancement detected in IAs using vessel wall MRI and hemodynamic features derived from CFD [153, 154]. Luminal hyperintense signals, attributed to inflammation and specific flow characteristics, were analyzed alongside patient-specific CFD simulations, which provided detailed hemodynamic parameters such as velocity, pressure, and shear stress over the cardiac cycle. The analysis revealed that parameters like KE and vortex formation showed a correlation with signal suppression observed in vessel wall MRI, providing insights into the interaction between flow dynamics and imaging findings in IAs.

Validation conducted in this thesis

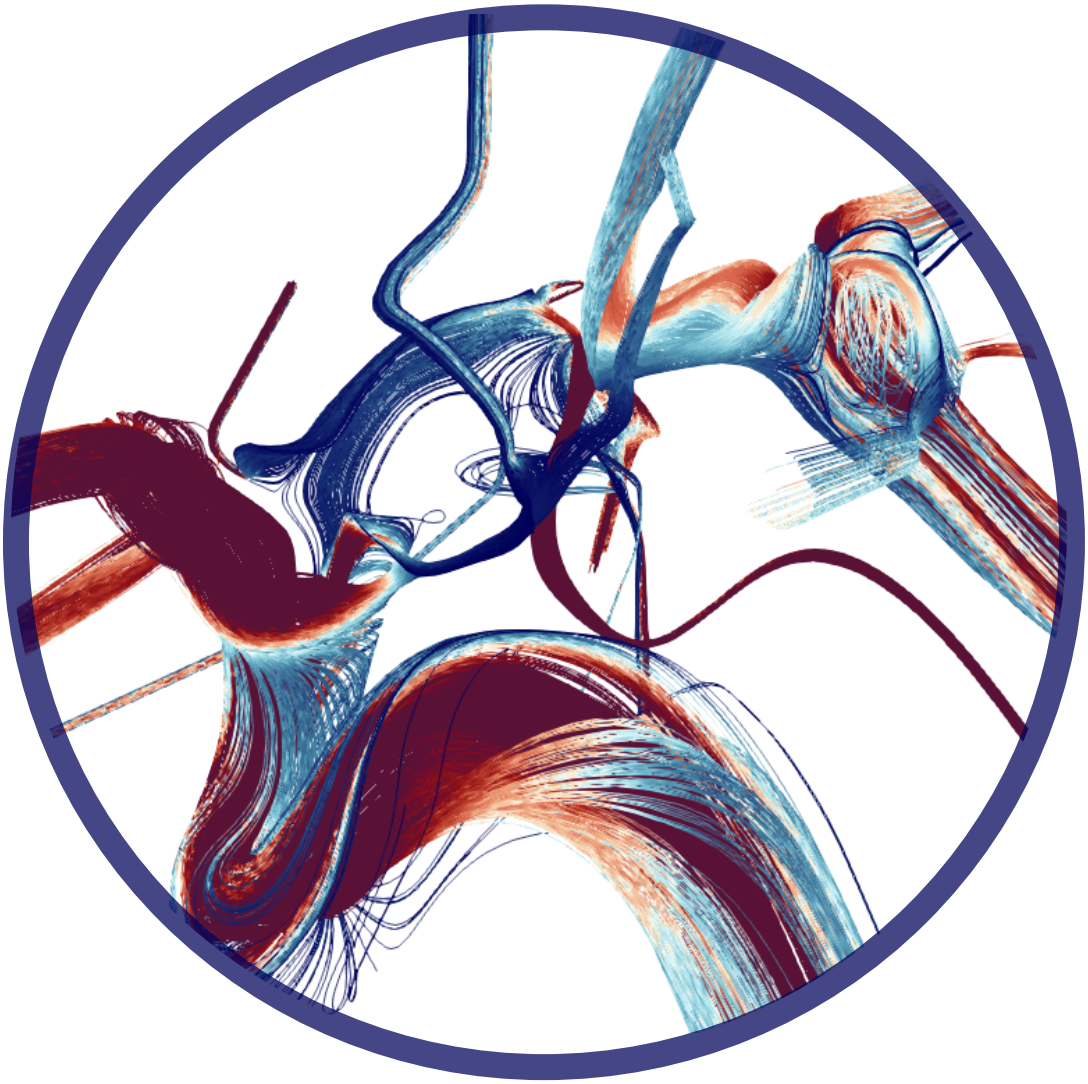
The methods carried out in this thesis were differently validated, taking the comparison to literature on the one hand and to in vitro data on the other hand into account. In the first part, image-based blood flow simulations of neurovascular vessels and pathologies, focusing on IAs are performed and evaluated. Validation of these simulations has been conducted extensively in the past, comparing the simulation results to in vitro experiments as well as to in vivo measurements as already mentioned before [254, 90, 56, 246].

The second part of this thesis includes in vitro investigations based on PTV to validate the novel methodologies with experimental data for the neurovascular pathologies. Further processing steps will thus be explained in section 4.5. Moreover, in a study performed prior to this thesis, the comparison of two CFD modeling approaches based on two medical imaging methods of the moving left ventricle were conducted and compared to MRI and Doppler data as well [156]. This is the basis for the cardiovascular modeling approach in the second part of this thesis. In the study, the influence of imaging modalities and computational approaches on intraventricular flow simulations using CFD are evaluated. MRI and transthoracic echocardiography data from a volunteer were used to reconstruct ventricular anatomy, serving as input for the two CFD approaches. The results showed comparable valve velocities between methods, consistent with in vivo measurements. The findings highlighted the reliability of CFD for intraventricular flow analysis.

Chapter 3

Part 1: Impact of segmentation, vasculature complexity, and outlet boundary condition in image-based blood flow simulations of intracranial aneurysms

---

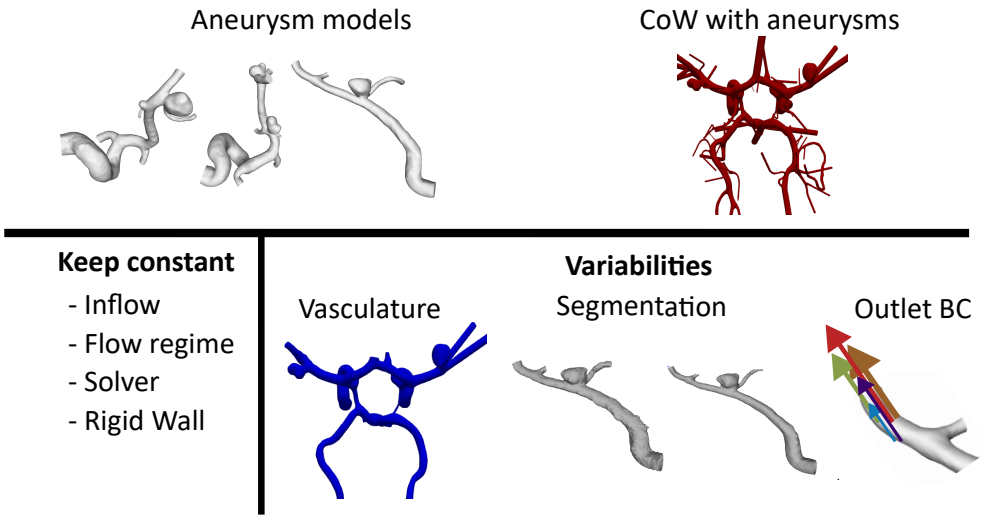


Outline

Image-based blood flow simulations of IAs primarily rely on medical imaging as the only patient-specific input. Several assumptions must be made to accurately perform these simulations. Improving modeling approaches with respect to these assumptions is crucial for a realistic representation of the blood flow. This chapter examines three key modeling variations and their impact on intra-aneurysmal hemodynamics: 1) aneurysm lumen segmentation, 2) vessel vasculature complexity and 3) outlet BC. First, an overview of common modeling assumptions is provided, followed by a detailed analysis of these three variations. The influence of each approach (1-3) on intra-aneurysmal hemodynamics will be evaluated, and the interaction of lumen segmentation and vessel vasculature complexity with the effects of BCs will be further examined.

This chapter is partially based on the following publications:
Korte, J., Voß, S., Janiga, G., Beuing, O., Behme, D., Saalfeld, S., & Berg, P. (2023). Is Accurate Lumen Segmentation More Important than Outlet Boundary Condition in Image-Based Blood Flow Simulations for Intracranial Aneurysms? Cardiovascular Engineering and Technology, 14(5), 617–630.
Korte, J., Gaidzik, F., Saalfeld, S., Janiga, G., & Berg, P. (2024). Image-based Hemodynamic Simulations for Intracranial Aneurysms: The Impact of Complex Vasculature. International Journal of Computer Assisted Radiology and Surgery, 19(4), 687–697.

Graphical abstract



The refinement of image-based hemodynamic simulations for IAs is an ongoing process that addresses uncertainties and assumptions within the modeling framework. This chapter begins with an overview of prior research exploring different strategies for improving conventional image-based hemodynamic simulations. Key sources of variability are identified, and existing limitations in simulation accuracy are highlighted. In the subsequent sections, the three selected aspects of modeling variations (1. aneurysm segmentation, 2. vessel vasculature complexity, and 3. outlet BC) are analyzed in detail.

3.1 Variabilities in image-based blood flow simulations of intracranial aneurysms

A wide range in variabilities to enhance conventional image-based hemodynamic simulations exist. This section examines the previous research in the three aspects focused on in this chapter: image segmenation, vasculature complexity, and outlet BC. Moreover, it gives an overview over the further variabilities of medical imaging, reconstruction, blood modeling, inflow BC, wall modeling, and solver. The limitations associated with common assumptions in computational simulations are addressed and analyzed focusing on the improvement of accuracy.

Image segmentation

Although segmentation is generally known to have a high impact on the hemodynamic outcome, only few studies have included the variations of segmentation. Many research groups follow specific segmentation methods, which then remains the standard application. Moreover, the use of specific automated softwares (open-source or comercially available) contains variabilities in the segmentation outcome impacting realistic replications of the true vessel lumen [30]. The term of *segmentation* in this field of research is originally solely the voxel grid conversion of the medical images into a virtual surface model. Often, the term is used as a synonym for additional processing steps regarding the surface model. These steps include removing artifacts, defining model dimensions by trimming the vascular structures, and, where necessary, re-meshing and smoothing the surface [97].

To explore variability in segmentation approaches, international challenges have been organized by research groups. These challenges provide standardized datasets and specific research questions to be addressed by participating teams worldwide. For instance, Valen-Sendstad et al. initiated "The 2015 International Aneurysm CFD Challenge" [295], where raw imaging data in DICOM format was distributed to 28 participating research groups (see Table 3.1). Each group independently segmented the data, reconstructed the vascular geometry, and performed hemodynamic simulations. As anticipated, the results exhibited substantial variability across the groups, particularly in segmentations and subsequent hemodynamic parameters such as WSS and velocity. Harmonization of the derived parameters was achieved only through normalization.

Another world-wide challenge is the Multiple Aneurysms AnaTomy CHallenge 2018 (MATCH). The challenge conducted by Berg et al. aimed to assess the uncertainty of hemodynamic results only due to segmentation variability [26, 28] (Table 3.1). Here, 26 international research groups participated and provided segmentation results as well as a rupture risk assessment. The results could be compared with high-resolution 2D DSA scans and revealed a general overestimation of the vessel cross-sectional area of all groups, in addition vessel anomalies were not accurately processed.

Table 3.1: Representative studies analyzing segmentation variability in regard of segmentation routine (varying research groups), segmentation software (Commercial: Mimics, Materialise; Open Source: 3D Slicer, The Slicer Community), and segmentation algorithm (Region Growing Threshold, Chan-Vese model, Threshold-Based Level Set).

Study	Cases included	Reason for variablity	Max. Variation in WSS
The 2015 International Aneurysm CFD Challenge [295]	5	Segmentation routine (28 Research Groups)	56%
Multiple Aneurysms AnaTomy CHallenge 2018 [26]	5	Segmentation routine (26 Research Groups)	51%
Bertolini et al. 2022 [30]	1	Segmentation software	$\leq 5\%$
Sen et al. 2024 [273]	45	Segmentation algorithm	24%

Bertolini et al. compared two segmentation methods, validating their findings experimentally in 2022 [30]. Their study, which included the aortic root and coronary arteries, demonstrated minimal percentage differences in hemodynamic results for larger vessels (see Table 3.1). Similarly, Sen et al. compared three manual segmentation techniques—region growing, threshold-based level set, and the Chan–Vese model for segmenting aneurysm medical imaging data in 2024 [273]. Their evaluation across 45 patient-specific aneurysms revealed a difference among the methods, which was more pronounced in smaller-diameter vessels. Timmins et al. in 2020 and Ivantsits et al. in 2022 conducted challenges in regard to the automated detection and segmentation of IAs based on medical image datasets, whereas Ivantsits et al. supplemented their challenge with a rupture risk estimation [291, 127]. As no hemodynamic assessment was conducted, these are not listed in Table 3.1. They found that the best possible option to achieve a realistic assessment is obtained with machine learning algorithms.

The studies show that the application of different segmentation methods results in an inconsistency in the underlying data. Since segmentation has a direct impact on the resulting hemodynamic outcomes, it is essential to conduct investigations to determine the best possible level of accuracy.

Vasculature complexity

As numerical studies on intracranial hemodynamics are often used to assess rupture risk-related parameters, accurately investigating these parameters is essential for achieving clinically applicable outcomes [57, 132]. Most models in these studies typically include only a single inlet and a limited number of outlets near the IA, thereby restricting the complexity of the vascular geometry considered [295]. The exclusion of vessel branches and the resulting reduction in outlet count can alter the hemodynamic interactions between cerebral arteries, potentially affecting flow distributions and pressure conditions [55]. Therefore, incorporating nearby bifurcations and increasing the number of outlets should be further investigated to better understand their impact on hemodynamics.

Investigations including the CoW were performed, but these still covered only a restricted region of interest as listed in Table 3.2. For example, Ren et al. captured eight patient-specific CoW models and implemented artificial stenosis to analyze the varying hemodynamic effects [248]. They found that the variation in model vasculature caused a subsequent variation in pathological effects. Moreover, they concluded that varying outlet counts can further affect these results. Sutalo et al. performed CFD simulations of the complete CoW model and compared

these to geometric modifications focusing on vessel stenosis [287]. In their study, the variation of the vasculature affected the flow rates through the arteries, which can further affect the hemodynamic outcome when analyzing neurovascular pathologies. The full CoW model in their study included only ten outlets. Fabbri et al. studied the varying anatomical impacts by reconstructing the CoW model and analyzing the numerical particle tracks [77]. They found a significant impact of the CoW reconstructions on the particle flows. This was also found by Zhu et al. who studied varying anatomical CoW structures focusing on vessel stenosis [335].

Table 3.2: Representative studies investigating the CoW including varying outlet counts and pathologies.

Study	Cases included	Outlet count	Pathology
Ren et al. [248]	8	6	Artificial stenosis
Sutalo et al. [287]	1	6	Artificial stenosis
Fabbri et al. [77]	1	13	Emboli
Zhu et al. [335]	1	8	Artificial stenosis

Advancements in medical imaging technology have enabled the acquisition of higher-resolution images and more precise segmentation of small vessel branches. This progress facilitates the incorporation of a greater number of outlet cross-sections in hemodynamic simulations, allowing for the development of more accurate and patient-specific models. Such improvements are expected to significantly influence hemodynamic outcomes, warranting further evaluation to quantify their impact.

Outlet boundary condition

In image-based hemodynamic modeling of cerebral vessels, specific outlet BCs are used, being applied depending on the availability of data and the research focus.

- **Zero-pressure:** One widely adopted approach in cerebral image-based blood flow simulations is the use of zero-pressure outlet BCs, which was used in many studies in the past [295, 172].By setting a constant pressure, the total pressure distribution in the system can be affected and lead to an over- or underestimation of the blood flow. Thus, recent studies found this assumption to be less suitable to replicate realistic flow conditions [158, 62].

- **Flow-splitting:** To overcome these inaccuracies, providing a splitting value at each outlet was implemented. This splitting value is the division of the inlet flow into the separate vessels depending on geometrical parameters. The flow splitting method by Murray's law, as introduced in 1926 [205], builds on the proportional relationship between vessel flow rate and diameter and was applied by several studies in the past [63, 274]. The method leads to a division of the flow based on the cross-sectional area of the outlet, neglecting the vessel's bifurcations and shape. Rajabzadeh-Oghaz et al. compared the flow splitting values based on Murray's law with in vivo PC-MRI measurements and found deviations of up to 15.3 % [243].

- **Advanced flow-splitting:** To optimize the splitting approach, the complete vessel included in the simulation should be considered when estimating the outlet flow. In this regard, Chnafa et al. [62] highlighted the critical role of adequate outflow BCs, introducing a sophisticated flow-splitting tool capable of accommodating arbitrary vascular geometries. Building on the work by Chnafa et al., Saalfeld et al. enhanced the flow-splitting approach by incorporating vessel morphology into the calculations [205]. Thus, not only the previous bifurcation and cross-sectional areas, but also the shape of the cross-section was considered. In their study, five different methods including the proposed approach,

the approach by Chnafa et al. and, additionally, the zero-pressure and Murray's law conditions were evaluated and compared. This demonstrated the ability to account for the most realistic aspects of outflow BCs. Saalfeld et al. further investigated hemodynamic effects using the advanced splitting method [258, 155]. Their results showed an impact of the outlet BC on the magnitude of the hemodynamic parameters with higher values for the advanced methods and lower for the zero-pressure condition.

- **Windkessel models:** Recent studies have utilized advanced flow-splitting algorithms in combination with Windkessel models as outlet BCs.This approach is considered to replicate physiological flow conditions more accurately, as it accounts for the Windkessel-like behavior of blood flow through arterial vessels. However, achieving realistic results heavily depends on precise parameter tuning, which remains a critical challenge [215]. Due to the difficulty of obtaining direct pressure measurements within cerebral arteries, parameters are often derived from literature rather than being patient-specific [152]. Torii et al. investigated the application of Windkessel models as outlet BCs in the simulation of an IA, comparing their performance to zero-pressure BCs. Their findings indicated that the use of the Windkessel model did not produce significant differences compared to simulations employing Murray's power law, suggesting limited sensitivity of the results to the outlet BC model in this context [187].

Despite these advancements, state-of-the-art research is still lacking the implementation of these methodologies. As vascular regions of interest with increasing numbers of outflow cross-subsections are more frequently studied, the integration of realistic outflow BCs is becoming even more important.

Further variabilities

In addition to the three aspects analyzed in detail, other variabilities influence hemodynamic outcomes. Although these factors are not the primary focus of this chapter, they are briefly summarized. Furthermore, the specific applications implemented for each variability are outlined.

- **Medical imaging:** In neurovascular pathologies the wall movement is neglected in most studies and the rigid vessel structure captured. In this regard, Ramachandran et al. compared four imaging modalities comprising 3D RA, CTA, contrast enhanced MRI, and time-of flight (TOF) MRI, which did not show any significant difference in resulting aneurysm morphology [244, 305]. Nevertheless, Brinjikji et al. [44] and Schneiders et al. [268] compared the influence of DSA and 3D RA on more than 200 IAs. Both studies found higher neck width of the IA based on the RA data. Geers et al. identified the aneurysm neck as the critical region and additionally quantified its impact on hemodynamic parameters [94]. They compared ten IAs imaged with 3D RA and CTA and observed differences in neck size (CTA ostium surface area 33.0 % larger on average) and in small vessels with diameters of 0.7–1.0 mm. While qualitative flow patterns showed good agreement, hemodynamic parameters varied significantly. The studies mentioned reveal the importance of high-resolution medical imaging when analyzing hemodynamics and morphology of vascular pathologies. Nevertheless, in most cases the medical imaging depends on the available machines. As imaging always depends on the available possibilities, no further evaluation of the imaging impact is conducted in this thesis.

- **Image reconstruction:** Following medical imaging, an intermediate reconstruction step is required to prepare the image for segmentation. This process, typically performed by the imaging software, affects the final image quality through trade-offs between spatial

resolution and noise reduction. Berg et al. analyzed six reconstruction modes and found that variations in the neck region led to differences in hemodynamic parameters exceeding 17 % [23]. However, in this study, the patient-specific data were acquired in a clinical setting, where reconstruction parameters were predetermined and could not be influenced.

- **Blood modeling:** As already examined in section 2.6.2, a variety in blood models assigned in hemodynamic simulations exist in the literature. In CFD studies, blood is conventionally modeled as a Newtonian fluid, despite its inherently Non-Newtonian behavior. Comparative analyses of Newtonian and Non-Newtonian viscosity models have demonstrated variations in hemodynamic parameters, such as WSS, which may influence the evaluation of IA rupture risk and thrombus formation [222, 319]. However, studies indicate that flow patterns remain largely consistent across models, with only minor dependencies on viscosity assumptions [176]. While Non-Newtonian models provide a more physiologically accurate representation, particularly in regions of low shear rates, the Newtonian assumption remains widely utilized due to its computational efficiency [275, 58]. Given these considerations, the adoption of a constant viscosity model is deemed appropriate for the present chapter.

- **Inflow boundary condition:** Simulations based on CFD require sufficient inlet BCs. Several studies were performed in the past, dealing with the impact of varying inflow conditions on intra-aneurysmal hemodynamics [16, 227, 184]. Typically, time-dependent velocity or volume flow rate curves are defined at the inlet of the aneurysm vessel model. These curves are characterized primarily by the magnitude and profile over the cardiac cycle, which can be classified using for example the patient's age, heart rate or body dimensions [75]. Some studies were able to use patient-specific measurements, based on Doppler ultrasound or phase-contrast MRI. For example Alaraj et al. [9] applied a developed technique to quantify the blood flow in cerebral vessel previously introduced by Zhao et al. [333]. With the use of a noninvasive optimal vessel analysis - NOVA - software the vessel segmentation and volume flow rates could be derived. Many other studies lack these patient-specific data. Moreover, single measurements may not be fully representative, as they fail to account for varying conditions and lifestyle situations. As a result, flow curves from literature are commonly used with the flow rate scaled according to the vessel diameter using a power law. Valen-Sendstad et al. [298] investigated the scaling of inflow rates according to a varying inlet cross sectional area. The study included models of 37 internal carotid artery aneurysm cases and specific results showed that the choice of the measured location introduced a 17 % average uncertainty in flow rates. They demonstrated a better agreement with physiological flow rates when the square law was applied for scaling instead of cubic law. This highlighted the significant uncertainty introduced by inlet BC selection and according scaling assumptions. Li et al. compared intra-aneurysmal hemodynamics simulated firstly using patient-specific BCs and secondly using generic assumptions [170]. Focusing on key parameters like TAWSS, and OSI, the results showed that patient-specific BCs significantly improved the accuracy of the results. Varying inflow conditions considering generic and patient-specific flow rates were also evaluated by Pereira et al. [227]. Results showed that accurate CFD predictions, including flow patterns and WSS distributions, require non-truncated inlet vessel models. Significant differences in hemodynamics within aneurysmal regions were observed between the generic inlet BCs Womersley and Plugflow. The studies highlight the importance of accurately measured patient-specific inflow curves for achieving reliable hemodynamic outcomes in simulations. However, such measurements are often unavailable, particularly in patients with severe conditions who cannot undergo additional clinical procedures. Furthermore, when such measurements are

obtained, they frequently lack the temporal resolution necessary to adequately replicate patient-specific flow dynamics.

- **Wall modeling:** While the wall lumen itself can be captured with medical imaging, the varying internal wall parameters are dificult to quantify [86, 305]. To include wall properties and stress-strain behavior accurately, fluid-structure interaction (FSI) simulations can be performed. Ma et al. extracted the aneurysmal vessel wall parameters from transcranial Doppler and MRI measurements and thus elucidated the intra-aneurysmal hemodynamics with FSI [183]. They observed the variable interaction of hemodynamic and biomechanical parameters. The results demonstrated that a need for realistic acquisition of pathological and anatomical data exist. However, a trade-off between the computational effort and lack of material data as well as the accuracy of results have to be carefully considered. Therefore, in this thesis, the vessel wall is always held rigid.

- **Solver:** A variety of solvers exist that apply the finite volume method to calculate hemodynamics in vascular pathologies. These solvers can be configured with different convergence criteria and methods, all of which influence the results. Additionally, variations in spatial and temporal resolution are possible, which also affect the outcomes. This was previously investigated in an internationally conducted challenge, where participants were provided with a model and boundary conditions and were asked to perform simulations and report the resulting parameters and settings [283]. Variations of more than 10 % in resulting hemodynamics were observed between different solver applications. Further insights into the varying effects of high- and low-resolution simulations, particularly those performed with commercially available or self-built solvers, will be provided in Chapter 4. For conventionally used solvers, a base mesh size of 0.1 mm and a spatial and temporal discretization of 1 ms were suggested in previous studies [25].

3.2 Contribution

Patient-specific hemodynamic simulations derived from medical imaging have become an indispensable tool for analyzing blood flow with high spatial and temporal resolution. These simulations are particularly valuable for assessing the state of vascular diseases, monitoring their progression, and quantifying associated risks. One of the most critical neurovascular pathologies are IAs, which vary widely in size, shape, and location and may even be present as multiple IAs in the same patient. Although the mechanisms underlying their development are poorly understood, hemodynamic parameters such as velocity, WSS and OSI are considered key factors associated with aneurysm rupture [57, 132]. Consequently, improving our understanding of patient-specific hemodynamic environments is crucial for refining the treatment criteria and management strategies for IAs [175].

IAs occur often within the intracranial vascular architecture, the so called CoW, playing a critical role in cerebral hemodynamics [175]. An understanding of cerebral vascularization is essential for advancing medical knowledge and clinical practice. In recent research a conventional hemodynamic modeling of the CoW and IA hemodynamics has been established, comprising specific key approaches. The variabilities in these conventional modeling approaches consist of the medical imaging, its segmentation, the choice of the included vasculature complexity and of the simulation settings: spatial and temporal discretization (this will be dealt with in Chapter 4), chosen solver, blood modeling, vessel wall modeling and BCs (inflow and outflow conditions). As explained in section 3.1, these comprise several settings, which are specifically

defined by each research group depending on the aim of the current research question. In studies lacking realistic measurements and in vivo conditions, assumptions regarding the BCs are made, or mathematical models implemented. In previous work, the impact of specific pre-processing and modeling approaches was evaluated. However, their interacting effect has not been fully understood yet.

This chapter investigates the critical role of vasculature complexity, lumen segmentation and the chosen outlet BC on intra-aneurysmal hemodynamics in patient-specific data. For this purpose, advanced flow-splitting methods are employed and compared to the commonly used outlet BC approaches, such as the zero-pressure BC. The analysis extends the Multiple Aneurysms Anatomy Challenge 2018 [26], which involved segmentation contributions from 24 groups across 13 countries for five patient-specific IAs. In addition to that, high-resolution 7 Tesla TOF MRI data are utilized to construct a complex 3D surface mesh containing 60 outlet vessel cross-sections. By incorporating a range of segmentations and a complex vasculature model, the analysis captures real-world variability introduced by manual processing, enabling a realistic evaluation of the interplay between segmentation, model complexity and outflow BCs.

First the considered models comprising the physiological CoW vasculature and the aneurysm models are presented. Second, the methodological procedure of the model pre-processing is explained. This includes the real-world segmentation variability of the aneurysm models and the CoW vasculature model segmentation. The complex vasculature is furthermore reduced by cutting specific outlets to achieve an additional trimmed version of the CoW. Two aneurysm models were manually stitched onto the physiological complex and trimmed CoW vasculature to achieve an artificial pathological model. Further methodological procedures comprise the application of five outlet BCs, whose different approaches are explained. Conventional hemodynamic blood-flow simulations were performed based on the pre-processed medical images and the according data analysis is introduced. Third, the impact of each of the modeling variations (vasculature complexity, real-world segmentation variability, outlet BC) on the local hemodynamics is analyzed. In the following, the interaction between the outlet BC and the pre-processing variability (model complexity and segmentation) is evaluated. The findings are related to recent literature. The research questions of this chapter can thus be summarized as follows:

Research questions

A. How does the individual impact of variability in vasculature complexity, lumen segmentation and outlet BC affect the hemodynamics in image-based blood flow simulations of IAs?

B. How does the interaction effects of variations between model complexity and segmentation with the outlet BC affect the hemodynamics of the image-based blood flow simulations of intracranial aneurysms?

3.3 Methodology

3.3.1 Patient cohort

The geometrical foundation of this chapter is a CoW model derived from a healthy subject and five IAs from a single patient. The CoW model was initially segmented into a complex version with 60 outlets and subsequently refined into a trimmed version with 10 outlets. The aneurysms were segmented into three peri-aneurysmal models: two IAs in peri-aneurysmal model 1, two IAs in peri-aneurysmal model 2, and one IA in peri-aneurysmal model 3. Additionally, two of the five IAs were further integrated into the CoW models through a stitching process, as detailed in the following sections.

Circle of Willis model

The 3D surface segmentation was derived from high-resolution (0.32 mm isotropic) TOF MRI data, obtained from a healthy subject using a 7 Tesla MRI scanner (Siemens Healthineers, Erlangen, Germany) [150]. To mitigate motion artifacts and preserve the visibility of small vessels, the imaging included prospective motion correction. The marching cubes algorithm was subsequently employed to extract a 3D surface model from the segmentation mask. The surface was then refined using Laplacian smoothing to reduce surface irregularities. Manual post-processing followed, which involved removing artifacts and disconnected surface regions. The inlets and outlets of the vessel model were then cut perpendicular to the centerline of the vessel and extruded in normal direction to minimize BC effects.

The final model consisted of a complex vascular model featuring 60 outlet branches, which is shown in Figure 3.1 in red. To incorporate vasculature complexity effects in this chapter, this model was further reduced to a trimmed version of the CoW. For this, vessel parts comprising 50 small outlets were cut preserving the main vessels of the CoW and the model manually adjusted to a trimmed model (10-outlets), by filling and smoothing incoherent surface areas. The trimmed model is shown in Figure 3.1 in blue.

Intracranial aneurysm models

The IA models used in this chapter were derived from previous research investigating the effects of segmentation variability and involve five IAs from a single patient who experienced a subarachnoid hemorrhage [26, 27]. Two of these aneurysms (A and B) were located on the right MCA (peri-aneurysmal model 1), another two (C and D) on the left MCA (peri-aneurysmal model 2), and the fifth (E) on the left posterior inferior cerebellar artery (peri-aneurysmal model 3). The three peri-aneurysmal models are shown in Figure 3.2 together with a detailed view of the five IAs.

To acquire the vessel lumen for the patient-specific IAs, 3D rotational angiography with an isotropic spatial resolution of 0.28 mm was conducted using an Artis Q angiography system (Siemens Healthineers AG, Forchheim, Germany). Within the previous study, a worldwide scientific challenge was conducted and the medical image data provided for individual segmentation to compare the results afterwards. Subsequently, 26 different groups performed the segmentation as part of this challenge [26, 27]. Participants did not receive any specific guidelines to ensure a diverse range of segmentation techniques. 2 of the 26 groups provided non-usable segmentation data, thus they needed to be excluded from the challenge and the participating research groups reduced to a count of 24.

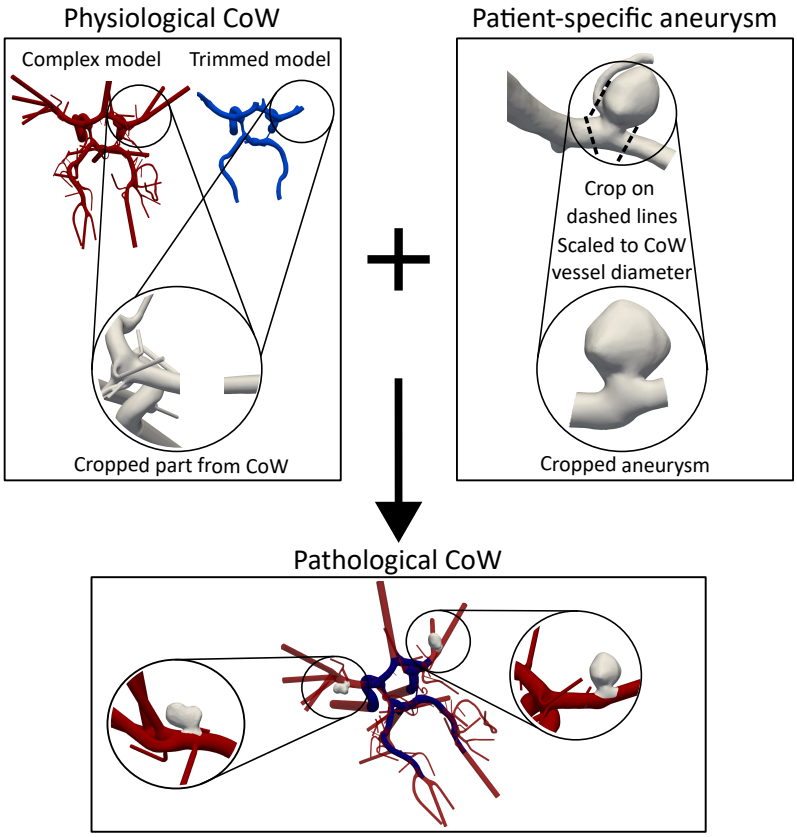


Figure 3.1: Underlying workflow of pathological Circle of Willis (CoW) model creation: Cropping the complex (red) and trimmed (blue) CoW model at the two locations for the IA implementation. Additional cropping of the peri-aneurysmal models by excluding dome and parent vessel from the domain. Stitching of the patient-specific IAs onto the complex and trimmed physiological CoW model.

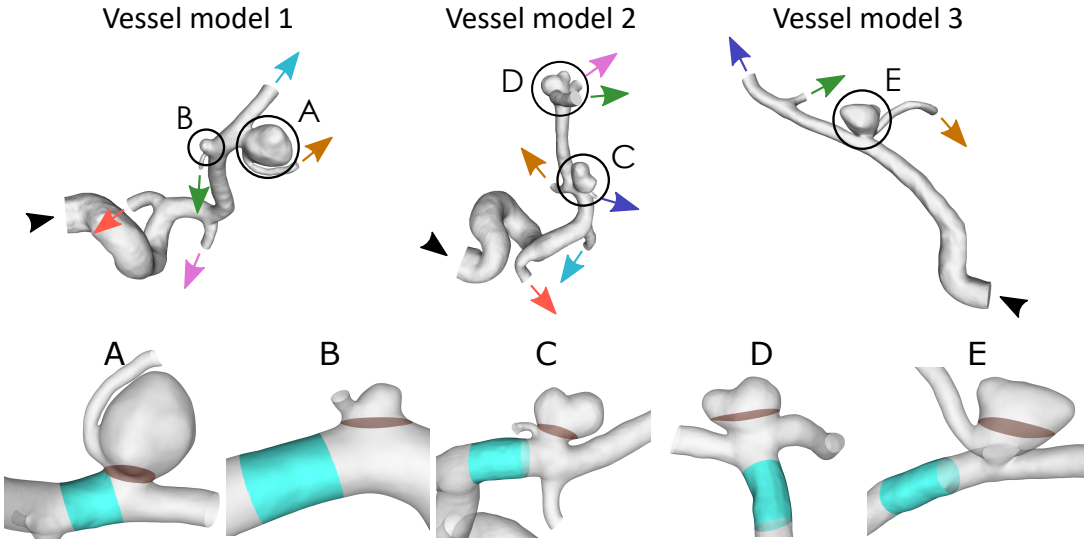


Figure 3.2: Top: Patient-specific peri-aneurysmal models 1-3 with the five aneurysms in total (peri-aneurysmal model 1: IA A & B, peri-aneurysmal model 2: IA C & D, peri-aneurysmal model 3: IA E). Black arrowheads depict the inlets, colored arrows the outlets. Bottom: Zoom on each IA (A-E), including the visualization of the parent vessel (blue) and ostium surface area (brown). Note that IA A and C were used for stitching on the CoW vasculature.

Combination of circle of Willis and intracranial aneurysm models

The original CoW model was captured in non-pathological condition and to establish a more complex scenario, with an increased clinical relevance the pathological state was manually created. For this, two of the five IAs were integrated into both, the complex and trimmed, CoW models. This ensured the possibility to further investigate the effect of vasculature complexity and varying outlet BCs under pathological conditions. The IAs were chosen according to their location: One located at the right MCA (IA A) and the other at the left MCA (IA C). These have the most outlets lying between the inlet and each IA, thus, strongest impact of the vasculature complexity is expected.

To prepare the combination of the IAs with the physiological CoW, the exact locations of the two IAs within the complex and trimmed CoW models were examined by positioning peri-aneurysmal model 1 and peri-aneurysmal model 2 (recall Figure 3.2) correctly within the complex and trimmed CoW model. This step of registering the models was conducted in Blender (v3.1, Blender Foundation, NL). Moreover, to ensure a similar parent vessel circumferential dimension, the peri-aneurysmal models were scaled up to an overlap of the diameter of the CoWs' and the IA parent vessels' walls.

To combine the IAs with the CoW models, a combination workflow of the model stitching was established, which is shown in Figure 3.1. Initially, the regions of the CoW models corresponding to the locations of the IAs were cropped, leaving a gap to facilitate the addition of the aneurysm models. Subsequently, the chosen IAs were cropped at the boundaries of their parent vessels. As visualized in Figure 3.2 IA A and IA C both have a small outlet vessel close to the aneurysm neck. These small vessels were additionally cut from the IA dome before the stitching process to prevent the 60 and 10 outlets of the CoW models. Subsequently, the overlapping segments of the parent vessels of the two IA models were merged and smoothed together with the cropped parts of the trimmed and complex CoW models.

3.3.2 Variabilities in hemodynamic modeling

As explained in section 2.6, variabilities in hemodynamic modeling, with varying impact on the hemodynamic outcome of CFD in medical applications exist. Three aspects, of which knowledge is still missing in the literature, are considered in this chapter: 1) the vasculature complexity, 2) the segmentation, and 3) the outlet BC.

The further assumptions which need to be set for the hemodynamic simulation (medical imaging, image reconstruction, blood modeling, inflow BC, wall modeling and solver) were set invariable in this chapter to keep a comparable basis. As medical images were provided in reconstructed state, it was not possible to analyze any variation in this regard. Moreover, since no patient-specific inflow conditions were known for these cases, a representative inlet curve scaled on the inlet's cross-sectional area was chosen. This was suggested to be most effective in the literature [298]. Additionally, keeping the inflow equal ensures a comparable basis between the models. This applies to the blood and wall modeling as well. To keep an equal basis, a constant density and viscosity was chosen for the fluid within the simulations, which will be further explained in section 3.3.3, and the walls were assumed to be rigid.

This chapter presents the three chosen aspects of variability in modeling vasculature complexity, segmentation, and outlet boundary condition in that order, explaining the approaches and variations within.

Vasculature complexity

To analyze the impact of the chosen vasculature complexity on the hemodynamics inside the IAs, the complex (60 outlets) and trimmed (10 outlets) CoW models were considered. This model reduction was conducted to facilitate comparisons with existing CFD studies of the CoW (Figure 3.1). The resulting parameters defining the inlets and outlets of the two models are shown in Table 3.3. Note that each CoW model has three inlets, namely the left and right ICA and the BA.

Table 3.3: Inlet area of the CoW models at each of the three inlet branches, respectively (left and right ICA and BA). Shown together with the outlet count and sum over all outlet cross-sectional areas for the complex and reduced model.

	Inlet area	Outlet count		Mean outlet area (mm^2)	
	(mm^2)	complex	reduced	complex	reduced
ICA r	8.76	17	4	21.76	16.96
ICA l	2.07	9	2	26.85	8.86
BA	2.00	34	4	27.47	15.17

Segmentation

The impact of the variation and accuracy in segmentation was implemented by considering the results of the real-world challenge as explained in section 3.3.1. The five IAs chosen for this chapter were previously handed out to the research community within a worldwide challenge [26, 27]. Hereby, 24 segmentations of the raw imaging data were performed and served as a basis for further investigations.

For two of the IAs, high-resolution 2D reference images were available, which facilitated the quantification of the segmentation accuracy. IA E demonstrated significant segmentation variability across the different groups when compared to the 2D digital subtraction angiography reference data [26]. Given the interest in understanding the impact of segmentation variations, this particular aneurysm was selected for further analysis in this thesis, incorporating the segmentation results from all participating groups. The according segmentations are shown in Figure 3.3.

Outlet boundary condition

Regarding the outlet BC, five modeling approaches were chosen and applied to the one chosen IA (IA E) including the 24 segmentations. For the remaining four aneurysm models, one segmentation was used. This was chosen based on the mean value of the evaluated hemodynamic parameters over all segmentations. Moreover, the outlet conditions were applied to the trimmed CoW vasculature. Due to the high outlet count of the complex model, restriction in the flow splitting tool existed and thus, the complex model could not be considered in this context.

The first condition (BC1) applied, was the commonly used zero-pressure approach, where a constant pressure of $p = 0$ is set at each outlet. Next, two flow-splitting approaches based on Murray's law were implemented. Murray's law describes the proportional relationship between the flow rate in a vessel and its diameter [62]. By considering mass conservation and excluding branch junctions, this relationship was expressed with power exponents of $n = 2$ (BC2) and $n = 3$ (BC3) [205]. In Equation (3.1) the relationship is presented, showing the proportionality between flow rates Q_i and diameters D_i for each vessel cross-section (i).

$$\frac{Q_i}{\sum Q_i} = \left(\frac{D_i}{\sum D_i}\right)^n \tag{3.1}$$

Another flow-splitting method (BC4) is based on Murray's law, but is applied locally at each bifurcation, considering circular vessel cross-sections [62]. The power exponent for BC4 was set to $n = 2$, making it closely related to BC2, with both following the same proportionality law. However, BC4 offered a refinement by assessing flow distribution locally at each branch point as defined in Equation (3.2) [62].

$$\frac{Q_1}{Q_2} = \left(\frac{D_1}{\sum D_2}\right)^2 \tag{3.2}$$

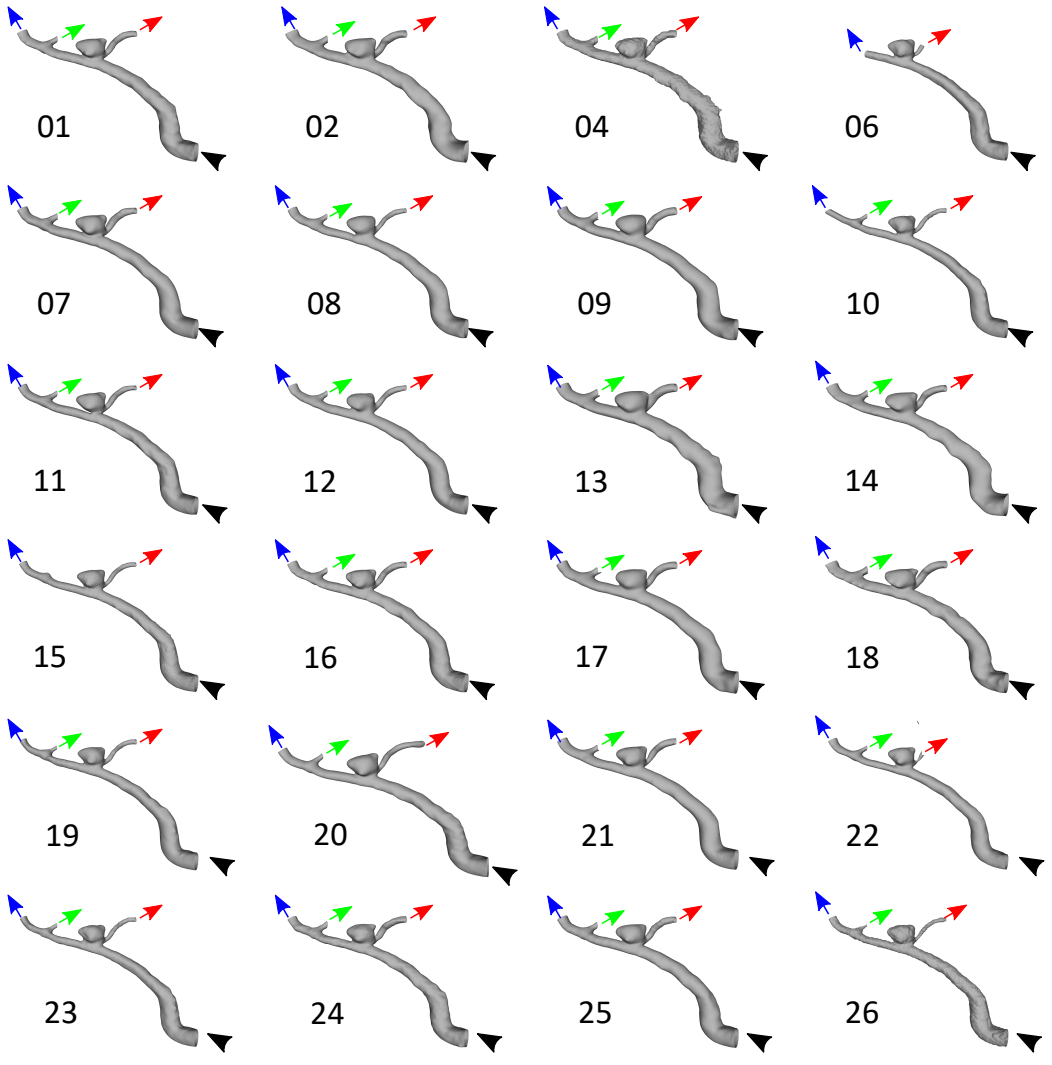


Figure 3.3: Presentation of the 24 variations in segmentation of peri-aneurysmal model 3 including IA E. Again, black arrowheads depict the inlet and colored arrows the outlets. 26 groups participated in providing segmentations of the peri-aneurysmal model, while 2 groups needed to be excluded from the data analysis.

The fifth BC (BC5) introduced an improved flow-splitting model that accounted for the actual local vessel cross-section [259]. It adapted the method used for BC4, but instead of using the squared diameter, it utilized the true luminal cross-sectional area (equation (3.3)). This

area was approximated as a polygonal surface derived from a ray-tracing approach, with rays projected from the vessel centerline to the surface boundary [259]. Since this method considered the greatest geometric variability, it was used as the reference model in the comparison, serving as a substitute for ground truth in the absence of in vivo flow data.

$$\frac{Q_1}{Q_2} = \frac{A_1}{\sum A_2} \tag{3.3}$$

The equation-based BCs BC2-5 showed an incremental improvement in calculating the flow-splitting values, with each step enhancing upon the previous one. In contrast, as BC1 involved a constant pressure condition and BC3 used a power exponent of $n = 3$, BC1 and BC3 did not correlate with the vessel cross-section.

3.3.3 Numerical investigation

The impact of the variabilities in pre-processing and modeling was assessed by evaluating the hemodynamics inside the aneurysms and vessels. These hemodynamic results were achieved by performing numerical simulations and subsequent numerical analysis. The steps required to perform these simulations and analyses are explained in the following.

Hemodynamic simulations

Numerical hemodynamic simulations were performed for each peri-aneurysmal model 1-3 and the complex and trimmed CoW as presented in Table 3.4. For peri-aneurysmal models 1-2 one segmentation result was used and for peri-aneurysmal model 3 (aneurysm E) all 24 segmentation results. For all these models, five outlet BCs (BC 1-5) were applied, apart for the complex CoW, which was solely analyzed using BC2. Distinct inlet BCs were applied to the CoW and the peri-aneurysmal models, tailored to the availability of measurement data from PC-MRI and the specific objectives of the analyses (see Table 3.4). For the peri-aneurysmal models, in the absence of direct measurement data, representative inlet flow curves from the literature were utilized, varying based on the anatomical location of the vessel [75]. In contrast, for the complex and trimmed CoW models, physiological measurement data obtained from high-resolution PC-MRI were available [89, 285]. These data were applied to the three inlets BA, left ICA, and right ICA of both the complex and trimmed CoW models. To analyze the trimmed CoW model using the five outlet BCs, literature-based inflow data was applied by scaling the curves according to the inlet cross-sectional areas. This provided a comparable basis for evaluating the interaction between vasculature complexity and the chosen outlet BC, as the same IAs could be analyzed once in the trimmed CoW model and once in the peri-aneurysmal models. The corresponding inlet flow curves are illustrated in Figure 3.4.

Table 3.4: Overview of the simulations conducted for this chapter, classified using model basis, source (PC-MRI or literature (Lit.)) of inflow boundary condition (BC), chosen outlet BC and resulting simulation (Sim.) count.

Model	Inflow BC	Outlet BC	Sim. count
Peri-aneurysmal model 1 (IA A & B)	Lit.	BC 1-5	5
Peri-aneurysmal model 2 (IA C & D)	Lit.	BC 1-5	5
Peri-aneurysmal model 3 incl. 24 segmentations (IA E)	Lit.	BC 1-5	120
CoW complex with IAs A & C (60 outlets)	PC-MRI	BC 2	1
CoW trimmed with IAs A & C (10 outlets)	PC-MRI	BC 2	1
	Lit.	BC 1-5	5

The models were similarly discretized with a maximum spatial cell size of $\Delta x = 0.07 - 0.125$ mm to ensure a solution independent from mesh settings. Due to the large geometry of the CoW models, a bigger mesh size of 0.125 mm was set to reduce numerical effort. Three to four prism layers were set with a prism layer stretching of 1.3, according to mesh independency studies performed in previous works and the established mesh settings used in [133]. This resulted in a cell count of 1.9-2.6 million cells for the peri-aneurysmal models, 4.7 million cells for the complex CoW model and 2.6 million cells for the trimmed version (both with the stitched IAs). For each simulation, the finite volume solver STAR CCM+ (2021.3 v16.6, Siemens Product Lifecycle Management Software Inc., Plano, TX, USA) was used.

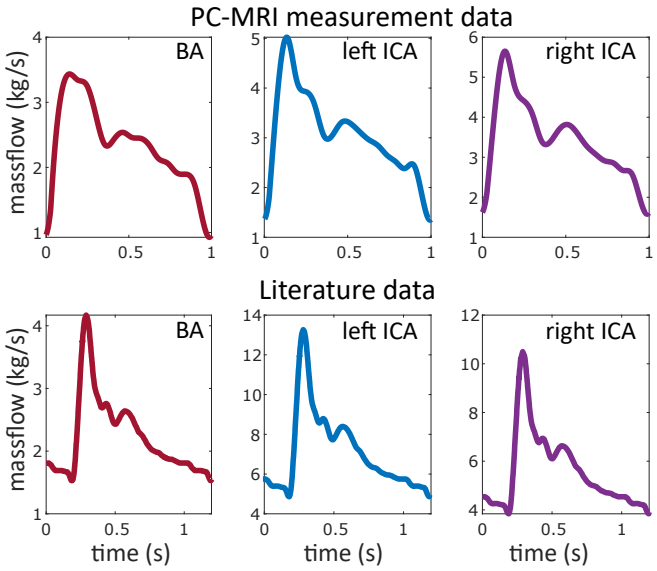


Figure 3.4: Inflow BCs for the three inlets basilar artery (BA), left internal carotid artery (ICA), and right ICA from phase-contrast magnetic resonance imaging (PC-MRI) measurements for the CoW inlets and inflow curve data derived from literature for the vessel model inlets (1-3). Note, that the literature data were additionally scaled to be used for the CoW model inlets when comparing the intra-aneurysmal hemodynamics of IA A and IA C within the vessel models and within the trimmed CoW vasculature.

The timestep size was set to $\Delta t = 0.001\,\mathrm{s}$ for each simulation and the flow assumed to be laminar. The blood was assumed to be Newtonian [176]. Blood density was then set to $\rho = 1055\,\mathrm{kg\,m^{-3}}$ and viscosity to $\eta = 0.004\,\mathrm{Pa} \times \mathrm{s}$. Within each simulation, three cycles were considered, to ensure cycle independence and only the last cycle was considered for analysis. In total 137 time-dependent simulations were performed taking the variations in modeling approaches into account as depicted in Table 3.4.

Post processing

To assess how the varying approaches influenced numerical flow predictions, key hemodynamic parameters were analyzed both qualitatively and quantitatively. The analysis was conducted using ANSYS EnSight 2021 v10.2 (ANSYS, Inc., Canonsburg, PA, USA) and MATLAB R2020b (MathWorks, Inc., Natick, MA, USA). Specific parameters required the definition of a reference parent vessel section, chosen as the vessel segment closest to the aneurysm neck [25, 306]. The chosen parent vessel part is shown in Figure 3.2 (blue) together with the defined ostium surface (brown). The flow parameters analyzed were the blood velocity, vorticity, OVI, NIR, KE and KER.

Regarding the shear-related metrics at the aneurysm sac, TAWSS, nTAWSS, OSI and LSA were included [306, 207]. The parameter explanations and formulas are listed in section 2.5. All calculations defined as mean were based on the temporal mean over a complete cardiac cycle. Parameters associated with the aneurysm were averaged spatially over the aneurysm dome separated from the vessel by the defined ostium (recall Figure 3.2). To specify the complexity's impact of the model, additionally the flow rates were determined at all outlet surfaces of the vascular model and through the aneurysm neck (NIR).

3.4 Impact of variability in segmentation, vasculature complexity, and outlet boundary condition

This section evaluates the impact of the chosen variabilities in numerical blood flow modeling on the hemodynamic outcome. First, the impact of the chosen vasculature complexity, secondly, of the segmentation and lastly of the outlet BC are considered.

3.4.1 Vasculature complexity

Figure 3.5 illustrates the qualitative visualization of the hemodynamics inside the stitched IAs for the complex and trimmed model. Specifically, TAWSS, OSI and velocity are visualized, each normalized by their temporal average. The velocity field within the IA is presented by a plane through each aneurysm dome colored with the normalized velocity. This velocity distribution did not show differences in the qualitative visualization between the two IAs. On the aneurysmal wall, however, qualitative differences in shear stress distribution and oscillatory effects occurred. IA A featured an increase in TAWSS after trimming of the vasculature, whereas IA C featured a decrease. Regarding OSI, an increase for both IA A and C appeared after model trimming. The observed variations in the increase of IA A and decrease of IA C in TAWSS at the walls highlight the influence of the CoW complexity. As the locations vary, the vasculature complexity influences the hemodynamics differently.

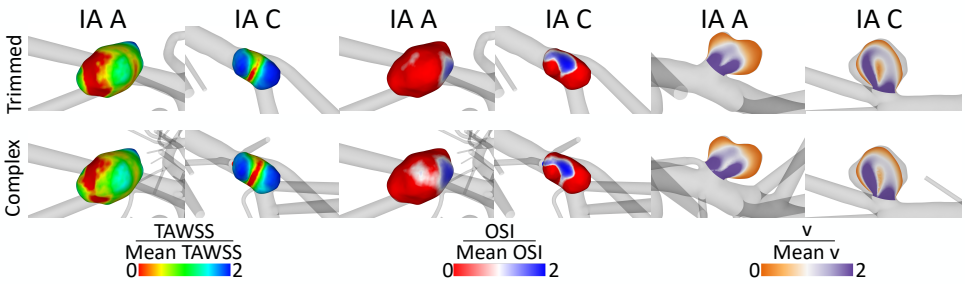


Figure 3.5: Qualitative representation of the hemodynamic parameters time-averaged wall shear stress (TAWSS), oscillatory shear index (OSI), and velocity (v) inside the dome of IA A and IA C within the complex and trimmed CoW vasculature model. Hemodynamic parameters are normalized by their mean value.

The quantitative assessment of intra-aneurysmal hemodynamics (see Figure 3.6) demonstrated the influence of vascular modeling, consistent with the qualitative findings. The impact varied depending on the IA location, with an increase in average velocity and TAWSS observed in IA A, while IA C exhibited a corresponding decrease within the trimmed vasculature. Notably,

an increase in OSI was observed for both aneurysms. This difference is caused by the inclusion or exclusion of vessel branches, leading to a general overestimation of the flow within the trimmed model. This effect of parent vessel artery exclusion on the aneurysmal hemodynamics was also investigated by Castro et al. [50]. They compared the CFD-based intra-aneurysmal hemodynamics of seven patient-specific IA cases, which included the segmented parent vessel artery, with manually processed cases that consisted only of the IA dome merged with straight vessels serving as parent arteries. Their results demonstrated that including the parent artery is crucial for accurately replicating the inflow jet into the IA.

Moreover, Ren et al. previously demonstrated that geometric differences in the CoW model influence hemodynamics due to patient-specific anatomical variations [248]. They constructed ten variations of the posterior circulation of the CoW and analyzed the collateral capacity of each model. Their findings indicated that collateral capacity varied depending on the specific location within the CoW. Similarly, Valen-Sendstad et al. reported variations in intra-aneurysmal hemodynamics influenced by the inclusion of surrounding vasculature in the analyzed IA [295]. Their results stemmed from an international challenge in which 26 research groups were provided with raw image data of five IA cases. Each group performed independent segmentations and simulations before submitting shear stress outcomes. The observed variability in included vasculature highlighted the critical need for standardized guidelines for both engineers and clinicians.

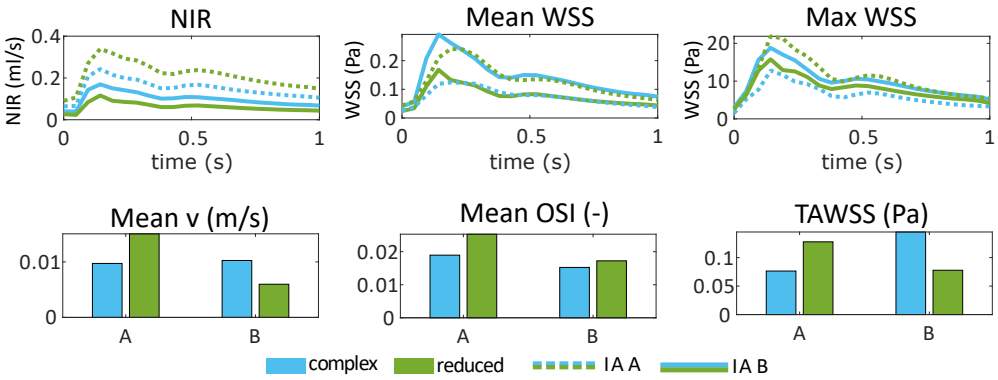


Figure 3.6: Representation of the neck inflow rate (NIR), average wall shear stress (WSS), and maximum (max) WSS over one cardiac cycle for IA A and IA C within the complex and trimmed model. Additionally, the mean values inside the IA dome of velocity, OSI and TAWSS are presented below.

Further previous studies have reported varying results regarding the relationship between IA location, hemodynamics, and rupture risk, highlighting its complexity. For example, Zhou et al. investigated the association between significantly decreased average WSS—by more than 60 %—and IA rupture [334]. Their conclusion was based on a review of 14 studies analyzing IA rupture risk and related hemodynamic factors. As demonstrated in this chapter, variations in vasculature complexity can also lead to a 60 % reduction in peak systolic TAWSS for the IA located in the left MCA, whereas this effect was not observed for the IA in the right MCA. The majority of past studies assessing IA rupture risk included only vessels in close proximity to the IA, often excluding bifurcations and distal branches [57, 287]. Notably, studies that did not incorporate complex vasculature but focused solely on the relationship between hemodynamic parameters and rupture risk may have led to misleading assumptions regarding clinical applicability [310, 334].

Thus, incorporating the highest possible vasculature complexity into simulations is recommended to achieve the most physiologically accurate representation. However, due to limitations in medical imaging, reconstruction techniques, and numerical requirements, careful consideration must be given to IA location and the associated vascular complexity. The IAs analyzed in this chapter, located in the right and left MCAs, exhibited sensitivity to model complexity, with the left MCA model showing a greater influence on hemodynamic results. These findings underscore the critical role of aneurysm location in determining the level of vascular detail required for numerical simulations. Specifically, the anatomical position of the IA dictates whether a highly detailed vasculature is necessary. This thesis highlights the need for location-specific and geometry-driven approaches in IA modeling to ensure clinically meaningful insights. This thesis reinforces the need for location-specific and geometry-driven approaches in IA modeling to ensure clinically meaningful insights.

3.4.2 Segmentation

To evaluate the impact of lumen segmentation, the OVI inside the IA dome and the TAWSS on the aneurysmal surface are presented for each segmentation of IA E in Figure 3.7. Together with the qualitative results, the mean values of TAWSS and TA velocity spatially averaged in the aneurysm dome are shown as bar plots. For the presented cases, the commonly applied BC2 was used. The results reveal OVI values higher than 0.1 for all cases in the neck area of the IA dome. No oscillatory effects occur at the left side of dome. The highest effects occur in the bifurcation area as seen within groups 2, 4, 9, 12, 13, 14, and 17. The OVI isosurfaces showed high differences in magnitude over all cases and no specific relation or pattern could be derived. This applies as well to the TAWSS distribution. Here, a relation to the smoothness of the wall surface could be derived, as higher TAWSS values appeared for groups 4, 24, and 26, which feature especially rough surfaces.

However, as seen in the plots, groups 2, 14, 17, and 23 revealed high TAWSS values and featured a smoothed wall. The quantitative velocity values differed in a similar way as the TAWSS values over the segmentations. This effect of the segmentation was also found by Voß et al. and Goubergrits et al. [306, 100] in studies previously performed to this thesis, based on the same dataset. Their studies underscore how variability in aneurysm segmentation significantly impacts hemodynamic simulation accuracy, limiting comparability across studies. The neck, in particular, showed high variation in its definition; however, it was found to be highly sensitive to segmentation accuracy [24].

This calls for standardized, accurate segmentation and consistent geometry assessment to minimize errors and improve rupture risk predictions in clinical settings. Establishing standards for image segmentation is recommended to support the development of reliable risk models. Future analyses with larger, more diverse aneurysm data sets would further improve prediction accuracy. Moreover, the application of segmentation methods based on machine learning like introduced by Rezaeitaleshmahalleh et al., Timmins et al. or Ivantsits et al. could improve segmentation accuracy in the future [250, 291, 127]. Rezaeitaleshmahalleh et al. investigated two segmentation approach using artificial intelligence, which were further compared to manual segmentation data [250]. Their results showed a good agreement in all morphological parameters. This can be a step forward to automated segmentation processes, which could overcome the influence of manual wall surface smoothing and neck shape definition.

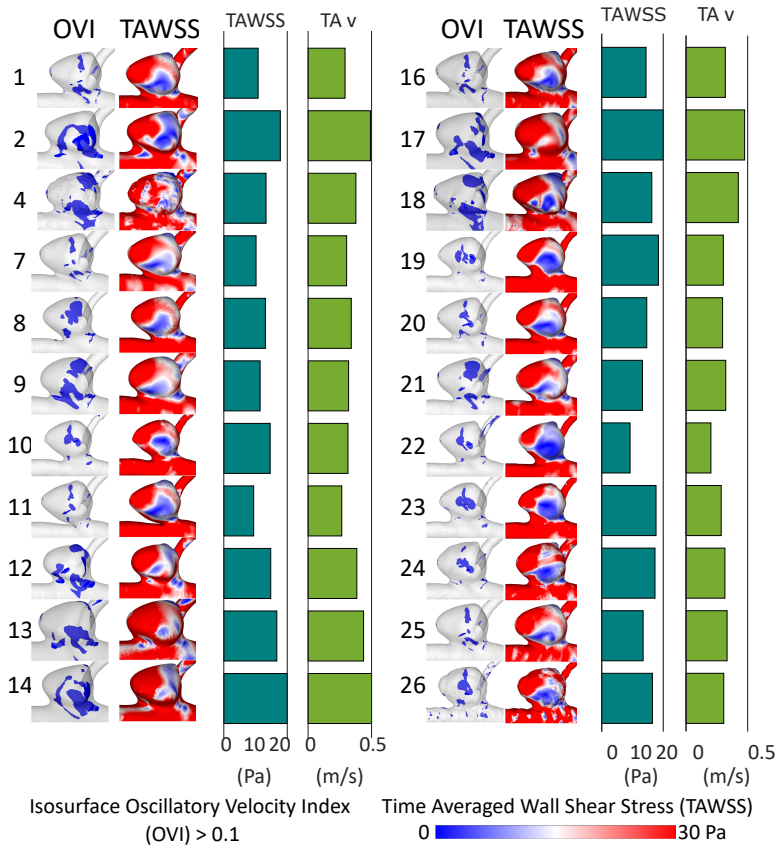


Figure 3.7: Qualitative and quantitative hemodynamics within IA E based on the 24 varying segmentations and BC2. The oscillatory velocity index (OVI) and time-averaged wall shear stress (TAWSS) are shown qualitatively, while the mean inside the IA dome of TAWSS is as well presented quantitatively together with the mean TA velocity (v).

3.4.3 Outlet boundary condition

Table 3.5 provides the outlet flow splittings associated with each BC for the chosen vessel models comprising the five IAs. The BCs influence the vessel outflow distribution either indirectly (BC1) or directly (BC2–5), resulting in specific splitting value ratios. In the case of BC1, the splitting values are computed post-simulation based on the resulting hemodynamic data. For the remaining BCs (BC2–5), the splitting values are derived from the geometric model and determined before the simulation. Each splitting value represents the proportion of the total outflow assigned to each outlet. Additionally, the percentage deviation of each BC1-4 to BC5 is shown in brackets. In Table 3.6 the according values of the 10 outlets of the trimmed CoW model are presented.

To assess the influence of BCs on aneurysmal flow dynamics, the qualitative results of all models for each BC are presented comparatively in Figure 3.8. A cross-sectional plane through each IA, color-coded by the temporal mean KE is shown to represent the intra-aneurysmal results. Subsequently, the mean TAWSS is shown regarding the wall-related results. Each column in the figure contrasts the effects of different BCs, while rows display the differences across IA models. In all cases, the incoming flow generates a vortex within the aneurysm, where KE was generally higher near the aneurysm wall and lower within the aneurysmal sac, regardless

of the applied BC. However, notable differences in KE magnitude emerged. Specifically, BC1 and BC3 exhibited lower KE levels within the aneurysm than BC2, BC4, and BC5, with the highest KE levels observed in BC4 and BC5 consistently across all IA models. Although the spatial distribution of TAWSS appeared similar across BCs for each IA model, differences in magnitude were evident, reflecting the KE differences. Consistent with the KE findings, TAWSS is slightly reduced under BC1 and BC3 compared to the other conditions, reaffirming the distinct impact of these BCs on aneurysmal hemodynamics.

Table 3.5: Splitting values of the five aneurysm cases with IA A & B and IA C & D being located at the same vessel. The percentage deviation of each splitting value to its counterpart calculated with BC5 is shown in brackets.

		BC 1	BC 2	BC 3	BC 4	BC 5
IA A & B	O 1	0.513 (+41)	0.401 (+25)	0.465 (+35)	0.345 (+13)	0.301
	O 2	0.209 (-9)	0.207 (-10)	0.173 (-31)	0.239 (+5)	0.227
	O 3	0.002 (-900)	0.016 (-25)	0.004 (-400)	0.019 (-5)	0.020
	O 4	0.011 (-555)	0.054 (-33)	0.023 (-213)	0.069 (-4)	0.072
	O 5	0.265 (-44)	0.322 (-18)	0.335 (-14)	0.328 (-15)	0.381
IA C & D	O 1	0.397 (+36)	0.295 (+14)	0.351 (+28)	0.255 (+0)	0.254
	O 2	0.187 (-1)	0.143 (-31)	0.119 (-58)	0.218 (+14)	0.188
	O 3	0.011 (-1009)	0.030 (-307)	0.011 (-1009)	0.139 (+12)	0.122
	O 4	0.086 (+59)	0.095 (+63)	0.064 (+45)	0.026 (-35)	0.035
	O 5	0.138 (-56)	0.181 (-19)	0.170 (-26)	0.194 (-11)	0.215
	O 6	0.180 (-3)	0.256 (+27)	0.284 (+35)	0.167 (-11)	0.186
IA E	O 1	0.164 (-62)	0.236 (-13)	0.181 (-47)	0.274 (+3)	0.266
	O 2	0.098 (-82)	0.182 (+2)	0.123 (-45)	0.190 (+6)	0.178
	O 3	0.738 (+25)	0.581 (+4)	0.697 (+20)	0.536 (-4)	0.555

Table 3.6: Splitting values of the five BCs of the trimmed CoW model. The percentage deviation of each splitting value to its counterpart calculated with BC5 is shown in brackets.

	BC 1	BC 2	BC 3	BC 4	BC 5
O 1	0.17 (-16.80)	0.20 (0.04)	0.22 (10.08)	0.18 (-7.40)	0.20
O 2	0.11 (-45.18)	0.16 (-0.44)	0.16 (-0.70)	0.15 (-7.93)	0.16
O 3	0.10 (37.71)	0.07 (17.59)	0.08 (21.87)	0.06 (-5.67)	0.06
O 4	0.02 (-110.23)	0.05 (1.30)	0.03 (-83.53)	0.07 (35.38)	0.05
O 5	0.22 (25.11)	0.18 (10.62)	0.22 (23.99)	0.16 (-0.29)	0.16
O 6	0.05 (35.14)	0.04 (20.30)	0.03 (-5.41)	0.03 (6.38)	0.03
O 7	0.06 (-0.23)	0.05 (-15.11)	0.04 (-31.15)	0.07 (14.52)	0.06
O 8	0.08 (-13.06)	0.07 (-19.40)	0.05 (-60.38)	0.08 (-11.38)	0.09
O 9	0.11 (8.06)	0.10 (-5.24)	0.09 (-21.94)	0.11 (8.35)	0.10
O 10	0.09 (-4.30)	0.08 (-15.26)	0.09 (-1.64)	0.09 (-9.82)	0.10

As presented in Figure 3.9, the quantitative results reflect the results found out qualitatively. Notable differences in magnitude developed due to the choice of the BC, with each BC consistently affecting the hemodynamics similarly across all IAs, irrespective of the IA model. Although the patient-specific geometry crucially influenced the unique flow dynamics within each IA, the overall changes in flow magnitude remained generally consistent across different IAs. When realistic flow-splitting methods (BC2, BC4, and BC5) were applied, high average velocity, KER, and TAWSS as well as lower LSA were observed, while these values were lower

with BC1. This aligned with findings by Chnafa et al. and Saalfeld et al., who developed and examined advanced flow-splitting techniques, showing that moving away from the standard zero-pressure assumption and using refined splitting methods yields more accurate parameter estimations [62, 205].

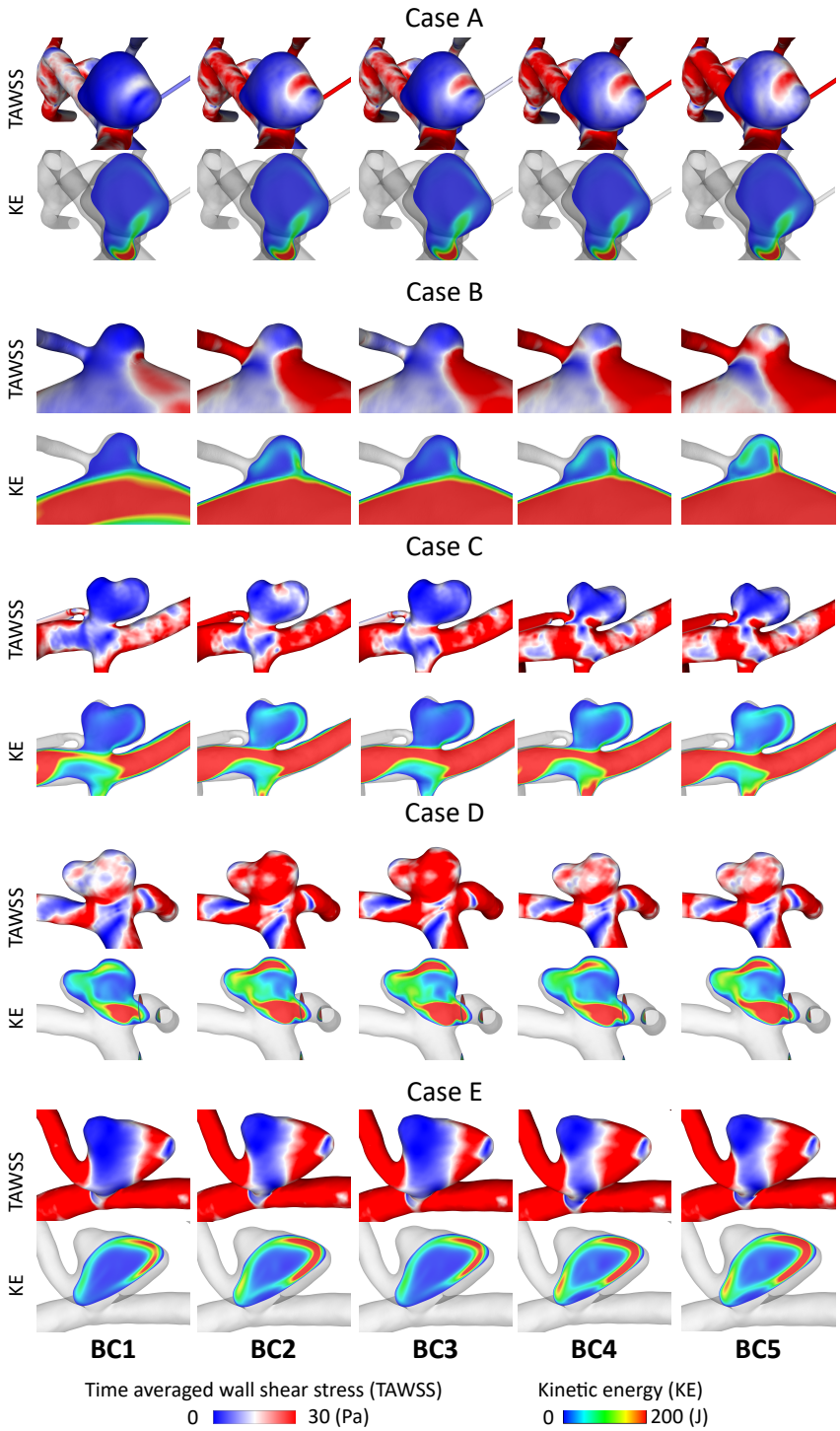


Figure 3.8: Qualitative illustration of the five IAs analyzed with the varying BCs (BCs). The IA models are presented for one chosen segmentation. Time averaged wall shear stress (TAWSS) and kinetic energy (KE) are shown over all five BCs.

Makino et al. compared the application of varying BCs to numerical simulation of IAs using

as well zero pressure (BC1), Murray's law with exponents $n = 2$ (BC2), and further power exponents $n = 2.5, n = 3$ (BC3), $n = 3.5, n = 4$ [187]. They found that Murray's law and its related power laws were more physiologically grounded than the zero-pressure assumption. This was also found in the underlying data as for all IAs (except IA D), the results obtained with BC3 closely align with those of BC1.

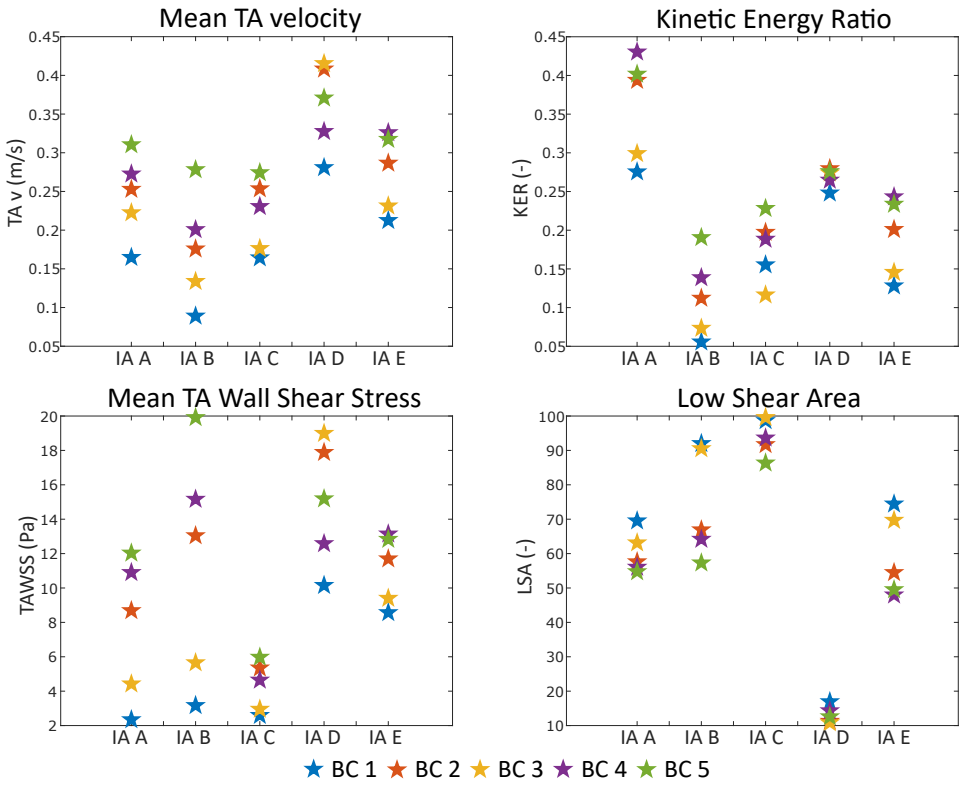


Figure 3.9: Plots of the resulting hemodynamic parameters mean time averaged (TA v) velocity, kinetic energy ratio (KER), mean TA wall shear stress (TAWSS), and low shear area (LSA) inside the five aneurysm models with the chosen segmentation. The results are presented over the five BCs (BC1-5).

Additionally to the comparison of the BC's impact on the intra-aneurysmal flow, its impact on the vessel flow in the CoW model was evaluated. In Figure 3.10 the qualitative results of the temporal mean velocity on five chosen planes are presented together with the quantitative mean and temporally resolved flow rates through these planes. Plane locations throughout the CoW model are shown at the top.

Looking at the velocity visualization, planes 1 and 5 featured similar distribution over the BCs with differences in magnitude. This difference was also reflected in the quantitative plots. In contrast, planes 2 and 3 showed a difference in distribution and magnitude, with distributions by BC4 and BC5 being more similar. The results from BC2 were closest to these two methods. Relating the distribution to the plane locations, the overestimation of BC1, especially at plane 3, became clear, which is located close to an outlet with the smallest cross-sectional area compared to the remaining outlets (see Table 3.6). Between the inlet and the planes 4 and 5 an equal amount of outlets exist within the CoW. The BC method had only a low impact on these planes with even lower impact on plane 4 (Max. difference between BCs: $\Delta 0.03\,\mathrm{mL\,s^{-1}}$(Plane 4); $\Delta 0.04\,\mathrm{mL\,s^{-1}}$ (Plane 5)). This might be related to the smaller diameter of the vessel, which minimized the outflow.

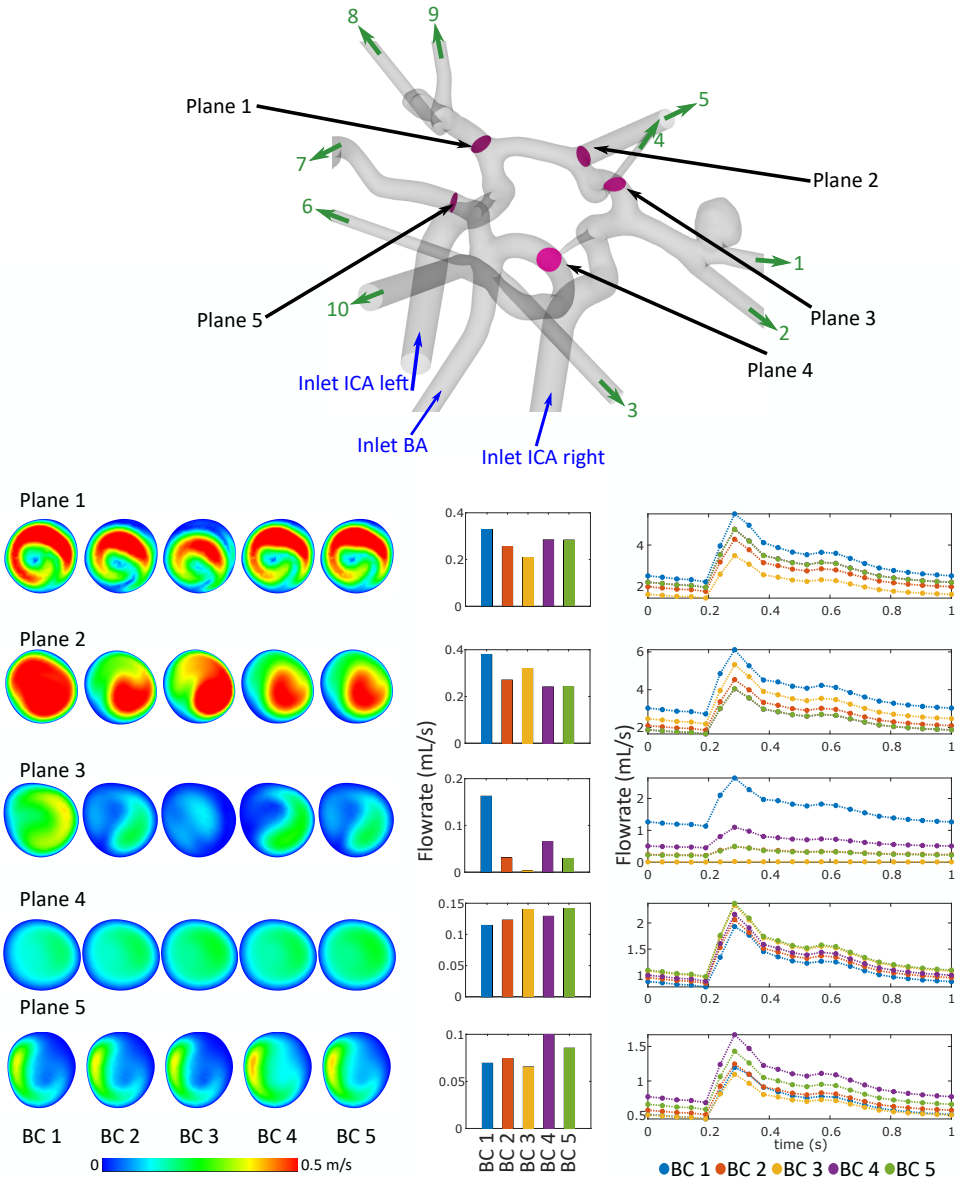


Figure 3.10: Left: Qualitative illustration of the TA velocity on five chosen planes inside the trimmed Circle of Willis vasculature. Plane locations are shown on the top. Middle: Temporally averaged flow rates at each plane over all five BCs. Right: Time resolved flow rates at each plane over all five BCs.

Taking the transient flow curves into account, differences between the curves especially occurred during the systolic peak and acceleration phase. While the flow for all curves remained nearly static for the first fifth of the cardiac cycle (until 0.2 s), especially at planes 3 and 5 flow resulting from BC1 overestimated the increase during peak systole. The results confirmed the high impact of the chosen BC approach on the hemodynamics as was shown by Chnafa et al. and Saalfeld et al. [62, 205]. However, the hemodynamics based on the peri-aneurysmal models 1-3 showed that BC1 and BC3 revealed in general lower results than BC2, BC4, and BC5 (see Figure 3.9). This was not present in the CoW hemodynamics. This leads to the assumption, that the BC effect varies depending on the chosen vasculature complexity.

Due to the high variability observed with BC1 and BC3, which includes the underestimation of hemodynamics within the vessel models and overestimation within the CoW, the use of these approaches is not recommended for future research. Instead, advanced flow-splitting models should be employed to achieve more accurate simulations. The results of this chapter

indicate that the flow-splitting approach based on Murray's law with an exponent of $n = 2$ (BC2) closely approximates the effects of the more advanced splitting techniques (BC4 and BC5). Thus, if the application of advanced models is not feasible, BC2 should be used as an alternative, as it demonstrated results that most closely align with those of the advanced models.

3.5 Interaction between segmentation, vasculature complexity, and outlet boundary condition

In the previous section a relevant influence has been shown for the three individual variabilities. This section invasives if these variabilities interact with each other and if they might be reinforced or equalized by the interaction. The two interactions with the BCs are evaluated separately starting with the lumen segmentation (section 3.5.1) and then moving to the vasculature (section 3.5.2).

3.5.1 Boundary condition effects and segmentation

To emphazise firstly the high impact of the segmentation on the estimation of the splitting values in regard of the varying BCs, these values are presented in Figure 3.11. Here, the differing splitting values between each segmentation and between each BC is clearly visible. An overall trend of the segmentation impact can be derived, as BC1 and BC4 revealed a higher splitting value for outlet 3 than the others. Nevertheless, the splitting value of oulet 3 varied within a range of 23.67 % (BC1), 30.16 % (BC2), 22.62 % (BC3), 31.86 % (BC4), and 25.56 % (BC5). The BC has a similar impact on the distribution of the three splitting values when compared per segmentation.

In Figure 3.12 on the left, the resulting TAWSS is presented for the chosen aneurysm case (IA E) over all BCs and segmentations. On the right, the corresponding isosurface of the velocity for the velocity value $0.3\,\mathrm{m\,s^{-1}}$ is shown. These qualitative results revealed the hemodynamic differences especially between the segmentations. The distribution is more similar over the BCs than over the segmentations. With differences in segmentation, a higher variability in distribution and magnitude occurred. The analysis revealed that while the interaction between BC and lumen segmentation was not immediately visible in qualitative results, an interplay did emerge. Examining the key hemodynamic parameters, mean velocity and TAWSS, differences were observed across BC1–BC5. BC1 and BC3 generally produced lower mean velocity and TAWSS values, whereas BC4 and BC5 yielded higher values. BC2 and BC4 showed intermediate behavior, and BC1, representing the common zero-pressure BC consistently defined the lower bound of results. These findings highlight how the chosen BC influences hemodynamic outcomes, which was already shown in section 3.4.3.

While high differences are present between the 24 segmentations, group 22 show the highest underestimation of hemodynamic parameters, whereas groups 13 and 14 substantially overestimated the hemodynamics. Groups 2, 4, 9, 17, and 18, also presented an overestimation higher than 20 %. Regarding TAWSS, varying differences on the wall become clearly visible over the groups: Especially groups 2, 4, 21, 25, and 26 showed differences in TAWSS, which cannot be seen in the remaining cases. Moreover, the TAWSS distribution varied with lower TAWSS closer to the parent vessel (groups 1, 6, 7, 9, 11, 12, 18, 21, 25, 26) or closer to the aneurysm tip (groups 13, 14, 17, 22). These high variabilities in TAWSS based on varying segmentations

were also found by Valen-Sendstad et al. [295]. However they did not include the interacting effect of the outlet BCs.

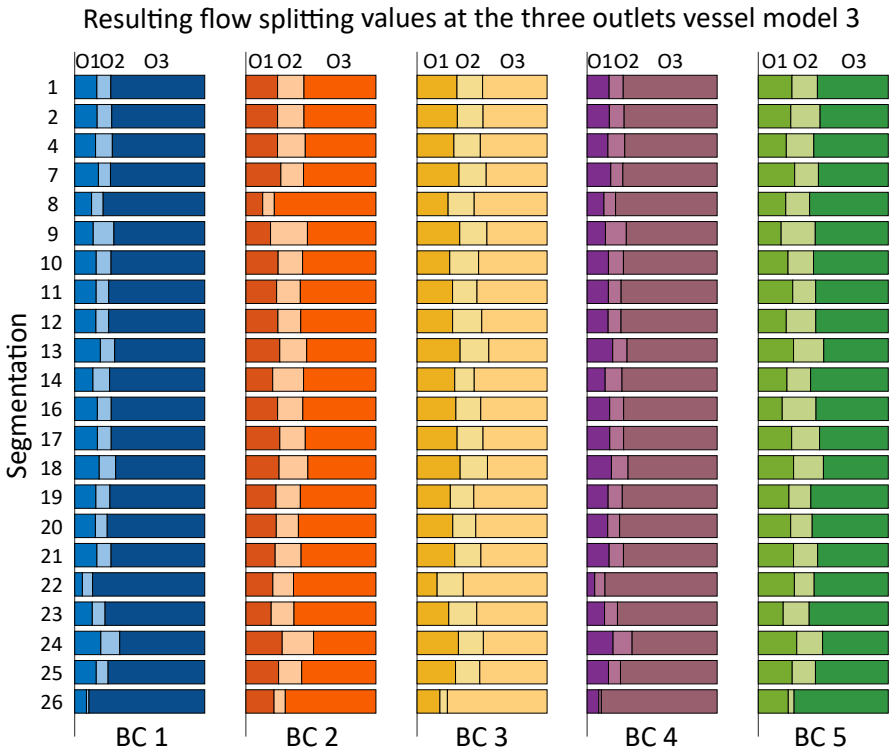


Figure 3.11: Resulting flow splitting distribution from the five BCs (BC1-BC5) for each outlet (O1-O3) of vessel model 3 (IA E).

The flow jet represented by the isosurface of the velocity on the right in Figure 3.12 depicts a similar direction and distribution of the velocity for all cases (segmentation and outlet BC). The outlet BC has the effect as described above with BC2, BC4, and BC5 yielding higher, and BC1 and BC3 lower values. Here, the variation in segmentation did not reveal a high impact on the flow jet distribution. Solely for groups 4 and 26 some differences can be seen in the isosurface when compared to the remaining groups. In the other cases, the segmentation has only impacted on the magnitude of the isosurface, with an overestimation in groups 2, 9, 13, 14, 17 and an underestimation in groups 11 and 22.

In Figure 3.13 the temporally and spatially averaged parameters TAWSS and mean velocity across BCs and for various segmentations are shown quantitatively. To overcome deviative effects by outliers, the 10 groups with outliers (defined as values deviating by more than three times absolute medians from the median solution) are marked with smaller sized dots in the graphs (groups 2, 4, 9, 12, 13, 14, 17, 18, 22, 26). Both parameters were affected by segmentation and outlet BC in a similar manner. Moreover, these results illustrate how particular BCs deviate in response to the segmentation and vice versa. Notably, the segmentation of group 22 presented the lowest hemodynamic values, suggesting an underestimation relative to the reference, whereas group 14 suggested a corresponding overestimation.

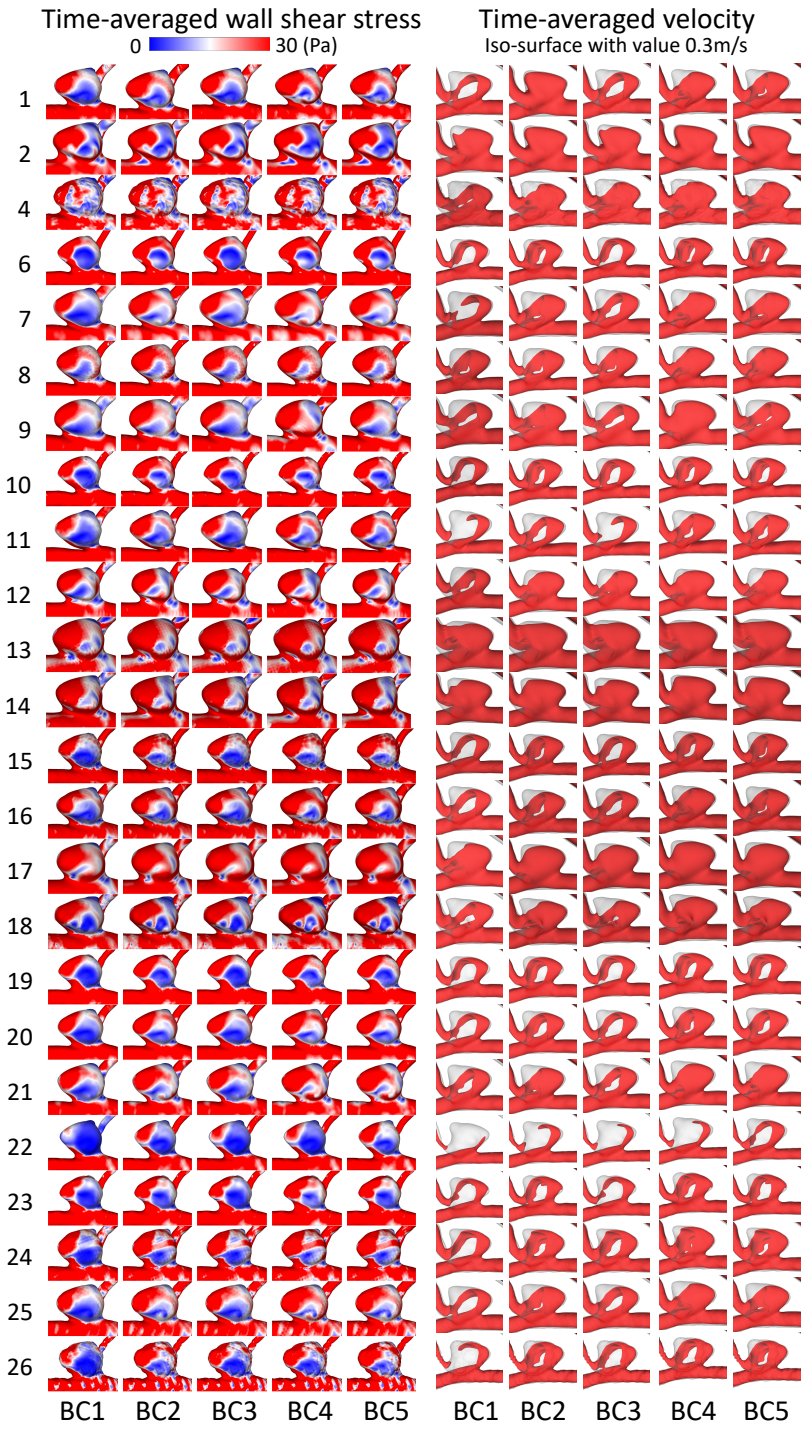


Figure 3.12: Visualization of the differences in hemodynamics based on varying segmentations and boundary conditions (BCs). The varying BCs are shown coloumn-wise and the different segmenations row-wise. Left: Time-averaged wall shear stress (TAWSS) of IA E over the 24 segmentations and five BCs. Right: Isosurface of the TA velocity (v) of IA E over the 24 segmentations and five BCs.

The interplay shown in these graphs highlighted the constantly similar effect of the outlet BC, with BC1 marking the lowest bound over all cases and BC3 the second lowest value. BC2, BC4, and BC5 revealed higher values for all cases, being closer together and for most of the cases having BC4 as the highest bound. Interestingly, the effect of the segmentation approach was much higher.

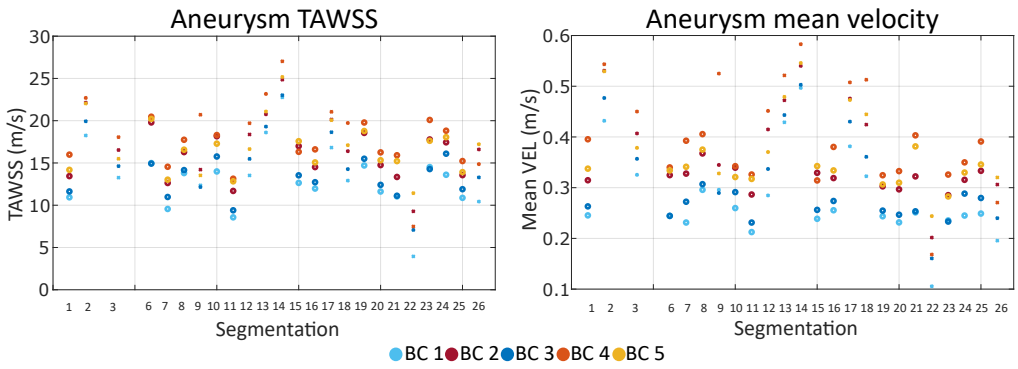


Figure 3.13: Plots of the mean values inside the dome of IA E of the TA wall shear stress (TAWSS) and TA velocity. X-axis is depicting the segmentations, while the BCs (BCs) are presented each with a unique color. Small circles are the groups defined as outliers.

To further investigate this similar effect of the BCs, their impact on wall-related parameters and flow dynamics within IA E was further assessed through boxplots presented in Figure 3.14. This analysis was conducted for all segmentations and adjusted by excluding outliers (red boxes). Additionally to TAWSS and velocity, the parameters nTAWSS, mean vorticity (ω), KER, and LSA were examined here. BC2, BC4, and BC5 generally showed higher nAWSS, mean ω, and KER values, but lower LSA than BC1 and BC3, suggesting a clear BC trend across segmentations. When outliers were excluded, the overall distribution of values decreased, strengthening the finding that each BC responds similarly to segmentation adjustments.

Table 3.7 highlights the standard deviation of the four hemodynamic parameters relative to their mean values, with a notable reduction in deviations after excluding low-fidelity segmentations (=outliers) and BCs BC1 and BC3. This reduction was especially marked for nAWSS and KER, demonstrating the importance of high-quality segmentations in reducing parameter variability. Even with high-fidelity segmentations, some deviation (up to 20 %) remained, showing the inherent sensitivity of hemodynamic results to segmentation. Thus, higher accurate segmentation is more important to reduce varying hemodynamics than outlet BC.

Table 3.7: Averaged deviation from mean value before and after exclusion of segmentation outliers in % over the five BCs (BCs) (top rows) and before and after exclusion of BC1 and 3 in % over the five BCs (bottom row). The subsequent reduction is shown in brackets after each value pair. Chosen hemodynamic parameters: Vorticity (ω), kinetic energy ratio (KER), low shear area (LSA), normalized TA wall shear stress (nAWSS).

	Mean ω	KER	LSA	nAWSS
	before/after exclusion of outlier segmentations (reduction in %)			
BC 1	21.8/14.5 (33)	51.0/11.5 (78)	35.0/14.3 (59)	31.4/10.8 (66)
BC 2	19.2/12.9 (33)	38.7/10.6 (73)	36.9/16.5 (55)	23.9/8.7 (64)
BC 3	19.4/13.4 (31)	47.4/14.1 (70)	37.1/17.2 (54)	28.6/12.7 (56)
BC 4	17.6/8.5 (52)	40.6/17.6 (57)	45.0/20.8 (54)	26.2/11.4 (57)
BC 5	15.5/10.2 (34)	35.7/14.4 (60)	33.8/19.4 (43)	21.8/10.1 (53)
	Before/after exclusion of BC1 and BC3 (Reduction)			
All segmentations	17.2/13.5 (22)	16.2/7.1 (56)	11.1/6.3 (44)	12.2/3.8 (69)

The findings underscore the crucial effect of segmentation fidelity on hemodynamic outcomes. Variations in nAWSS and LSA are strongly affected by segmentation quality, which can introduce outliers, as shown in Figure 3.14. The influence of BCs became more pronounced in

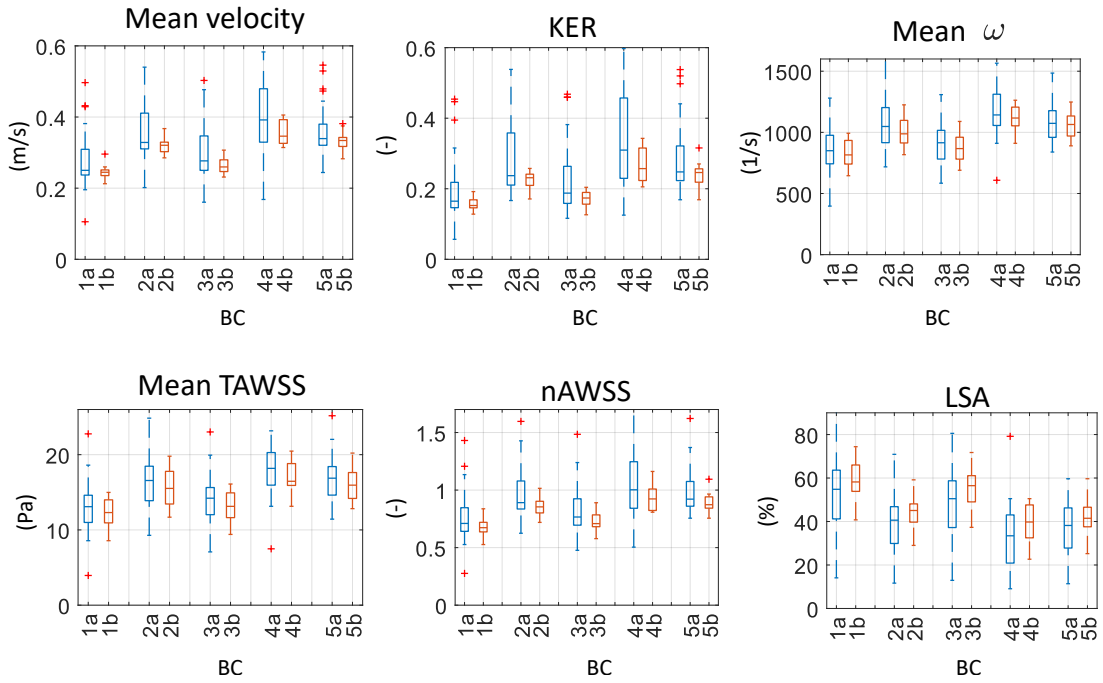


Figure 3.14: Boxplots presenting the distribution of the hemodynamic parameters mean velocity, kinetic energy ratio (KER), mean vorticity (ω), mean TA wall shear stress (TAWSS), normalized TAWSS (nAWSS), and low shear area (LSA) over all segmentations. Blue boxes represent the distribution over segmentations with outliers (marked with a) and red boxes the distribution without outliers (marked with b).

cases with poor segmentation, suggesting that segmentation accuracy is a dominant factor in obtaining reliable hemodynamic metrics. High-fidelity segmentations are particularly crucial for studies focused on geometric markers related to aneurysm rupture risk, where realistic segmentation minimizes variability induced by BCs [310]. TAWSS, nTAWSS, and KER, which are metrics linked to aneurysm rupture risk, showed critical variations across segmentations, which could lead to inconsistent assessments of rupture potential [324]. Cebral et al. quantified specific hemodynamic parameters associated with IA rupture [52]. Their findings indicated that a Kinetic Energy Ratio (KER) value of 0.226 was associated with ruptured IAs, while lower KER values (0.19) were linked to unruptured IAs. As shown in Figure 3.14, segmentation accuracy has a significant impact on KER values, and inaccurate segmentations could lead to erroneous rupture predictions based on outlier data. Past studies associating specific hemodynamics like high KER, low TAWSS and nAWSS with pathological changes in aneurysms might have reached different conclusions if more accurate BCs had been used. Therefore, improving segmentation fidelity not only reduces parameter variability but also strengthens the clinical applicability of hemodynamic simulations in aneurysm studies [296, 232].

3.5.2 Boundary condition effects and vasculature complexity

Following the analysis of the interaction between BC and segmentation, this section addresses the interaction between BC and vascular complexity. For this purpose, the hemodynamic results obtained using the five outlet BCs of the IAs within the trimmed CoW model are considered. The qualitative presentation of the TAWSS and KE distribution in IA A and IA C is shown for the trimmed CoW in Figure 3.15. Variation between the presented outlet BCs revealed differences in hemodynamic parameters across the IA models. For IA A, KE showed almost no variation across the BCs, suggesting minimal sensitivity to BC changes. In contrast, IA C exhibited a more pronounced response (higher KE values occurring under BC2, BC4, and BC5).

These observations point to a model-dependent influence of BCs on hemodynamics. Interestingly, previous studies identified similarities between BC1 and BC3, as well as between BC2 and BC4-5. This clear trend of BC behavior is also evident in Figures 3.9 and 3.13. These results show comparable parameter magnitudes for BC1 and BC3 on one side and for the remaining BCs on the other. This pattern was also emphasized by a previous study by Saalfeld et al. [259], who investigated the five BCs on eight IAs and found a similar behavior of the parameter magnitude response to the BCs. However, such patterns were not consistently observed in the IAs within the trimmed CoW model. In Figure 3.16 the quantitative results for IA A and IA C in the trimmed CoW are shown. IA A exhibited the lowest parameter values with BC1 and the highest with BC3, while BC2-5 lay in between. In contrast, IA C produced the lowest velocities with BC3, BC4, and BC5, and the highest with BC1 and BC2. These observations highlight a divergence in the response to BCs in IA C compared to IA A.

This suggests that the inclusion of vascular complexity causes the results to react more independently from specific BCs. However, the accuracy of BCs remains critical for achieving realistic hemodynamic results, as their influence cannot be entirely disregarded, particularly in models lacking vascular detail. Overall, these findings demonstrate the varying interplay between BCs and vascular complexity in determining IA hemodynamics. Incorporating vascular structures changes previously observed BC-related similarities, underscoring the necessity of vascular inclusion for accurate and clinically relevant simulations.

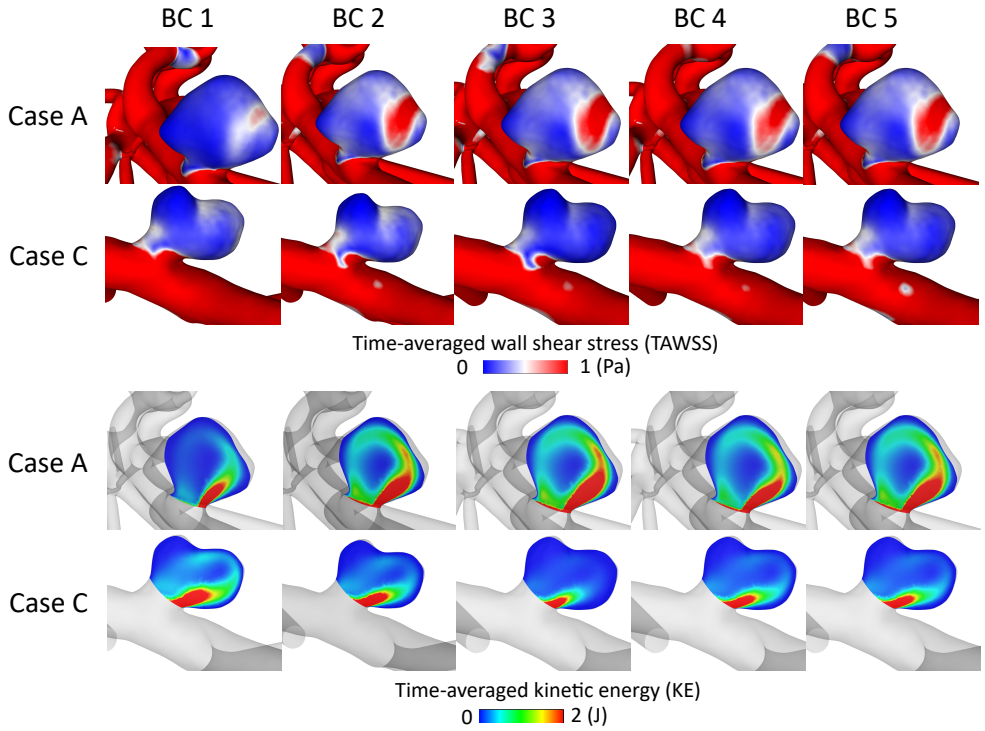


Figure 3.15: Qualitative hemodynamics of IA A and IA C within the trimmed CoW vasculature. Time-averaged wall shear stress and TA kinetic energy are presented over the five BCs (BCs).

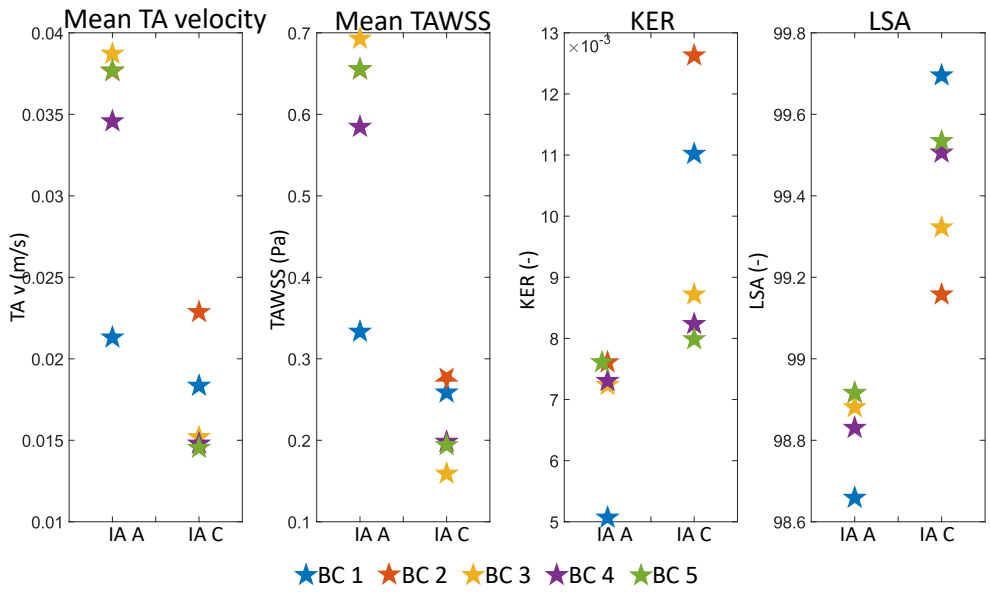


Figure 3.16: Plots of the temporally and spatially averaged parameters velocity, time-averaged wall shear stress (TAWSS), kinetic energy ratio (KER), and low shear area (LSA) within the two IAs A and C over the five outlet boundary conditions (BCs). Note that the y-axis, depicts values of low ranges (TAv: 0.01-0.04 $\mathrm{m\,s^{-1}}$; TAWSS: 0.1-0.7 Pa; KER: 5-12·10^{-3}; LSA: 98.8-99.6)

3.6 Limitations

This subsection discusses the limitations of the present study, emphasizing methodological, computational, and experimental constraints that may affect the interpretation and generalizability of the results. Firstly, one primary limitation is the use of only six cases (one CoW model and five aneurysm models), which restricts the broader applicability of the findings. Although 24 different segmentations were part of a detailed study on segmentation variability, they do not fully capture real-world diversity in IA anatomy [306, 100, 26]. Nevertheless, including the variation in BCs, 120 simulations were conducted analyzing these IAs alone, which involves a large numerical effort. Moreover, the CoW case selected featured a complex vascular structure that has not previously been documented in the literature. The thorough segmentation process required substantial time and effort, emphasizing its detailed and robust nature.

Secondly, the inlet BCs derived from PC-MRI measurements have limited spatial resolution, potentially leading to an underestimation of flow dynamics. However, because the data acquisition occurs during the MRI scan, the resulting waveform can be considered as subject-specific as possible under the given conditions. Thirdly, assumptions were made regarding the inclusion of inlet mass flow rates derived from the literature, modeling blood as a Newtonian fluid, and using a normal-resolution approach (time step $\Delta t = 1$ ms, volume mesh base size $\Delta x =$ 0.07–0.1 mm). However, all simulations followed consistent settings, meeting recent recommendations for neurovascular hemodynamic studies [25]. The resolution level is standard in image-based hemodynamic CFD research of IAs and is suitable here given the focus on mean flow values, rather than capturing highly-resolved fluctuations, which are particularly critical in studies of time-dependent phenomena [53, 294, 162]. This will be further addressed in Chapter 4.

Fourthly, the study lacks a ground truth for validation, as no precise in-vivo measurements of patient-specific flow-splitting were available. Consequently, the most realistic existing models were used as reference points [62, 205]. This will as well be further considered in the following chapter. Lastly, while the included IAs were patient-specific, they were integrated into a model of a healthy CoW. Additionally, the inflow waveforms applied were obtained from the same healthy individual. Despite this limitation, the addition of the IAs was carefully performed to ensure anatomical accuracy. The IA necks were preserved, and the aneurysms were scaled to match the diameter of their parent vessels.

3.7 Conclusions

The modeling of image-based blood flow simulations has increased in recent years, particularly for analyzing pathological conditions and their relation to risk assessment. As medical imaging often serves as the only patient-specific foundation for these simulations, the development of widely accepted standards for modeling and processing assumptions have been developed. However, careful consideration must be given to these assumptions, particularly when numerical hemodynamic outcomes are intended for clinical research and application. Thus, this chapter focused on evaluating the impact of three key modeling assumptions on IA hemodynamics, namely vasculature complexity, vessel and aneurysm lumen segmentation, and applied outlet BCs. The analysis emphasizes both the individual effects of these assumptions and their interactions. The primary goal was to determine which assumptions require the highest level of accuracy and which can tolerate lower precision when studying IA hemodynamics.

Five patient-specific IAs, incorporating real-world segmentations contributed by 24 international research groups, as well as a manually processed subject-specific CoW model were involved

in this chapter. In total, 137 hemodynamic simulations were conducted, and the resulting parameters were evaluated systematically to provide recommendations for improving modeling of IA simulations.

The results of this chapter underscore the importance of high-accuracy lumen segmentation in IA hemodynamic simulations. Comparisons across five BCs revealed variation in parameter magnitudes. When high-fidelity lumen segmentation is employed, the influence of BCs on hemodynamic deviations is reduced. These findings demonstrate that precise lumen segmentation has a more substantial influence on hemodynamic predictions than the choice of outlet BC. To achieve such accuracy, the use of high-resolution 2D imaging is recommended as it facilitates detailed segmentation and enhances the overall fidelity of neurovascular models. Additionally, vasculature complexity highly influenced flow magnitudes and distribution. Interestingly, the impact of BCs did not align with trends observed in prior studies that excluded complex vasculature, highlighting the necessity of including vasculature to achieve realistic simulations. These results suggest that employing highly complex models be crucial for generating accurate and clinically relevant insights into IA hemodynamics. To further enhance the accuracy of neurovascular blood flow simulations, advanced flow-splitting methods should be utilized. At a minimum, the application of Murray's law with an exponent $n = 2$ is recommended to optimize the realism and reliability of hemodynamic predictions.

Research questions

A. How does the individual impact of variability in vasculature complexity, lumen segmentation and outlet BC affect the hemodynamics in image-based blood flow simulations of IAs?

   ⇒ Model complexity and lumen segmentation both affect the magnitude and distribution of hemodynamic parameters, particularly those related to the vessel wall. A clear trend is observed in the magnitude of hemodynamic results based on the applied outlet BC, with higher values occurring when advanced flow-splitting methods are used. However, no impact of the outlet BC on the spatial distribution of these parameters was identified.

B. How does the interaction effects of variations between model complexity and segmentation with the outlet BC affect the hemodynamics of the image-based blood flow simulations of intracranial aneurysms?

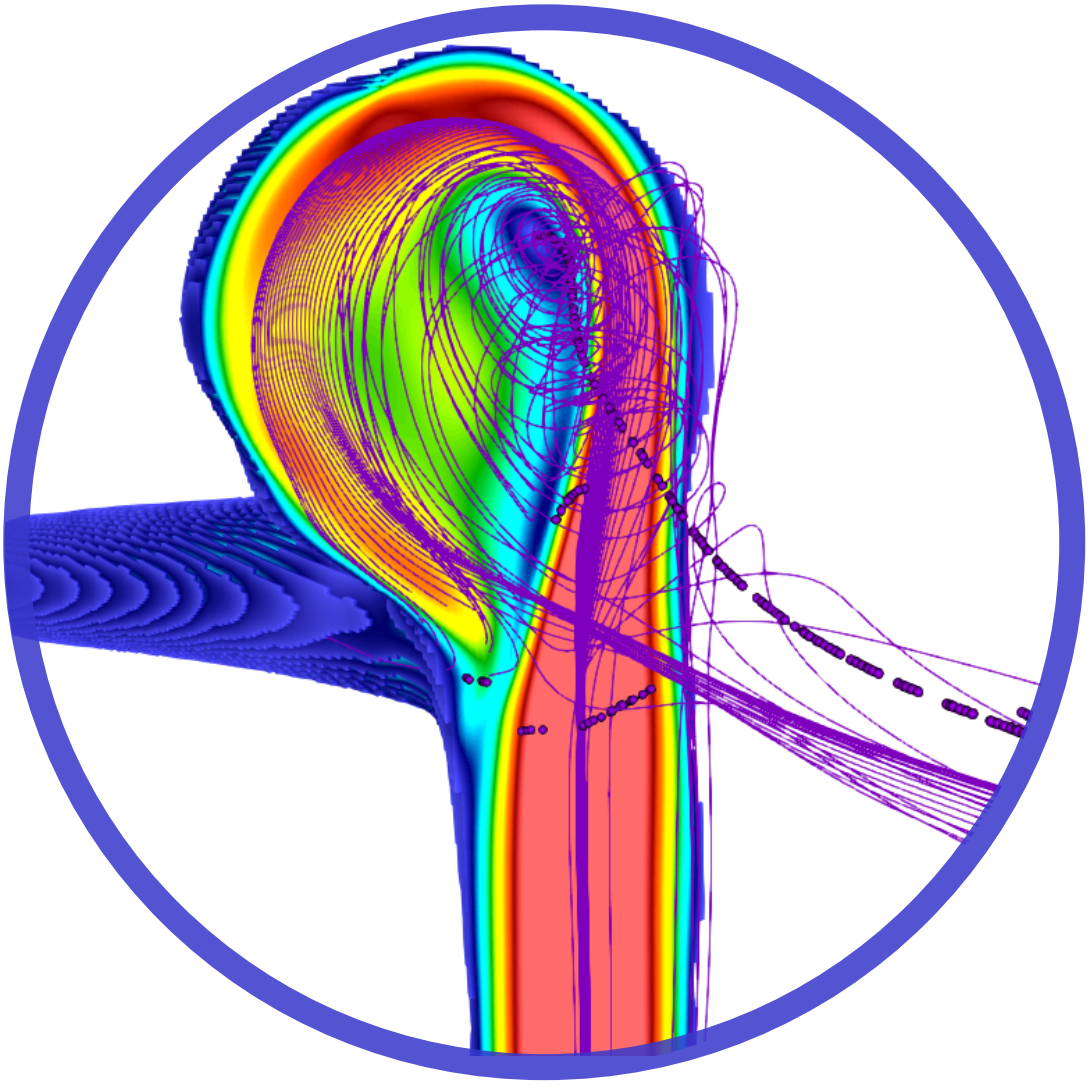
   ⇒ With improved segmentation accuracy, the influence of BCs reduces. When a more complex vascular network is incorporated into IA hemodynamic analysis, the impact of BCs no longer follows the same trend. Therefore, future research should prioritize high-precision geometric modeling over outlet BC refinement.

Future research will need to focus on analyzing a larger cohort of IA and CoW cases to validate and strengthen the findings of this chapter. Expanding the dataset will include also the addition of IAs at various anatomical locations in the CoW model, such as the ICA or the ACA, to investigate the impact of altered flow patterns on intra-aneurysmal hemodynamics. Additionally, obtaining imaging data from patient-specific pathological CoW models will enable the analysis of IA hemodynamics in realistic, naturally occurring pathological geometries rather than artificially constructed models. Such an approach would ensure that inflow conditions are directly representative of pathological states, providing a more accurate and clinically relevant assessment of hemodynamic behavior. Moreover, the missing ground-truth could be overcome in the future with the inclusion of in vivo or at least in vitro analyis of the outflow conditions

and true intra-aneurysmal hemodynamics. These experimental approaches would allow for a direct comparison between measured and simulated hemodynamics under varying assumptions. These assumptions would also include the implementation of rest and exercise conditions in the analysis to derive effects of elevated heart rates on the hemodynamic outcome in the vascular system. By bridging the gap between in silico and in vitro modeling, the reliability and clinical applicability of IA hemodynamic simulations could be significantly enhanced. Thus, in the following chapter of this thesis (Part 4), the focus was set on the investigation of rest and exercise condition effects on vascular hemodynamics which were moreover validated with in vitro experimental data.

Chapter 4

Part 2: Influence of rest and exercise conditions on flow parameters in vascular pathologies

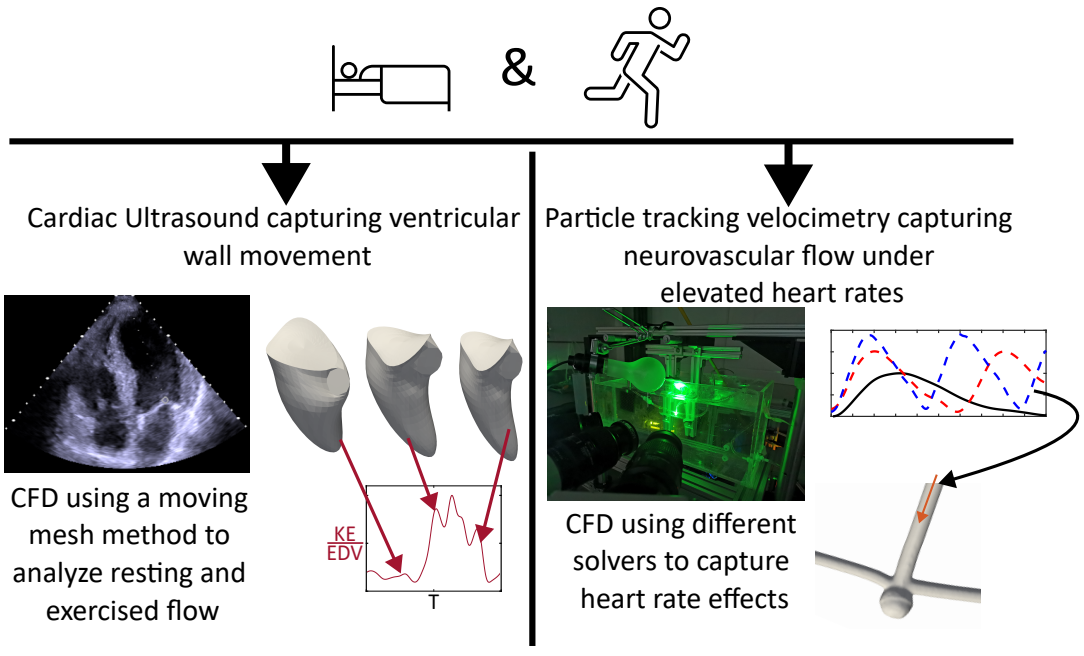


Outline

Since medical images are predominantly acquired at rest, the evaluation of hemodynamics under exercise conditions is often overlooked, despite its clinical importance. This chapter examines the impact of rest and exercise on vascular hemodynamics, with a particular focus on cardiovascular and neurovascular flow dynamics. By integrating exercise conditions into both in vivo medical imaging and in silico analyses, hemodynamics can be assessed through image-based blood flow simulations. Following a review of the implementation of rest and exercise in numerical vascular analysis, this chapter presents the methodology for incorporating these conditions into in silico simulations. Finally, the effects of rest and exercise on cardiovascular and neurovascular hemodynamics are evaluated in detail.

This chapter is partially based on the following publications:
Korte, J., Rauwolf, T., Thiel, J.-N., Mitrasch, A., Groschopp, P., Neidlin, M., Schmeißer, A., Braun-Dullaeus, R., Berg, P. (2023). Hemodynamic Assessment of the Pathological Left Ventricle Function under Rest and Exercise Conditions. Fluids, 8(2), 71. [157]

Graphical abstract



This chapter focuses on advancing the understanding of cardio- and neurovascular flow dynamics under rest and exercise conditions. A review of the related literature is presented first. This review examines previous studies on hemodynamics during exercise, as well as the methods employed to implement exercise conditions in computational models of the cardiovascular and neurovascular systems.

The key aspects of this chapter comprise the inclusion of MI, a cardiovascular pathology not addressed in prior investigations in this thesis and the neurovascular pathology of IAs. This enables a comprehensive analysis of how rest and exercise conditions impact both cardio- and neurovascular systems. Following the review, the contribution of this chapter is outlined, with research questions posed to frame the investigation. The methodology employed to address these questions is subsequently detailed. Finally, the results are presented and the impact of rest and exercise on the flow dynamics in chosen cardio- and neurovascular pathologies are examined.

4.1 Analysis of rest and exercise conditions in vascular flows

The analysis of vascular hemodynamics using image-based CFD simulations often centers on patient-specific geometries, such as the morphology of blood vessels or pathological features like IAs. However, these simulations commonly overlook other individualized factors and are typically based on medical imaging obtained during rest. This static and idealized approach has notable limitations, as previous studies have demonstrated significant variations in cerebral hemodynamics under postural changes, such as transitions from lying to standing or sitting to standing [221].

Under dynamic conditions like exercise, the cardiovascular system adapts by increasing heart rate, resulting in elevated blood flow, greater kinetic energy, and increased wall shear stress throughout the vascular network. Cerebral blood flow, which was long thought to remain constant during exercise due to the cerebral autoregulatory mechanisms, has been shown in recent studies to increase in response to heightened neuronal activity and metabolic demand [220]. Additionally, intra-vessel blood velocity in cerebral vessels has been observed to rise during exercise, further underscoring its significant impact on hemodynamics. Exercise is also widely acknowledged for its beneficial effects on functional capacity, a phenomenon observed across various age groups. For instance, Antunes et al. demonstrated that individuals aged 45 to 75 experienced exercise-induced improvements comparable to those observed in younger populations [11].

The following section reviews the behavior of the vascular system under rest and exercise conditions. A detailed analysis is provided, first focusing on the cardiovascular system and then on the neurovascular system, with particular emphasis on the incorporation of exercise into CFD simulations and its associated effects on flow dynamics.

Impact of rest and exercise condition on the cardiovascular flow dynamics

Cardiac MRI is the gold standard for evaluating cardiac morphology and systolic function, offering high spatial resolution and additional structural and functional assessments, such as fibrosis and myocardial energetics. However, its use for exercise imaging remains limited, likely due to the lack of MR-compatible exercise equipment and suitable imaging sequences as was found out by Nabi et al. and by Beaudry et al. [208, 20].The inclusion of exercise in the investigation of cardiac flow with medical imaging is important, as it provides a dynamic un-

derstanding of cardiac function. Some studies have already incorporated exercise imaging using varying methods:

- **Erect cycle ergometer radionuclide angiocardiograms:** In studies performed in 1978 by Rerych et al. and by Bates et al. first insights into the cardiac flow were investigated using erect cycle ergometer radionuclide angiocardiograms [249, 18]. The procedure of erect cylcing during radionuclide angiography is shown in Figure 4.1 on the left. The studies highlighted angiocardiography as a simple, noninvasive method to evaluate myocardial function during exercise. Normal subjects showed a doubling of heart rate, tripling of cardiac output, and an increase in ejection fraction (66 % to 80 %) during exercise [249]. Bates et al. who investigated patients with coronary artery disease found lower systolic and diastolic blood pressure in patients compared to the normal subject control group [18].
- **Supine cycle ergometer MRI:** In 1998 Niezen et al. investigated the impact of rest and exercise condition on the cardiac flow using supine cycle ergometer MRI [217]. The procedure is visualized in Figure 4.1 in the middle. The heart rate and the flow volume in the aorta as well as in the pulmonary artery rised during exercise, while the heart rate rise was significant when compared to rest. Beaudry et al. demonstrated the clinical feasibility of supine exercise MRI [20]. Proof-of-concept results revealed a significant increase in both heart rate and stroke volume. In a recent study performed by Schulz et al. real-time phase-contrast cardiac MRI and right heart catheterization were used to measure cardiac output during exercise in patients with heart failure with preserved ejection fraction (HFpEF) [270]. In this context, validation of cardiac MRI against catheterization was sought. Patients with identifiable HFpEF exhibited a significantly lower stroke volume during exercise compared to those with masked HFpEF or non-cardiac dyspnea. The validation demonstrated a strong agreement between cardiac MRI and right heart catheterization, underscoring its potential to reduce the need for invasive procedures in clinical practice.
- **Handgrip MRI:** Impact of handgrip exercise (Figure 4.1 on the right) on the arterial flow waveforms was investigated by Zhang et al. [329]. They used a 3-Tesla MRI scanner to derive the flow data during rest and exercise. They found a significant increase in arterial pressure and blood flow through the choroid membrane. Von Knobelsdorff-Brenkenhoff et al. investigated 53 healthy subjects under rest and handgrip exercise in a 3T MRI scanner, showing significant increases in heart rate, blood pressure and cardiac output [147]. This setup demonstrated the impact of handgrip exercise on the cardiovascular flow dynamics.

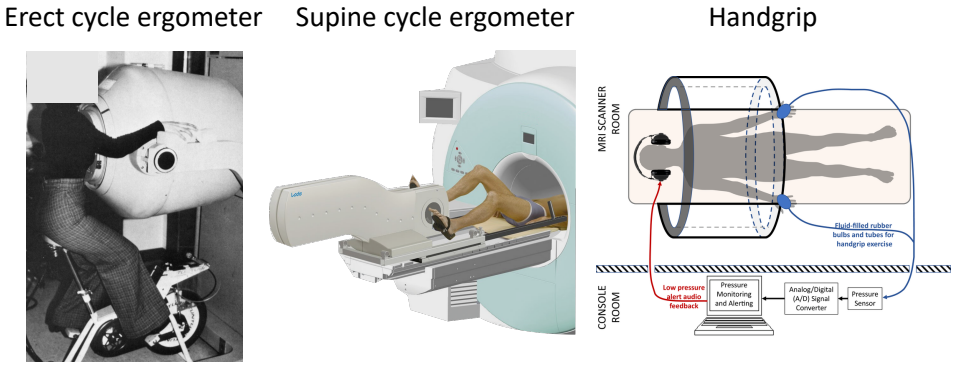


Figure 4.1: Representation of the incorporation of exercise into medical imaging processes. Figure adapted from [18, 1, 194].

The integration of exercise can also be effectively incorporated into CFD simulations through the implementation of varying heart rates. Meschini et al. investigated the impact of heart rate

on intraventricular hemodynamics and mitral valve dynamics in a healthy human left ventricle (LV) using DNS, coupled with a structural solver for the ventricle and mitral valve [195]. Heart rates of 40 bpm, 60 bpm, 100 bpm, and 140 bpm were applied. At lower heart rates, reduced flow rates resulted in weaker mitral jets, lower blood kinetic energy, and diminished WSS on valve leaflets. In contrast, higher heart rates produced faster flow jets, increasing blood kinetic energy and WSS. Higher heart rates shorten diastasis duration, leading to overlap of early (E-wave) and late (A-wave) diastole. This enhances mitral leaflet mobility, increasing the orifice area during diastole.

The studies referenced demonstrate that exercise significantly influences cardiac output and, consequently, intra-ventricular hemodynamics. This highlights the importance of incorporating exercise when investigating these dynamics to derive meaningful clinical recommendations for managing pathologies. However, the detailed intra-ventricular hemodynamics were not thoroughly addressed in these studies and are therefore addressed in this thesis. The feasibility of incorporating exercise into clinical practice has been demonstrated using methods such as cycle ergometry or handgrip exercise, with handgrip exercise being particularly suitable for routine clinical applications due to its practicality. A notable limitation of the studies is their reliance on MRI or radiation-based imaging modalities. For pediatric patients or individuals with severe pathologies, where these imaging techniques may be less ideal, cardiac ultrasound presents a safer and more accessible alternative.

Impact of rest and exercise condition on the neurovascular flow dynamics

As already mentioned in section 2.6.3, in recent studies, high frequency fluctuations were found in IAs. These fluctuations were only visible when high resolution CFD was applied [296]. They are supposed to be especially identifiable during exercise compared to rest [144]. In a broad investigation, Khan et al. analyzed 50 IA cases using high-resolution CFD and physiological inflow rates to evaluate high frequency fluctuations [142]. Flow instabilities were identified in half of the cases, which were undetectable via in vivo analysis. However, studies explicitly examining the effect of varying heart rates on hemodynamic fluctuations in IAs are lacking in the literature.

Jiang et al. performed image-based hemodynamic CFD using three varying heart rates for the inflow waveforms to analyze the impact of exercise on intra-aneurysmal flow behavior [137]. In their study large eddy simulations were applied. They found an increased WSS with rising heart rate. Moreover, they associated the level of influence of exercise conditions with the aneurysm geometry. Valen-Sendstad et al. performed DNS to investigate the occurrence of high frequency fluctuations in IAs using a literature-based pulsatile inflow curve [296]. The flow showed transition to turbulence shortly after peak systole, followed by relaminarization during diastole. Predominant frequencies ranged between 1–500 Hz. Their study confirms the occurrence of turbulence in IAs. The application of low-resolution numerical simulations (LRNS) have proven inadequate for capturing high frequency fluctuations in intra-aneurysmal hemodynamics. However, this approach has been widely utilized to study exercise conditions in neurovascular flows. In previous studies, varying methods were employed to implement exercise conditions, as medical imaging techniques commonly used for cardiac flow analysis were not feasible in this context. In these studies several heart rates with varying pulse frequencies were applied, mostly ranging between 60 bpm (rest) to 127 bpm (exercise).

- Sekhane et al. provided preliminary results of the analysis of increasing inflow waveforms into a patient-specific IA model [272]. The chosen heart rates increased from 66 bpm to 92 bpm by 1 bpm, respectively (beats per minute (bpm)). Hemodynamics were derived using conventional hemodynamic modeling as described in chapter 3. The increasing

heart rate significantly disrupted the hemodynamic parameters within the IA and altered the flow-pressure relationship within the aneurysmal sac, leading to increased stagnation. Fluctuating pressure patterns with multiple regions of elevated pressure were observed in the aneurysmal sac.

- Sarrami-Foroushani et al. analyzed the intra-aneurysmal hemodynamics using CFD simulations based on the CTA medical images of an ICA aneurysm [263]. In their study, three representative heart rates were considered, which were set to 60 bpm, 93 bpm and 127 bpm to mimick the rest and exercise conditions. The heart rate choice was based on the analysis of Sato et al. [264], who investigated the regulation of blood flow in the ICA and VA during graded dynamic exercise, aiming to identify differences in cerebrovascular responses using Doppler ultrasound. Ten young women performed cycling exercises at 30 %, 50 %, and 70 % of their peak oxygen uptake. The results showed that blood flow in the ICA increased at lower exercise intensities but plateaued at 70 % of peak oxygen uptake, while blood flow in the VA continued to rise proportionally with increasing workload. The CFD simulations of Sarrami-Foroushani et al. revealed intuitive effects, such as higher WSS, due to an increased heart rate. Some counter-intuitive trends were observed, particularly in areas of excessively low or elevated WSS, underscoring the complexity of aneurysm hemodynamics.

- Bowker et al. analyzed the impact of exercise condition in IAs, using patient-specific image-based blood flow simulations and considering varying inflow waveforms to mimick rest and exercise [39]. Here, a heart rate of 69.6 bpm was taken for rest and of 120.7 bpm for exercise. In their analysis, WSS showed no significant increase during simulated exercise. However, a reduction in relative residence time was observed during exercise, which may offer potential benefits by enhancing nutrient delivery to cells within the aneurysmal tissue. Geers et al. performed image-based blood flow CFD simulations using steady-state and transient inflow wave forms including rest and exercise conditions to compare the impact on the intra-aneurysmal hemodynamics [92]. Here, the waveforms were based on the investigations from Bowker et al., using heart rates of 69.6 bpm for rest and 120.7 bpm for exercise. The results showed that a realistic inflow waveform is crucial for detailed investigation of cerebral blood flow, with increased WSS during exercise compared to rest conditions.

- Tang et al. implemented the exercise conditions by increasing the flow waveform at rest by 50 % and as well performed image-based blood flow simulations to derive the vessel hemodynamics within the abdominal aorta [288]. Compared to resting conditions, exercise resulted in increased WSS and decreased OSI across different sections of the abdominal aorta, particularly in the infrarenal region. These changes support the hypothesis that exercise promotes unidirectional laminar flow and reduced flow oscillations. The study highlights the advantages of computational methods in providing detailed, three-dimensional analyses of flow patterns and their potential role in understanding cardiovascular health.

- Koep et al. investigated how age, sex, and exercise intensity influence cerebrovascular responses during isometric handgrip exercise in 78 healthy adults [148]. Blood flow velocities were measured via transcranial Doppler and Duplex ultrasound. Results showed that velocity in the MCA and PCA increased with exercise intensity, but in the ICA and VA remained unchanged. MCA velocities were reduced with aging but unaffected by sex. This highlights the age-specific attenuation of cerebral blood flow during isometric exercise.

- Moncion et al. evaluated the impact of acute exercise and exercise training on cerebrovascular hemodynamics in adults after stroke in a systematic review [199]. Descriptive analysis

indicated that exercise training may enhance cerebral blood flow and cerebrovascular reactivity to carbon dioxide in stroke survivors. However, meta-analysis of three acute exercise studies found no significant changes in MCA velocity during moderate-intensity exercise compared to rest. The findings suggest that cerebrovascular hemodynamic responses during acute exercise may be attenuated post-stroke, while aerobic exercise training appears beneficial for cardiovascular health and function.

The incorporation of varying heart rates has proven to be a viable method for assessing exercise conditions. However, recent studies utilizing DNS have not yet integrated exercise scenarios. Therefore, the application of varying heart rates in DNS is recommended to improve the understanding of exercise-induced hemodynamics. Additionally, existing DNS studies lack adequate validation performed under exercise conditions. This part of the thesis aims to address these gaps, focusing on enhancing the reliability and applicability of DNS for studying hemodynamic changes in IAs associated with exercise.

4.2 Modeling requirements to assess the impact of rest and exercise on vascular flow conditions

Implementing exercise conditions into image-based hemodynamic CFD simulations for vascular vessels and pathologies presents various challenges and possibilities, particularly concerning cardio- and neurovascular geometries. Accurate modeling of these geometries is crucial for capturing the hemodynamic changes induced by exercise. For cardiovascular geometries, the dynamic movement of the ventricular walls plays a critical role in intra-ventricular flow dynamics. These wall movements, which are significantly altered during exercise, must be carefully modeled to accurately reflect their impact on the flow patterns within the heart. Such changes provide valuable insights into the physiological adaptations of the cardiovascular system under increased workload conditions. In neurovascular geometries, the focus shifts towards the choice of flow solvers and modeling approaches to assess the effects of elevated heart rates on cerebral hemodynamics. The heightened cardiac output and resultant changes in blood flow necessitate sophisticated modeling techniques to ensure accurate predictions of flow behavior in the cerebral vascular network. In the following, the key modeling requirements for integrating exercise conditions into CFD simulations are reviewed, with a specific focus on moving mesh modeling for cardiovascular vessels and DNS for neurovascular vessels.

Moving mesh modeling

Recent studies have implemented the moving walls of the heart into numerical simulation environment using varying medical imaging, solvers and methodologies:

- Xu et al. developed a mesh morphing approach, mimicking the deformation of the ventricle, which can be implemented in a CFD environment [322]. They validated their approach with PIV experiments, thus an elastic phantom model was firstly established, which then underwent PIV analysis. During this analysis the shape deformation of the model as well as specific flow rates were captured. The shape deformation served as a basis for the morphing approach, while the flow data was used for the validation. They found good agreement between the measured and calculated data, providing a useful mesh morphing algorithm for further cardiac analysis.

- Bavo et al. proposed a promising moving mesh method utilizing ultrasound imaging via transesophageal echocardiography [19]. They captured the 3D data of the ventricular shape over time, providing the patient-specific ventricular movement over one cardiac cycle. This approach was implemented in a CFD environment and served as a basis to derive patient-specific transient intra-ventricular hemodynamics. While effective, transesophageal echocardiography's invasive nature limits its routine clinical application [19]. Conversely, transthoracic echocardiography provides a non-invasive and radiation-free approach for capturing time-resolved images of ventricular volume [192]. This imaging technique can also be performed during low-intensity exercise.

- Nquyen et al. showed that MRI can serve as a foundation for patient-specific moving mesh simulations to evaluate intraventricular hemodynamics [216]. Their approach determined BCs based on the difference between inlet and outlet mass flow rates and the ventricular volume variation over time.

- Recent work by Goubergrits et al. and Obermeier et al. employed CTA scans deriving the ventricular motion to be implemented in CFD analysis [102, 218]. The patient-specific wall shape during peak systole and diastole and the respective ventricular volume over one cardiac cycle were derived from the CTA data. Based on a volume scaling over time, the transient ventricular wall motion was established. This method accounted for patient-specific ventricular volume, including detailed valve morphology, but did not incorporate patient-specific wall motion, and the associated radiation exposure poses a limitation for clinical application.

Direct Numerical Simulation

As discussed in Chapter 3, specific hemodynamic parameters, such as high or low WSS, have been associated with the rupture of IAs [53]. Recent studies have identified high frequency fluctuations within IAs, which are also linked to rupture risk [53, 299]. These fluctuations become more pronounced under elevated heart rates, such as those induced by exercise conditions [142]. Analyzing the occurrence of such fluctuations can provide valuable insights into IA rupture risks, as well as aid in identifying IA formation and growth [271] and informing treatment planning strategies [204].

CFD approaches, such as laminar Navier-Stokes equations (as presented in Chapter 3), unsteady Reynolds-averaged Navier-Stokes equations, or large eddy simulation, are frequently employed for IA hemodynamic analyses. These methods are effective for obtaining general insights, such as rupture-related parameters. However, they may lack the spatial and temporal resolution required to fully capture flow instabilities and fluctuations [2]. High-resolution analysis becomes crucial when investigating fine-scale flow features and transitions, particularly in the context of IAs. Only with high spatial and temporal resolution can advanced parameters, such as spectral entropy and turbulent kinetic energy, be accurately quantified [3, 6]. This is particularly true for analyzing flow instabilities within IAs [299]. Therefore, further investigations using DNS have to be considered. While DNS is computationally intensive, it offers unparalleled accuracy in resolving flow transitions and capturing high frequency fluctuations [2, 6].

- Valen-Sendstad et al. demonstrated that turbulence can occur in IAs when using highly resolved CFD simulations, particularly DNS, to study IAs in the MCA [296]. In a subsequent study, the same group identified high frequency fluctuations in bifurcation IAs but reported fewer fluctuations in sidewall IAs [162].

- Supporting this, Huang et al. recently applied the high-resolution lattice Boltzmann method to IAs and similarly detected the presence of high frequency fluctuations [124].
- Ford et al. conducted highly resolved numerical simulations on both idealized and patient-specific IA models, observing fluctuations with frequencies exceeding 120 Hz and 112 Hz, respectively, although these studies considered only a single inflow rate [83].
- Jain et al. examined the occurrence of transitional flow in IAs using subject-specific simulations with the lattice Boltzmann Method [131]. They noted that even at low Reynolds numbers ($\leq$500), physiological flows may exhibit turbulence-like behavior due to the intrinsic complex flow structures in IAs, necessitating advanced finite element schemes. Lattice Boltzmann simulations achieved unprecedented spatial (8 µm) and temporal (0.11 µs) resolutions, enabling the quantification of turbulent kinetic energy at Kolmogorov scales. Two aneurysms were analyzed: one previously classified as laminar and the other as transitional. The simulations revealed turbulent-like structures in the transitional IA, as expected, while the laminar IA did not show this behavior.

4.3 Mitral valve insufficiency

Mitral valve insufficiency, the cardiovascular pathology explored in this chapter, refers to the impaired function of the mitral valve, which allows regurgitation — blood flow from the ventricle back into the atrium during systole. This backward flow disrupts normal cardiac function and can lead to various clinical symptoms and complications. In Figure 4.2 the healthy and pathological MI is shown, visualizing the regurgitation of blood from the LV back to the atrium. The pathology has a prevalence of 11.7 % in the population with age over 75 years. Mitral valve insufficiency was separated by clinicians into four stages. Namely the non-limiting stage (MI I), the mild stage (MI II), the moderate stage (MI III), and the severe stage (MI IV) [209]. Bakkestrøm et al. investigated hemodynamic differences in patients with MI I and MI II/III at rest and during exercise using catheterization and multimodal imaging techniques, including echocardiography and MRI. Their findings highlighted significant differences in pulmonary capillary wedge pressure and arterial pressure between MI stages, but the study did not incorporate highly resolved hemodynamic analyses [17].

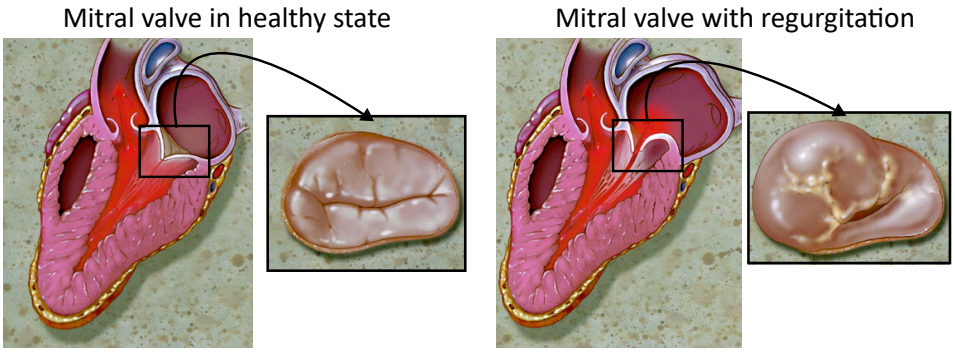


Figure 4.2: Visualization of the mitral valve once in healthy condition (left) and with regurgitation (right) namely MI. Figure adapted from [293].

Collia et al. explored the fluid dynamics of MI caused by MV prolapse, where incomplete leaflet closure leads to blood regurgitation into the atrium, with a focus on improving clinical assessment methods. A CFD model coupled with an asymptotic MV motion model was used.

The immersed boundary method was integrated with clinical imaging data. The study highlights the importance of accounting for false regurgitation and its association with thrombogenic risk, providing insights for refined clinical evaluations of MV insufficiency. Bennati et al. conducted CFD simulations in the LV, left atrium, and aortic root using a resistive immersed method and a turbulence model [22]. Systolic wall motion was reconstructed from Cine-MRI images, enabling segmentation of the mitral valve. Regurgitant scenarios included increased heart rates and left ventricular dilation. CFD with prescribed wall motion and an immersed mitral valve effectively described mitral valve regurgitation-associated hemodynamics and enabled comparisons of regurgitant scenarios. The findings revealed atrial flow transitioning to turbulence and provided key indices such as cardiac output and WSS.

4.4 Contribution

Vascular pathologies are closely influenced by blood flow patterns, with changes in specific hemodynamic parameters contributing to their development and progression. Exercise-induced increases in cardiac output and altered flow dynamics can significantly modify these parameters compared to rest. Understanding the hemodynamic differences between rest and exercise is critical for accurately predicting disease progression and optimizing treatment strategies. Incorporating both rest and exercise conditions into computational and clinical studies enhances the simulation of real-life scenarios, providing valuable insights into the effects of daily activities on vascular health and disease progression.

This chapter investigates the hemodynamic impact of rest and exercise in two vascular pathologies: MI, a pathological condition of the LV, which involves regurgitation of blood through the mitral valve into the left atrium, impairing cardiac function [78]. The latter crucially affects the blood flow into the aorta and thus into the neurovascular system by irregular elevation of heart rates (see section 2.1). Exercise is known to exacerbate the severity of MI, leading to a worsening of symptoms that vary crucially among individuals [286, 128]. However, the precise relationship between myocardial blood flow dynamics and exercise-induced changes in MI severity remains poorly understood. Patient-specific hemodynamic analysis, facilitated by image-based simulations, plays a crucial role in advancing the understanding of MI pathophysiology and guiding treatment strategies. Such simulations rely on accurately replicating ventricular wall motion to capture realistic flow dynamics [36, 64, 166].

Similarly, exercise is hypothesized to impact neurovascular hemodynamics, particularly in IAs. While IAs are traditionally thought to exhibit predominantly laminar flow due to relatively low mean flow velocities, their complex geometries and the pulsatile nature of blood flow frequently result in disturbed, non-laminar flow patterns [294]. Exercise-induced increases in blood flow pulsatility further amplify these complexities, often generating high-frequency velocity fluctuations. These fluctuations are believed to contribute to aneurysm destabilization and an elevated risk of rupture [323, 15, 299]. Detecting these high-frequency fluctuations requires high temporal resolution, posing technical challenges. While evidence increasingly underscores their role in aneurysm rupture risk, current CFD methods often rely on low-resolution simulations. This reliance highlights a significant gap in the comparative evaluation of high-resolution versus low-resolution approaches, underscoring the need for improved simulation techniques to better capture the hemodynamic complexities induced by exercise.

Thus, the aim of this chapter was to investigate the hemodynamic effects of rest and exercise conditions on MI and IA, with a focus on exercise-induced changes and their pathological implications. To achieve these objectives, first, image-based blood flow simulations are applied to

analyze left ventricular hemodynamics in 10 patients with varying stages of MI under resting and exercise conditions. Time-resolved echocardiographic imaging is utilized to capture patient-specific ventricular wall motion, modeled using a moving mesh approach. The primary goal is to identify potential hemodynamic markers capable of characterizing cardiac function based on MI stages and to evaluate the differential impact of rest and exercise on these parameters. In case of IAs, the necessity of high-resolution hemodynamic simulations to accurately capture the fluctuations is emphasized and thus, second, DNS are performed to evaluate hemodynamics at varying heart rates within a right middle cerebral artery bifurcation aneurysm. Volumetric PTV is used to validate intra-aneurysmal flow patterns, while conventional low-resolution CFD simulations are compared with DNS to assess the added value of high-fidelity simulations. The study hypothesizes that DNS can effectively detect high-frequency hemodynamic fluctuations in IAs, with their prominence increasing under elevated heart rates.

This chapter is organized as follows: First, the methodology is presented, which includes a detailed explanation of patient selection criteria and the integration of exercise conditions within the numerical analysis framework. Additionally, the fundamental solving approaches, specifically the moving mesh method and DNS, are discussed. Second, the results and discussion section is introduced, beginning with an evaluation of how exercise conditions affect cardiac hemodynamics, with a particular focus on MI. Following this, the impact of exercise on the occurrence of high-frequency fluctuations in IAs is analyzed using both high-resolution (DNS) and low-resolution CFD (LRNS) approaches.

The aim of this chapter can be summarized in the following research questions:

Research questions

A. Do exercise conditions significantly affect the cardiovascular hemodynamics when mitral valve insufficiency is present?

B. Can high-frequency fluctuations occur in neurovascular vessels under rest and exercise, providing insights into pathological conditions?

4.5 Methodology

4.5.1 Patient cohort

To investigate the impact of exercise condition on the hemodynamics, additionally to the cerebral circulation, the cardiovascular circulation focusing on the LV of the heart was considered. Thus, the cohort in this chapter comprised 10 pathological LVs, featuring mitral valve insufficiency at three varying stages (MI I, MI II, MI III), respectively, and an IA, located at the right MCA from patient-specific MR images [157].

The data of the pathological ventricles were assessed using transthoracic echocardiography with real-time 3D imaging. The movement of the ventricular walls could thereby be recorded and saved for the further analysis in this chapter. A Siemens ACUSON SC2000 ultrasound machine (Siemens ACUSON SC2000 Ultrasound System, 2016, SIEMENS Healthineers AG Munich, Germany) was used featuring a frequency of 4.5 MHz. These data were captured at the Division of Cardiology and Angiology, Department of Internal Medicine, University Hospital Magdeburg. For all of the ten patients, transient data with different time instances over the cardiac cycle ranging from $c = 9$ to $c = 22$ time instances were captured, respectively. The data is presented in Table 4.1. The table further comprises as well the MI stage of each patient and the end systolic and end diastolic ventricular volume under rest (re) and exercise (ex) of each patient. In Figure 4.3 the ventricle geometries for the end-systolic state are presented for each case.

The IA was segmented from the MR images and further reconstructed to serve as a basis to investigate the impact of exercise condition on the occurrence of high-frequency hemodynamic fluctuations in the cerebral circulation. Medical images were captured at Penn State University Hershey Medical Center (Hershey, PA, USA) and segmentation performed using the software 3D Slicer. Since the model was used in this study for PTV, direct numerical and low resolution numerical simulation, further adjustment had to be carried out. The IA dome was firstly manually cut from the remaining parent vessel part and a 3D vasculature created through the extrusion of the inlet and outlet vessels. These steps were necessary for the model to fit the experimental test rig. Model adjustments were performed in SolidWorks. The model is shown in Figure 4.3 in the bottom right.

4.5.2 Integration of rest and exercise conditions

In regard of the assessment of exercise condition and its impact on the vascular hemodynamics, the form of consideration of the patient data under rest and exercise depended on the pathology. Due to the movement of the ventricular walls, which changes with the condition (rest or exercise) the change in wall movement was considered for the ventricle pathology. In case of the IA pathology, only minimal wall movement appears in the neurovascular vessel walls, which are neglected in most recent studies and therefore were as well neglected in this thesis [252]. The impact of the condition can thus be mimicked by a variation in inflow BC, as already described in section 4.1. This mimicking was also applied in several previous studies [263, 92, 288].

Handgrip exercise of ventricular cohort

The patient data of the ventricular cohort is presented in Table 4.1. Data was first captured under rest. Afterwards, patients needed to perform physical exercise to increase the heart rate. This was established by the performance of handgrip exercise. Since no further body movement occurred, this is compatible with the medical imaging data acquisition. Handgrip features a reliable indicator of overall health, particularly for predicting functional ability, physical perfor-

mance, and even mortality risk in certain populations [241]. Exercise was performed for at least 2 minutes with a maximum of 4 minutes. Resulting heart rates during data collection varied between 47 bpm and 89 bpm (average 66.30 bpm ± 10.84 bpm) at rest, and between 89 bpm and 133 bpm (average 114.40 bpm ± 10.80 bpm) at exercise, see Table 4.1.

Adjustment of inflow conditions for aneurysmal cohort

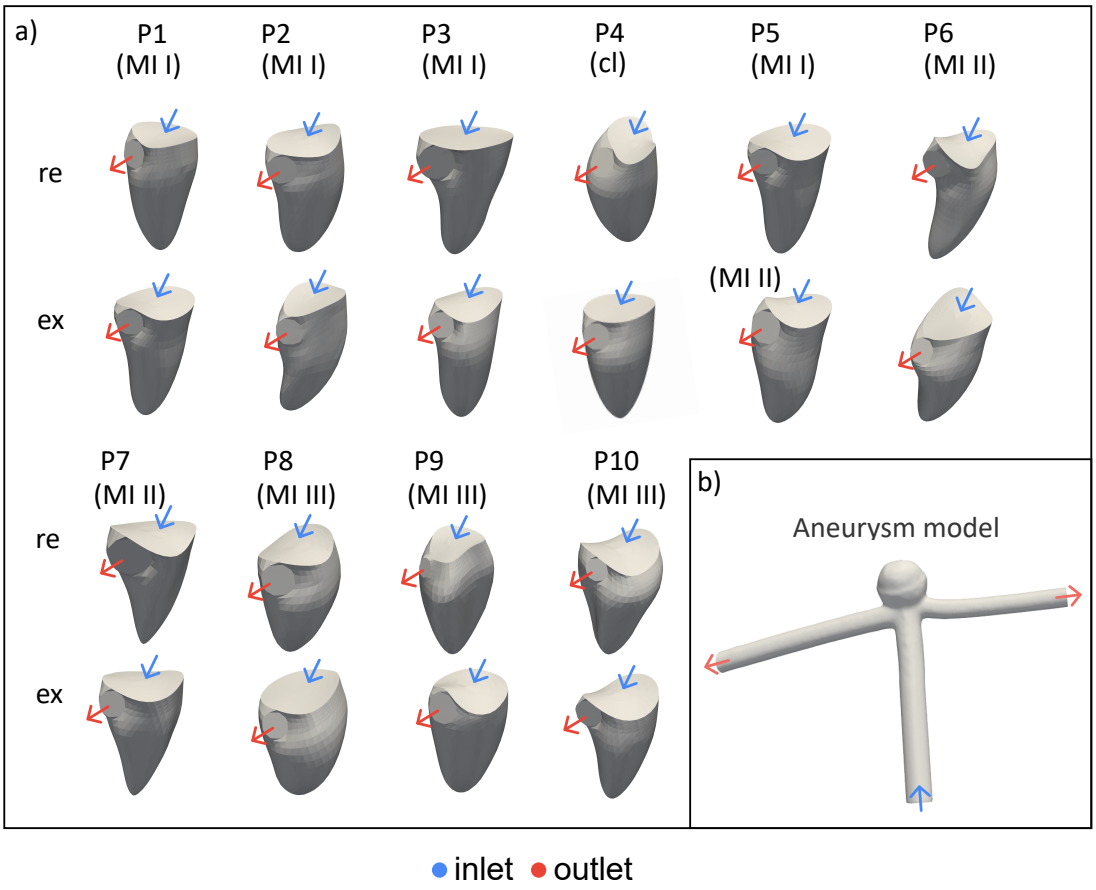


Figure 4.3: Visualization of the patient cohort of this chapter. a) For each patient the end-systolic geometry of the ventricle is shown for the rest (re) and exercise (ex) condition. The stage of the mitral valve insufficiency (MI) is shown in brackets for each case. b) The processed aneurysm model used for simulations is presented. For both, a) and b) the inlet and outlets are marked with blue (inlet) and orange (outlet) arrows.

To receive the rest and exercise conditions within the cerebral flow, varying heart rates were externally applied within the investigations, as presented in Table 4.2. As seen in the heart rate change within the measured ventricle data, an increase from 66 bpm to 114 bpm (in average) was visible from rest to exercise condition. Bowker et al. investigated intra-aneurysmal WSS during rest and exercise of the patient, by externally applied varying inflow velocities within the CFD simulations [39]. The velocity curves in their study featured an average heart rate of 69.6 bpm during rest and of 120.7 bpm during exercise. The chosen heart rate intensities optimally represented the varying cerebral blood flow perfusion and offered a practical approach by being achievable by the general population [115].

To cover this range, the three heart rates 60 bpm (HR1), 100 bpm (HR2), and 137 bpm (HR3) were chosen in this chapter. With a mean inlet diameter of 8.99 m^3 and a constant kinematic viscosity of $3.47 \times 10^{-6}\,m^2\,s^{-1}$ this resulted in the Reynolds numbers 551, 714, and 919. The

Table 4.1: Patient data of ventricular pathologies used in this chapter including the mitral valve insufficiency (MI) state from I-III and one clipped (cl) case, the captured time instances (n), the heart rate (HR), the end systolic volume (ESV), the end diastolic volume (EDV), and the ejection fraction (EF). All data are presented during rest and exercise conditions.

Case	MI		n		HR (bpm)		ESV (ml)		EDV (ml)		EF (-)	
	re	ex	re	ex	re	ex	re	ex	re	ex	re	ex
1	I	I	12	10	89	110	82.96	93.18	132.67	135.50	37.47	31.23
2	I	I	16	14	71	133	80.43	64.93	106.14	91.29	24.22	28.87
3	I	I	14	11	68	120	41.18	42.28	109.02	104.01	62.23	59.35
4	cl	cl	15	16	60	89	51.15	37.13	106.76	76.12	52.08	51.22
5	I	II	16	16	77	114	26.52	25.06	56.16	62.64	52.78	59.98
6	II	II	19	15	60	116	16.46	38.13	40.90	72.57	59.76	47.46
7	II	III	21	20	47	124	15.72	26.14	47.12	63.57	66.63	58.89
8	III	III	15	23	67	110	100.63	93.17	140.12	132.76	28.19	29.82
9	III	III	20	14	58	111	50.98	43.20	93.65	62.33	45.56	30.69
10	III	III	18	17	66	117	30.81	23.92	85.00	58.30	63.75	58.97

Table 4.2: Chosen heart rates and resulting inflow conditions comprising the mean inflow velocity and Reynolds number (Re) for the aneurysm investigation under rest and exercise.

	Heart rate (bpm)	Mean inflow velocity (m/s)	Re	State
HR1	60	0.18	551	Rest
HR2	100	0.233	714	Transition
HR3	137	0.3	919	Exercise

parameters are presented in Table 4.2 together with the related average inflow velocities.

4.5.3 Ventricular wall movement from ultrasound

To incorporate patient-specific wall motion as a BC within the ventricle simulation, a series of meshed surfaces (meshed surface count = n), one for each time instance, was generated. The surfaces featured corresponding surface nodes, respectively. The moving mesh method, as implemented previously by Grünwald et al., was selected to handle the dynamic wall motion in the CFD simulation [107, 214].

For input data preparation of the moving mesh method, the following steps were followed:

1. **Mesh generation for initial geometry:** The end-systolic geometry (timestep n=1) from the initial geometry standard triangle language (STL) file was imported into ANSYS SpaceClaim 2021 R2 in STL format, then meshed using ANSYS Meshing 2021 R2 (Ansys Inc., Canonsburg, PA, USA). The initial surface and the meshed surface for one representative case are shown in Figure 4.5. Each patient-specific model was assigned a base mesh size of 0.5 mm, resulting in a total cell count between 1.3 and 3.6 million cells, depending on the patient's end-systolic volume (ESV). To ensure reliable mesh resolution, mesh independence tests were conducted on the ESV geometry of one representative patient. Mesh base sizes of 1 mm to 0.3 mm were tested and the resulting mean intra-ventricular velocity varied by less than 2 % (see Figure 4.4). The 0.5 mm mesh size was chosen to ensure accuracy of the moving mesh's performance.

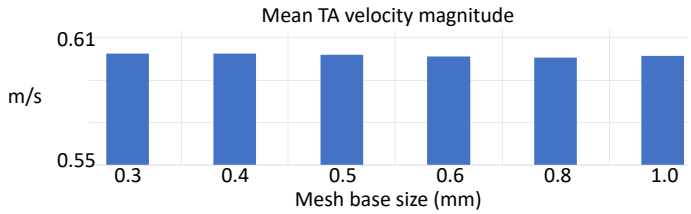


Figure 4.4: Mean time-averaged (TA) velocity magnitude inside the ventricle over six mesh base sizes included in the sensitivity analysis.

2. **Meshed surface node extraction:** After generating the mesh in ANSYS Fluent, the corresponding mesh points of the geometry are exported. For each cell node (C_i) on the meshed geometry's surface, the point ID and its x, y, z coordinates are stored in a file. This process ensures that the sequence of cell node queries is preserved. Consequently, the coordinates of cell nodes from subsequently loaded files (C_{i+1})can be correctly assigned to their original cell nodes.

3. **Node correlation between initial and meshed surface:** The cell nodes (C_i) of the meshed end-systolic geometry were aligned with the triangular faces on the initial geometry file surface as can be seen in the visualization of the "Overlap" in Figure 4.5. For each cell node (C_i), its exact position on the corresponding triangular face (defined by vertices P_1, P_2, P_3) of the initial geometry file was identified. Two factors were herefor established representing each positional cell-to-point correlation as visualized in Figure 4.5 "Node Correlation". The factors are called α and β and were computed based on the cross product and dot product principles: Cross product equals zero for colinear vectors, while dot product equals the product of their magnitudes. The resulting relation is depicted in Equation (4.1) and visualized in Figure 4.5 on the right.

$$P = P_2 + \alpha \cdot \overrightarrow{P_2P_1} + \beta \cdot \overrightarrow{P_2P_3} \tag{4.1}$$

   This approach allowed precise mapping of each meshed end-systolic geometry node on the corresponding initial geometry file geometry at each timestep.

4. **Node correlation across timesteps:** Since each STL geometry in the time series (timesteps c_1, c_2, ...,c_T) contained an identical number of cell nodes, this correlation enabled the creation of consistent mesh configurations across all timesteps.

5. **Interpolating continuous wall motion:** To smooth out the discrete movement between timesteps, a cubic spline interpolation was applied between each P_i and P_{i+1} mesh point. This interpolation, with 20 steps per geometry, facilitated a continuous mesh transition representing left ventricular movement over one cardiac cycle.

The transient mesh as established with the steps mentioned was prescribed within the simulation. Thus, with each timestep conducted the mesh was updated and subsequently the numerical solution performed. As BCs pressure curves were implemented. The curves were estimated based on Bernoulli's law within the ultrasound scanner [117].

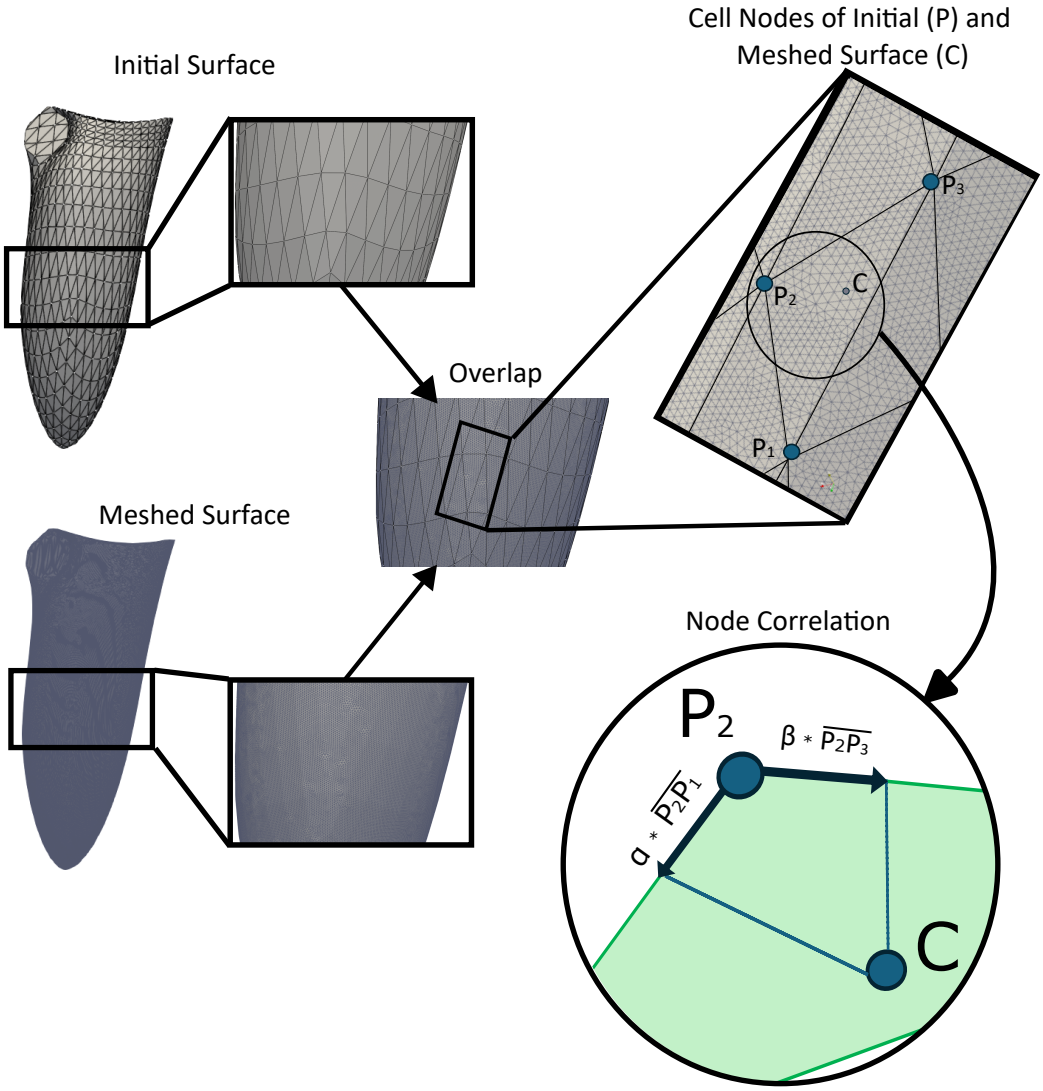


Figure 4.5: Visualization of the node relation between the initial mesh (points P_1, P_2, and P_3) and the meshed surface (point C) and the according calculation of α and β.

4.5.4 Intra-aneurysmal flow validation with volumetric particle tracking velocimetry

The experiments conducted as basis of this part of the chapter featured the volumetric (3D) PTV method shake-the-box (STB). To preserve a comparable basis, the simulation settings were based on these experiments. In the following the description of the experimental setup including the pre-processing of the model for the simulations is given. The visualization of the process is presented in Figure 4.6.

Phantom model creation and flow loop

The chosen aneurysm model, which was adapted to meet the experimental requirements as explained in section 4.5.1, was 3D printed using a LulzBot TAZ 5 printer (LulzBot, Fargo Additive Manufacturing Equipment 3D, USA). The adjustment of the phantom model to the flow loop required to bend the inlet to the side in outlet direction. Manual smoothing was carried out to prepare the walls of the model for embedding into polydimethylsiloxane (PDMS) Sylgard 184 with a refractive index of $n = 1.4130$. Immersion into PDMS set the basis to create a 3D

negative phantom model of the IA. Once the PDMS cured, the printed model could be dissolved with water, leaving the clear PDMS box as can be seen on the top left in Figure 4.6. The latter was further smoothed to achieve high transparency to thus being suitable for laser irradiation. This was important to ensure camera visualization of the flowing particles. For experimental use, the PDMS box was submerged in a solution of water and glycerol. This so-called surrounding fluid carefully matched the refractive index of the PDMS to minimize optical distortions.

The immersion of the model into the surrounding fluid was the first step to set up the experimental flow loop presented on the top right in Figure 4.6. Secondly, a computer-controlled gear pump pumped the working fluid through the model while being connected to the inlet and outlet tubes. The working fluid consisted of water, urea, and glycerol, mixed to match the density and kinematic viscosity of blood ($\rho = 1142\,\mathrm{kg\,m^{-3}}$, $\nu = 3.47 \times 10^{-6}\,\mathrm{m^2\,s^{-1}}$). The pump was programmed to simulate flow with specific magnitudes and frequencies corresponding to three heart rates, representing resting (60 bpm) and the two elevated exercise rates (100 bpm and 137bpm).

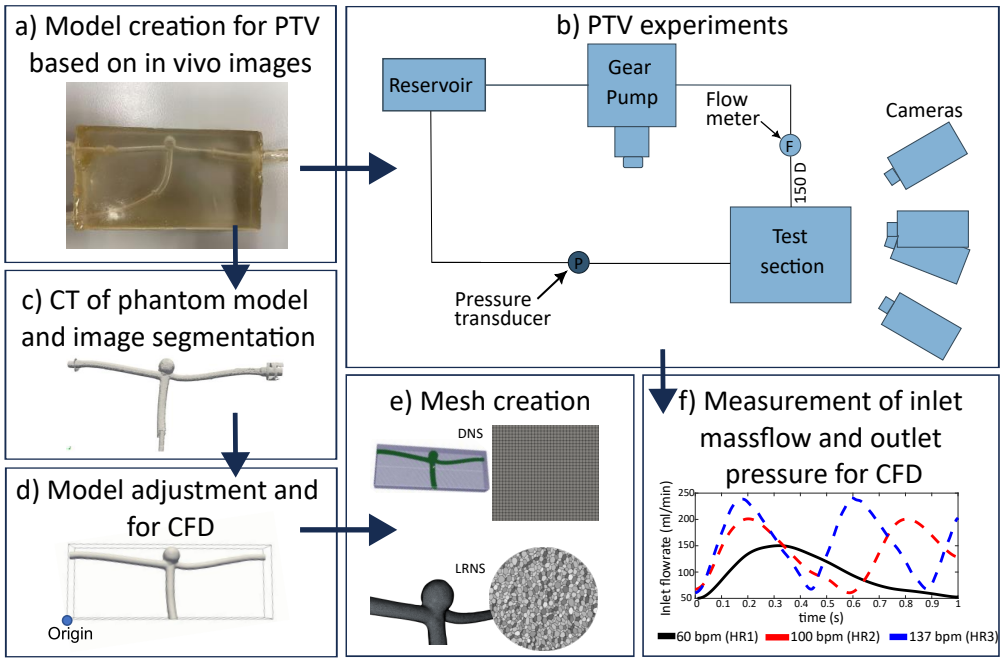


Figure 4.6: Representation of the processing steps of the neurovascular analysis in this chapter, starting with the phantom model creation (a). This model was used in the experimental particle tracking velocimetry (PTV) setup (b). Moreover, the model was used to establish the virtual model for the simulations (c-e). Inflow and outlet pressure curves measured during the experiments were provided to CFD (f).

To measure the inlet flowrate a flow meter (Transonic Inc., Ithaca, USA) was placed in front of the inlet and after a 150-diameter-length tubing to ensure a fully developed inflow. The pressure at the two outlets was monitored using pressure transducers (Omega, PX309). The resulting inflow curves are presented in Figure 4.6 on the bottom right. The experiments were performed at the Department of Mechanical Engineering, The Pennsylvania State University USA.

Volumetric particle tracking velocimetry and data visualization

Fluorescent particles, 19 µm in size, were added to the fluid and illuminated by a 12 cm laser sheet (Photonic Industries, $\lambda = 527\,\mathrm{nm}$. The fluorescent light from the particles was recorded using four high-speed Phantom VEO440 cameras: one centered perpendicular to the region of in-

terest and three positioned at approximately 30° angles. These settings provided images of 1280 × 852 pixels, with frame rates of 1600 Hz (HR1), 2000 Hz (HR2), and 2500 Hz (HR3). This allowed for a maximum particle displacement of 18 pixels, with a resolution of 18.4 μm/pixel [140].

Particle images were captured and processed in Davis 10.0 (LaVision Inc., Göttingen, Germany), achieving an initial root Mean Square fit error of 0.49 pixels, which was reduced to 0.00605 pixels through an iterative volume self-calibration method. The STB algorithm was used, to compute the 3D particle tracks [265]. Parameters for STB included a triangulation error limit of 3.0 voxels, 12 outer iterations for particle addition, and 8 inner iterations for particle refinement, with particle position adjustments set to 0.8 voxels. Particles closer than 0.1 voxels were removed to improve data clarity.

The STB algorithm tracks were initially masked using the STL model geometry from simulation pre-processing (which will be explained in the following) to exclude the particle tracks outside of the geometry. Then they were converted from a Lagrangian to an Eulerian flow field on a grid with $0.3\,\mathrm{mm}^3$ spatial resolution using MATLAB. Temporal grouping was performed by including only each fourth image to increase particle track density and thus the gridding accuracy. However, this led to reduced frame rates of 400 Hz, 500 Hz, and 625 Hz for HR1, HR2, and HR3, respectively. Denoising was applied using proper orthogonal decomposition with autonomous entropy line-fit thresholding [43, 279], followed by universal outlier detection with a window size of (5 × 5 × 5) and a threshold tolerance of 2.5. Finally, phase-averaging was performed over 13 cycles for each heart rate to achieve consistent flow patterns across conditions.

Processing of experimental data for simulations

For the phantom model to serve as a basis in the simulations, a CT scan had to be taken of the PDMS box, to derive the exact model geometry shown on the left in Figure 4.6. After segmentation of the scan, a 3D virtual model was produced, which had to be adjusted by removing artifacts and smoothing the wall. The latter were important to ensure the possibility of a numerical mesh creation for the numerical solution [158]. As necessary for the simulation, the inlet and outlets were cut to be planar. Additionally, the DNS mesh required all inlets and outlets to be parallel to the coordinate planes, so the bent inlet used in the experiments could not be replicated in the numerical analysis (see Figure 4.6 bottom left). To achieve parallel alignment and a fully developed flow profile, the inlet surface was cut perpendicular to the coordinate plane. Since the geometry model processed for numerical investigations was used for STB particle track masking, no further registration between DNS and STB was necessary.

Extending to the inlet and outlets was not feasible due to limits in computational effort in DNS. Since the LRNS should feature identical conditions, the vessels were not extruded as well. This led to the flow directly entering the aneurysm without fully developing over a certain vessel length. Thus, a fully developed inflow profile was set at the inlet plane within DNS and LRNS. Here, the radial velocity (v_{rad}) was estimated using the inlet's midpoint, the mean inlet velocity (v_{mean}), the vessel's inlet radius R and the radial distance r as presented in Equation (4.2).

$$v_{rad} = 2 \cdot v_{mean} \cdot \left(1 - \frac{r^2}{R^2}\right) \tag{4.2}$$

The inflow curves measured experimentally, reflecting the three selected heart rates HR1–HR3, were incorporated as BCs in the numerical simulations. Due to noise in the experimental data, inflow and pressure curves were smoothed using the curve fitting toolbox in MATLAB (R2022a, The MathWorks, USA). Outlet pressure curves recorded during the experiments were applied

in LRNS. However, in DNS, due to numerical constraints, a static outlet pressure matching environmental conditions had to be used.

4.5.5 Hemodynamic investigation: Moving mesh, direct numerical and low resolution simulation

Three numerical methods were used in this chapter to investigate the exercise condition in the cardiovascular and cerebral circulation. Since the ventricular wall movement served as a BC to implement the exercise state, a moving mesh method (1) had to be applied within the cardiovascular numerical assessment.

Regarding the assessment of the neurovascular circulation, the impact of exercise needed to be analyzed using a high-resolution approach, since the possibility of finding high-frequency fluctuations existed. Thus, two approaches, direct numerical (2) and low resolution numerical (3) simulations were compared. DNS was chosen since it is assumed to be able to resolve high-frequency velocity fluctuations. LRNS represents the state-of-the-art numerical approach to analyze intra-aneurysmal flow dynamics as was exentsivly studied in Chapter 3. Moreover, a comparison to LRNS provides the opportunity to prove that the implementation of DNS is necessary for this purpose.

Fluid properties

In DNS and LRNS, the fluid mimics the experimental working fluid conditions. Thus, blood was modeled as a Newtonian fluid, with density and viscosity values selected to replicate those in the experiments ($\rho = 1142\,\mathrm{kg\,m^{-2}}$, $\nu = 3.47 \times 10^{-4}\,\mathrm{m^2\,s^{-1}}$). In the moving mesh method, the fluid was modeled Newtonian as well, setting a dynamic viscosity of $0.004\,\mathrm{Pa} \times \mathrm{s}$. The density was chosen to be $\nu = 1055\,\mathrm{kg\,m^{-2}}$ with the blood being modeled as incompressible.

Ventricular moving mesh simulation

CFD simulations were conducted to solve the Navier-Stokes equations using the finite volume solver ANSYS FLUENT 2021 R2, incorporating the moving mesh method. This approach was implemented through user-defined functions coded in C and compiled within the solver environment [107]. At each simulation timestep, the current mesh was updated before the fluid solver advanced with 30 iterations per timestep, meaning that the timestep size was dependent on both the mesh configuration and the cycle duration.

Valve dynamics were simulated by treating valves as wall boundaries when closed. For modeling myocardial infarction stages, the orifice was represented as a circular section at the center of the inlet surface, which functioned as a pressure inlet during systole. This section occupied approximately 10 % of the inlet surface area for MI stage I and 20 % for MI stages II/III. A pressure-based coupled solver combined with the k-ω-SST turbulence model was applied. For the two-equation Reynolds-averaged Navier-Stokes the turbulent Prandtl number for k was set to 1.176 (inner) and 1 (outer), and a low-Reynolds-number correction of α*=1. The convergence criteria were set at $1 \cdot 10^{-3}$ for k and ω [328, 95].

Direct numerical simulation of an intracranial aneurysm

The DNS were performed using the in-house solver DINO [4, 5]. DINO implements a sixth-order central finite difference scheme for spatial discretization and for time integration a fourth-order explicit Runge–Kutta method. A structured computational mesh consisting of 19 million

grid points was used to discretize the domain (see Figure 4.6 bottom middle) and served as the base DNS configuration. The aneurysm wall geometry was represented using an immersed boundary method, enhanced with advanced directional ghost-cell techniques [60]. The time step size was dynamically controlled based on the Courant-Friedrichs-Lewy (Courant-Friedrichs-Lewy ≤ 0.25) condition, with a range between $1 \cdot 10^{-10}$ s and $5 \cdot 10^{-10}$ s. In DNS no turbulence model is required. To achieve fully developed hemodynamic conditions, three cardiac cycles were simulated, with only the results from the final cycle used for analysis. The DNS simulations were executed on the high-performance computing system SuperMUC-NG, utilizing approximately 1500 processors and requiring 24 hours of wall clock time [169].

A mesh sensitivity analysis was conducted to assess the impact of grid resolution on the numerical results. Three different mesh resolutions were considered: a coarse grid (9 million grid cells), an intermediate grid (21 million grid cells), and a fine grid (50 million grid cells). Six probe locations within the computational domain were selected to monitor the root mean square (RMS) velocity magnitudes. The analysis showed that the variation in the RMS velocities between the three grids was minimal at probe locations in the bifurcation area (probes 1 and 3). The RMS of the velocity decreased by 12 % from the fine to the intermediate grid and just by 4 % from the latter to the coarse grid (probe 1). For probe 3, the difference was even lower with a decrease by 2 %. However, at another probe, these differences were more pronounced, indicating higher sensitivity to the mesh resolution in certain regions of the domain. Based on these results, the medium grid was selected as the optimal mesh resolution for the simulations. This decision was guided by a balance between numerical accuracy and computational cost, as the medium grid provided sufficiently accurate results while remaining computationally feasible.

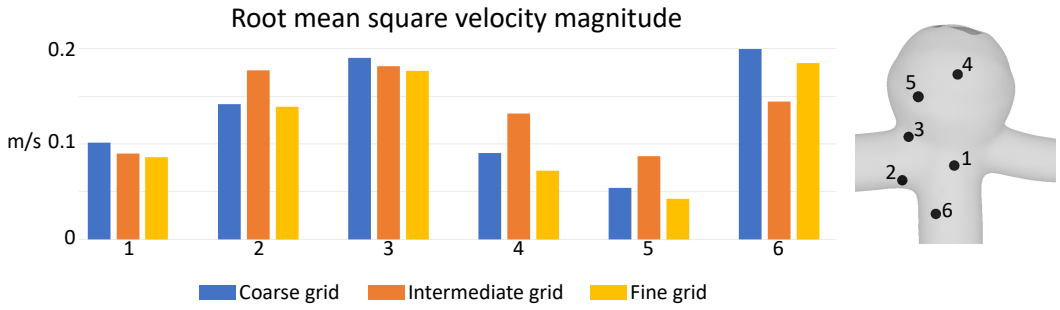


Figure 4.7: Root mean square (RMS) of the velocity components at four representative probes inside the vascular domain obtained from three different meshes.

Low-resolution simulation of an intracranial aneurysm

To compare the results derived from DNS with the low resolution counterpart, conventionally used image-based blood flow simulations within the commercial solver STAR CCM+ (v17.6, Siemens, Germany) were carried out. The method was chosen since it is usually applied for the evaluation of intra-aneurysmal hemodynamics and its relation to rupture in recent literature (see Chapter 3) [25]. STAR CCM+ was here preferred to ANSYS Fluent due to the easier availability ressources. Both codes are very similar in performance. Thus, the mesh conditions were chosen based on this strategy, with polyhedral cells and a base size set to 0.1 mm. The computational domain comprised 1.17 million finite volume cells, with a time step of 0.001 s applied using an implicit first-order temporal discretization. Simulations were conducted on the university cluster with 16 cores, requiring 2–4 hours per simulation. A comparable overview of the two simulation approaches is presented in Table 4.3.

Table 4.3: Detailed key settings of the two simulation approaches for the neurovascular flow simulation to resolve high-frequency fluctuations, Low resolution numerical simulation (LRNS) and direct numerical simulation (DNS).

Solver	Grid size (cells)	Timestep (s)	Inlet	Outlet	Runtime
DNS	21 million	Variable with thresholds 10^{-10} - 5^{-10}	measured	constant	24h
LRNS	1.17 million	0.001	measured	measured	2h

4.5.6 Post-processing

Focus in this chapter was set to evaluate the impact of rest and exercise condition on the pathological cardiovascular and neurovascular flow. For this, different parameters inside the ventricle and IA were considered.

Velocity and vorticiy

First, the velocity and vorticiy (ω) were considered, which were calculated within ANSYS EnSight 2021 R2. According parameter formulas are depicted in section 2.5. Within the ventricles these parameters were spatially averaged over the full ventricular domain. Mean parameters were spatially averaged inside the domain and temporally averaged over one cardiac cycle. In case of the aneurysmal analysis, two intersecting planes were defined, cutting through the aneurysm dome. Additionally, specific probes were positioned near the aneurysm wall, inside the dome, and within bifurcation areas. To facilitate qualitative and quantitative assessments, spatial averages of velocity and ω were computed across the planes using MATLAB (R2021b, MathWorks, USA). The hemodynamics on each plane were then normalized by its plane-wise spatial mean. In probe-based comparisons, only numerical data was analyzed due to registration errors and resolution differences in the experimental data. MATLAB and Python were used to compute probe-based velocity and ω via RMS and time-resolved comparisons.

Given potential minor misalignment in aneurysmal data from experiments and simulations, a voxel-wise comparison was conducted. Numerical data was spatially discretized, and hemodynamic parameters averaged to new voxels corresponding to the STB grid. Voxelization was performed using ANSYS EnSight (v19, ANSYS, USA), with each voxel averaging values based on the nearest mesh points. In regard of visualization, temporally averaged distributions of velocity and ω magnitudes on both planes were normalized by the plane mean and plotted using Paraview (v5.10.1, Kitware Inc., USA). Quantitatively, violin plots illustrated the distribution of temporally averaged and peak velocity as well as ω data. These plots, adapted from previous studies [120], included data from STB, DNS, LRNS, and voxelized numerical results.

Kinetic energy as cardiac marker

The KE plays an important role within cardiovascular research to evaluate cardiac function. Since it was recently formulated to serve as an indicator of healthy cardiovascular function the KE was evaluated inside the ventricular domain, [316]. To evaluate the difference between the rest and exercise impact and across MI stages I, II, and III, statistical tests were performed. These comparisons used a two-sided Student's t-test with a significance level of p=0.05.

Power spectral density as marker for neurovascular flow state

To characterize turbulence, power spectral densities (PSD) were calculated for selected probes. The PSD describes how energy is distributed across different frequencies in the flow. Thus, PSD

capture turbulence characteristics across an energy-containing range, an inertial subrange, and a dissipation range. At large scales (low wave numbers), the PSD show a peak, indicating the dominant energy-containing eddies. The energy is here injected into the system. At the inertial subrange, Kolmogorov's theory predicts that the PSD follow a power-law behavior for homogeneous isotropic turbulence as presented in Equation (4.3), including the energy spectrum E(k) and the wave number k [193].

$$E(k) \propto k^{-5/3} \tag{4.3}$$

This scaling reflects the self-similar transfer of energy across scales in the inertial subrange. At small scales (high wave numbers), the PSD steeply declines. This corresponds to the dissipation range, where energy is converted to heat by viscosity. PSD of the velocity magnitude was calculated using Welch's method in Python's SciPy library, as detailed in [6].

4.6 Impact of rest and exercise on cardiac hemodynamics

This chapter analyzes the effect of rest and exercise condition on pathological cardiovascular hemodynamics. First, the implemented wall modeling in the simulation and kinetic energy are evaluated. Second, the intraventricular flow behavior is further investigated.

4.6.1 Implementation of ventricular wall movement and resulting transient kinetic energy

To implement the cardiovascular wall movement, the medical imaging technique of ultrasound was used as explained in section 4.5.1. Ultrasound was selected as the imaging modality due to its significant clinical applicability [59]. However, as the resolution is spatially low, in this study, the valve geometries and movements could not be captured and segmented from the imaging. However, the high temporal resolution allowed for the acquisition of the patient-specific wall movement. Moreover, ultrasound is particularly valuable for assessment of pathologies such as MI during exercise, as demonstrated by Voilliot et al. [304]. Compared to imaging techniques such as CTA or MRI, ultrasound offers the advantages of being a cost-effective, widely accessible, and low-risk method for patients [226]. From a clinical perspective, the value of ultrasound imaging comprises especially suitability for dynamic studies during exercise, aligning with prior findings on its applicability in MI assessment [304]. As explained in section 4.1, the implementation of exercise during medical imaging is still challenging, especially when analyzing cardiac related geometries.

In Figure 4.8 the KE distribution together with the vortex formation visualized by the Q-criterion at the end-systolic and end-diastolic state of each patient during rest and exercise is shown. Below these distributions representations of the transient KE normalized by the end-diastolic volume is shown together with the specific volume curve of each patient, respectively. Each cardiac cycle is normalized by its length. The findings revealed distinct variations between rest and exercise conditions, as well as between MI stages. Volume and normalized KE curves demonstrated a clear relationship between wall motion and hemodynamic performance. Volume reductions during systole coincided with peaks in KE. During diastole, smaller KE peaks were observed across all patients.

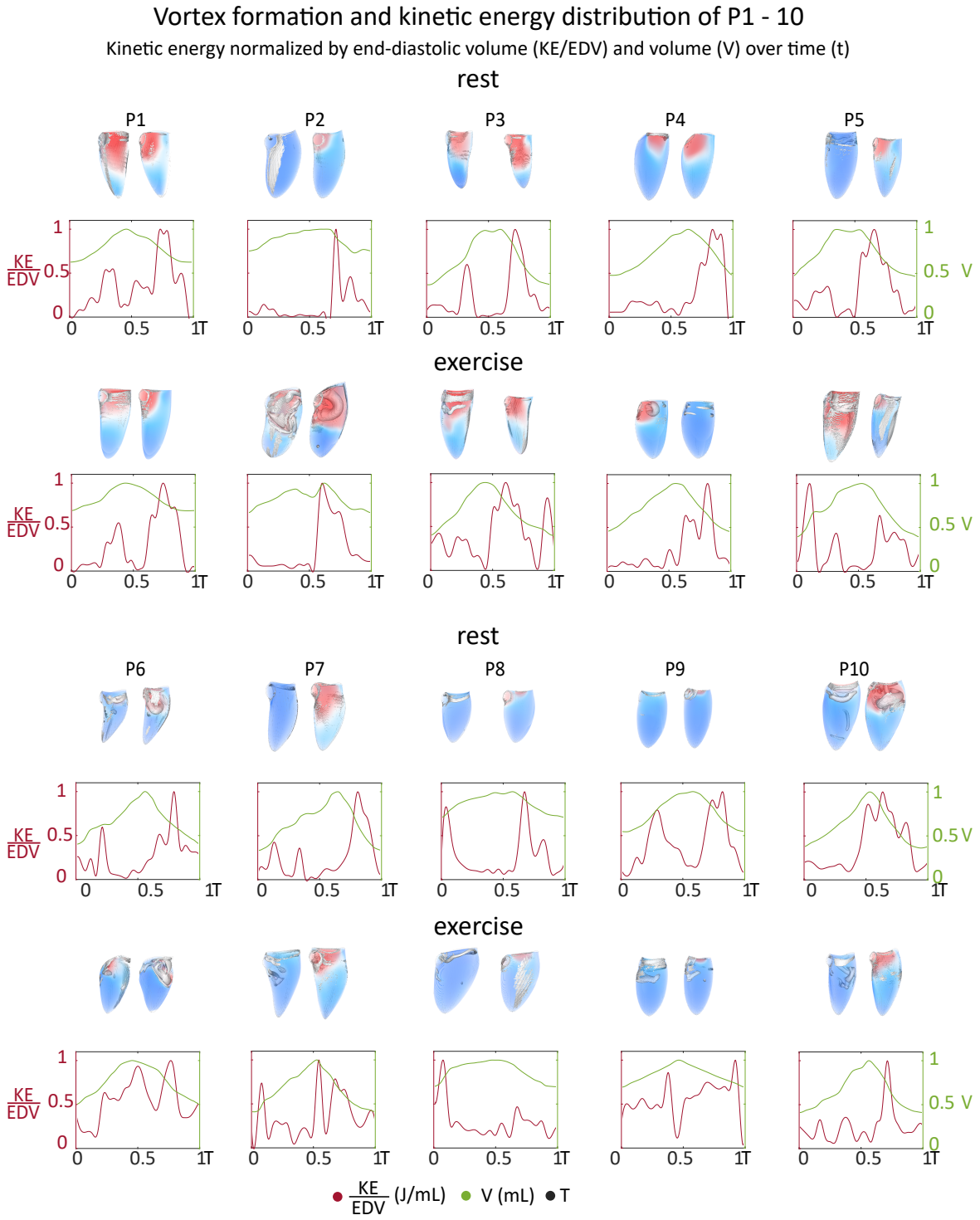


Figure 4.8: Qualitative visualization of the kinetic energy distribution in the systolic and diastolic state of each patient during rest and exercise. The resulting transient intra-ventricular kinetic energy (KE) normalized by the end diastolic volume (EDV) are shown in red below each visualization together with the change in volume (V) over time in green.

However, variations in these patterns emerged depending on the MI stage and activity level. For instance, during exercise, end-diastolic volume increased in some patients (P1, P5-7), while ejection fraction improved in others (P2, P5, P8). Notably, patients with more severe MI stages (MI II/III) exhibited lower KE overall compared to those in earlier stages (MI I). Interestingly, during systole, KE was generally higher than during diastole, though this trend reversed during

exercise for MI I patients (P1-5), where KE decreased during systole. Conversely, for patients with MI II/III (P6-10), systolic KE increased during exercise. Such stage-specific differences highlight the impact of MI severity on LV dynamics. Additionally, qualitative visualizations of KE distribution and vortex formations confirmed distinct flow patterns that were stage- and activity-dependent. By linking KE and volume changes, the results confirm previous research suggesting their interdependence in LV hemodynamics. For instance Al-Wakeel et al. found also a relation between intraventricular KE and left ventricular volume in patients suffering from MI [308].

4.6.2 Intraventricular pathological flow behavior under rest and exercise

This section explored intraventricular hemodynamics in patients with MI at rest and during exercise using patient-specific simulations derived from ultrasound imaging. In Table 4.4 the specific ventricular hemodynamics for rest and exercise are shown. Statistical tests were conducted comparing the rest and exercise conditions of all patients for each parameter and the resulting p-value is presented at the bottom. Key hemodynamic parameters, including kinetic energy normalized by end-diastolic volume (KE/EDV), velocity, vorticity, maximum systolic KE/EDV, and maximum diastolic KE/EDV, were analyzed to examine differences between rest and exercise.

Table 4.4: Resulting hemodynamics inside the patient data under rest (re) and exercise (ex). The p-value describes the statistical comparison between rest and exercise per parameter. Kinetic energy (KE); end-diastolic volume (EDV); velocity (VEL); vorticity (ω); maximum systolic (max sys); maximum diastolic (max dias); standard deviation (SD).

	Spatial and temporal mean									
	KE/EDV		VEL		ω		max sys KE/EDV		max dias KE/EDV	
	re	ex	re	ex	re	ex	re	ex	re	ex
1	11.07	4.39	0.11	0.06	13.46	9.57	18.66	0.13	34.00	14.38
2	3.41	16.34	0.05	0.12	10.23	35.23	3.33	10.17	23.00	63.60
3	15.45	14.86	0.12	0.13	22.61	24.04	42.82	10.77	71.27	36.16
4	6.3	6.79	0.07	0.08	10.74	15.02	5.21	0.63	28.52	29.96
5	8.04	16.56	0.08	0.13	21.7	28.69	9.76	8.21	27.70	69.05
6	7.34	5.93	0.09	0.08	29.34	22.09	15.82	4.34	26.55	10.54
7	4.64	4.27	0.07	0.07	17.7	16.65	6.86	2.62	16.08	10.39
8	0.96	1.92	0.03	0.05	6.81	10.34	9.75	5.67	3.09	9.75
9	1.96	1.94	0.04	0.05	8.5	7.58	3.57	0.94	4.50	3.32
10	7.81	3.51	0.09	0.06	23.82	17.4	17.21	3.18	20.00	12.45
Mean	6.70	7.65	0.08	0.08	16.49	18.66	13.30	4.66	25.47	25.96
SD	4.12	5.61	0.03	0.03	7.24	8.42	11.17	3.72	18.03	22.28
p-value	0.73		0.6		0.56		0.04		0.94	

The results provided insights into the LV's functional adaptation to exercise and the effects of MI severity. The findings reveal that maximum systolic KE/EDV significantly decreased during exercise (p=0.04), while other parameters, such as mean KE/EDV, vorticity, and maximum diastolic KE/EDV, showed non-significant trends. The observed reduction in maximum systolic KE/EDV during exercise aligns with earlier studies showing that exercise capacity diminishes in patients with mild cardiac dysfunctions [104]. Thus, systolic KE could serve as a potential marker for evaluating cardiac function in MI patients, offering insights into how exercise influences the LV's ability to adapt to hemodynamic demands.

In contrast to KE, vorticity showed differing results during late diastole when analyzing resting and exercise conditions. While vorticity was higher during exercise, patients with MI stage II/III exhibited elevated vorticity at rest compared to exercise. This finding aligns with the observations of Stöhr et al. [284], who reported pronounced left ventricular vortex dynamics in MI patients compared to reduced vortex formation in healthy individuals. However, these differences did not reach statistical significance, necessitating further investigation to draw definitive conclusions regarding the comparison.

Despite the comparison between rest and exercise, additionally the comparison of the MI stages is considered. In Table 4.5 the mean values comparing the MI stages independent from rest and exercise condition are compared. A significant difference was observed in mean VEL (p=0.01) and maximum diastolic KE/EDV (p=0.03) between MI stages, with MI I patients exhibiting higher values than MI II/III. Higher velocities occurred in MI I patients, particularly during rest and exercise, aligning with their higher ejection fractions. The analysis further identified increased vorticity during exercise, highlighting enhanced vortex formation. However, patients with MI II/III displayed higher vorticity at rest compared to exercise, in agreement with prior studies suggesting reduced vortex formation in severe MI [104].

Table 4.5: Resulting hemodynamics inside the ventricles averaged over patients 1-5 and patients 6-10 to compare the effect of the MI stages. Kinetic energy (KE); end-diastolic volume (EDV); velocity (VEL); maximum systolic (max sys); maximum diastolic (max dias); standard deviation (SD).

	KE/EDV	VEL	max sys KE/EDV	max dias KE/EDV
Mean P1-P5	0.12	0.10	0.11	0.45
SD	0.07	0.03	0.11	0.30
Mean P6-P10	0.07	0.06	0.10	0.20
SD	0.05	0.02	0.11	0.19
p-value	0.08	0.01	0.80	0.03

4.6.3 Limitations

Due to the absence of statistical significance for some differences the need for further investigation is highlighted. The computational approach employed in this study utilized patient-specific left ventricular wall motion derived from ultrasound imaging, providing detailed insights into flow patterns and KE distribution. However, several limitations must be acknowledged, with the segmentation method being the most critical. The use of smoothed ventricular walls introduces biases that may affect the accuracy of flow simulations. As discussed in Chapter 3, an accurate segmentation method is essential for achieving realistic hemodynamic outcomes. This level of precision could not be fully ensured when using the automated segmentation software TomTec. Nonetheless, this approach represented the best available method for obtaining transient moving ventricular walls. Another limitation arises from the simplified representation of the heart valves, which constrained the analysis. Since the valves were modeled as fixed orifices without dynamic functionality, realistic inflow dynamics could not be fully captured. However, as this simplification was applied uniformly across all cases, the comparative analysis remains valid. Additionally, assumptions regarding blood incompressibility and the non-fully closing inlet surfaces during simulations likely influenced velocity profiles and pressure boundaries. These factors should be considered in future studies to further enhance the accuracy of patient-specific hemodynamic simulations.

Despite these challenges, the results highlighted the potential of ultrasound-based hemodynamic analysis as a non-invasive tool for evaluating cardiac function. The results moreover emphasize significant differences in LV function between rest and exercise, as well as across

MI stages, supporting the use of KE/EDV and VEL as potential markers for cardiac dysfunction. The workflow effectively integrates imaging data and numerical simulations, offering high-resolution insights into patient-specific LV dynamics, which is critical for non-invasive assessment in heart failure patients.

4.7 Appearance of transitional flow in an intracranial aneurysm during rest and exercise

This section assesses the effect of rest and exercise on intra-aneurysmal hemodynamics. Focus was set on the solver used for the simulations to derive this effect and on the possibility to capture high-frequency fluctuations in the flow dynamics. The simulations were further validated experimentally.

4.7.1 Validation of aneurysmal flow under rest and exercise using volumetric particle tracking velocimetry

Validation was performed as described in section 4.5.4 and the focus was set on examining the velocity and vorticity when comparing numerical simulations and experiments. Two planes and 58 probes placed inside aneurysm dome were considered for the analysis.

Velocity

In Figure 4.9 the normalized TA velocity distribution on two planes through the aneurysm dome is presented. The locations of the planes are shown at the top of the figure. The different modalities are shown column-wise and the heart rates row-wise. A general similar velocity distribution was found when comparing the modalities at both planes, which was expected. Nevertheless, especially regarding the magnitude, differences between the experiments and simulations were visible qualitatively, especially when looking at HR1 (Re=551).

At plane 1, which is located closer to the aneurysm tip, a circular jet formation is visible in the numerical results. With DNS, a closed circle was visible with slightly lower velocities at the top, whereas with LRNS lower velocities occurred at the bottom of the dome. With PTV, the circular formation was visible at HR2. For the remaining HRs, areas of higher velocity appeared at the bottom right of the dome. At plane 2, which is located closer to the bifurcation, a clear inflow jet was visible at the right. This jet is replicated with PTV at HR2 and HR3. Within HR1 lower velocities with PTV occurred and the inflow jet is only slightly visible. Quantitatively, the DNS and LRNS results were similar, with the most visible differences at the mid part of the plane.

This was also reflected within the quantitative results of velocity magnitudes across the different heart rates and modalities, which are presented using violin plots for normalized TA and peak velocities of the two planes (Figure 4.10). Violin plots depict the distribution and density of the analyzed variables. Separate plots are shown for the TA velocity on plane 1 (left column) and plane 2 (right column), for all three heart rate cases. For the two numerical modalities, velocity magnitudes (and also vorticity, which is presented later) were further analyzed after virtual voxel averaging to align their spatiotemporal resolution with that of the PTV experimental method.

For STB, slight variations in velocity distributions across heart rates were observed, with a skewed distribution for velocities above the mean. In contrast, numerical data showed minimal

dependence on heart rate, with only slight increases in the distribution of values above the mean for HR2 and below the mean for HR1 and HR3. The LRNS and DNS exhibited comparable TA velocity ranges, with mean velocities of approximately 1-1.32 $\mathrm{m\,s^{-1}}$ across all heart rates. Following voxelization, the sub-mean peak in the LRNS violin plot disappeared, resulting in a closer match between the shapes of LRNS and DNS plots. However, the velocity distributions retained consistent density profiles from minimum to maximum values in the voxelized LRNS data.

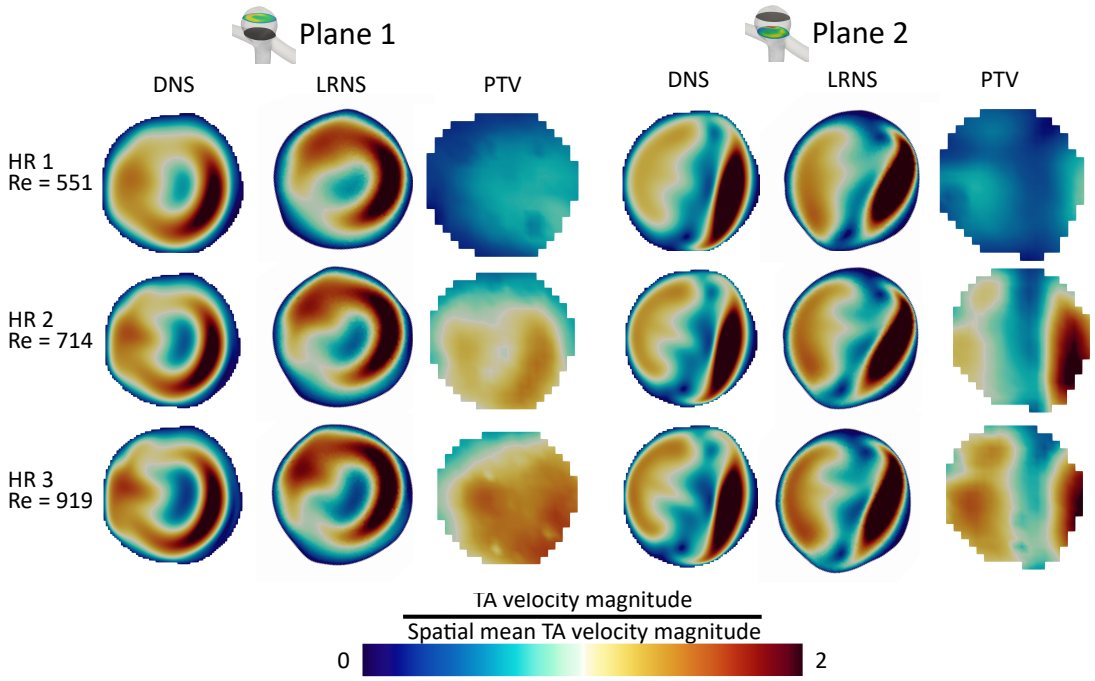


Figure 4.9: Qualitative distribution on plane 1 (left) and plane 2 (right) of the time-averaged (TA) velocity magnitude normalized by each plane's spatial mean value. DNS - direct numerical simulation; LRNS - low-resolution numerical simulation; PTV - particle tracking velocimetry.

Table 4.6: Mean normalized time-averaged (TA) velocity magnitude (v) values at planes 1 and 2.

	Mean TA v (Plane 1)			Mean TA v (Plane 2)		
	HR 1	HR 2	HR 3	HR 1	HR 2	HR 3
STB	1.00	1.0	1.00	1.00	1.00	1.00
DNS	1.00	1.00	1.00	1.00	1.00	1.00
DNS voxelized	1.04	1.04	1.04	1.05	1.05	1.05
LRNS	1.00	1.00	1.00	1.00	1.00	1.00
LRNS voxelized	1.41	1.37	1.37	1.62	1.50	1.50

Additionally to the violin plots in Figure 4.10, the mean TA velocity magnitude values are presented in Table 4.6. The results reveal similar mean values between numerical (DNS and LRNS) and experimental (STB) results for both planes. Voxelization especially increased LRNS velocity. However, voxelization impacted the distribution of the violin by reducing the second peak at velocities lower than the mean at plane 1. Regarding plane 2 DNS and STB exhibited equivalent normalized values across all HRs. This equivalence diminished slightly after voxelization, resulting in a mean velocity difference of 0.05 $\mathrm{m\,s^{-1}}$ across HR1-HR3. Similarly, mean TA velocities for LRNS and STB were identical, though voxelization introduced larger discrepancies (Δ 0.62 $\mathrm{m\,s^{-1}}$ for HR1, Δ 0.50 $\mathrm{m\,s^{-1}}$ for HR2 and HR3).

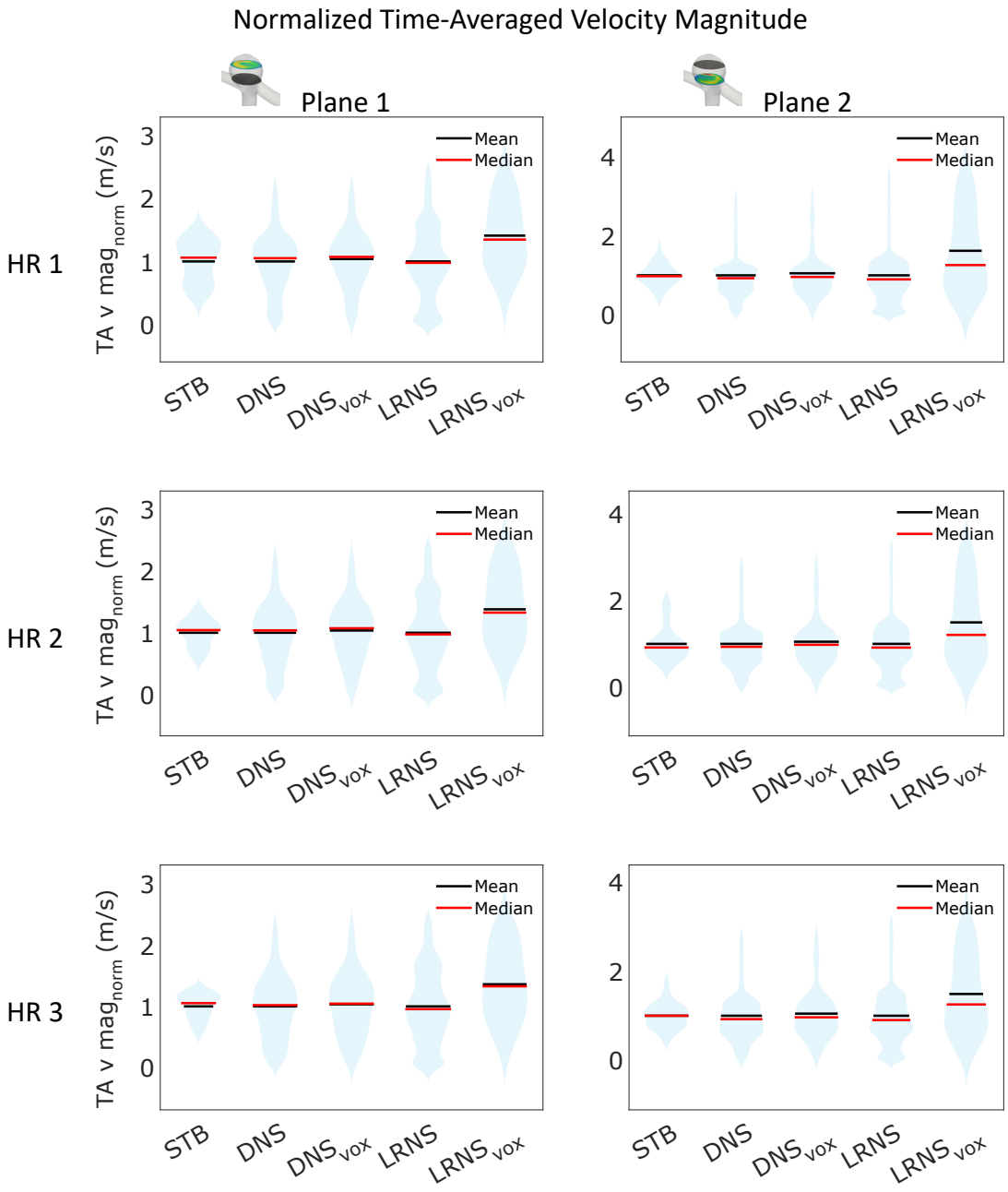


Figure 4.10: Violin plots of time-averaged (TA) velocity magnitude (v mag) normalized by each plane's spatial mean value. Violins are shown for each heart rate (HR) 1-3 for the experiments (shake-the-box - STB), direct numerical simulation (DNS), low-resolution numerical simulation (LRNS), whereas the results of the two simulation approaches were further voxelized (vox) to match the STB grid size.

The qualitative and quantitative comparisons between the numerical simulations and experimental data in this study demonstrated good agreement, particularly with respect to velocity measurements. Similar levels of concordance between low-fidelity numerical simulations and particle image velocimetry/PTV have been reported in previous studies [245, 98]. Despite normalization of the velocity fields in this study, experimental velocities were consistently lower than those obtained from CFD. This observation aligns with the findings of Raschi et al. [245], who validated PIV against low-resolution numerical simulations in an aneurysm model. Their study identified the greatest discrepancies between the two methods in regions near vessel walls and in areas of slow flow.

Vorticity

Qualitative distribution of TA vorticity at the two planes through the aneurysm dome is presented in Figure 4.11. Again, the modalities are shown column-wise and the heart rates row-wise, with plane 1 on the left and plane 2 on the right. The comparison of vorticity distributions revealed differences in both magnitude and structure between the two numerical methods. LRNS exhibited lower vorticity magnitudes across both planes, particularly in the inflow jet region, compared to DNS and STB. Notably, DNS captured distinct vortex structures within the aneurysmal dome, which were also observed in the STB experimental results, with these features being most prominent in the HR2 case. In contrast, LRNS failed to resolve the intra-aneurysmal circulation, and its vorticity patterns showed minimal variation with changes in heart rate. Conversely, DNS demonstrated strengthening vortex structures as heart rate increased, particularly evident in the intra-aneurysmal region.

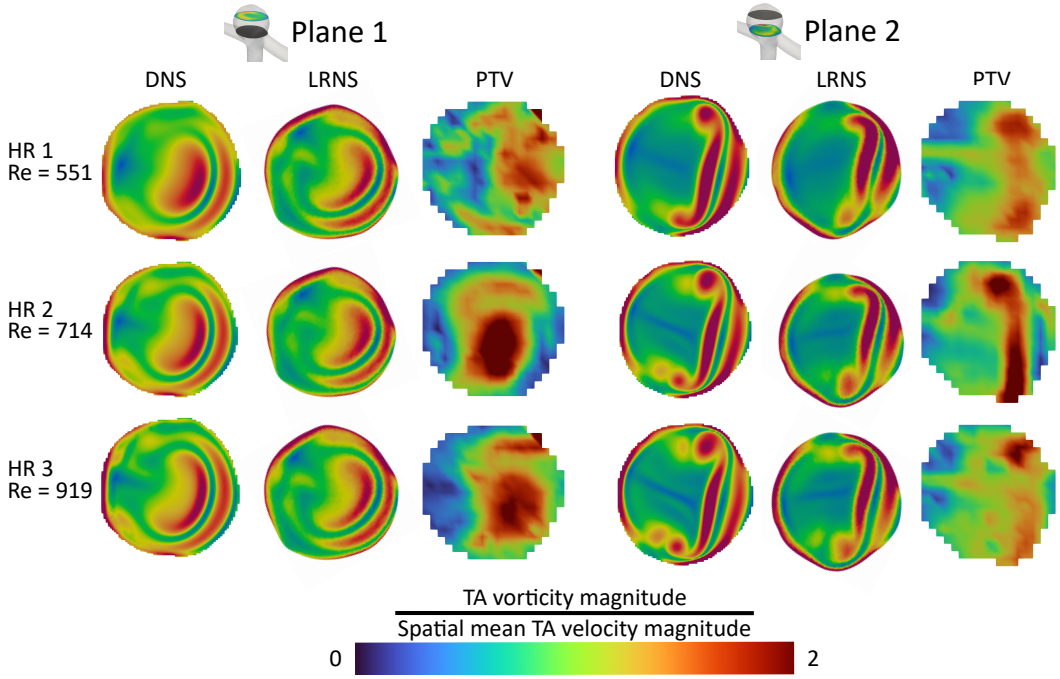


Figure 4.11: Qualitative distribution on plane 1 (left) and plane 2 (right) of the time-averaged (TA) vorticity magnitude normalized by each plane's spatial mean value. DNS - direct numerical simulation; LRNS - low-resolution numerical simulation; PTV - particle tracking velocimetry.

Quantitatively, the TA vorticity is shown in Figure 4.12 visualized again by violin plots. The distribution of vorticity as depicted by the shape of the violins is similar at plane 1 and plane 2 when comparing variation between modalities. The specific mean values are additionally presented in Table 4.7. At plane 1, STB showed the largest distribution, while LRNS showed the lowest for all HRs. DNS results were very close to the STB results, featuring additionally similar mean values of $1\,\mathrm{s}^{-1}$. Voxelization had almost no effect on the DNS data, while the LRNS voxelization showed a strong increase of the resulting vorticity.

Regarding plane 2, the overall vorticity distribution was similar between simulations and experiments. However, the STB results exhibited higher median TA vorticity compared to DNS. Voxelization had minimal impact on DNS but broadened the vorticity distribution for LRNS. While the mean vorticity values for STB, DNS, and LRNS were consistent at 1 s across all

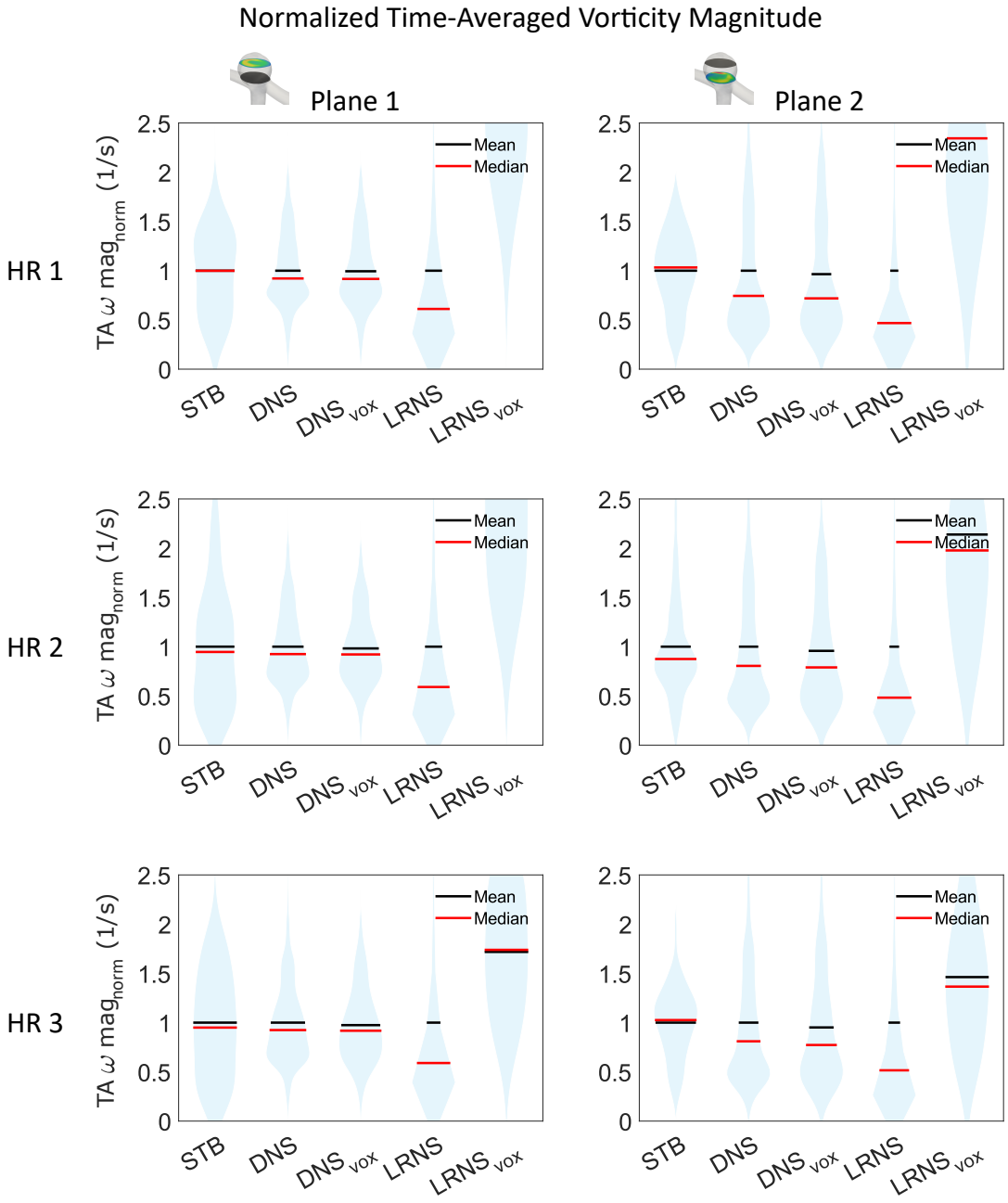


Figure 4.12: Violin plots of time-averaged (TA) vorticity magnitude (ω mag) normalized by each plane's spatial mean value. Violins are shown for each heart rate (HR) 1-3 for the experiments (shake-the-box - STB), direct numerical simulation (DNS), low-resolution numerical simulation (LRNS), whereas the results of the two simulation approaches were further voxelized (vox) to match the STB grid size.

heart rates, voxelization altered these values. For DNS, voxelization slightly reduced the mean vorticity ($\Delta 0.04\,\mathrm{s}^{-1}$ to $0.05\,\mathrm{s}^{-1}$ across HR1–HR3), whereas for LRNS, it led to a notable increase ($\Delta 1.71\,\mathrm{s}^{-1}$ for HR1, $\Delta 1.14\,\mathrm{s}^{-1}$ for HR2, $\Delta 0.46\,\mathrm{s}^{-1}$ for HR3).

This study highlights that DNS provides a closer match to experimental vorticity distributions compared to LRNS, which showed substantial limitations in capturing critical vortical structures, particularly in high-intensity flow regions. These findings align with previous work by Abdelsamie et al. [6], who also noted LRNS's inability to resolve detailed vortex features. The inability of LRNS to accurately represent intra-aneurysmal flow is likely due to its spatial

Table 4.7: Mean normalized time-averaged (TA) vorticity magnitude (ω) values at planes 1 and 2.

	Mean TA ω (Plane 1)			Mean TA ω (Plane 2)		
	HR 1	HR 2	HR 3	HR 1	HR 2	HR 3
STB	0.99	1.00	1.00	1.00	1.00	1.00
DNS	1.00	1.00	1.00	1.00	1.00	1.00
DNS voxelized	0.99	0.98	0.97	0.96	0.95	0.95
LRNS	1.00	1.00	1.00	1.00	1.00	1.00
LRNS voxelized	3.24	2.62	1.71	2.71	2.14	1.46

and temporal resolution constraints, which restrict its ability to capture turbulent-like instabilities that may be present in the aneurysm, as suggested by the experimental data [48].

Voxelization was applied to normalize spatial resolution and assess whether it could enhance the agreement between numerical and experimental results. While voxelization improved LRNS's alignment with experimental distributions, it also introduced overestimation and flattened velocity distributions, failing to meet its intended purpose. In contrast, DNS retained its ability to accurately represent experimental flow behavior even after voxelization, underscoring its robustness. These findings suggest that DNS is better suited for replicating complex experimental flow phenomena, even when analyzed at coarser resolutions.

4.7.2 Occurrence of high-frequency fluctuations under rest and exercise conditions

Following the validation of the resulting hemodynamics, the occurrence of high-frequency fluctuations is considered in this section. Firstly, the impact of the chosen solver on the ability to capture these fluctuations is evaluated. Secondly, the occurring flow dynamics, especially regarding the occurrence of high-frequency fluctuations under exercise conditions are analyzed.

Capability of the numerical solver to capture the intra-aneurysmal flow behavior

Figure 4.13 on the top presents comparisons between DNS and LRNS velocity probes, focusing on the RMS velocity at selected locations within the aneurysm dome as shown on the top. The analysis begins with a loop along the aneurysm wall, tracing the trajectory of the primary inflow jet. DNS exhibited slightly lower RMS values than LRNS in the first half of the dome but slightly higher values in the second half, with the largest differences reaching $\Delta 0.04\,\mathrm{m\,s^{-1}}$ for HR1 and HR2, and $\Delta 0.05\,\mathrm{m\,s^{-1}}$ for HR3. Within the aneurysmal dome, similar variations were observed, with RMS differences of $\Delta 0.03\,\mathrm{m\,s^{-1}}$ for HR1, decreasing as heart rate increased ($\Delta 0.06\,\mathrm{m\,s^{-1}}$ for HR3).

At the mid of the dome, and the left and right bifurcations, larger discrepancies between DNS and LRNS were evident, with maximum differences of $\Delta 0.08\,\mathrm{m\,s^{-1}}$ for HR1 and $\Delta 0.09\,\mathrm{m\,s^{-1}}$ for HR2 and HR3. Comparatively, DNS exhibited lower RMS values at the left bifurcation and higher values at the right bifurcation relative to LRNS. Probe-wise comparisons indicated that LRNS consistently predicted higher velocities in the mid-aneurysm regions compared to DNS. Furthermore, noticeable differences in flow behavior between the left and right outflows were observed, with LRNS producing greater asymmetry than DNS. The velocity RMS at the inlet of the IA were similar across the modalities. Comparing these results to those at probes inside the aneurysm and outgoing vessels showed that discrepancies only occurred in the critical region of the IA.

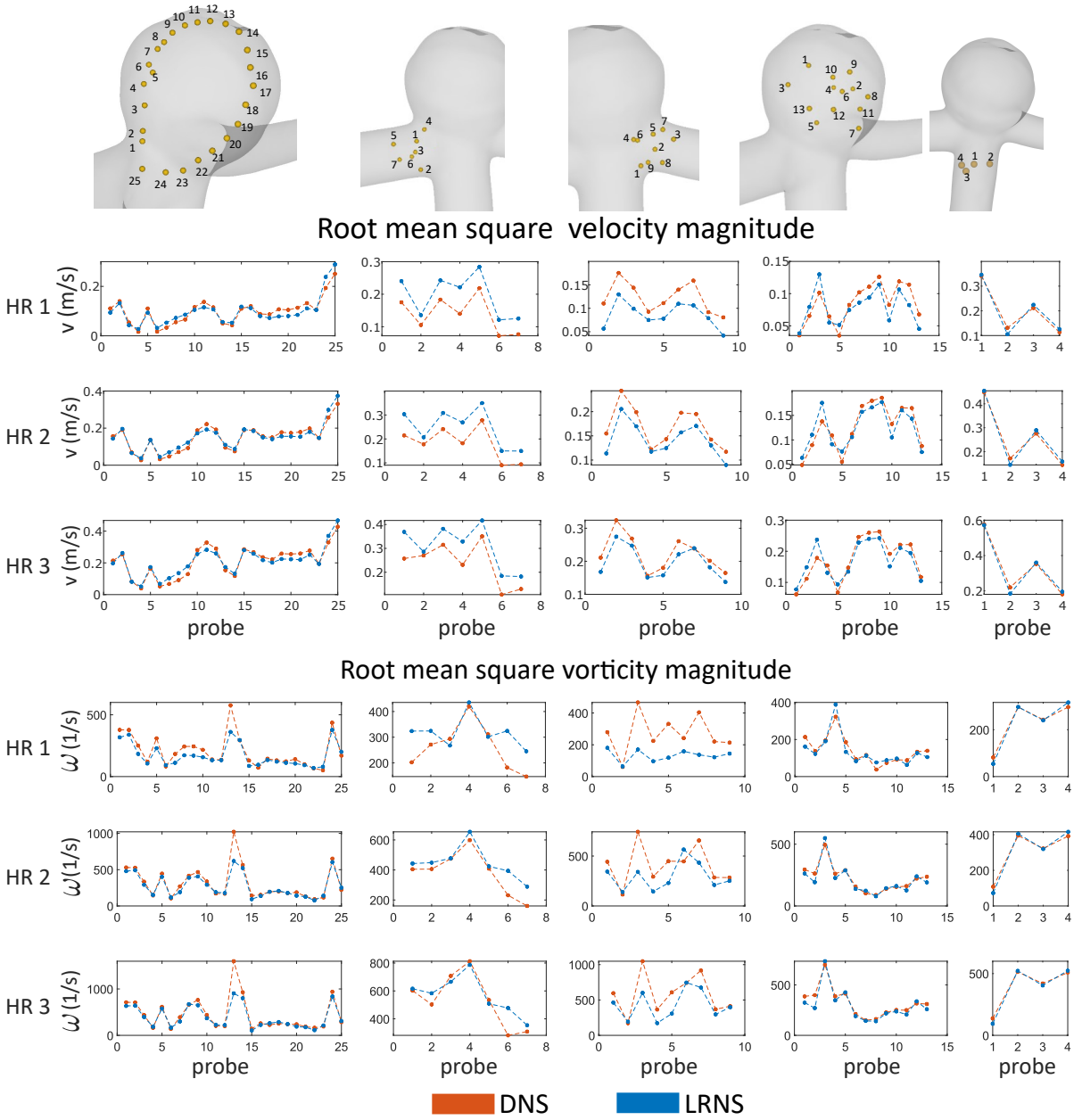


Figure 4.13: Root mean square (RMS) of the velocity magnitude (v) and vorticity magnitude (ω) of chosen probes inside the intracranial aneurysm model. The RMS are shown for the two numerical solvers (direct numerical simulation - DNS; low-resolution numerical simulation (LRNS)) over the three heart rates (HR) 1-3. The probes are separated by location, depicting a loop around the aneurysm dome, the middle of the dome, the bifurcation area (left and right) and the inlet area.

While the overall velocity profiles between DNS and LRNS showed reasonable agreement, substantial differences were apparent in vorticity predictions. LRNS provided an unrealistic depiction of vorticity, failing to accurately capture the complex flow dynamics within the aneurysm, as corroborated by qualitative and distribution analyses (Figure 4.11). These findings are consistent with previous studies. For instance, Jain et al. observed fluctuations in intracranial aneurysm flow using high-resolution CFD methods, which were not captured by LRNS [130]. Similarly, Huang et al. used the lattice Boltzmann method to detect transitions in aneurysmal flow dynamics, further underscoring the limitations of low-resolution approaches [124]. In this thesis, the numerical simulations were also validated against PTV under varying heart rate con-

ditions. The observed discrepancies between DNS and LRNS suggest that low-resolution CFD methods, such as LRNS, are insufficient for detecting high-frequency fluctuations in aneurysmal flow. The use of a laminar solver in LRNS was essential for consistency with conventional intracranial aneurysm modeling practices and for comparability with existing literature.

As within DNS, no turbulence model is employed, any fluctuations are purely a result of intrinsic flow dynamics. Despite the absence of a turbulence model, high-frequency fluctuations naturally emerged in DNS, highlighting the unsteady and complex nature of the flow within the aneurysm. These results emphasize the superior ability of DNS to capture intricate flow phenomena compared to LRNS, particularly in regions where vorticity and unsteady flow dynamics are critical.

Impact of heart rate on flow dynamics

To further investigate the occurrence of high-frequency fluctuations in IAs, in-depth analysis of numerical intra-aneurysmal flow behavior was carried out. In this regard, six probes were strategically placed within the aneurysm to investigate the transient velocity and vorticity magnitude, as well as the power spectral density (PSD) at key regions, including near-wall areas, the aneurysm ostium, and bifurcations. These probes provided detailed insights into the flow behavior across all three heart rates. In Figure 4.14 the transient velocity, in Figure 4.15 the transient vorticity and in Figure 4.16 the PSD at the chosen probes are plotted comparing the results of DNS and LRNS.

At near-wall probes (probes 1 and 5) LRNS overestimated peak velocity, particularly during systole, a phenomenon not observed in DNS. While LRNS vorticity values were comparable to DNS at HR1, differences grew with increasing HR, resulting in higher LRNS peak values for both velocity and vorticity. At probe 5, LRNS showed higher peak velocities during systole compared to DNS. At probes in the aneurysm center (probes 3 and 6) velocity and vorticity curves exhibited similarities between DNS and LRNS. This pattern was consistent across all heart rates. At probes in bifurcation areas (probes 2 and 4) DNS recorded lower peak velocity values compared to LRNS, while vorticity curves remained within a similar range across all HRs. DNS produced higher peak velocities than LRNS. Differences reduced at probes 2 and 4 with increasing HR, although probe 4 revealed discrepancies in vorticity curves despite similar velocity profiles.

The PSD analysis as shown in Figure 4.16 quantified energy distribution across different frequency ranges, revealing critical differences between DNS and LRNS. At HR1, DNS captured higher energy levels in the high-frequency dissipation range, while LRNS exhibited higher energy in the energy-containing range. At HR2, PSD slopes showed similar trends between DNS and LRNS, but DNS consistently captured greater energy dissipation. At HR3, DNS demonstrated crucially higher energy levels across all three frequency cascades: the energy-containing range, the inertial subrange, and the dissipation range. The largest discrepancies between DNS and LRNS were observed in the inertial and dissipation ranges, particularly at mid-aneurysm and bifurcation probes (probes 2, 4, and 6).Flow disturbances quantified with the PSD became more pronounced with increasing heart rates. At HR1, no significant disturbances were observed, while HR2 revealed minor disturbances at probe 2 during late systole. At HR3, disturbances were detected across all probes, particularly during late systole. Notably, bifurcation probes exhibited changes in declining velocity values with increasing heart rates, whereas mid-aneurysm probes showed overshooting peak velocities at higher heart rates.

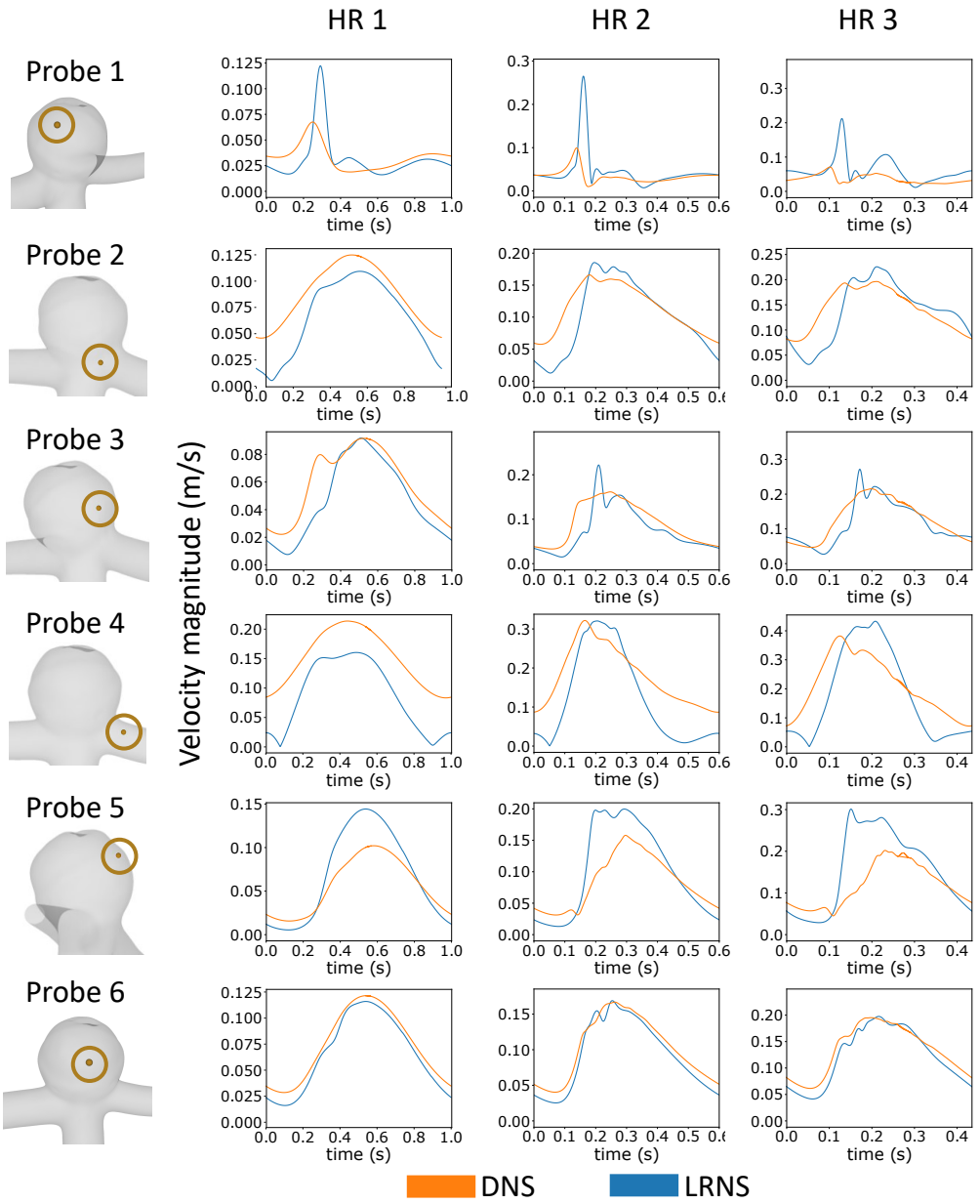


Figure 4.14: Transient velocity magnitude over one cardiac cycle of six chosen probes for the two numerical solvers direct numerical simulation (DNS) and low-resolution numerical simulation (LRNS).

Higher heart rates were associated with increased inflow peak velocities, stronger jets, and enhanced vorticity within the aneurysm. At HR3, DNS revealed high-frequency fluctuations in flow behavior, as confirmed by the PSD analysis. These findings were consistent with studies by Ford et al. [83] and Khanafer et al. [144]. They reported higher Reynolds numbers and more complex vortex structures at elevated heart rates. While IAs are traditionally regarded as laminar flow environments, DNS revealed naturally occurring high-frequency fluctuations, corroborating findings by Valen-Sendstad et al. [299, 296, 162]. These fluctuations occurred without the application of turbulence models, indicating intrinsic flow instabilities. Prior studies have emphasized the prevalence of such instabilities, particularly in bifurcation aneurysms [162, 124, 83], which were also confirmed in this study.DNS thus proves essential for capturing high-frequency fluctuations and resolving intricate flow dynamics in IAs under high heart rate conditions.

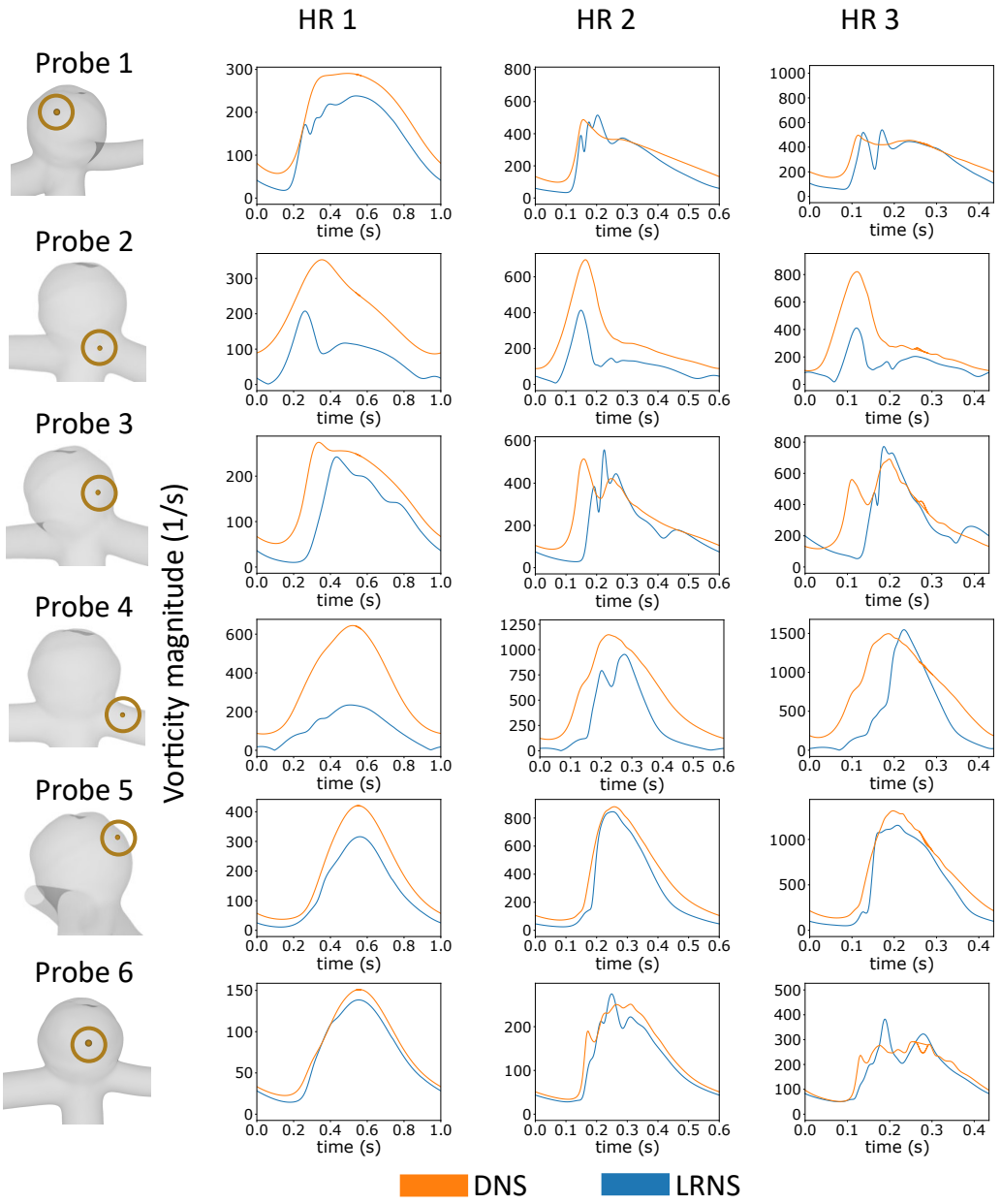


Figure 4.15: Transient vorticity magnitude of chosen probes for the two numerical solvers direct numerical simulation (DNS) and low-resolution numerical simulation (LRNS).

In contrast, LRNS raised concerns about artificially elevated PSD values at HR1, suggesting potential inaccuracies or "fake turbulences" that do not represent true flow dynamics. This highlights a fundamental limitation of LRNS in detecting high-frequency fluctuations. Further specialized turbulence quantification like laser Doppler anemometry would be necessary to quantity the occuring turbulence wihtin the experiments in detail [109]. However, validation through PTV already demonstrated that only high-fidelity DNS could accurately resolve detailed flow structures, particularly when looking at the qualitative vorticity distribution. These results solidify DNS as the more reliable approach for capturing the complex dynamics of IAs, particularly under high heart rate conditions.

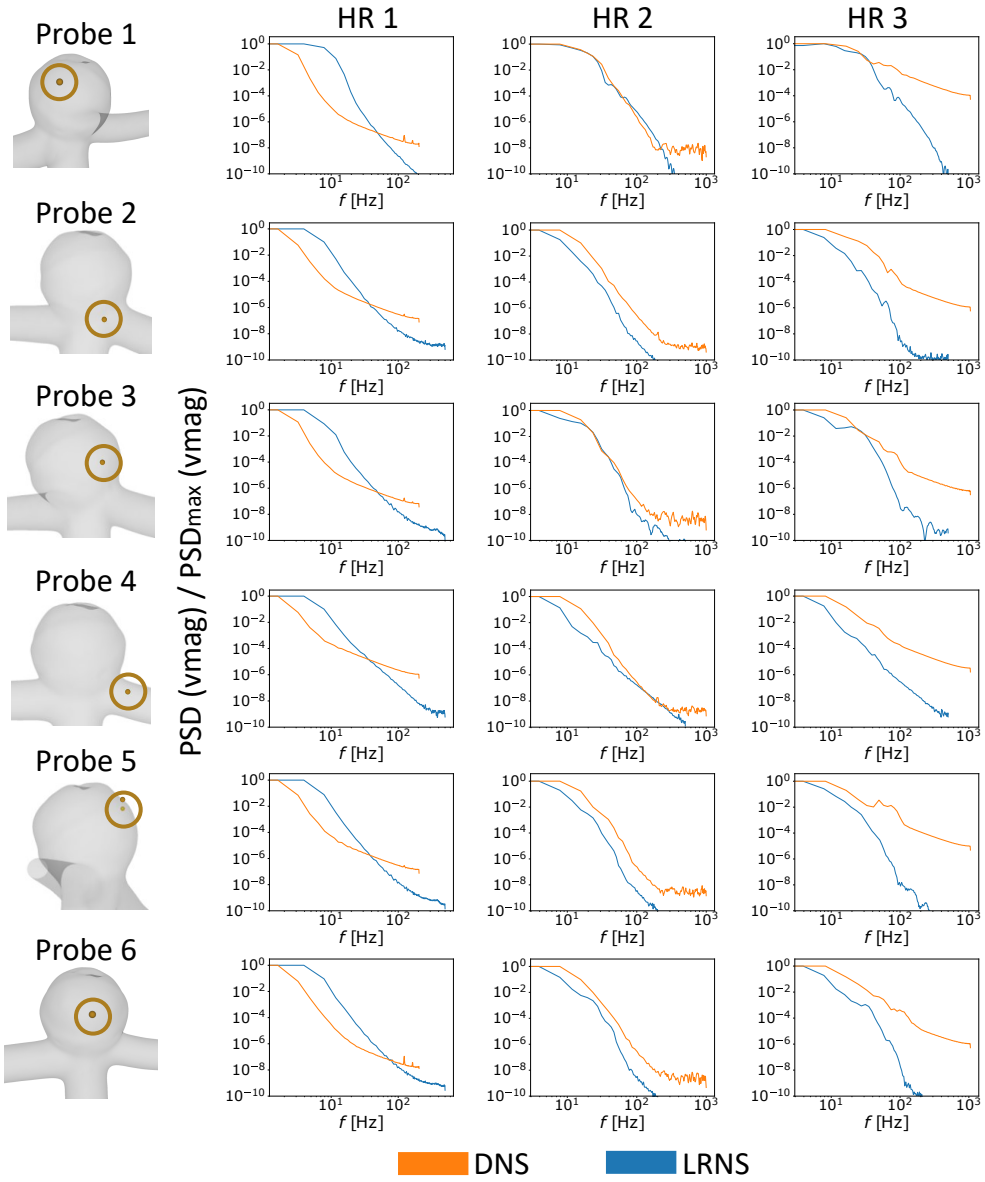


Figure 4.16: Power spectral density (PDS) of chosen probes for the two numerical solvers direct numerical simulation (DNS) and low-resolution numerical simulation (LRNS).

4.7.3 Limitations

DNS provided the most comprehensive insights into intra-aneurysmal flow structures, capturing essential flow dynamics and serving as a reliable reference in the absence of experimental validation. However, the computational demands of DNS remain a significant limitation, requiring extensive effort for model preparation, simulation runtimes, and high-performance computing resources. These demands highlight the need to justify DNS implementation in clinical practice, where detecting high-frequency fluctuations must be critically prioritized. Despite this challenge, DNS can serve as a foundational dataset for developing AI-based models, which could bridge the gap between high-fidelity simulations and clinical applications [13]. Currently, LRNS remains a more practical option for analyzing temporally averaged flow quantities due to its accessibility and lower computational costs.

Moreover, only one aneurysm geometry was analyzed in this study. While it provided detailed insights, generalizing the findings requires analysis of additional cases to establish statistical sig-

nificance. Despite this, the inclusion of three different modalities (DNS, LRNS, and experimental approaches) across three heart rates resulted in nine unique variations, each necessitating significant computational and experimental effort. Differences in inflow conditions posed a limitation, as the experimental phantom model had a curved inlet, whereas the simulations assumed a straight inlet. This discrepancy arose due to constraints in the experimental setup and the DNS mesh generation process. However, normalization of flow parameters minimized the impact of these differences, ensuring consistency in the comparisons.

The aneurysm model and flow conditions were not fully patient-specific. Modifications were made to the geometry for experimental feasibility, and the use of a blood-mimicking fluid was necessary due to the lack of in vivo data and the requirements of the experimental pump system. Despite these constraints, the geometric and inflow conditions were maintained as patient-specific as possible. Blood was modeled as Newtonian fluid, which was shown to not affect hemodynamic outcomes significantly [176, 200]. Additionally, high-frequency fluctuations could not be fully resolved in the LRNS simulations due to the use of a laminar solver. This choice aligned with standard practices in IA hemodynamic assessments and avoided artificially induced fluctuations from turbulence models. However, this limitation restricted LRNS's ability to capture the unsteady flow dynamics detected by DNS.

4.8 Conclusion

In this chapter the hemodynamic effects of rest and exercise conditions on two vascular pathologies, namely the MI and IA, were investigated. For MI, the focus was set on how exercise worsens retrograde blood flow severity, influencing left ventricular dynamics. For IAs, the role of high-frequency velocity fluctuations, which are amplified by elevated heart rates during exercise, was examined in relation to aneurysm destabilization and rupture risk. Using patient-specific hemodynamic simulations and high-resolution computational techniques, this chapter aimed to enhance understanding of these conditions and to address gaps in current methodologies for assessing exercise-induced hemodynamic changes. Ultrasound-based patient-specific ventricular wall motion was incorporated into simulations of MI to calculate hemodynamic parameters with high precision. In case of IAs, high-resolution and low-resolution finite volume solving approaches with rigid walls were considered. The exercise condition was implemented by patient-specific left ventricular ultrasound scans during handgrip exercise within the MI and by applying elevating heart rates within the IA investigation.

The findings within the cardiac simulations demonstrated significant differences in maximum systolic KE between rest and exercise conditions. Additionally, differences were observed between patients with MI stage I and those with higher MI stages (II or III) in mean velocity and maximum diastolic KE, respectively. Analysis of KE curves over the cardiac cycle indicated that energy dynamics depend on patient-specific ventricular volume changes, emphasizing the critical importance of accurate segmentation of ventricular wall motion for reliable hemodynamic assessment. This analysis furthermore demonstrated the feasibility of the proposed workflow, which can be applied to larger patient cohorts for further investigation.

In case of neurovascular analyses, this study demonstrates that high-frequency fluctuations in IAs are detectable with DNS and become more pronounced at higher heart rates. The analysis showed that both DNS and LRNS produced qualitatively similar velocity fields and aligned reasonably well with experimental data. However, LRNS fell failed to capture complex vorticity structures and high-frequency fluctuations, which are critical for understanding IA hemodynamics. The results emphasize the importance of high-resolution numerical approaches, such as DNS, for accurately resolving the intricate flow dynamics within aneurysms. These advanced

techniques are vital for reliable assessment of aneurysm behavior and have the potential to improve clinical decision-making regarding rupture risk prediction. While the computational demands of DNS remain a barrier to routine clinical use, its ability to provide detailed reference datasets highlights its value in optimizing the development of AI-driven models and enhancing future hemodynamic evaluations.

Research questions

A. Does exercise condition significantly affect the cardiovascular hemodynamics when mitral valve insufficiency is present?

   ⇒ Maximum systolic kinetic energy showed a significant reduction from rest to exercise condition comparing all considered patients. Velocity and maximum diastolic kinetic energy were significantly reduced in patients with MI II or MI III compared to those with MI I.

B. Can high-frequency fluctuations occur in neurovascular vessels under rest and exercise, providing insights into pathological conditions?

   ⇒ Under exercise conditions, high-frequency fluctuations occur, which can only be accurately captured using high-resolution numerical approaches such as DNS. These fluctuations are associated with disturbed flow and may provide valuable insights into pathological conditions, including IA formation and associated risk factors. Therefore, a detailed analysis of these fluctuations is crucial for identifying hemodynamic markers relevant to disease progression and clinical assessment.

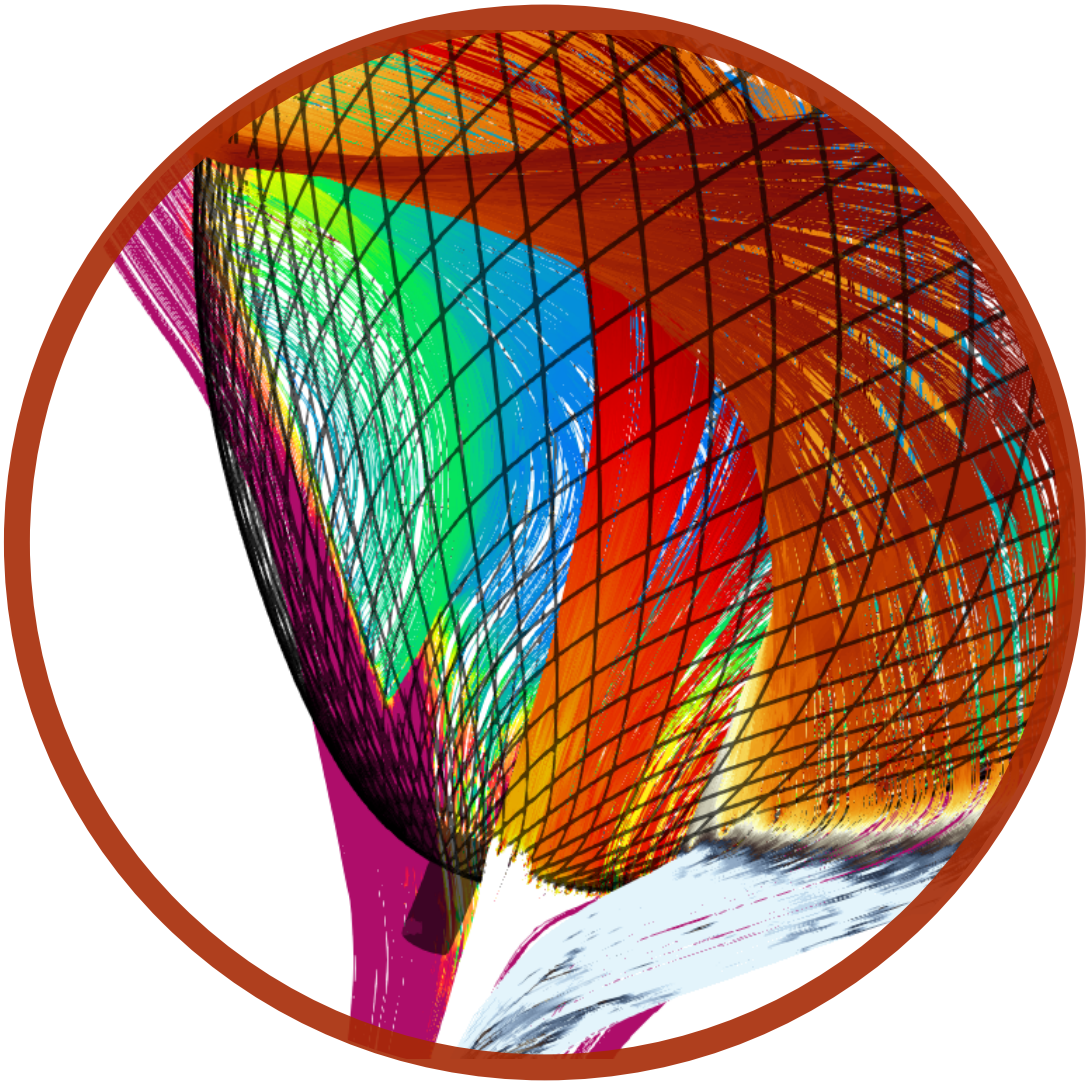
Future directions include refining ventricular segmentation techniques to incorporate valves and achieve more anatomically accurate left ventricular geometries. Comparing ultrasound-derived data with higher-resolution imaging modalities, such as MRI, and incorporating a larger patient cohort, including healthy controls, would enhance the clinical relevance of the findings, as was pre-liminary introduced previously [156]. Validation of computational results using advanced imaging analyses like cardiac MRI, could further improve the accuracy of the method. These advancements would strengthen the utility of the moving mesh method for understanding left ventricular hemodynamics and evaluating therapeutic interventions in MI patients.

In addition to advancements in simulations, further progress in experimental methods is essential. Integrating laser Doppler measurements to capture turbulence within the flow would enable a more detailed investigation of high-frequency fluctuations, especially in neurovascular pathologies. A bigger cohort of aneurysm models should be analyzed in future work to strengthen the findings in this study. Here, fully patient-specific models and models with varying complexity and surrounding parent vessels can be considered. Thus, the clinical applicability of the detection of high-frequency fluctuation in IAs can be driven forward. Furthermore, patient-specific measurements obtained from medical imaging techniques such as PC-MRI can serve as a valuable basis for comparison with numerical simulations, thereby enhancing validation efforts. In the future, in vivo measurements with improved resolution may further contribute to the accuracy and reliability of hemodynamic assessments. At present, PC-MRI enables the comparison of simulation results with measured flow data, though at a low resolution, as will be introduced in Chapter 5. Moreover, as treatment devices have been found to increase oscillatory effects in neurovascular flow [253], the investigation of the occurrence of high-frequency fluctuations can be extended to the analysis of treated vascular pathologies. High-frequency simulation ap-

proaches, as investigated in this chapter, are, however, not yet feasible for integrating treatment options into the simulation framework. Currently, the integration of treatment options into the simulation relies on low-resolution numerical simulations as the gold standard, as will also be specified in the following chapter.

Chapter 5

Part 3: In silico assessment of aneurysmal hemodynamics after deployment of the Contour Neurvascular System

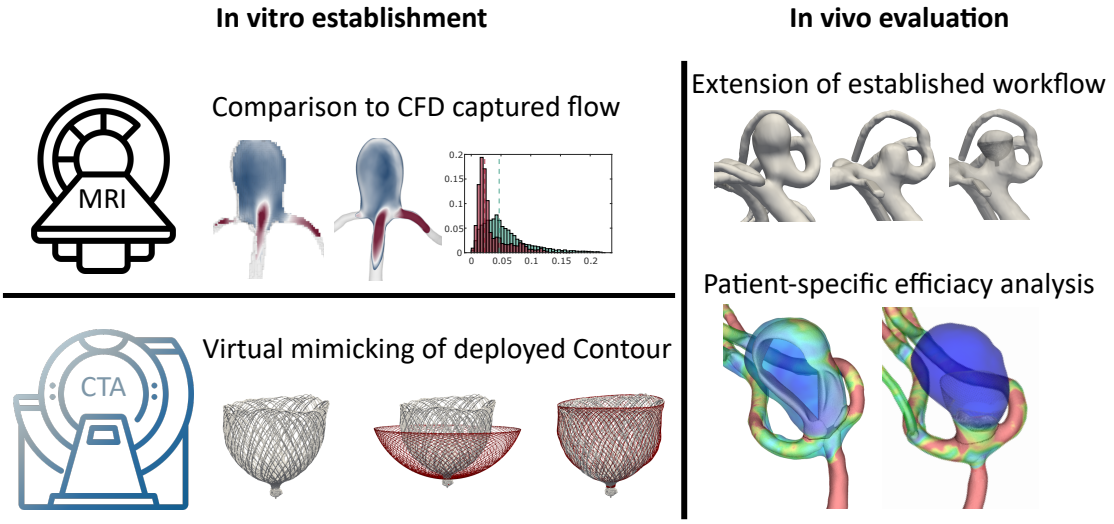


Outline

Different treatment options exist to prevent aneurysm rupture or growth. However, wide-necked bifurcation aneurysms (WNBAs) are still not well suitable for conventional endovascular methods. Therefore, the novel flow disrupter Contour Neurovascular System was recently introduced and requires in-depth analysis of the treatment effect. A detailed review on endovascular treatment of IAs is given, followed by the introduction into the in silico analyses conducted. The latter were based on in vitro analyses for validation and furthermore on in vivo investigations to improve the clinical applicability.

This chapter is partially based on the following publications:
Korte, J., Gaidzik, F., Larsen, N., Schütz, E., Damm, T., Wodarg, F., Hövener, J.-B., Jansen, O., Janiga, G., Pravdivtseva, M. S. & Berg, P. (2024). In Vitro and In Silico Assessment of Flow Modulation after Deploying the Contour Neurovascular System in Intracranial Aneurysm Models. Journal of NeuroInterventional Surgery, 16(8), 815-823.

Graphical abstract



Minimally-invasive endovascular treatment has been developed to become the standard of care for neurovascular pathologies like IAs. However, varying shapes of IAs need subsequently varying treatment devices to best restore the pre-pathological state and prevent IA growth and rupture risk. In this chapter the focus is set on the treatment of wide-necked bifurcation aneurysms, which are favorable for flow disrupting devices due to their shape and location.

A novel flow disrupting device, the Contour Neurovascular System (Contour) has been developed recently and was tested on its efficacy in WNBAs (Stryker, Kalamazoo, MI, USA). This research needs to be extended, especially using numerical analyses by image-based blood flow simulations. In this chapter, first the previous work on the efficacy of the Contour and its comparison to conventional flow disrupting and flow diverting devices is reviewed. In the following, this chapter presents the methodology and results of the in silico investigation of the Contour efficacy based on in vitro and in vivo data.

5.1 A long-term effective device to treat wide-necked bifurcation aneurysms

The Contour, an innovative endovascular device designed to treat specifically WNBAs, is shown in Figure 5.1. Unlike traditional methods, such as coiling or flow-diverter stents, the Contour is a next-generation intrasaccular flow disruptor. It is placed within the aneurysm sac at the level of the neck, where it modifies the blood flow dynamics to enhance thrombosis within the aneurysm sac while preserving the flow through the parent vessel.

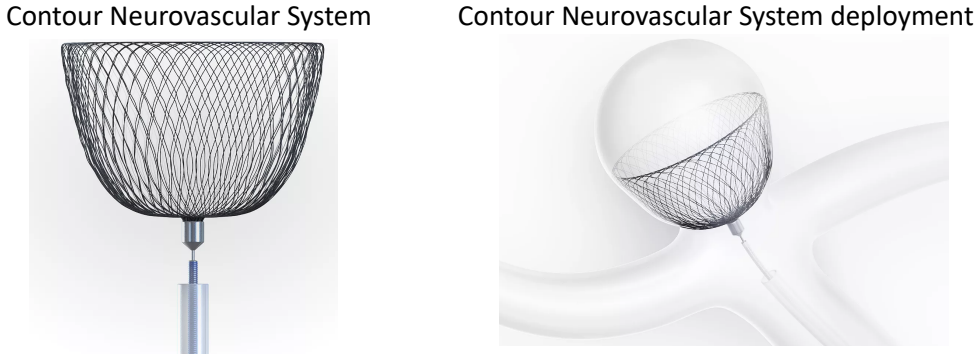


Figure 5.1: Visualization of the Contour Neurovascular System (Contour) pulled out of catether but not fully extracted on the left. The shape memory induces the recovery of the umbrella-like shape. On the right, the Contour is shown during deployment into a wide-necked bifurcation aneurysm. Figure adapted from [65].

The Contour is produced by the manufacturer in five different sizes ranging from 5 mm to 14 mm diameter as presented in Table 5.1. Specific guidelines and suggestions exist in regard of the device choice depending on the aneurysm size. The aneurysm neck diameter and dome width thresholds for the specific device size are shown as well in Table 5.1. Each threshold is separated with a difference of Δ 1 mm neck size and Δ 1.5 mm dome width. If a case happens to be at borderline, the bigger Contour size is usually chosen. All Contour sizes are considered in this thesis depending on the aneurysm size as suggested. However, this choice is in the end determined by the operating neurointerventionalist.

Table 5.1: Contour size deployment guideline.

Contour diameter (mm)	Aneurysm neck (mm)	Aneurysm width (mm)
5	2.0 - 3.0	2.0 - 3.5
7	3.0 - 5.0	3.0 - 5.5
9	4.0 - 6.0	5.0 - 7.5
11	5.0 - 8.0	7.0 - 8.5
14	7.0 - 10.0	8.0 - 10.5

Several studies focusing on the in vivo analysis of the Contour performance showed its efficacy and safety when treating unruptured WNBAs as summarized in Table 5.2. Bhogal et al. investigated three patients and included a three-months follow up (FU) [31]. They found an occlusion of more than 66 % for all cases. In the FU, one Contour was found to be displaced into the aneurysm dome. Mostafa et al. considered in vivo data of eight wide-necked basilar tip IAs in their study, including a FU of sixth months after implantation [203]. The in vivo analysis showed promising results with six of the aneurysms being fully occluded after six months, one after 24 months. One aneurysm needed reintervention after six months. Akhunbay-Fudge et al. found an occlusion rate of 55 % in eleven patients treated with Contour in one year [8].

Biondi et al. were able to consider a study cohort of 53 patients and took the rate of successfully implanted Contours into account [33]. In their study, 90 % were implanted with success of which 31 % showed an immediate occlusion, 62 % after one day, and 81 % after 3 months. 90 % were fully occluded after one year. Liebig et al. featured a successful implantation rate of more than 94 % within 34 patients and found successful occlusion of 44 % after 6 months and of 69 % after 12 months [174]. Griessenauer et al. performed in 2024 the largest multicenter study with an inclusion of 279 aneurysm cases [105]. They found that the most deployed Contour sizes were the 7 mm (39 %) and 9 mm (25 %) versions and the IAs treated were mostly located at the MCA (26.5 %) or ACA (26.2 %). In more than 91 % of the aneurysm an occlusion of Raymond-Ray scale 1 or 2 was achieved within one year.

Gallo-Pineda et al. included 25 IAs in their in vivo analysis finding an occlusion rate of 65.5 % within one year [79]. Their analysis revealed a displacement of the device in five cases in the FU analysis, which was found to affect the patient's health (4 % of their patients). The authors suggested that device displacement especially during intervention can be overcome with further training of the neuroradiologist before implementation. The effect of the displacement can additionally be addressed by carrying out in silico analyses of varying Contour positionings. In this regard, Bellanger et al. found in a one and a half year FU of one Contour case that the device was displaced into the aneurysm dome [21]. Dange et al., however, conducted a 3-months FU and found a stable placement of the Contour. They further investigated the demographics and characteristics of the aneurysms and patients [68]. The 13 ruptured IAs, which were treated in their study, showed a positive treatment effect of the Contour. Radomi et al. investigated the positive in vivo outcome of treating IAs with the Contour, which confirmed the findings mentioned [242].

Moreover, the Contour has been used to treat acutely ruptured IAs both as a stand-alone device and in combination with coils [51, 69, 315, 72]. For instance, Cavasin et al. reported a successful case in which a patient was treated using a combination of Contour and coiling, demonstrating the feasibility of this approach [51]. Similarly, Diana et al. conducted a retrospective analysis of 15 patients, where the Contour was successfully deployed in 13 cases, achieving an occlusion rate of 84 %, further emphasizing its potential in clinical practice [72]. Additionally, Wodarg et al. concluded that using the Contour with adjunctive coiling is a safe and technically feasible method for managing ruptured aneurysms, supporting its role as a viable treatment option [315].

Table 5.2: In vivo analyses conducted to assess the performance of the Contour Neurovascular System. For each study the count of included patients, the highest occlusion rate at last follow up in months (m) and complications that occurred are listed.

Study	Year	Cases	Occlusion rate (Follow up)	Complications
Akhunbay-Fudge et al. [8]	2020	11	55 % (12m)	-
Bhogal et al. [31]	2021	3	≥66 % (3m)	Displacement of 1 case
Biondi et al. [33]	2023	53	90 % (12m)	10 % no successful implant
Dange et al. [68]	2022	13	92 % (3m)	-
Gallo-Pineda et al. [79]	2024	25	65.5 % (12m)	Displacement of 5 cases
Griessenauer et al. [105]	2024	279	91 % (12m)	-
Liebig et al. [174]	2022	34	69 % (12m)	6 % no successful implant
Mostafa et al. [203]	2023	8	87.5 % (24m)	Reintervention of 1 case (6m)
Radomi et al. [242]	2024	76	57.1 % (12m)	10.5 % no successful implant

A systematic review by Ghozy et al. analyzed six studies [174, 8, 31, 33, 315, 72], encompassing 131 intracranial aneurysms (IAs) treated with Contour alone or in combination with coils, and reported a pooled adequate occlusion rate of 84 % [96]. Despite these promising outcomes, clinical experience with the Contour remains limited. Most of the studies included in the review were retrospective in nature, relying on follow-up data derived from angiographic imaging (X-ray-based) and clinical neurological assessments. Notably, only one study incorporated MRI-based follow-ups, which highlighted crucial metal-induced artifacts from the implant [8]. Jagtiani et al. focused on the review of patient-specific in vivo data, analyzing outcomes of Contour deployment and its effectiveness in real-world clinical scenarios [129]. Complementing this, Günkan et al. conducted a comprehensive meta-analysis that synthesized current data on the safety and performance of the Contour within the CoW, offering a broader perspective on its clinical utility [108].

The efficacy of the Contour device was also investigated through experimental in vitro analysis. In an earlier investigation, washout time for an angiographic contrast agent observed through DSA was used as an indirect metric for evaluating the Contour's efficacy [185]. This approach, however, was constrained by its reliance on two-dimensional flow analysis. Pravdivtseva et al. further explored the influence of device size on occlusion performance, demonstrating superior occlusion rates when smaller Contours (e.g., 5 mm) were deployed compared to larger variants (11 mm and 14 mm) [237]. These experiments employed 3D-printed aneurysm models, and occlusion was assessed in vitro using PC-MRI. While this methodology offers the advantage of controlled experimental conditions, it is also subject to limitations, including imaging artifacts induced by the device and the inability to evaluate blood flow proximal to the Contour [255].

The positive outcome in these studies was primarily based on medical images, however, no in-depth numerical analysis of the treatment effect on hemodynamics was performed based on in vivo data. Moreover, the Contour is primarily designed to disrupt and redirect blood flow within the aneurysm sac. However, to date, the precise flow modulation induced by the Contour has not been directly quantified. Numerical image-based blood flow simulations play a crucial role in understanding the detailed interaction between the device and the surrounding blood flow, providing insights into flow reduction, wall shear stress distribution, and neck coverage efficacy. These analyses are critical for predicting long-term outcomes, and improving deployment strategies, which are particularly important when considering the complex nature of aneurysmal hemodynamics. Integrating numerical simulations with clinical data would enhance the evaluation of the Contour's performance and further validate its role in neurovascular interventions.

5.2 Efficacy of the Contour Neurovascular System compared to other treatment devices

As mentioned beforehand, several endovascular treatment devices exist for IAs, which are chosen depending on the aneurysm size, shape and location and the underlying assumed rupture risk. However, the border of which device to choose is not always clear and the advantages and disadvantages have to be considered and balanced. Thus, in this section, the comparison of the Contour to remaining devices, namely flow diverting and flow disrupting devices is conducted to point out these (dis-)advantages.

Flow diverters

FDS are endovascular devices designed to treat IAs, particularly large, wide-necked, or fusiform aneurysms that are difficult to manage with traditional coiling or surgical clipping. Unlike conventional methods that aim to directly fill or exclude the aneurysm sac, flow diverters work by altering blood flow dynamics at the aneurysm site to promote natural healing and remodeling of the parent artery. A representative FDS is shown in Figure 5.2 extracted from the catheder (left) and during deployment into an IA (right).

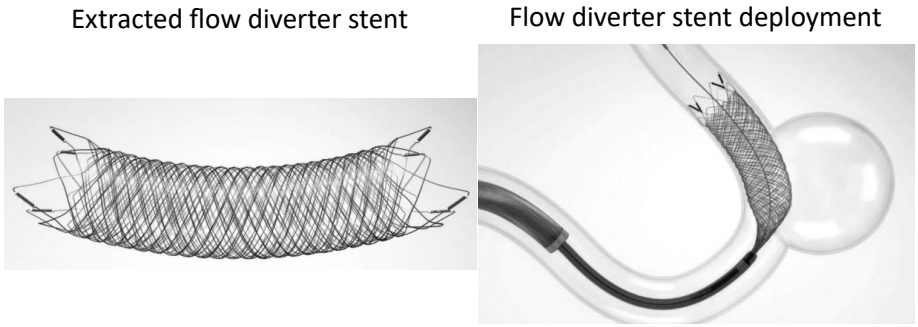


Figure 5.2: Visualization of the conventional FDS extracted and during deployment in an IA with a catheder. Figure adapted from [219].

Endovascular therapies, such as the placement of FDS, are well-established for reducing rupture risk in SIAs by modulating blood flow into the aneurysm [231]. The therapeutic goal is to achieve intra-aneurysmal flow stagnation, facilitating thrombus formation that ultimately leads to aneurysm occlusion. Additionally, the WSS along the treated vessel's scaffolding is restored to levels observed in the parent vessel before aneurysmal formation [145]. Clinically, experiences with application of FDS have been extensively reported in the past [228]. An overview of five representative studies (chosen due to their high case count) analyzing the FDS performance in vivo is given in Table 5.3.

Table 5.3: In vivo analyses conducted to assess the performance of the flow diverter stents. For each study the count of included cases, the highest occlusion rate at last follow up in months (m) and complications that occurred are listed.

Study	Year	Cases	Occlusion rate (Follow up)	Complications
Byrne et al. [46]	2010	70	49 % (4m)	4 % morbidity, 8 % mortality
Kulcsar et al. [164]	2010	12	58 % (3m)	1 BA occlusion, 25 % neurological events
Lubicz et al. [179]	2010	34	69 % (6m)	15 % morbidity, 4 % mortality, 33 % parent artery stenosis
Maimon et al. [186]	2021	32	83.3 % ()	17.8 % clinical complications
Wagner et al. [307]	2012	26	68 % (6m)	5 % morbidity, 5 % mortality

Byrne et al. proposed a multicenter study of 70 patients treated over eight months [46]. Silk FDS were deployed alone in most cases (81 %) or with coils. Early results showed a 4 % permanent morbidity and 8 % mortality, with complications including deployment challenges, parent artery thrombosis (11 %), and delayed symptom worsening. The study highlights the need for careful patient selection to optimize safety and efficacy. In a prospective study of 29 patients with 34 fusiform or wide-necked unruptured aneurysms by Lubicz et al., Silk stent placement alone was successful in 90 % of cases [179]. However, the technique showed a high delayed complication rate, with 4 % mortality and 15 % morbidity. Complications included delayed aneurysm rupture, thromboembolic events, and mass effect symptoms. Angiographic follow-up at six months revealed a 69 % complete occlusion rate but significant parent artery stenosis in 33 % of cases. While effective in some cases, the high complication rate suggests this technique should be reserved for selected patients.

Kulcsar et al. evaluated 12 patients with basilar artery aneurysms also treated with the Silk FDS in a retrospective study [164]. The FDS successfully covered critical vessels, including the basilar bifurcation and origins of major cerebral arteries. While the procedure was generally well-tolerated, complications included one acute basilar artery occlusion and three symptomatic neurological events during a mean follow-up of 16 weeks. These findings suggest that FD implantation in the basilar artery is feasible but should be reserved for otherwise untreatable aneurysms due to the risk of late ischemic events in perforating arteries.

In addition to the purely clinical assessment, FDS were investigated using in silico modeling based on medical imaging and fast virtual stenting tools [134, 317]. Advances in computational modeling provide significant opportunities for understanding hemodynamic behavior and predicting treatment outcomes. Image-based blood flow simulations using CFD and virtual treatment approaches offer non-invasive means to model both the hemodynamic alterations and the therapeutic effects without imposing additional procedures or discomfort on patients [138].

For example, Ouared et al. investigated the hemodynamic effects of FDS in treating twelve patient-specific sidewall IAs using CFD over a 12-month follow-up [223]. Virtual stent placement demonstrated that a significant reduction in intra-aneurysmal velocity ($\geq$35 %) was necessary for successful aneurysm occlusion. The findings highlighted that reducing intra-aneurysmal velocity is critical for effective FDS treatment outcomes. Lyu et al. compared the effect of treating a WNBA with Contour or FDS using virtual deployment and in silico analysis [181]. The Contour provides the advantage of not occluding side branches located close to the aneurysm neck. With an additionally higher and faster occlusion of the aneurysm, the results showed that Contour is superior over FDS especially for WNBAs.

Flow disrupters

Flow disruption is an endovascular approach used to treat IAs by disrupting the blood flow entering the aneurysm, promoting thrombosis inside the aneurysm dome while preserving normal blood flow in the parent artery. By reducing the stress on the aneurysm walls and isolating the sac from circulation, flow disruption can prevent rupture and aid aneurysm healing. Unlike traditional FDS, flow disrupting devices are specifically designed to block the IA neck while maintaining arterial patency. Next to the Contour, the WEB device was designed as a rather novel flow disrupting device. The WEB features a cylindrical shape as shown in Figure 5.3

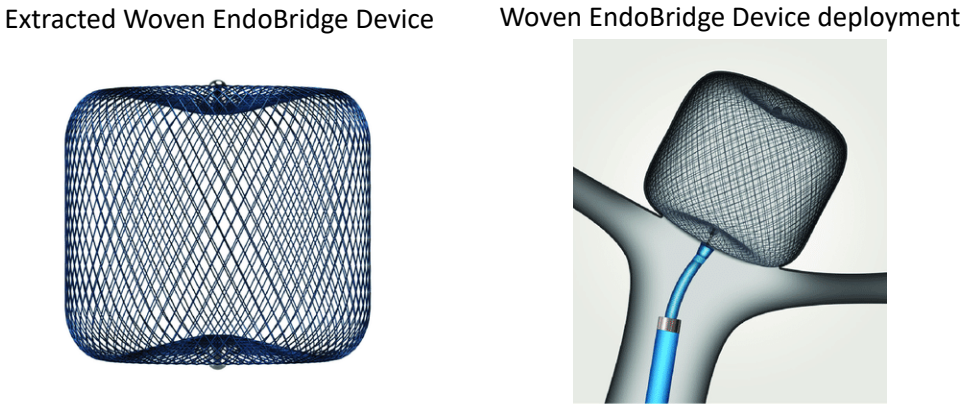


Figure 5.3: Visualization of the WEB device extracted and during deployment in an IA with a catheder. Figure adapted from [74].

Pierot et al. performed a 5-year follow-up analysis of 95 WNBAs treated with the WEB and confirmed its safety, with no device-related adverse events reported [230]. Complete occlusion was achieved in 51.6 % of aneurysms, neck remnants in 26.3 %, and aneurysm remnants in 22.1 %. Adequate occlusion was observed in 77.9 % of cases, with a low retreatment rate of 11.6 %. These results highlight the stability and efficacy of the WEB device over the long term.

Fujimoto et al. studied the occlusion rate in 41 WNBAs treated with the WEB [88]. The long-term outcome in their study showed that 78.8 % of all aneurysms featured full occlusion after 15.3 months, revealing the crucial durability of aneurysm occlusion through WEB. Cortese et al. analyzed a single-center database with 215 IAs as treated with the WEB, which demonstrated a 79.5 % rate of adequate aneurysm occlusion and a 62.8 % rate of complete occlusion over an 18-month follow-up [66]. Aneurysm height, irregular shape, and WEB shape modification were associated with increased recurrence, while a higher WEB oversizing ratio significantly improved occlusion outcomes. Their findings highlight the importance of device sizing and aneurysm morphology in optimizing WEB treatment success.

Due to the similar disruptive behavior of the Contour and WEB device, several studies have been carried out in the recent years to evaluate both devices on a comparable basis. Hecker et al. analyzed prospective clinical data treated with the Contour or WEB device comparatively [113]. The in vivo analyses showed, that the Contour achieved higher occlusion rates than the WEB which was significantly proven. Moreover, the Contour had a lower rate of occurrence of retreatment with flow diverting or embolization devices. Lastly, a significance regarding the deployment time with the Contour deployment being faster than WEB deployment was found. On the opposite, Gärtner et al. found shorter deployment times with WEB than with Contour with a median time of 22 minutes (Contour) and 27.5 minutes (WEB) [91]. They compared 48

patient-specific aneurysms with half of it being treated with the Contour and the other half with the WEB device. Their results showed that lower occlusion times occurred with Contour than with WEB. However, the learning curve of Contour deployment was higher, since no significant difference in the procedure time between the first and last Contour case was found. Regarding the WEB procedure, a shorter deployment time was measured within the last compared to the first procedure.

Table 5.4: In vivo analyses conducted to assess the performance of the WovenEndoBridge (WEB) device. For each study the count of included cases, the highest occlusion rate at last FU in months (m) or years (y) and complications that occurred are listed.

Study	Cases included	Occlusion rate (Follow up)	Complications
Pierot et al. [230]	95	51.6 % (5y)	-
Fujimoto et al. [88]	41	78.8 % (15.3m)	-
Cortese et al. [66]	215	62.8 % (18m)	WEB modification

5.3 Contribution

As the hemodynamics in IAs and their relation to rupture were studied in Part 1 and Part 2 of this thesis, the importance of efficient treatment options becomes clearly apparent. With the first endovascular minimally-invasive treatment of cerebral pathologies performed in 1964 by Luessenhop and Velasquez, endovascular treatment options became more and more applied in the standard of care within the last decades. The minimally-invasive approach comprises flow diverting and flow disrupting treatment options. The choice of flow disrupter or flow diverter often depends on the IA shape, size and location as explained in sections 5.1 and 5.2. For example, intrasaccular coiling provides most efficient treatment of side wall IAs with ostium near side branches, whereas FDS are especially efficient for fusiform and giant IAs [271]. Coil embolization is a well-established method for the endovascular treatment of IAs [198]. However, treating WNBAs with coils presents significant challenges, as it typically requires the use of adjunctive devices such as stents or balloons [82]. These additional devices complicate the procedure, leading to relatively low aneurysm occlusion rates (approx. 40 %) and high complication rates (approx. 21 %) [82].

Therefore, novel flow disrupting devices, like the Contour Neurovascular System (Contour; Stryker) and the Woven EndoBridge Device (WEB; Terumo Neuro) were established. These devices mean to disrupt the flow like invasive clipping techniques at the neck of the IA. They are stand-alone devices, which means that no further stents are needed for employment and treatment, as it can be possible for coil embolization. An additional advantage of these newer devices is their ability to be used without necessitating concomitant platelet inhibition, which reduces the associated risks and procedural complexity [74]. The associated research emerged in the in vivo, in vitro and in silico approaches to derive the effectiveness of the devices [231, 88]. While the WEB has been extensively studied in clinical trials, the Contour remains under clinical investigation. Early findings indicate that the Contour offers better occlusion rates and easier deployment compared to the WEB [91]. However, further studies are required to validate these outcomes, and long-term efficacy and safety need to be thoroughly evaluated before it can be widely adopted in clinical practice [96, 105].

Building on these findings, this thesis incorporates the comparison of in vitro experiments with in silico hemodynamic simulations modeled on the basis of the experimental setup [149]. Hemodynamic analysis is critical for assessing aneurysm stability and the efficacy of treatment

devices [280]. However, prior studies have been restricted to short-term analyses and rely exclusively on in vitro data, without extending their findings to long-term or in vivo evaluations.

The aim of this chapter was to quantify the impact of Contour placement on the intra-aneurysmal hemodynamics in WNBAs. The aneurysm data analyzed comprised 8 patient-specific (in vivo) and 4 phantom models (in vitro), which were based on patient-specific data. Time-resolved CFD was used to simulate the intracranial flow. The phantom models were additionally used in PC-MRI experiments to assess the hemodynamics before and after Contour placement. For the patient-specific cases longitudinal FU data was available for 6 out of these 8 patients, allowing the analysis of the longitudinal Contour displacement and its effect on the hemodynamics possible.

This chapter firstly presents the patient cohort and the methodological framework for establishing the virtual Contour deformation for hemodynamic modeling. This includes the imaging and segmentation processes of patient and phantom data, as well as of the Contour. The latter is digitally modeled and virtually incorporated into IA models to replicate in vivo and in vitro locations and deformations. Secondly, the hemodynamic simulations and the corresponding in vitro measurements are explained. Thirdly, model assumptions and subsequent resulting hemodynamics are discussed, with particular attention given to numerical and imaging constraints, alongside an evaluation of the validation against in vitro measurements. Following this, the numerical results regarding the effect of the Contour on treatment outcomes, focusing both on short-term effects and the influence of device positioning and displacement over time on hemodynamics, will be further discussed. The research questions serving as a basis for the analyses in this chapter are presented below.

Research questions

A. Does the Contour Neurovascular System provide a numerically and experimentally proven stable and efficient blood flow disrupter for intracranial aneurysms?

B. What is the effect of different positionings and longitudinal displacement of the Contour Neurovascular System on the intra-aneurysmal flow reduction and branch flow modulation?

5.4 Methodology

To analyze the performance of the Contour and the impact of displacement on intracranial hemodynamics based on in vivo and in vitro data, a complex processing workflow was developed, which is presented in Figure 5.4. The individual steps will be explained in the following sections. Included here are first the data base, explained in section 5.4.1, second the imaging (section 5.4.2), third aneurysm dome stitiching in section 5.4.3 and the Contour digitalization in section 5.4.4. Fourth the virtual Contour deployment is outlined (5.4.5). Lastly, the hemodynamic simulation setup will be explained in section 5.4.6.

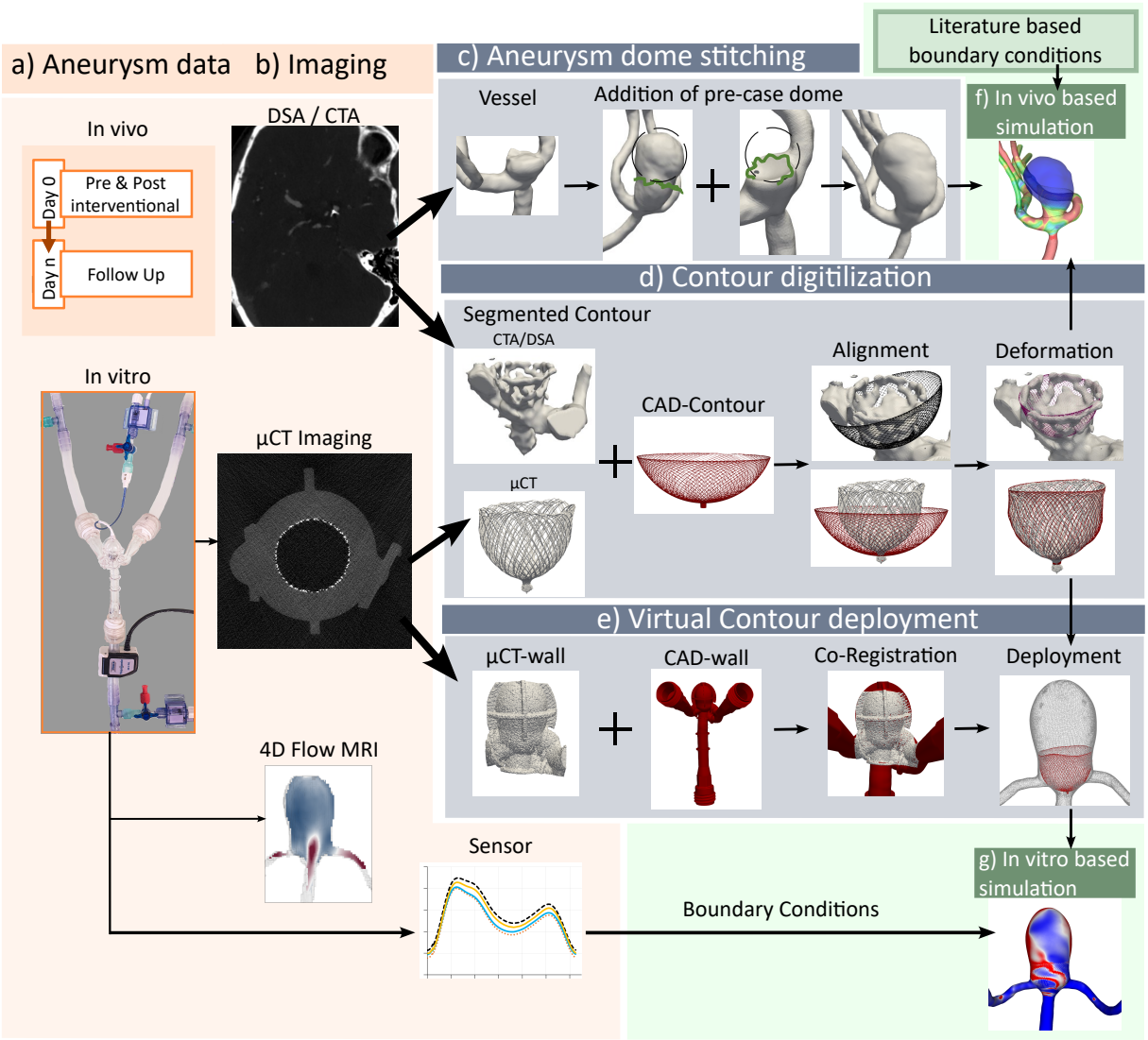


Figure 5.4: The underlying complex methodology pipeline used in this chapter. The pipeline is structured into six subitems marked with a-f. a) Representation of the database from intervention including two FUs (patient-specific data) and from experiments (phantom model data). b) Medical imaging of the two datasets including the imaging of the Contour. c) Workflow to extract the true aneurysm dome from the pre-state to be stitched on the post-interventional and FU states of the patient-specific data. d) Processing pipeline to digitalize the Contour from medical imaging for the use in the numerical simulations. e) Workflow to achieve the correct placement of the Contours inside the virtual phantom models. f/g) Performance of hemodynamic simulation based on in vivo (f) and in vitro (g) based data.

5.4.1 Patient cohort

The in vitro and in vivo aneurysm data considered for analysis of the efficacy of the Contour in this thesis were derived from PC-MRI experiments (in vitro data) and longitudinal image-based patient-specific data (in vivo), see Figure 5.4a). In the remainder of this chapter, the patient-specific models are referred to as P (P1-P8) and the phantom models as M (M1-M4). The in vitro aneurysm data were designed based on a patient-specific basilar tip aneurysm. By removing vessel artifacts and vascular branches an artificial aneurysm model was established. The aneurysm dome was remodeled to replicate variations in size, and thus four similar shaped IA models with varying dome volume were created. The models were designed as WNBAs, featuring a similar dome-to-neck ratio (1.2 ± 0.1), and shared a consistent parent vessel along with posterior cerebral arteries. The models were then 3D printed, producing four basilar tip aneurysm models as presented in Figure 5.5 (labeled M1-4).

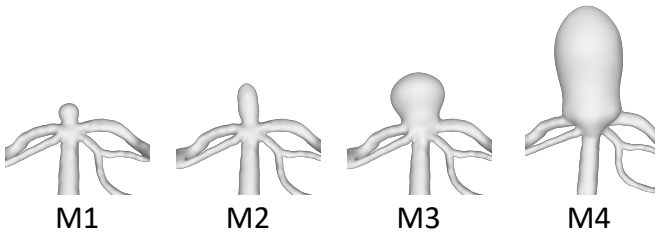


Figure 5.5: Visualization of the four phantom models M1-M4 used in this chapter.

The virtual models used for CFD simulations differed slightly from those employed for PC-MRI measurements. Specifically, the superior cerebral arteries, initially included in the models for experimental purposes, were partially occluded during the 3D printing process due to their small size. To ensure consistency between PC-MRI and CFD analyses, the superior cerebral arteries were excluded from the virtual models used in CFD simulations. The exclusion of the branches was evaluated in regard to derive their impact on the intra-aneurysmal hemodynamics. For this, comparative numerical simulations were performed of one case (M3) in treated and untreated state with and without exclusion of side branches.

In the in vitro models 10 Contours were implanted in total, while M1 had 2 implantations (C1-2), M2 had 3 (C3-5), M3 had 4 (C6-9) and M4 had 1 (C10). The devices varied in size: five with a diameter of 5 mm (C1–C5), four with 11 mm (C6–C9), and one with 14 mm (C10), respectively. Variations of deployment and aneurysm sizes are presented in Table 5.5.

Table 5.5: Overview over the model basis of the in vitro based data. For each case M the implanted Contour variations (C) and sizes are presented, together with the aneurysm sizing parameters intracranial aneurysm (IA) height, neck diameter (D), and dome diameter (D).

Case	Treatment variations	Size (mm)	IA height (mm)	Neck D (mm)	Dome D (mm)
M1	C1-C2	5	3.5	2.7	3.2
M2	C3-C5	5	6.9	2.8	3.3
M3	C6-C9	11	8.4	6.7	8.4
M4	C10	14	16.4	9.2	10.2

Regarding the in vivo data basis, 8 patient-specific WNBAs captured with 3D medical imaging techniques before and after the deployment of the Contour (pre- and post-intervention) were considered. Two FU imaging datasets (FU1 and FU2) were acquired for 6 out of these 8 patients at various temporal intervals, ranging from 3.1 to 26.7 months after intervention.

The treatment of the in vivo cases as conducted by the neurointerventionalist included four Contour sizes, ranging from 5mm over 7 mm and 9 mm to 11 mm. The selection of size and according WNBA was carried out by an experienced neurointerventionalist. In Table 5.6 the patient data including imaging protocols and FU time points are provided.

Table 5.6: Overview over the patient-specific in vivo data including the medical imaging applications digital subtraction angiographic (DSA) or computed tomographic angiography (CTA). The months after intervention are shown in brackets behind the imaging for FU1 and FU2 caes. Additionally, the employed Contour size as well as the aneurysm specific parameters sac volume (V) and ostium area (OA) for the pre-interventional state are demonstrated. Pre-interventional (pre), post-interventional (pos), first follow-up (FU1), second follow-up (FU2).

Case	Medical imaging and time ranges				Size	Aneurysm specifics (pre state)	
	Pre	Post	FU1 (months)	FU2 (months)	(mm)	Sac V (mm^3)	OA (mm^2)
P1	DSA	CTA	CTA (6.0)	CTA (8.5)	7	35.19	15.90
P2	DSA	CTA	CTA (5.5)	CTA (10.3)	9	122.30	15.50
P3	CTA	DSA	-	-	7	122.69	18.21
P4	DSA	DSA	-	-	7	130.61	13.47
P5	DSA	DSA	CTA (6.4)	CTA (14.3)	9	133.75	14.93
P6	DSA	DSA	DSA (3.3)	DSA (10.8)	9	159.04	22.85
P7	DSA	DSA	DSA (5.9)	DSA (11.5)	11	193.74	39.72
P8	DSA	CTA	DSA (6.5)	DSA (17.1)	9	286.69	16.31

5.4.2 In vitro and in vivo imaging

The next step comprising the medical imaging is separated in three parts: the in vitro PC-MRI of the phantom models, the μ-CT scanning of the Contours within the phantom models, and the in vivo medical imaging of the patient data.

In vitro experiments comprised the four aneurysm models, which were firstly considered at pre-state without Contour. Secondly, the ten Contours were deployed across the four IA models (see Table 5.5). Devices were deployed under fluoroscopy by a neuroradiologist from University Hospital Kiel (UKSH) with more than 10 years of experience. For each of these 14 variations, MRI experiments were conducted to measure the flow inside the aneurysm and the surrounding vessels.

The models were incorporated into a closed-loop flow system, where a saline solution was circulated at an average flow rate of $150\,mL\,min^{-1}$ to replicate the physiological flow conditions observed in the basilar artery in vivo (Ismaltec MCP Standard, Cole Parmer, USA). Pressure waveforms were continuously monitored over time at both the inlet and outlet of the system and specifically at the apex of the IA sac using pressure sensors. Flow measurements were obtained at the inlet of the vessel model using flow sensors (ME8PXL-M12, Transonic System Inc.; PRESS-N-000, PendoTech). The resulting flow and pressure waveforms at the inlet and outlets are presented in Figure 5.6.

Flow dynamics within the IA models were assessed using PC-MRI, conducted on a 3 Tesla (3T) whole-body MR scanner equipped with a 32-channel head coil (Ingenia CX, R5 V6.1, Philips Healthcare, The Netherlands) (Figure 5.4b)). The imaging protocol employed a time-resolved PC-MRI sequence with full 3D coverage (PC-MRI), achieving a temporal resolution of 63 ms and a spatial resolution of (0.75x0.75x0.75)mm^3.

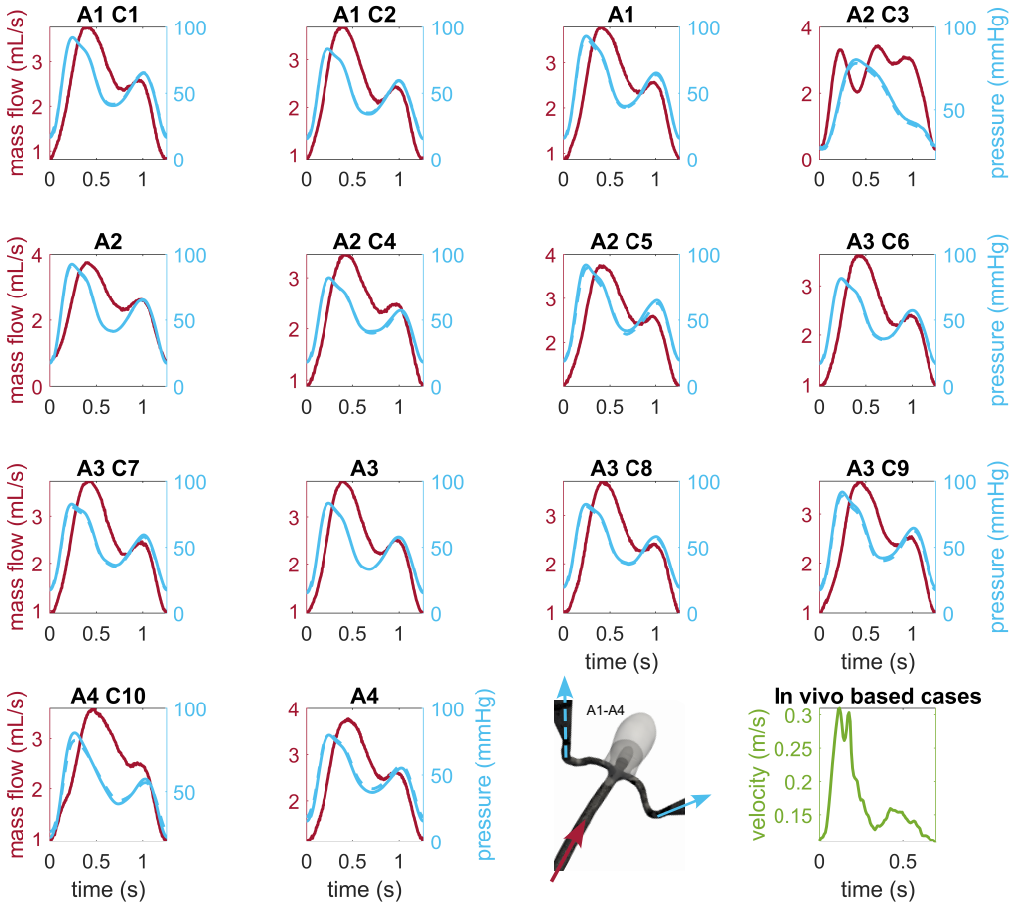


Figure 5.6: Flow (mL) and pressure (Pa) curves for the phantom models. At the inlet a massflow was set (shown in red on left y-axis) and at the outlet a pressure curve (shown in blue on the right y-axis). For each model without (M1-M4) and with (C1-C10) Contour the resulting curves are presented. On the bottom, the phantom model is shown depicting the inlet and outlets. Additionally, the flow curve based on the literature, which was used for the patient-specific data is presented.

The velocity-encoding parameter was set to 75 cm s^{-1}, approximately 10 % higher than the maximum velocity detected at the inlet without the presence of the Contours. Data post-processing, including linear phase offset correction, velocity aliasing rectification, and vessel segmentation, was performed using GTflow software (V3.1.12, Gyrotools, Switzerland). Additionally, μ-CT scans of the Contour and the wall of the phantom model were captured, deriving the exact deformation and placement of the Contour within the model. This served as a basis for registration of Contour and vessel, which will be further explained in section 5.4.5. In vivo imaging was performed at the University Medical Center Schleswig-Holstein using the Allura Xper FD 20/10 system (Philips, Best, Netherlands), and at the University Hospital of Magdeburg with the Axiom Artis Q system (Siemens Healthcare, Erlangen, Germany), utilizing 3D DSA and CTA. The scanner in Magdeburg features a resolution between 512×512×155 to 512×512×355 with voxel sizes of 0.28–0.47 mm^3. The resolution of the scanner in Kiel was 384×384×384 with an isotropic voxel size ranging from 0.16–0.3 mm^3. Vessel and Contour models were captured during equal scans, thus no further registration between Contour and aneurysm model was needed. Segmentation of the in vivo images was performed using the region growing algorithm within the software MeVisLab (v3.4.2; Fraunhofer MEVIS, Bremen, Germany) [281].

5.4.3 Aneurysm dome stitching

Within the in vivo imaging, the device crucially reduced the flow of contrast agent into the aneurysm dome. Thus, the IA sac was not captured with DSA or CTA images of the treated cases (see Figure 5.4c). For the hemodynamic simulation, the geometry of the aneurysm dome is necessary for correct flow estimation. Therefore, the pre-treatment state was taken into account and the according aneurysm dome cut from the bottom part of the aneurysm dome.

The resulting IA sac geometry was then manually stitched to the post-treatment vessel in Blender (v3.1, Blender Foundation, Amsterdam, NL) as shown in Figure 5.4c: *Addition of pre-case dome*. The neck and bottom part of the IA dome were preserved from the medical images. Solely the top part of the dome was added here, which meant a preservation of the aneurysm neck curve and ostium. The walls were additionally smoothed at the locations of the stitching. This procedure was performed for each case, respectively.

5.4.4 Contour digitalization

The scans of the Contour to capture the shape of the deployed Contours inside the aneurysm were based on differently resolved imaging data for in vitro and in vivo images (μ-CT or CTA/DSA). Nevertheless, similar processing steps were performed. The process of the digitalization of the segmented Contour models is explained in Figure 5.4d).

A direct use of the segmented Contour from the medical images in the numerical simulation was impractical due to limitations in the spatial resolution, which introduced high artifacts. These artifacts included artificially thickened wire segments and occlusions within sections of the Contour. Thus, a 3D computer-aided design model of the Contour (CAD-Contour) was created based on the manufacturer's 2D schematics of the unconstrained Contour (Fusion 360 2.0, Autodesk, USA). The CAD-Contour consisted of 72 equidistant circular elements, arranged radially and connected at the Contour base, near the radiopaque marker. This design represented the undeployed configuration, which would subsequently change shape upon deployment.

A precise replication of the employed Contour by the virtual counterpart was highly important to most realistically mimic the experiments and the in vivo placements. To accurately capture the deployed shape observed in the in vitro (μ-CT) and in vivo (CTA/DSA) images, an alignment of the CAD-Contour to the segmented data needed to be performed. Through a rigid transformation the CAD-model was registered to the segmented in vivo and in vitro Contour data, respectively (see Figure 5.4d): *Alignment*). The radiopaque markers were used as connecting points for this registration.

Then the CAD-Contour had to undergo a modification to conform to the segmented Contour shape. For this a lattice deformation tool in Blender was used. The modifier allowed a volume-retaining deformation of the Contour struts to match with the segmented Contour. Thus, a smooth adaptation of the digital model matching the actual deployed configuration of the Contour was achieved. This constrained version of the CAD-Contour was subsequently used for high-resolution CFD simulations. A detailed comparison of the CAD-Contour and segmented Contour was performed qualitatively and by quantifying geometrical parameters of both models, see section 5.5.

5.4.5 Virtual Contour deployment

Within the in vitro data, the initial positions in the coordinate system were different for the virtual IA models and the CAD-Contours. To accurately position the CAD Contours within

the IA sac, a multi-step process was employed (see Figure 5.4e)). The correct position of the Contour in the phantom models could be observed through the μ-CT images, nevertheless, the imaging quality was too low for a direct use within the simulations. Thus, to find the correct position, first the segmentation of the wall of the phantom model was aligned with the corresponding CAD model of the aneurysm wall. To achieve this alignment, an iterative closest point algorithm was conducted in MeshLab (MeshLab 2022.02, ISTI - CNR, Pisa, Italy). This minimized the distances between the two surfaces and ensured the correct registration. Second, the transformation matrix was derived from this process and applied to the CAD Contours. Since both, the CAD wall and the CAD model of the aneurysm, share the same coordinate system, this transformation ensured that the Contours were accurately registered within the CAD representation of the aneurysm sac.

5.4.6 Hemodynamic investigation

The hemodynamic investigation includes the performance of the numerical simulations based on the medical images of the aneurysm vessel and the processed Contour data as well as the subsequent data analysis. The goal of the numerical simulations based on in vitro data was to best mimic the experiments and to establish a ground truth for further simulations based on in vivo data.

Numerical simulation

In order to set up the simulations, the spatial discretization used a base size of 0.1 mm in vessel and aneurysm areas. The Contour needed higher resolution discretization with up to 0.001 mm refinement at the struts. This resulted in a total cell count of 2 to 11 million among the models depending on Contour and IA size. As explained in section 2.4, the commercial solver Star CCM+ was used for solving the Navier-Stokes equations in the discretized models. This finite-volume method was again applied for the underlying cases. Further simulation settings were established based on the data for the in vivo and in vitro cases separately (Figure 5.4f) and g)). Thus, the BCs and fluid properties differed between the in vivo and in vitro cases.

Since within the in vitro experiments inlet flow and outlet pressure curves were measured, these could be individually used for each case, respectively. Moreover, water was used as working fluid in the experiments. To ensure a comparative basis between simulations and experiments, viscosity and density of the working fluid were applied as fluid properties in the simulation (dynamic viscosity: $0.001\,\mathrm{Pa}\times\mathrm{s}$, density: $998\,\mathrm{kg\,m^{-3}}$). The impact of the neglecting clinically realistic fluid properties was additionally analyzed, by applying the viscosity and density of blood (dynamic viscosity: $0.004\,\mathrm{Pa}\times\mathrm{s}$, density: $1055\,\mathrm{kg\,m^{-3}}$) for one case (C14).

For simulations based on in vivo data no measured flow curves were available and thus, a flow curve based on literature was applied at each model inlet [75]. An equal flow curve for each case was used to ensure a comparable basis. At the outlets, a splitting value based on Murray's law with power exponent n=2 was applied as this was found to be the most accessible in this thesis (see Chapter 3). The fluid was set to mimic blood optimally using a Carreau-Yasuda model. The density was set constant with the value of $1055\,\mathrm{kg\,m^{-3}}$ and fluid model parameters were set as follows: infinite shear rate = $0.0035\,\mathrm{Pa}\times\mathrm{s}$; zero shear rate = $0.16\,\mathrm{Pa}\times\mathrm{s}$; relaxation time = 8.2 s; power constant = 0.2128; shear-thinning control parameter = 0.64 [260].

In summary, 42 transient hemodynamic simulations were performed, comprising 12 pre-interventional (4 in vitro and 8 in vivo), 18 post-interventional (10 in vitro and 8 in vivo), 6 first follow-up and 6 second FU (solely in vivo) simulations. The overview of the performed simulations is presented in Table 5.7.

Table 5.7: Overview over the simulations conducted for the content of this chapter, divided by medical imaging basis and the states after intervention. First follow-up (FU1), second follow-up (FU2).

Imaging basis	Pre-interventional	Post-interventional	FU1	FU2
In vivo	8	8	6	6
In vitro	4	10	-	-

Data analysis

As shown in Figure 5.7a), the extraction of the ostium was established differently for the patient-specific (in vivo) and the phantom model (in vitro) based data. Since the phantom models featured equal peripheral vessels with the increasing aneurysm dome size, the exact same plane location was chosen for these cases. The flat plane was set in the IA neck area. Regarding the in vivo based data, each IA featured an individual size and shape. Thus, the true ostium was extracted using the automatically calculated neck curve, which was estimated with the "Neck Curve Extraction"-Tool by Saalfeld et al. [256].

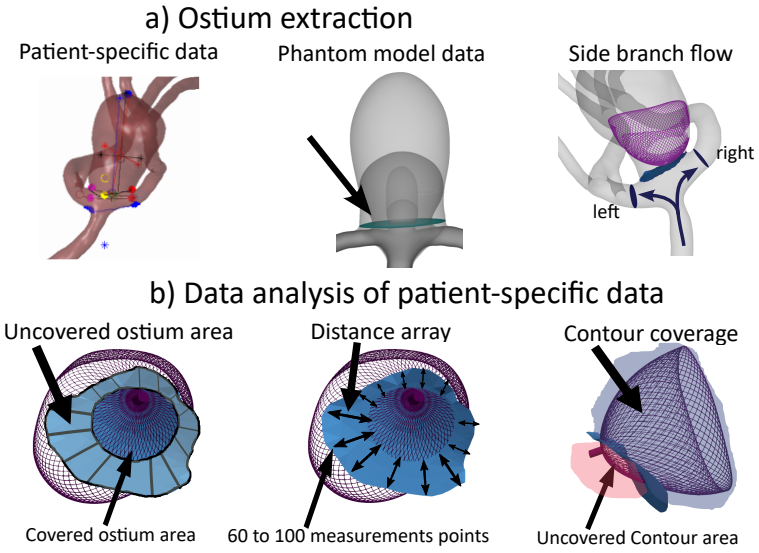


Figure 5.7: The ostium extraction for the patient-specific and phantom data is shown on the top (a). On the bottom (b), the data analysis of the patient-specific data regarding the morphological interaction between ostium surface and Contour is presented.

The patient-specific in vivo based data was further analyzed morphologically by estimating the uncovered ostium area (UOA), the distance array, and the Contour coverage (CC) as depicted in Figure 5.7b). The UOA describes the array of the ostium surface, which is not included inside the Contour. The distance array is the array of the circular estimated distances between the Contour crossing the ostium surface and the neck curve. The CC is the area of the Contour, which is included inside the aneurysm dome, while the dome is separated from the remaining vessel by the ostium surface.

To compare the experimental PC-MRI data with the CFD velocity results, velocity fields obtained from both PC-MRI and CFD simulations within the IA sac were interpolated on a uniform grid with a resolution of 0.3 mm. To evaluate the high-resolution intra-aneurysmal flow from CFD simulations, several hemodynamic parameters were analyzed. These included OSI, OVI, NIR, TA WSS, velocity magnitude (v), KE, and ICI. Parameter formulas are explained in section 2.5. Additionally, for the in vitro based data, aneurysm turnover time (TOT), which is defined as the aneurysm sac volume divided by the NIR, was determined.

The separation of flow dynamics in the parent vessel due to the Contour was evaluated by examining changes in flow through the side branches to estimate the effect of the Contour on the parent vessel flow. This was determined by measuring the flow across a plane placed perpendicular to the flow direction in each branch. For the cases based on in vitro data, flow distribution in the left and right PCA was normalized relative to the total outlet flow. This was useful due to the exact same outlet count for each of the 10 treated cases.

For the estimated hemodynamic parameters, the treatment effect (TE) was calculated to derive the impact of the Contour deployment. The TE is estimated by considering any hemodynamic parameter (P) before and after Contour deployment, normalized as shown in the following equation (5.1).

$$TE = \frac{Mean(P_{treated}) - Mean(P_{untreated})}{Mean(P_{untreated})} \tag{5.1}$$

Statistical tests were performed to compare the pre- and post-interventional state of the in vivo and in vitro based data. The follow-up states were compared to the pre-interventional states for the patient-specific data. Additionally, the morphological parameters UOA and CC were compared to the hemodynamic parameters per time instance. The Wilcoxon rank-sum test with a p-value of 0.05, was used to assess statistical significance (MATLAB R2022a, The MathWorks, Natick, USA).

5.5 Reliability of the Contour processing workflow

This part focusses on the evaluation of the methodology applied in this chapter. First, the adaptation of the CAD-Contour model to the real segmented model is considered. Second, the adjusted geometric and fluid modeling are examined. Third, the comparison of the simulated and measured flow parameters are analyzed in this regard. In the following section 5.6 the hemodynamic results are further evaluated.

5.5.1 Contour fitting

Since the segmentation of the Contour could not be used in the numerical assessment due to unrealistic strut thickness and fusion (recall section 5.4.4), a digitalization of the Contour was introduced within the methodology. This resulted in the Contour being virtually fitted to the realistic model, which raised the question, if the fitted model can represent the realistic shape of the Contour. For this, a comparison of the μ-CT Contour models and the fitted models was carried out, whereas the μ-CT scans were chosen over the CT scans from in vivo imaging due to higher resolution outcome. In Figure 5.8 four cases are exemplarily presented with the segmented model in purple and the fitted model in green. Based on the qualitative representation, the fitted

models clearly match their segmented counterpart. As visible within model M2 C3 (Figure 5.8) the segmented Contour showed an unfolding of the double layered mesh. This could not be replicated within the virtual Contour.

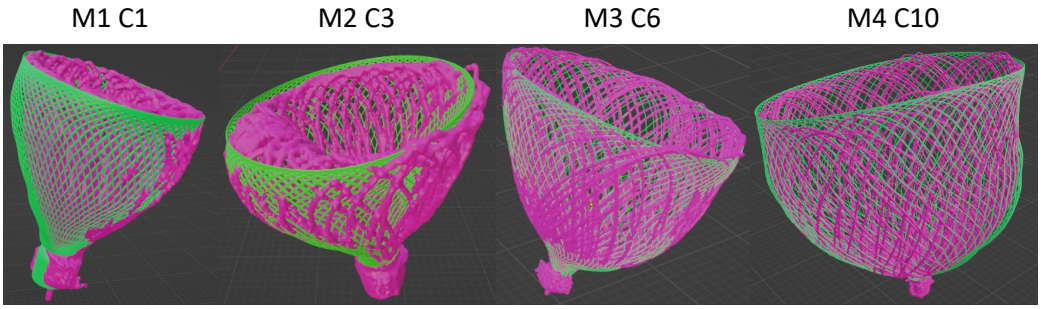


Figure 5.8: Qualitative comparison of the scanned (purple) and virtually mimicked (green) Contour for four representative cases, including a configuration from each phantom model size (M1 C1, M2 C3, M3 C6, and M4 C10).

Moreover, specific geometrical parameters are shown in Table 5.8 depicting the difference in strut thickness, Contour diameter and Contour area. Since the strut thickness was captured with medical imaging and provides the highest deviation to the realistic model, here the highest percentual difference to the fitted model occurred (percentual maximum difference = 409 %). However, the fitted model provides the strut thickness from the actual employed device, which stays constant within employment. The mean diameter changed with a maximum average of 2.28 % difference (C14) and the total area with a maximum difference of 4.42 % difference (C05). These results indicate the good agreement between the μ-CT and virtual Contour.

Table 5.8: Comparison of mean strut thickness, mean diameter and total area of the segmented (µCT) and fitted (CAD) Contour for the three in vitro Contour sizes 5 mm, 11 mm, and 14 mm. Parameters are averaged over each Contour size.

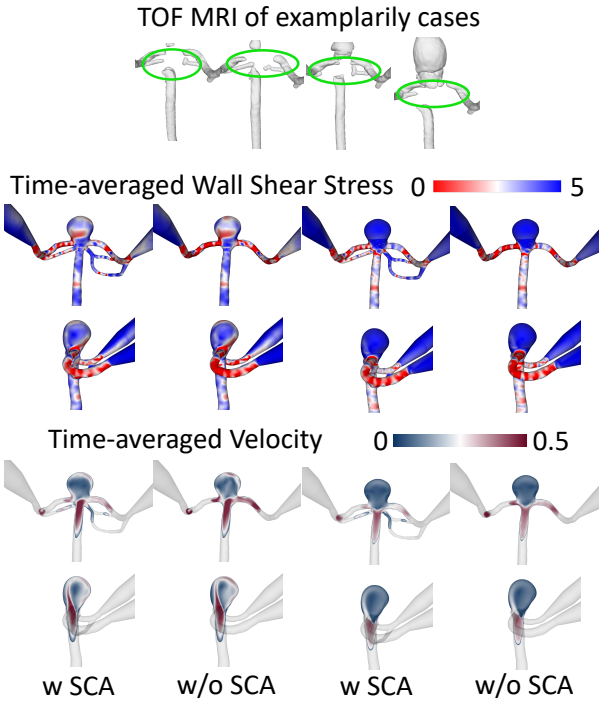
	C5		C11		C14	
	CAD	µCT	CAD	µCT	CAD	µCT
Mean strut thickness (mm)	0.02	0.07	0.02	0.08	0.022	0.09
Mean Diameter (mm)	2.50	2.53	7.15	7.16	8.56	8.76
Total Area (mm^2)	26.79	28.03	151.03	155.00	254.16	256.07

Recent studies on numerical virtual treatment analysis have based device deployment on CAD models of the device rather than on segmentations. Cebral et al. and Appanaboyina et al. investigated the treatment effect of flow diverters by placing CAD-models of the FDS into the treated vessel model's surfaces captured with medical imaging [54, 12]. Here the stent deployment was mimicked by the shape of the vessel wall. Mantilla et al. further investigated device deployment using the Sim&Size simulation software (Sim&Cure, Montpellier, France) [188, 189]. With this software, the vessel and device geometry are reconstructed based on the medical imaging data with the use of a Marching Cubes algorithm. In this thesis, the in vivo and in vitro shapes of the device were captured and subsequently used for modeling instead of the vessel walls. This was especially important since the unusual shape of the Contour is not fully adherent to the vessel wall.

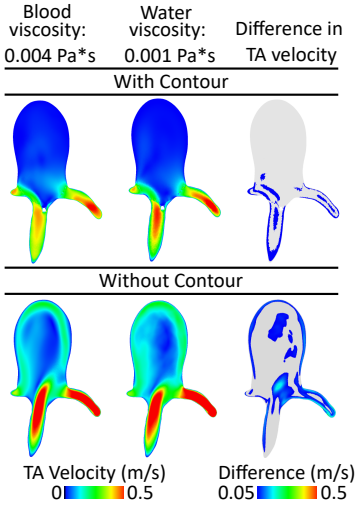
5.5.2 Geometric and fluid modeling

The in silico models based on the experiments needed to be adjusted to serve as a comparable basis to the experiments. However, this led to non-realistic modeling of the geometric models

and fluid properties. To confirm that the use of these restrictions had no negative effect on the results, a numerical identification of resulting deviations when applying clinically non-realistic assumptions was performed. This included the evaluation of the impact of the extraction of further side branches and of the fluid modeling as blood or as blood mimicking mixture.



(a) Visualization of the TOF magnetic resonance images (MRI) of the phantom models with Contour. Green circles highlight the areas with high artifacts due to Contour. Qualitative hemodynamic comparison of one representative case with (w) and without (w/o) the inclusion of the side branches. Time-averaged (TA) wall shear stress and TA velocity are shown.



(b) Comparison of the use of different fluid properties: blood viscosity vs. water viscosity in one representative phantom model case with and without Contour.

Figure 5.9: Resulting qualitative variations due to method adjustments necessary to implement the virtual analysis of the treatment outcome due to Contour and the related comparison to in vitro investigations.

In Figure 5.9 the resulting impact of the model adjustments are presented for exclusion of the side branches (Figure 5.9a) and variation in fluid properties (Figure 5.9b). In Figure 5.9a on the top, one exemplarily image of the TOF MRI of each case after Contour deployment is shown. The missing or perforated arteries are marked with green arrows. Additionally, the qualitative simulation results of model M3 with (M3 C6) and without (M3) Contour are shown comparatively with exclusion and inclusion of the side branches. The results showed, that exclusion did not significantly impact the hemodynamic changes within the aneurysms associated with the placement of the Contour. This applied as well to the impact of the chosen fluid properties. In Figure 5.9b a plane through the aneurysm vessel colored with the TA velocity is exemplarily shown for model M10 and M10 C14 simulated with the two different fluid properties. Additionally, the differences higher than $0.05\,\mathrm{m\,s^{-1}}$ between the two blood modeling approaches are visualized. These differences are relatively small, occurring primarily near the vessel wall and remaining below $0.1\,\mathrm{m\,s^{-1}}$. To minimize deviations in result validation, it was essential to use fluid properties consistent with those in the experiments. Similarly, recent studies comparing numerical simulations with experimental techniques such as PIV or in vitro imaging have also employed blood properties that closely mimic experimental conditions [224].

5.5.3 Comparison to in vitro measurements

The IA phantom models were scanned with PC-MRI before and after placing the Contour in the IA neck. Thus, an in vitro comparison could be carried out once with, once without Contour to verify the simulations. The latter was especially important, due to high artifacts caused by the Contour in MR images. The analysis of the impact of the Contour on the aneurysmal hemodynamics thus needed to be further performed with CFD. Since this thesis contains the first numerical investigation of the Contour performance, a comparison of the CFD results with in vitro images was particularly important. Qualitatively, this was ensured by comparing the velocity fields in the artifact-free regions, and quantitatively by comparing measured pressure data and velocity distribution before Contour deployment.

Qualitative comparison

The velocity fields computed from CFD simulations in the untreated IA models closely matched the velocity fields observed in PC-MRI, as shown in velocity magnitude distribution on the three planes through the IA in Figure 5.10. For the aneurysm model M4, both modalities captured the flow jet entering the IA sac; however, the CFD simulation depicted a broader jet that was slightly displaced towards the right side of the IA wall. In model M3, while the flow jet was clearly visible in the CFD simulation, the PC-MRI did not show the flow adhering closely to the wall. Nevertheless, the overall flow patterns were consistent across both techniques.

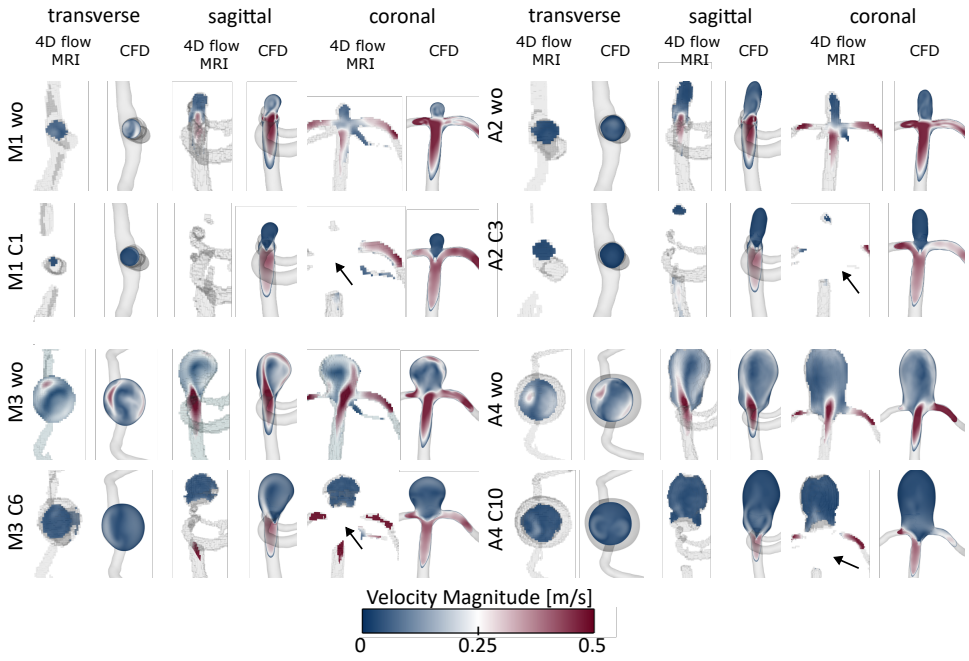


Figure 5.10: Comparison of resulting velocity distribution from PC-MRI and CFD, captured on three planes through the aneurysm model (transverse, saggital, and coronal) presented for all cases without Contour and for one example per IA size with deployed Contour (C1, C3, C6, and C10). Due to metal artifacts, the flow around the Contour could not be captured after treatment (marked with black arrows).

In the smaller aneurysm models (M1 and M2), the CFD simulations exhibited detailed velocity structures that were not present in the PC-MRI results. This was mainly due to the limited spatial resolution of PC-MRI, particularly in small IAs. Moreover, the presence of velocity noise was comparable to the actual flow velocities observed at the IA's center and the walls. A close

qualitative alignment between CFD and MRI flow results was found previously by Roloff et al. [254] and Puiseux et al. [238]. Roloff et al. analyzed intra-aneurysmal flow with PIV, PC-MRI, and CFD. They found a good agreement between the modalities, though especially PC-MRI could not provide in-depth insight into the flow due to low spatial resolution. Puiseux et al. investigated the flow through a pipe, using as well in vitro MRI and based the BC of the simulations on the experiments. However, in their study, the occurrence of turbulence was investigated, which led to the use of a large eddy simulation (LES) approach. The latter was not necessary to be applied in this chapter, since no focus on turbulence investigation was set in the specific research question. Further investigation of turbulence in IAs captured by simulations and experiments were already discussed in Chapter 4. Isoda et al. performed comparisons between PC-MRI and CFD looking at the velocity vector fields in IAs [126]. They found at least moderate agreement between the outcome of the two modalities as well.

The PC-MRI results showed prominent artifacts near the radiopaque markers of the Contour as shown in Figure 5.10 with black arrows. This affected the accuracy of phase-based flow encoding. Additionally, the flow reduction inside the aneurysm sac resulted in velocities even under the noise threshold of PC-MRI, complicating post-treatment hemodynamic assessments, especially in small aneurysms. Consequently, analysis of MRI-measured velocity fields was restricted to regions free of artifacts. The inability of PC-MRI to capture device-near flow due to metal artifacts was found in the past and could not be solved until today [37].

Quantitative comparison

In Figure 5.11 the distribution of velocity magnitude is shown comparing CFD and PC-MRI for each aneurysm model without Contour. Smaller aneurysms (M1 and M2) had a higher relative propability of low velocity values measured by PC-MRI compared to CFD. The median velocity for M1 was $0.056\,\mathrm{m\,s^{-1}}$ in PC-MRI and $0.11\,\mathrm{m\,s^{-1}}$ in CFD. For M2, these were $0.023\,\mathrm{m\,s^{-1}}$ (PC-MRI) and $0.047\,\mathrm{m\,s^{-1}}$ (CFD). In contrast, for A3, the median velocities were comparable between the two modalities ($0.179\,\mathrm{m\,s^{-1}}$ for PC-MRI and $0.163\,\mathrm{m\,s^{-1}}$ for CFD), while for M4, the PC-MRI median value was slightly higher ($0.115\,\mathrm{m\,s^{-1}}$) compared to CFD ($0.09\,\mathrm{m\,s^{-1}}$).

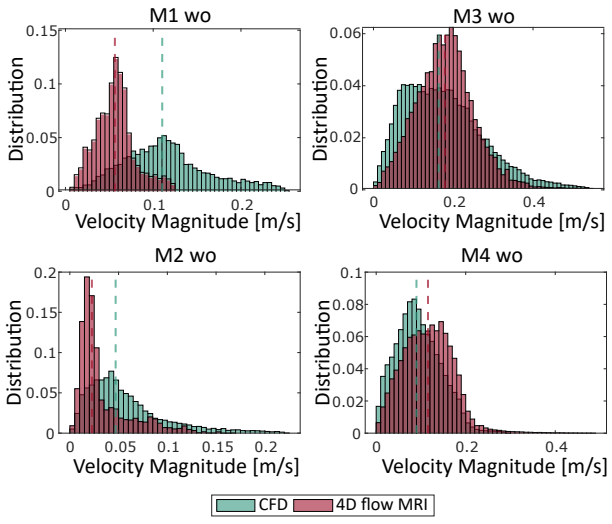


Figure 5.11: Distribution of velocity magnitude captured with PC-MRI and CFD, presented for all cases without Contour (M1-M4). Dashed vertical lines depict the median values.

The analysis of histogram plots revealed the highest differences between the two modalities in the smaller IAs (difference of mean velocity magnitude normalized by maximum velocity: M1: $\Delta 0.22\,\mathrm{m\,s^{-1}}$ and M2: $\Delta 0.1\,\mathrm{m\,s^{-1}}$). These discrepancies can be attributed to several factors, including the higher influence of measurement noise (compared to the bigger IAs), inhomogeneities from the 3D-printing process, or registration errors that may affect the accuracy of the acquired data. Additionally, the presence of the side branches in the 3D-printed models, which were excluded from the virtual CFD model, could contribute to deviations between the results [236].

In contrast, the larger aneurysm models (M3 and M4) exhibited greater agreement between the two modalities (difference of mean velocity magnitude normalized by maximum velocity: M3: $\Delta 0.044\,\mathrm{m\,s^{-1}}$ and M4: $\Delta 0.067\,\mathrm{m\,s^{-1}}$). Velocity fields for these models were more consistent, and the primary flow characteristics, such as the flow jet and median velocity values, were largely in alignment. These findings are consistent with the observations of Sindeev et al., who demonstrated compatibility between MRI and CFD in intracranial aneurysm studies [278].

In Figure 5.12 the pressure curves, measured at the tip of the IA dome, are shown for all models once without and once with deployed Contour (C1, C3, C6, and C10). Looking at these curves a strong agreement across the entire cardiac cycle was visible in all cases. Mean deviations of only 6 % without the Contour and 8 % with the Contour occurred. Related studies mostly focus on WSS estimations with MRI instead of direct pressure measurements, finding a good agreement as well [121].

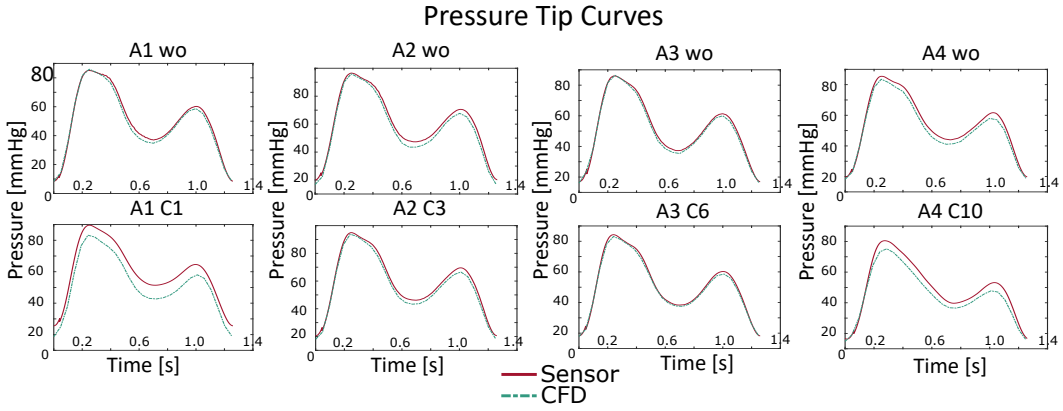


Figure 5.12: Time-dependent pressure curves at the IA tip measured with PC-MRI and CFD, presented for all cases without Contour and for one example per IA size with deployed Contour (C1, C3, C6, and C10).

5.6 Advantages of the Contour Neurovascular System

In this part of the results and discussion the efficacy of the Contour is evaluated based on the resulting hemodynamic parameters using both in vivo and in vitro data. The short-term effect and a systematic analysis of varying Contour positionings as well as the longitudinal displacement will be considered in this regard.

5.6.1 Short-term treatment outcome

The short-term treatment outcome was analyzed for the 8 patient-specific and the 10 phantom model cases, respectively. First, the qualitative outcome focusing on the WSS and second the quantitative treatment effect focusing on NIR, TAWSS, velocity, KE, ICI, and OSI were considered.

Qualitative Contour placement and time-averaged wall shear stress

In Figure 5.13 the deployment of the Contour is presented for each case together with the qualitative visualization of the TAWSS. Looking at the phantom models, the majority of the Contours were positioned near the center of the parent vessel, with some exceptions: models M2 C5 and M4 C10 were slightly shifted towards the right, while M3 C7 was displaced toward the left PCA bifurcation. Relative to a vertical centerline through the aneurysm model, these deviations ranged from 1° to 5°.

The patient-specific data indicated that most Contours were positioned centrally within the aneurysm neck, representing the optimal placement. However, slight lateral shifts were observed in P4 and P5. A discrepancy between the modeled and patient-specific data was evident in the vertical placement of the Contour, with the modeled Contours positioned lower within the bifurcation area, whereas the patient-specific Contours did not extend as far beyond the IA. Displacment of the Contour is supposed to impact the intra-aneurysmal flow reduction and flow modulation into side branches, which is less concerning when FDS or coiling is applied. However, the devices carry disadvantages like occlusion of small peripheral vessels (FDS) or the missing applicability on WNBAs (coils) [290, 177].

Regarding WSS, a reduction in intra-aneurysmal values was observed following Contour deployment in all cases. For M1 and M2, especially the neck featured higher WSS which was reduced after Contour deployment. Moreover, for M2, the Contour increased WSS on the left and decreased WSS on the right side branch. Within M3, the reduction seemed qualitatively higher than within the smaller models. Here, WSS in the left side branch was increased as well while a decrease was visible in the right one. This applied also to M4. The patient-specific cases showed a reduction in WSS on the aneurysmal wall and an increase at the walls of the side branches after deployment. The shift of the increase and decrease of WSS on the side branches, as found in the modeled cases, was visible for P5 and P7 as well. Remaining cases showed a general increase in WSS in the side branches with no general change compared to the pre-interventional cases.

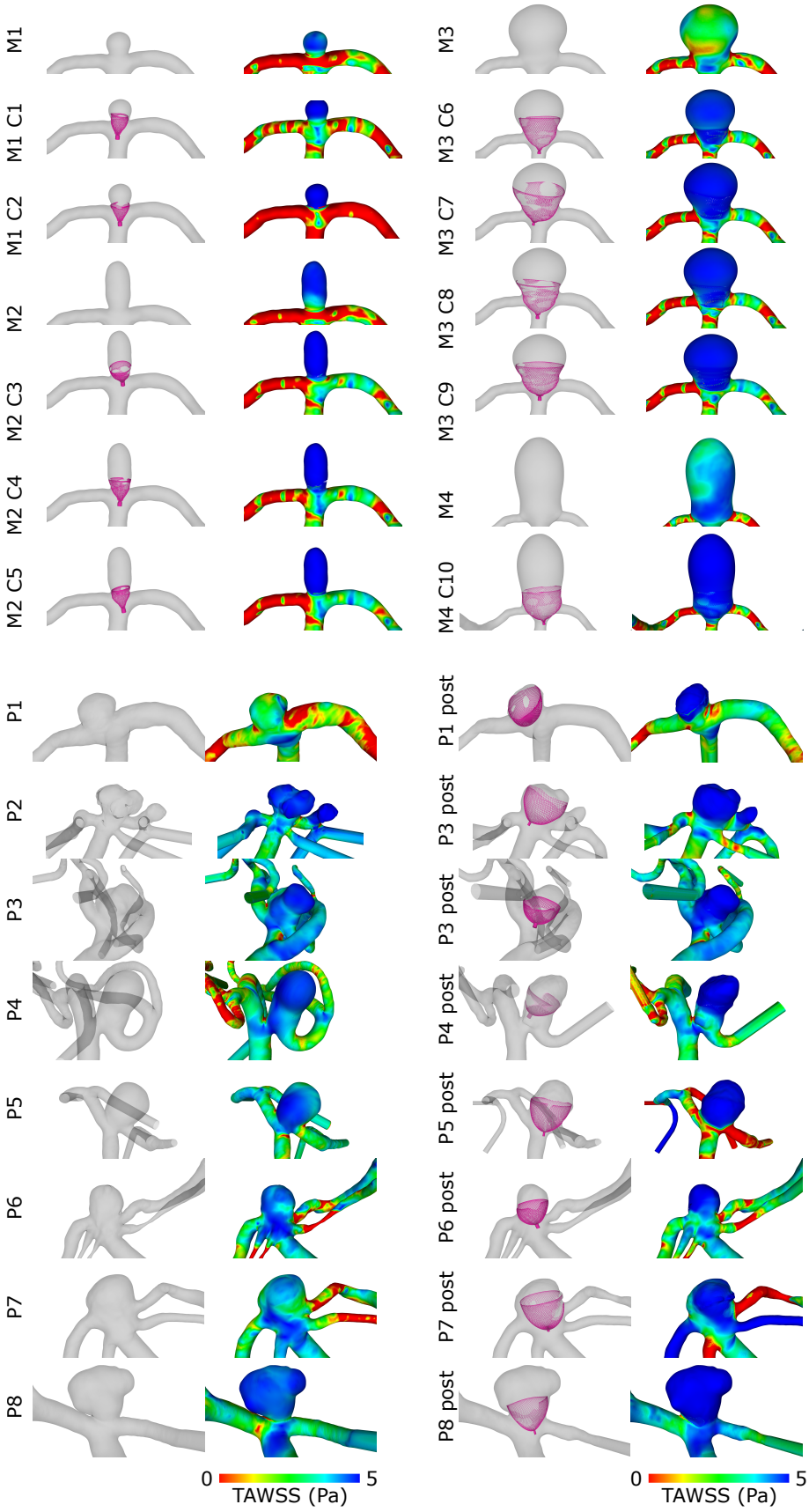


Figure 5.13: Modeled (M1-M4) and patient-specific (P1-P8) aneurysm cases before (left) and after (right) Contour deployment. Once shown with transparent wall to visualize the aneurysm shape and Contour position, once with the vessel wall colored with time-averaged (TA) wall shear stress (TAWSS).

Quantitative intra-aneurysmal Contour efficacy

The treatment effect (TE) directly after deployment as seen in the qualitative WSS reduction was also found for the qualitatively analyzed parameters (Table 5.9). For each parameter considered, a significant reduction was found, except for OSI. Within the patient-specific data, OSI even increased significantly after deployment. This aligns with findings from Roloff et al., who reported increased OSI within aneurysms after FDS implantation [253]. While malpositioning of FDS has been shown to increase OSI, it minimally impacts flow reduction. This suggests that precise placement of the Contour could mitigate increases in OSI. Notably, high OSI has been linked to aneurysm recanalization following coil embolization [146].

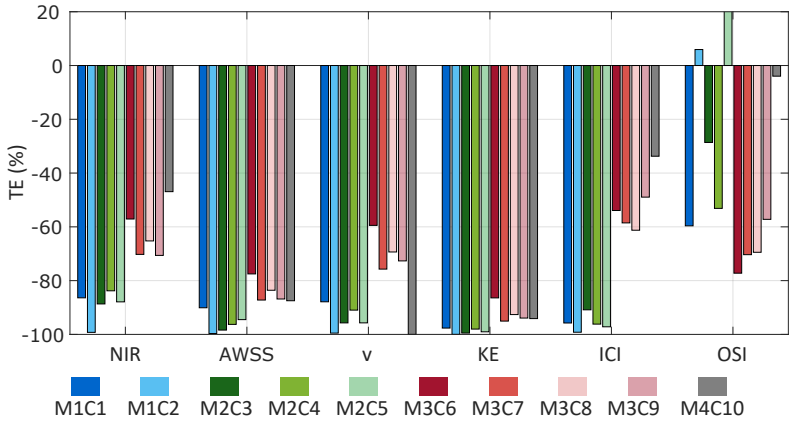
Thrombus formation, which is critical for aneurysm occlusion, is closely associated with prolonged aneurysm TOT. The calculated TOT values (recall Table 5.9) showed significant increases across all models post treatment, reinforcing the device's therapeutic efficacy and its potential to promote thrombus formation. These findings align with previously observed washout time increases in the same aneurysm models using DSA [237].

Table 5.9: Overall mean value of spatially and temporally averaged parameters without Contour (pre-interventional) and with Contour (post-interventional) presented for the cases based on in vitro data (left) and on in vivo data (right). Mean values and standard deviations (SD) are shown together with the according p-value. Significant parameters reduced by the placement of the Contour for the cases analyzed are marked with a '*'.

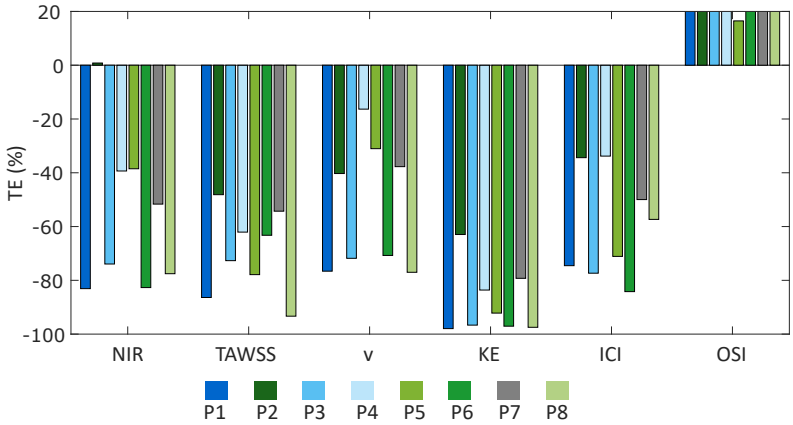
	In vitro based data			In vivo based data		
	mean±SD		**p-**	**mean±SD**		**p-**
	without	**with**	**value**	**without**	**with**	**value**
NIR*	1.46±1.28	0.53±0.62	0.002	0.74±0.38	0.32±0.24	0.0078
TAWSS*	1.35±0.73	0.17±0.17	0.002	0.54±0.30	0.16±0.11	0.0030
V*	0.12±0.05	0.03±0.03	0.002	0.10±0.02	0.04±0.02	0.0002
KE*	16.03±11.9	1.06±1.29	0.002	0.68±0.79	0.07±0.09	0.0004
ICI*	1.43±1.23	0.64±0.84	0.002	-0.06±1.71	-0.25±0.59	0.3350
OSI	0.08±0.02	0.05±0.04	0.105	0.02±0.01	0.09±0.06	0.0038
TOT*	0.28±0.15	3.46±3.9	0.002	0.28±0.29	0.63±0.52	0.0339

The detailed analysis of the remaining parameters NIR, TAWSS, ICI, TOT, and intra-aneurysmal flow metrics, such as KE and velocity, however, revealed significant reductions across all cases. Taking the detailed reduction of each case additionally into account, which is presented in Figure 5.14, the variation in TE becomes clear. In the figure, the TE of each case per chosen hemodynamic parameter is shown with the in vitro based cases in the top plot and the in vivo based cases in the bottom plot. Despite high variations and even increases in OSI, all cases show a strong reduction after treatment for the chosen hemodynamic parameters.

In comparison to other intrasaccular devices, especially the WEB has also proven to be effective in case of IA occlusion [230, 225]. However, the efficacy of the WEB is influenced by aneurysm geometry, as device sizing depends on aneurysm width and height, with a height limit of approximately 10 mm. In contrast, the Contour operates independently of aneurysm height, as it is positioned directly at the aneurysm neck [72], demonstrating comparable efficacy regardless of aneurysm height. Comparing the results to the effect from intra-saccular coiling, the Contour showed similar reductions in intra-aneurysmal flow. However, flow reduction following coiling has not been significantly correlated with aneurysm occlusion [101]. While coiling preserves parent vessel flow, it is technically more complex and unsuitable for WNBAs without the addition of stents or balloons.



(a) Representation for the phantom model cases based on in vitro data.



(b) Representation for the patient-specific cases based on in vivo data.

Figure 5.14: Post-interventional treatment effect (TE) in % of all cases for the hemodynamic parameters neck inflow rate (NIR), TA wall shear stress (TAWSS), velocity (v), kinetic energy (KE), inflow concentration index (ICI), and oscillatory shear index (OSI).

A comparing of TE between the Contour and FDS, exhibited smaller reductions in NIR within FDS (ΔNIR $\leq$ 29 %), TAWSS (ΔTAWSS $\leq$ 23 %), and velocity (Δv $\leq$ 20%) within the aneurysm [67]. Kulcsár et al. [163] suggested that reductions in TAWSS and velocity are key contributors to aneurysm occlusion, although they did not establish specific predictive thresholds. While FDS deployment is effective, it carries risks such as occlusion of small lateral branches and is less suitable for bifurcation aneurysms [41], challenges not encountered with the Contour [33]. However, the Contour is less optimal for small-neck aneurysms compared to in-vessel devices like FDS [8].

According to Ouared et al., a reduction in velocity exceeding 35 % following FDS placement is indicative of successful aneurysm occlusion [223]. In this thesis, velocity reductions surpassed 60 % in all in vitro based cases, highlighting a potentially effective occlusion. Regarding the in vivo based cases, reduction is higher than approx. 35 %. This is consistent with findings from recent in vivo studies [51, 69, 96]. Only for P4 a lower TE of less than 20 % was achieved. When recalling Figure 5.13, this might be due to the high position of the Contour inside the IA dome, leaving space to blood flow into the bottom part of the dome.

5.6.2 Systematic evaluation of Contour placement impact on hemodynamics

The in vitro based modeled IAs provided a controlled framework for systematically investigating the influence of Contour size, positioning, and aneurysm height on estimated hemodynamics. A structured evaluation could be facilitated through a standardized set of aneurysm cases, incorporating variable Contour placements within consistent IA phantom models. The phantom models, derived from the underlying database, represented a single aneurysm morphology with variations in aneurysm height and multiple Contour placements within the same model. Thus, the following analysis gives a deeper insight into the effects of aneurysm height, Contour selection, and placement, based exclusively on in vitro experimental data.

Effect of Contour size

Within the deployment of Contours into the phantom models, four Contour sizes were chosen, of which the small size comprised the 5 mm Contour. This was placed into the IA phantom models M1 and M2 (models and deployments are presented in Figure 5.13). In Figure 5.14a these deployments are marked with blue and green shaded bars (C1-C5). The results revealed that, deploying a smaller-sized Contour resulted in a more pronounced reduction in NIR, TA WSS, velocity, KE, and ICI, compared to a larger-sized device. The latter comprised phantom model M3 deployed with four 11 mm devices, which are shown with red shaded bars in Figure 5.14a.

For the larger Contours in M3 (C6-9, compare Figure 5.13), reductions of more than 85 % were observed only in KE, while the reductions in general were smaller with C6-9 (48-95 % general reduction) than C1-5 (83-99 % general reduction). Pravdivtseva et al. also found better outcome with the smaller Contour sizes when focusing on washout time [237]. The general difference in flow reduction between the Contour sizes was interesting, however should always be set in context with the aneurysm dome size and the according coverage. The neck area and dome volume was bigger for M3 than M1/2, which could have led to a higher effect in flow reduction. Moreover, the flow into the smaller IAs was lower due to the smaller neck and might have facilitated the further reduction. In this regard, Radomi et al. found a better occlusion rate in the FU cases treated with Contour when larger device sizes were applied [242]. Subsequently, the largest Contour was deployed in the largest model (M4 C10) which is marked with a grey bar. C10 showed reductions of 87-100 % for TAWSS, v, and KE. Across all cases (C1-10), a general reduction exceeding 40 % was evident for these parameters, with the exception of ICI in C10.

Effect of aneurysm height

Apart from to the Contour size and the related neck area effect, the variation in aneurysm height could be evaluated through analysis of models M1 and M2. The aneurysm sacs of M1 and M2 were manufactured with different heights with the neck area remaining equal (recall Table 5.5). The dome height of M2 was nearly twice as tall as that in M1 featuring a height of 6.9 mm (M2) and 3.5 mm of M1. While both had comparable neck and dome sizes, this led to the implantation of the same Contour size (see Figure 5.14a). Thus, the effect of aneurysm dome height could be evaluated separately.

Interestingly, no significant difference in the TE was attributed to the variation in aneurysm height. For both sizes a TE higher than 80 % was found for NIR, TAWSS, v, KE, and ICI, as can be derived from Figure 5.14a (M1, blue shaded bars; M2, green shaded bars). The maximum difference was less than Δ 9.53 % for TAWSS, v, KE and ICI. Regarding the NIR, a maximum

difference of Δ 17.61 % occurred. Only OSI was drastically affected by the IA height, with increased OSI after deployment. However, this can be attributed to the mentioned unreliable OSI outcome after treatment [254]

Effect of Contour positioning

Regarding the positioning of the Contour, model M3 was considered in the evaluation, since four Contours (C6-9) were implanted in this phantom model featuring an angular deviation of up to 5°. The resulting variations in flow reduction can be seen again in Figure 5.14a (red shaded bars). The variation in positioning has been rarely studied yet [174, 106]. This thesis gives a first insight into the effect of positioning on hemodynamic outcome. The positioning affected the flow reduction with differences ranging from Δ 8.63 % for KE, Δ 13.53 % for NIR, and up to Δ 20.06 % for OVI.

Additionally to the variations in hemodynamics, the effect of positioning was further analyzed considering the branch flow alteration after Contour deployment. As the Contour is constructed to disrupt the flow and restore the blood flow through the parent vessel, the placement of the Contour likely might impact this aim. In Figure 5.15 (left) the proportion of the outflow to the total flow into the left and right vessel branch is shown for each phantom model in percent for the treated and untreated models. The mean outflow was normalized by the total outflow, to emphasize the alteration in outflow. The flow alters from 56 % (M1 wo) to 54 % (M1 C2) shift to the left for M1. For M2, from 53 % (M2 wo) to 48 % (M2 C5) shift to the left as well. M3 featured a shift from 50 % (M3 wo) to the left (48 % M3 C8) and to the right (52 % M3 C9). While for M1 and M2 the flow shifted for all Contour positions to the left branch, the flow alters for M3 with a shift to the left (M3 C6-8) and to the right (M3 C9). Within model M4, the outflow as well shifted slightly to the left (55 % M4 to 54 % M4 C10). In Figure 5.15 on the right, the resulting TE of the outflow alteration is shown for each treatment variation. Here, the highest TE of M2 C5 and the lowest of M3 C7 is clearly visible.

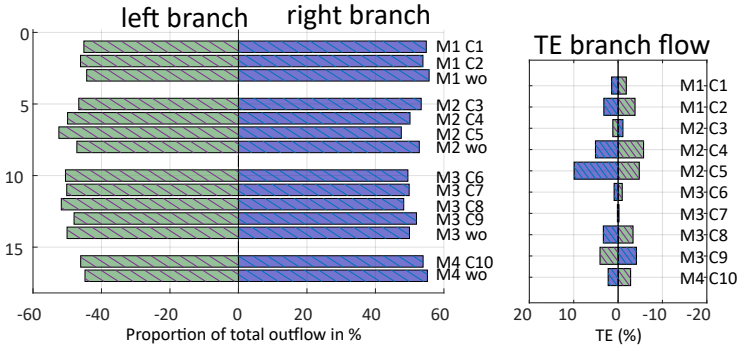


Figure 5.15: Outflow diversion into the two side branches of the phantom models. The proportion of the total outflow is shown on the left and the treatment effect (TE) comparing the case with and without Contour on the right.

Looking specifically at M3 with the four differently placed Contours C6-9, a total variation of 1 - 5 % in TE was found. A higher TE occurred within model M2, which has three different variations of the Contour placed in the similar aneurysm phantom. Here, the TE reached -10 % (M2 C5). Recalling Figure 5.13, the positioning of the Contour in M2 C5 is most shifted to the right branch, which probably caused the reduction of flow into the right vessel branch.

In comparison, devices such as the WEB and coil embolization conserve the parent vessel's flow entirely, as their placement is confined within the aneurysm sac, with no components extending into the parent vessel. This fundamental difference in deployment strategy emphasizes the need to evaluate the potential vascular impacts of Contour placement more comprehensively [230, 276]. Moreover, as in theses cases the healthy parent vessel flow is unknown for the in vivo based cases, a clear outcome is challenging to be derived from the resulting alterations. The radiopaque marker is meant to preserve the healthy parent vessel flow by mimicking the missing bifurcation. In the underlying analyses a comparison of the flow alteration from pathological to treated was performed. A comparison to a healthy version of the vessel would provide further insights into the Contour performance regarding flow alteration as was performed in Korte et al. [155].

5.6.3 Longitudinal Contour displacement and its impact on hemodynamics

In the patient-specific cases derived from in vivo data, six out of eight patients underwent two follow-up scans at varying temporal intervals after Contour deployment. The specific time points for follow-up imaging for each patient are detailed in Table 5.6. These additional longitudinal imaging datasets enabled a more comprehensive assessment of the treatment effects. Particular emphasis was placed on analyzing the displacement of the Contour over time. The evaluation focused on ostium-related hemodynamics and morphological interactions between the ostium and the Contour. Specifically, the analysis included, first, the velocity distribution across the ostium surface and the distance between the Contour and the neck curve of the ostium, second, the flow distribution into adjacent branches, and third, a comparison between intra-aneurysmal hemodynamics and the associated morphological parameters.

Ostium surface velocity and distance of Contour to neck curve

In Figure 5.16 the calculated ostium surfaces colored with the temporal mean velocity for each time instance (pre interventional, post interventional FU 1, and FU 2 are shown for the six patient data P1, P2, P5-8. Additionally to the velocity distribution on the ostium surface, the distance of the neck curve to the Contour crossing through the ostium is visualized with pie charts. The neck curve is the extracted curve on the aneurysm wall, which separates the parent vessel from the IA dome and serves therefor as boundary of the ostium surface as explained in section 2.1. The crossing of the Contour through the ostium separates the ostium into the part inside and outside of the Contour. The distance is visualized in mm with a scale from 0.25 mm to 1.75 mm.

As already found out with the investigation of the post-interventional data only, the velocity on the ostium surface decreased for all patients except for P2 after Contour deployment. This applied as well to the FU cases when compared to the pre-state. However, qualitatively no specific further reduction in flow on the ostium can be seen from post-interventional to FU1 or FU2. As visible especially in P1 FU1, P2 & P5 Post/FU1/FU2, and P8 FU1, the Contour reduced the flow on the ostium surface as expected and higher velocity was visible outside of the placed Contour. This applied to all cases in varying ranges. Since the numerical investigation of the longitudinal efficacy of the Contour is not yet further researched in existing studies, a comparison to in silico outcomes is difficult. Nevertheless, in vivo studies showed that the Contour has a longitudinal efficacy with an increasing reduction in flow over time [174].

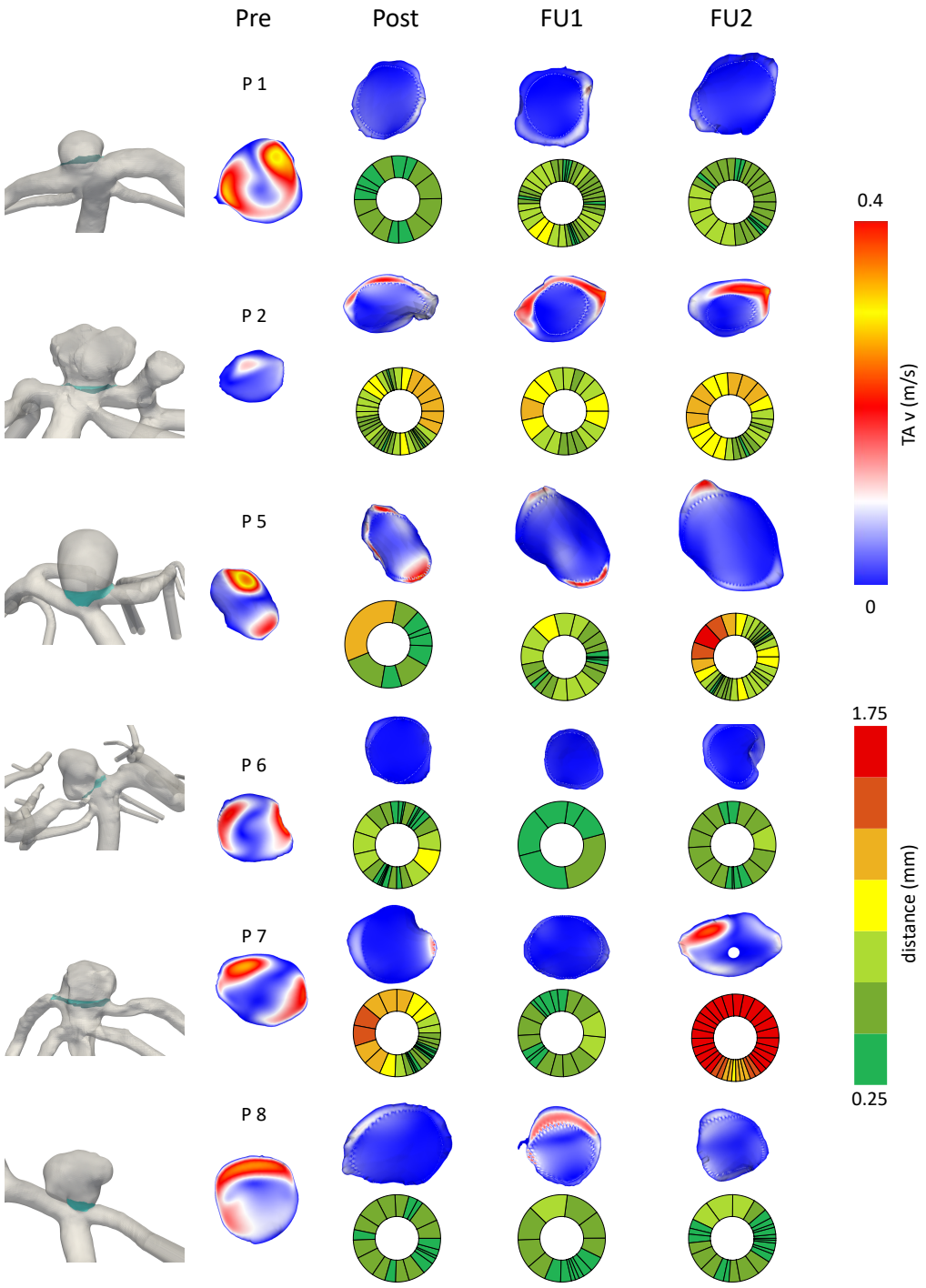


Figure 5.16: Qualitative visualization of the time-averaged (TA) velocity (v) distribution on the ostium surfaces of the six patient-specific cases including follow-up analysis. The according vessel model in pre-state is shown on the left with the ostium colored in blue. Additionally, the circular distances from the Contour crossing the ostium surface to ostium neck curve are shown as pie charts below each ostium.

This and further studies dealing with in vivo Contour deployment found an increase in flow reduction and a thrombus formation inside the Contour [79, 174, 114]. The latter could increase the flow reduction further, but is not reflected in this in silico approach due to numerical restrictions. Though simulation of thrombus formation in numerical hemodynamic analyses has further grown within the last few years, this highly important mathematical modeling is not yet fully understood and still carries a high computational effort [34]. Thus, here in this thesis each patient FU served as if the medical scan was carried out during intervention and no thrombus has formed yet. This led to the assumption that no further increase in TE could be found in the longitudinal qualitative evaluation.

Additionally, the space between the Contour and the aneurysm wall visualized by the distance pie charts were considered. As shown in Figure 5.16 the distance did not provide a specific longitudinal outcome by either an increase or decrease over time per patient. Moreover, qualitatively higher velocities can be either found in areas with low or high distances to the aneurysmal wall. This can be affected by the direction of the jet inflowing to the aneurysm directed by the parent vessel. Additionally, the radiopaque marker might influence the flow diversion into the aneurysm dome.

Side branch flow

Since the data comprised bifurcation aneurysms, the flow jet through the parent vessel directly led into the aneurysm dome, which was then diverted by the Contour. This affected the flow alteration through the two adjacent side branches of the vessel. In order to quantify this flow diversion of each of the six patients, the TE of outflow is shown in Figure 5.17. The TE was compared for all time instances to the pre-interventional state. As shown in Figure 5.7 the flow into the two adjacent vessel (left and right) was examined. Since flow alteration is meant to be preserved by the Contour, the aim is to keep a low TE in branch flow alteration. A positive TE depicts an increase in flow, while a negative TE depicts a decrease. The flow alteration did not reveal a specific trend regarding the longitudinal behavior. The TE of flow alteration increased for P1, P2 and P6, and decreased for P5. Within P7 and P8, a decrease from post to FU1 and an increase to FU2 was visible. Moreover, the magnitudes of the decrease and increase varied for all cases and time instances without any expressive trend. Here as well, no significant correlation to any morphological parameter was found to explain these alterations.
In comparison to the other flow disrupting devices, the Contour affects the parent vessel flow due to the radiopaque marker being placed outside of the aneurysm dome. This is not the case when a WEB device is applied [230] or coil embolization is performed [276]. However, the radiopaque marker should on the contrary serve as an aid to restore the pre-pathological flow condition through the parent vessel by mimicking the bifurcation. As already mentioned before, the comparison to the pre-pathological state could not be addressed in this thesis, making the evaluation of the effectiveness of the flow alteration challenging in this case.

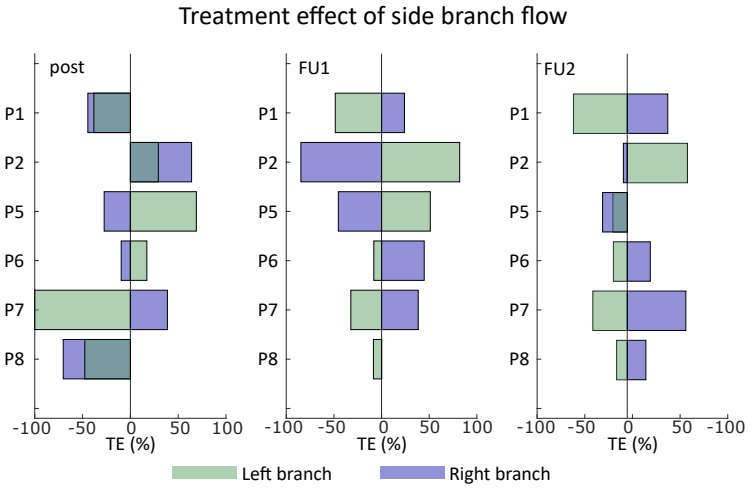


Figure 5.17: Longitudinal flow diversion into left and right vessel branch of the six patients including a follow-up investigation. For each time point (post-interventional (post), first follow-up (FU1) and second follow-up (FU2)) the treatment effect (TE) is shown in %.

Statistical comparison of hemodynamics and ostium related morphological parameters

In the previous section, the unsteady longitudinal outcome of the hemodynamic results was presented. In the databases given, no significant reduction of flow was found over time for any of the patients analyzed. Thus, in a next step, the area of the ostium not covered by the Contour was estimated and set into proportion to the full ostium surface area. The resulting proportion of uncovered area on the ostium is shown in the plot (top left) in Figure 5.18 for the six patients over time, respectively. Since for each patient the FU scans were captured in varying ranges, the FU1 and FU2 time points are spread between 4 to 17 months, which is depicted in the x-axis. Time instances are connected with dashed lines to better visualize each patient's course.

For P1 (dark blue) and P8 (light blue), the uncovered area increased with the first and decreased with the second FU. Whereas within P5 (yellow), P6 (purple) and P7 (green) the uncovered area decreased first and then increased (drastically for P7) at FU2. P2 (red) exhibited an increase in uncovered area over time. The second plot (top right) in Figure 5.18 presents the coverage of the Contour inside the aneurysm dome. Dome and parent vessel are separated by the ostium surface and the covered part of the Contour features the part inside the dome separated by the ostium. As expected, similar trends of longitudinal data of each patient can be found here as with the uncovered ostium area. The remaining four plots in Figure 5.18 represent the temporal and spatial (inside the IA dome for velocity and TAWSS or through the ostium for NIR and ICI) mean values per patient of chosen hemodynamic parameters over time. These data over the three time instances per patient did not show further significant longitudinal flow reduction, as was already seen in Figure 5.16. While the effect of the treatment showed a reduction for each case compared to the pre-interventional state (except for ICI mean value of P7 at FU2), no continuous scope was found for any of the analyzed parameters. The values of FU1 and FU2 showed significant reduction when compared to the pre-interventional state, but when comparing to the post-state values or with one another, no further reduction was found.

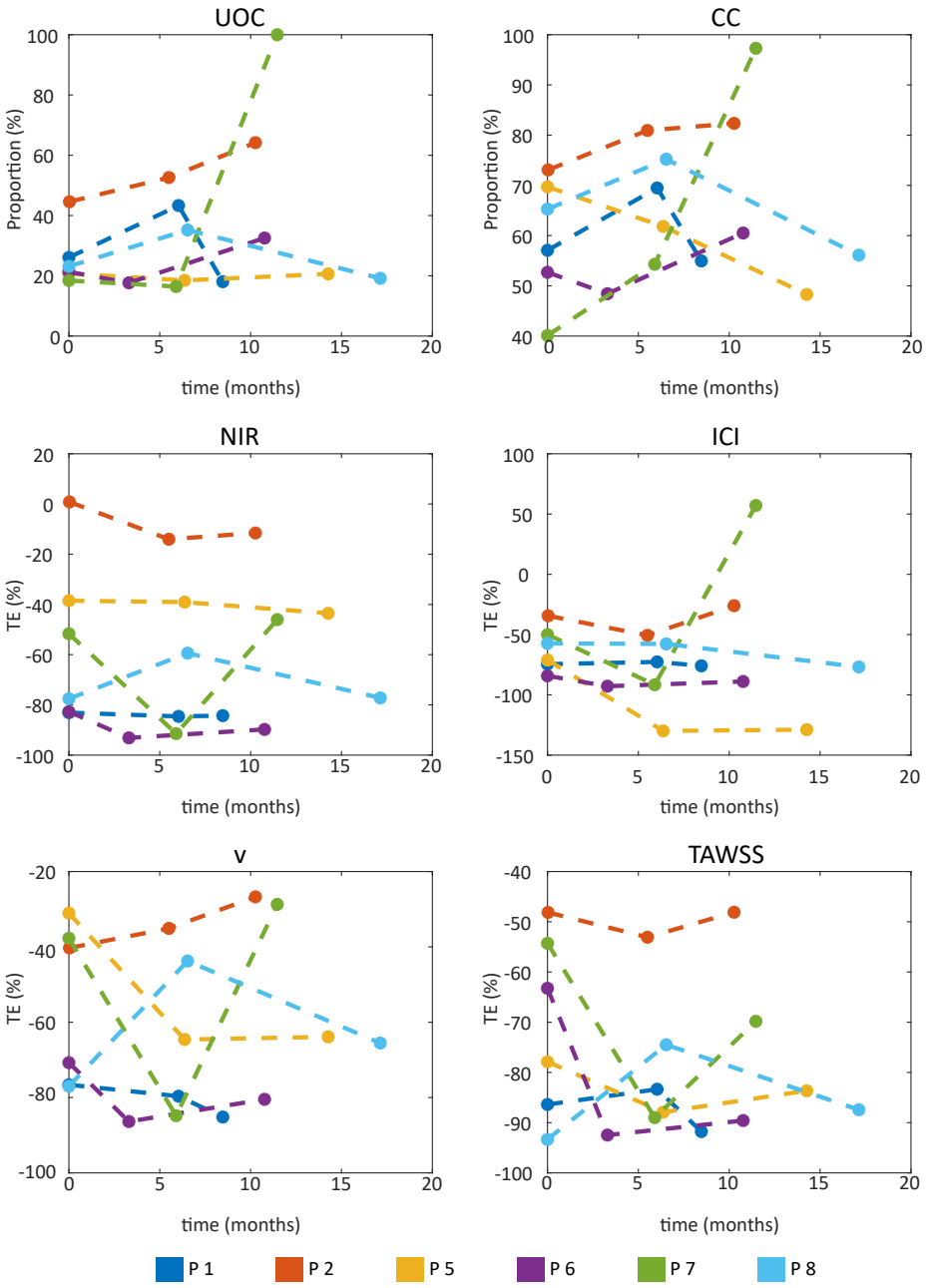


Figure 5.18: Longitudinal representation of the spatially averaged values of uncovered ostium area (UOA) by the Contour, the Contour coverage (CC) by the aneurysm dome, the mean neck inflow rate (NIR) and inflow concentration index (ICI), the mean velocity (v) inside the IA dome, and the TA wall shear stress on the aneurysm dome wall (TAWSS) for the six cases (P1, P2, P5, P6, P7, P8). The x-axis depicts the months passed after intervention.

Table 5.10: Mean values of the months, proportion of uncovered ostium area (UOA) and Contour coverage (CC) in % over all patient cases per time instant. For the hemodynamic parameters velocity, TA wall shear stress (TAWSS), neck inflow rate (NIR), and inflow concentration index (IC) the mean values of the treatment effect are presented in %. Statistical comparison of hemodynamic parameters with UOA showed significant relation (marked with *).

	post			**FU1**			**FU2**		
	mean	SD	p-value	mean	SD	p-value	mean	SD	p-value
Months	0.01	0.01		5.61	1.19		12.06	3.12	
UOA	25.72	9.59		30.62	15.37		42.43	33.15	
CC	59.66	12.25		65.03	12.47		66.59	19.02	
Velocity *	-55.57	21.38	0.002	-65.71	21.94	0.002	-58.42	25.18	0.002
TAWSS *	-70.55	18.13	0.002	-80.05	14.59	0.002	-78.39	16.76	0.002
NIR *	-55.44	33.05	0.002	-63.61	32.13	0.002	-58.73	30.25	0.002
ICI *	-61.92	18.23	0.002	-82.58	28.85	0.002	-56.58	64.66	0.026

This was not the case in the in vivo analyses in previous studies. Akhunbay-Fudge et al. [8], Liebig et al. [174], and Griessenauer et al. [105] found stable longitudinal flow reduction when examining in vivo data. As already mentioned, this might be due to expected thrombus in the aneurysm dome due to Contour placement, which was not mathematically modeled in the simulations in this thesis. Thus, independent from the longitudinal effect, the hemodynamic outcome was additionally traced back to the morphological results. The estimated hemodynamics were correlated to the uncovered ostium area. This is, to follow the aim of determining morphological markers, which most affect the positive hemodynamic outcome. In Table 5.10 the mean values over all patients at the three time instances (post, FU1, FU2) together with their standard deviation are shown for the parameters plotted in Figure 5.18. The correlation was calculated comparing the TE of the hemodynamic parameters velocity, TAWSS, NIR, and ICI with the ostium coverage, respectively. Hereby, the time instance-wise comparison including the six patients was performed.

The uncovered ostium area increased over time, showing the mean of 25.72 % for post, 30.62 % for FU1, and 42.43 % for FU2. Still, the increase was not statistically significant. Until today, the change in positioning of the Contour in the aneurysm dome was analyzed only in vivo. Here, Bhogal et al. found a displacement of the Contour up into the dome over time [31]. The FU scan was captured 3 months after intervention. This goes in line with the findings in these data, showing an overall displacement of the Contour into the dome. Moreover, Bellanger et al. placed a Contour in a MCA aneurysm, achieving correct placement during intervention and no positioning change in a six months FU. However, the one and a half year FU showed, that the device was displaced into the aneurysm dome and changed in shape ("reversed") [21]. This resulting displacement again matched with the findings in this thesis, but a change in shape to a reversed position was not found in the underlying data.

Nevertheless, the drawbacks of virtual segmentation errors and of in vivo imaging restrictions like artifacts and low resolution need to be kept in mind. The displacement described with the uncovered ostium area was further correlated with the hemodynamic results. The results showed that the uncovered ostium area significantly influenced each analyzed hemodynamic parameter at the post, FU1 and FU2 state over all patients, respectively. The corresponding p-values ($p \ll 0.05$) of the Wilcoxon-Test are shown in Table 5.10. The dependency indicated that with a higher uncovered ostium area only a lower TE of the hemodynamic parameters can be achieved, while a higher coverage of the ostium by the Contour increased the resulting TE.

These findings hold significant implications for the clinical application and training related to Contour deployment. Neurointerventionalists should prioritize the accurate placement of the Contour at the aneurysm neck, ensuring maximal coverage of the ostium area. The analysis revealed no significant correlation between Contour positioning and the diversion of flow into adjacent side branches (refer to Figure 5.17). This suggests that the placement of the Contour, including the orientation of its radiopaque marker, does not play a critical role in influencing side branch flow diversion. Instead, these results underscore the importance of achieving complete ostium coverage as a primary objective during the intervention.

5.7 Limitations

This study contains several limitations that may influence the interpretation and generalizability of the findings. First, efforts were made to simulate realistic Contour placements virtually; however, minor misalignments were observed. These include the deviations of the positioned shape and unfolding of the double-layered mesh. Despite these discrepancies, this approach represents the most feasible methodology for Contour placement and treatment outcome analysis, as direct use of micro-CT or CT-segmented Contours was not possible due to acquisition resolution and segmentation artifacts. Such a realistic virtual placement, allowing for detailed numerical evaluations of relevant hemodynamic parameters was implemented for the first time in this thesis.

Second, the CFD simulations employed generic input flow waveforms, modeled to mimic the cardiac cycle and mean flow rates observed in the basilar artery in vivo, rather than using patient-specific inflow conditions. This limits the direct applicability of the findings to individual patient cases. Third, in regard of the in vitro based data, the PC-MRI may suffer from insufficient spatial resolution, particularly in smaller IAs [234]. Additionally, metal artifacts, primarily caused by the radiopaque marker on the Contour, strongly impaired image quality. These artifacts were notably more pronounced for the Contour compared to a FDS [37]. Consequently, comparisons between CFD simulations and PC-MRI data were limited primarily to cases without the Contour, relying on pressure sensor measurements for validation.

Fourth, regarding the patient-specific data the segmentation method employed was conducted manually, relying heavily on the quality of the medical images and experience of the user. Manual smoothing of the aneurysm walls was performed separately for each case to ensure proper simulation performance. While necessary for achieving reliable CFD results, this process introduced potential segmentation errors, which are known to affect hemodynamic outcomes in CFD simulations [158]. To mitigate variability, an automated workflow was implemented to standardize the procedure and minimize segmentation-related discrepancies across cases. Moreover, the geometries of the treated patient-specific IAs were not entirely realistic, as the medical images of the IA sac were affected by artifacts due to the Contour. This was overcome by a manual adaption of the aneurysm tip based on the pre-interventional model, which was the best option to realize the numerical mesh for simulations.

Last, only 18 Contour placements were included resulting in a relatively small patient cohort and limiting the ability to draw definitive conclusions from the longitudinal results. While these cases provide valuable insights, the robustness and generalizability of the findings could be enhanced with a larger sample size. Despite this limitation, the chapter represents a pioneering effort in numerically analyzing the short-term and longitudinal in vivo and in vitro behavior of the Contour. These findings serve as a preliminary basis for future research involving larger patient cohorts.

5.8 Conclusion

Efficient treatment of IAs is crucial due to the influence of intra-aneurysmal hemodynamics on rupture risk. Traditional methods like coil embolization face limitations, particularly in WNBAs, often requiring adjunctive devices that increase procedural complexity and complication rates. Novel stand-alone flow-disrupting devices, such as the Contour and WEB, address these challenges by simplifying deployment and eliminating the need for adjunctive devices or platelet inhibition. As the efficacy of the WEB and coil embolization has been extensively studied in the past both clinically and numerically, especially the treatment outcome and safety of the Contour lacks in-depth analysis.

Thus, in this chapter the focus was set on the numerical evaluation of the treatment outcome when a Contour is deployed in WNBAs. Moreover, the impact of longitudinal Contour displacement on intra-aneurysmal hemodynamics is considered. The analysis included 8 patient-specific cases (with longitudinal follow-up for 6) and 4 phantom models (with in total 10 variations in device placement) using time-resolved CFD simulations. The latter cases could further serve as a basis for comparing the numerically assessed flow dynamics with PC-MRI experiments. The in vitro and in vivo Contour placement and deformation was mimicked using a complex virtual workflow, developed in this chapter of the thesis. By integrating in vitro experiments with in silico simulations and in vivo data, this chapter offered a comprehensive evaluation of the potential efficacy and safety of the Contour.

The novel complex workflow developed, enables the analysis of in vitro and longitudinal in vivo data of the accurate Contour placement, a method not previously addressed. This workflow represents a realistic and effective approach to numerically simulate the exact Contour placement and deformation and its subsequent effect on the intra-aneurysmal hemodynamics. The comparison to in vitro experimentally assessed flow data in the models revealed a good agreement with the numerical data.

The effectiveness of the Contour was demonstrated, providing the first detailed quantitative analysis of intra-aneurysmal flow reduction. The analysis of the short-term TE of the Contour placed inside the WNBAs revealed a significant positive reduction of flow into the IA domes for all cases considered. For both, the in vitro and in vivo based data, the Contour was found to be efficient in the in silico investigations. While Contour size had a greater impact on flow reduction, positioning influenced flow division into the side branches. These findings may be of high interest to neurointerventionalists concerning the clinical application and precise placement of the Contour, highlighting the need for further investigations into this effect.

In this chapter, the first patient-specific analysis of Contour performance was provided. The Contour displacement was evaluated longitudinally and related to intra-aneurysmal hemodynamics. Results indicated that uncovered ostium area significantly correlates with key hemodynamic parameters, namely NIR as well as the velocity and TAWSS over time. This emphasized the importance of proper Contour positioning and stability for long-term efficacy. The longitudinal hemodynamics could not be investigated due to numerical restrictions regarding thrombus modeling.

Research questions

A. Does the Contour Neurovascular System provide a numerically and experimentally proven stable and efficient blood flow disrupter for intracranial aneurysms?

   ⇒ The Contour Neurovascular System showed a significant positive flow reduction post-intervention of intra-aneurysmal and ostium-related parameters for all cases analyzed. Numerical investigations revealed a good agreement when compared to experimentally assessed flow dynamics.

B. What is the effect of different positionings and longitudinal displacement of the Contour Neurovascular System on the intra-aneurysmal flow reduction and branch flow modulation?

   ⇒ Systematic variations in positioning in angular shifts to the left and right have no significant effect on the treatment outcome of the intra-aneurysmal hemodynamics. The longitudinal displacement of the Contour Neurovascular System inside the aneurysm dome represented by the uncovered ostium area, however, showed a significant relation to the hemodynamics, leading to the assumption that a proper Contour placement covering the aneurysm ostium during intervention is highly important for the long-term effective outcome.

Future research will need to focus on advancing the evaluation of the Contour through computational approaches. In silico analyses investigating both the impact of variations in Contour positioning on hemodynamics to optimize deployment strategies and the placement of the Contour in non-established cases like side-wall IAs have to be considered. These further include the in silico analysis of Contour unfolding. Additionally, experimental and numerical comparisons will be performed using the same models to benchmark the performance of the Contour against other flow diverting devices. To better understand treatment outcomes, numerical simulations will include comparisons to pre-pathological flow conditions, enabling the assessment of flow preservation in side branches. Methodological advancements will need to incorporate thrombus formation modeling, providing critical insights into the long-term efficacy of the Contour. As the clinical deployment of Contours increases, there is a corresponding rise in recurrence cases. This necessitates a detailed investigation to identify the underlying causes of recurrence both in vivo and in silico.

Chapter 6

Final Conclusion

Outline

This chapter summarizes the key findings of this thesis, highlighting the main outcomes of the research. Additionally, potential directions for future work are discussed, outlining further investigations necessary to build upon the findings presented in this study.

6.1 Summary

Advancements in clinical imaging have enabled the reconstruction of high-resolution, patient-specific vascular models, providing a foundation for hemodynamic simulations using CFD. CFD has become a valuable tool in medical research, offering insights into complex hemodynamic phenomena. By incorporating reconstructed clinical images, patient-specific CFD simulations can be performed to assess vascular conditions non-invasively. These simulations provide both qualitative and quantitative data, supporting applications such as rupture risk assessment in asymptomatic aneurysms, treatment planning and optimization, complication management, and the development of innovative vascular implants.

Despite its potential, CFD-based hemodynamic analysis faces several challenges that limit its patient-specific accuracy. While medical imaging of the vascular lumen can realistically represent the anatomy, many aspects of the simulation require assumptions due to the lack of direct patient-specific measurements. Flow rate and pressure data are often unavailable, necessitating approximations that introduce variability in results. Additionally, reconstructing the vessel wall and determining the extent of vasculature to include in simulations remain inconsistent across research groups. Another critical limitation is that most medical images are acquired under resting conditions, while the impact of exercise on hemodynamics—despite its significant influence—remains largely overlooked in CFD analyses. Addressing these challenges is essential to enhance the clinical applicability of CFD in cerebrovascular research.

This thesis aims to refine and adapt CFD methodologies for clinical applications, with a specific focus on cerebrovascular research and treatment planning. A key objective is to identify and evaluate critical modeling parameters that influence the accuracy and reliability of CFD simulations in a medical setting. These modeling parameters include lumen segmentation, the vasculature complexity included in the analysis, the choice of outlet BC, the influence of rest and exercise, and the impact of the chosen numerical solver, especially in IA simulations. By systematically assessing these factors, this research enhances the clinical applicability of CFD models. Advanced CFD modeling is subsequently applied to evaluate the efficacy and support treatment planning for a novel flow-disrupting device designed to treat aneurysms in the cerebral circulation. The device's performance can be assessed through in silico analysis based on in vitro and patient-specific in vivo data.

The three aspects mentioned influencing the refinement of CFD methodologies — segmentation, vasculature complexity, and outlet BCs — are investigated in Chapter 3, with a focus on IAs. This part systematically evaluates five different outlet BC models, 24 real-world segmentations, and two vascular geometries. For each variation, an image-based CFD blood flow simulation was conducted using standardized assumptions for all other parameters. The hemodynamic outcomes were compared to assess both individual and interactive effects of these variations.

⇒ **Geometric accuracy is critical:** Outlet BCs primarily influence the magnitude of hemodynamic parameters. Simulations demonstrated that outdated models, such as zero-pressure boundaries, overestimated hemodynamic parameters, while advanced approaches, like model-specific flow splitting, led to lower parameter values. In contrast, variations in image segmentation affected not only the magnitude but also the distribution of flow and wall-related hemodynamics within the aneurysm. Accurate segmentation, ideally validated against 2D medical reference images, is essential for reliable numerical simulations. Additionally, including a more complex vasculature impacted both magnitude and distribution, emphasizing the need for maximal vasculature complexity for realistic hemodynamics.

⇒ **Boundary condition effects diminish with improved geometric accuracy:** The interaction between the three aspects showed that with more precise segmentation, hemodynamic variations due to BCs were reduced by up to 60 %. When a full vascular model was incorporated, BC effects changed or even disappeared, highlighting the importance of accurate anatomical modeling.

Beyond modeling methodologies, the thesis also examines the impact of rest and exercise on neuro- and cardiovascular flow in Chapter 4, focusing on both the LV in pathological states and IAs. Exercise conditions were measured for the LV and externally imposed for the IA. A moving-mesh method was implemented to simulate LV motion under rest and exercise conditions. For IAs, two CFD solvers were employed: a commercial solver preforming low-resolution simulations and an in-house DNS solver for high-resolution analysis. Validation was performed using volumetric PTV to confirm neurovascular flow simulations.

⇒ **Exercise reduces pathological cardiac energy:** In pathological LVs, kinetic energy during systole was lower in exercised cases compared to resting conditions. A similar reduction was observed when comparing mild and severe pathology, with kinetic energy decreasing during diastole in severe cases.

⇒ **High-frequency fluctuations in neurovascular pathologies:** Increased heart rates led to a rise in high-frequency velocity fluctuations within the IA dome. Power spectral density analysis at specific probe locations revealed these fluctuations, but only the high-resolution DNS solver could capture them. Lower resolution numerical simulations performed with commercial solvers failed to resolve the fluctuations, underscoring the need for high-fidelity simulations in neurovascular research.

The application of CFD in the medical field is particularly valuable for evaluating novel devices designed to treat vascular pathologies. Chapter 5 focuses on the Contour Neurovascular System, a device developed for the treatment of wide-necked bifurcation aneurysms. A workflow was established to simulate device placement based both on in vitro experiments and on in vivo medical imaging. This workflow was validated using in vitro imaging and PC-MRI flow data. Furthermore, in vivo medical data were used to analyze longitudinal device displacement within the aneurysm dome. Hemodynamic blood flow simulations were performed to assess intra-aneurysmal flow before and after treatment.

⇒ **Significant positive treatment outcome:** Hemodynamic parameters showed a substantial reduction after treatment across all cases, both in patient-specific and experimental data. Additionally, the simulated velocity values closely matched those measured in the in vitro experiments, validating the accuracy of the CFD approach. The workflow for virtual device placement was thus proven to be effective in replicating real-world deployment conditions.

⇒ **Proper device placement is crucial:** A systematic evaluation of in vitro based data showed that angular shifts of the Contour had no significant impact on treatment efficacy. However, longitudinal displacement within the aneurysm dome, as indicated by the uncovered ostium area, demonstrated a correlation with hemodynamic changes. Therefore, achieving complete coverage of the aneurysmal ostium should be a key objective.

This in silico analysis suggests that ensuring proper and stable device placement during intervention is essential for optimizing treatment outcomes.

This thesis highlights the importance of anatomical accuracy, appropriate BC selection, and physiological considerations in CFD modeling, offering critical insights for improving clinical applicability in cerebrovascular and cardiovascular research. Moreover, the potential of CFD simulations in assessing novel neurovascular devices, providing valuable insights into treatment efficacy and procedural optimization is highlighted.

6.2 Future Work

Future work involves several key directions aimed at advancing the modeling variability and clinical applicability of hemodynamic numerical simulations. One primary focus is the further improvement of modeling variability through comprehensive analysis of complex pathological vasculatures in comparison to their simplified versions. This effort should be complemented by the standardization of accurate segmentation methods, validated against high-resolution 2D medical imaging, to ensure consistent and precise input data for simulations. Another important path for future research is the extensive analysis of transitional flow states and their relationship to vascular pathologies, particularly IAs. Addressing this requires large cohort studies using high-resolution numerical simulations to derive clinically significant outcomes and treatment suggestions. However, given the high computational cost and time demands of high-resolution analysis, its direct clinical implementation remains challenging. Therefore, the development of AI-driven models is essential to establish a practical link, enabling the efficient application of transitional flow analysis in clinical settings. Further work should also explore the comprehensive evaluation of device placements, such as the Contour Neurovascular System, through in silico modeling. This includes the in silico analysis of varying device placements and positions to assess their impact on intra-aneurysmal thrombus formation and long-term treatment outcomes. This approach would enable a more comprehensive and rigorous assessment of device performance, thereby supporting more effective and precise treatment planning. Furthermore, the development and clinical integration of novel treatment devices could be facilitated addcontentsline accelerated by high-fidelity simulations that achieve widespread clinical acceptance.

On a broader scale, the integration of improved blood flow simulation and advanced treatment planning aims to enhance the understanding of cardio- and neurovascular pathologies in routine clinical practice. A primary objective of future research is the development of technically validated, evidence-based predictive tools capable of providing on-demand assessments of pathological states. For example, the ability to predict the rupture status of an IA and determine the necessity of treatment would greatly support clinicians in making informed, data-driven decisions. Furthermore, simulations could facilitate the evaluation of various treatment strategies, helping to identify the most effective approach and thereby optimizing patient care. Currently, clinical tools exist for the virtual testing of device placement in generic IAs (Sim&Size, Sim&Cure, Montpellier, France) [189]. By integrating blood flow analysis into these platforms, clinicians could predict the hemodynamic impact of treatment devices, leading to more accurate and efficient treatment planning. This approach could be informed by extensive trials using phantom models to investigate device deployment and positioning under diverse conditions, such as varying aneurysm shape, location, and size. Such integration would represent a major advancement in the personalization and optimization of vascular treatments, ultimately improving patient outcomes and streamlining clinical workflows.

Several specific steps are required to achieve these objectives:

⇒ **Automated Segmentation Methods:** Given the significant influence of segmentation on hemodynamic outcomes, as highlighted in Chapter 3, the development of reliable AI-driven segmentation techniques is essential [291]. These methods should provide standardized, accurate segmentation results that can be directly integrated into simulation workflows.

⇒ **Automated Simulation and Hemodynamic Assessment:** Building on segmented data, automated processes should be established to calculate intravascular flow and derive hemodynamis. This process should incorporate measured boundary conditions obtained from clinical practice to ensure realistic simulations. Additionally, accelerating the simulation process is vital to provide results fast for clinical decision-making.

⇒ **Large-Scale Clinical Trials:** To validate automated segmentation and simulation methods, extensive clinical trials with large patient cohorts are necessary. These trials should be further confirmed with in vivo and in vitro blood flow measurements and include long-term follow-up studies to assess the longitudinal effectiveness of simulation results.

References

[1] K. Z. Abd-Elmoniem, T. Yeramosu, J. B. Purdy, R. Ouwerkerk, J. R. Matta, H. Ishaq, K. Hawkins, K.-A. Curl, N. Dee, A. M. Gharib, et al. "The role of hiv as a risk modifier for coronary endothelial function in young adults". In: *Hiv medicine* 24.7 (2023), pp. 818–826.

[2] A. Abdelsamie, C. Chi, M. Nanjaiah, I. Skenderović, S. Suleiman, and D. Thévenin. "Direct numerical simulation of turbulent spray combustion in the spraysyn burner: impact of injector geometry". In: *Flow, turbulence and combustion* 106.2 (2021), pp. 453–469. DOI: 10.1007/s10494-020-00183-5.

[3] A. Abdelsamie, G. Janiga, and D. Thévenin. "Spectral entropy as a flow state indicator". In: *International journal of heat and fluid flow* 68 (2017), pp. 102–113. DOI: https://doi.org/10.1016/j.ijheatfluidflow.2017.09.013.

[4] A. Abdelsamie, G. Lartigue, C. E. Frouzakis, and D. Thévenin. "The taylor–green vortex as a benchmark for high-fidelity combustion simulations using low-mach solvers". In: *Computers & fluids* 223 (2021), p. 104935. DOI: 10.1016/j.compfluid.2021.104935.

[5] Abouelmagd Abdelsamie, Gordon Fru, Timo Oster, Felix Dietzsch, Gábor Janiga, and Dominique Thévenin. "Towards direct numerical simulations of low-mach number turbulent reacting and two-phase flows using immersed boundaries". In: *Computers & fluids* 131 (2016), pp. 123–141. DOI: 10.1016/j.compfluid.2016.03.017.

[6] Abouelmagd Abdelsamie, Samuel Voß, Philipp Berg, Cheng Chi, Christoph Arens, Dominique Thévenin, and Gábor Janiga. "Comparing les and urans results with a reference dns of the transitional airflow in a patient-specific larynx geometry during exhalation". In: *Computers & fluids* 255 (2023), p. 105819. DOI: 10.1016/j.compfluid.2023.105819.

[7] Y. Aghli, M. Dayyani, B. Golparvar, H. Baharvahdat, R. Blanc, M. Piotin, and H. Niazmand. "Image-based computational hemodynamic analysis of an anterior communicating aneurysm treated with the woven endobridge device". In: *Interdisciplinary neurosurgery* 25 (2021), p. 101251.

[8] C. Y. Akhunbay-Fudge, K. Deniz, A. K. Tyagi, and T. Patankar. "Endovascular treatment of wide-necked intracranial aneurysms using the novel contour neurovascular system: a single-center safety and feasibility study". In: *Journal of neurointerventional surgery* 12.10 (2020), pp. 987–992. DOI: 10.1136/neurintsurg-2019-015628.

[9] A. Alaraj, S. Amin-Hanjani, S. F. Shakur, V. A. Aletich, A. Ivanov, A. P. Carlson, G. Oh, and F. T. Charbel. "Quantitative assessment of changes in cerebral arteriovenous malformation hemodynamics after embolization". In: *Stroke* 46.4 (2015), pp. 942–947.

[10] K. Alsafi. "Radiation protection in x-ray computed tomography: literature review". In: *International journal of radiology and imaging technology* 2.2 (2016).

[11] L. M. Antunes-Correa, B. Y. Kanamura, R. C. Melo, T. S. Nobre, L. M. Ueno, F. G. Franco, F. Roveda, A. M. Braga, M. U. Rondon, P. C. Brum, et al. "Exercise training improves neurovascular control and functional capacity in heart failure patients regardless of age". In: *European journal of preventive cardiology* 19.4 (2012), pp. 822–829.

[12] S. Appanaboyina, F. Mut, R. Löhner, C. Putman, and J. Cebral. "Simulation of intracranial aneurysm stenting: techniques and challenges". In: *Computer methods in applied mechanics and engineering* 198.45-46 (2009), pp. 3567–3582.

[13] A. Arzani, J.-X. Wang, M. S. Sacks, and S. C. Shadden. "Machine learning for cardiovascular biomechanics modeling: challenges and beyond". In: *Annals of biomedical engineering* 50.6 (2022), pp. 615–627.

[14] M. H. Babiker, B. Chong, L. F. Gonzalez, S. Cheema, and D. H. Frakes. "Finite element modeling of embolic coil deployment: multifactor characterization of treatment effects on cerebral aneurysm hemodynamics". In: *Journal of biomechanics* 46.16 (2013), pp. 2809–2816.

[15] H. Baek, M. V. Jayaraman, P. D. Richardson, and G. E. Karniadakis. "Flow instability and wall shear stress variation in intracranial aneurysms". In: *Journal of the royal society, interface* 7.47 (2010), pp. 967–988. DOI: 10.1098/rsif.2009.0476.

[16] M. I. Baharoglu, C. M. Schirmer, D. A. Hoit, B.-L. Gao, and A. M. Malek. "Aneurysm inflow-angle as a discriminant for rupture in sidewall cerebral aneurysms: morphometric and computational fluid dynamic analysis". In: *Stroke* 41.7 (2010), pp. 1423–1430.

[17] R. Bakkestrøm, A. Banke, N. L. Christensen, R. Pecini, A. Irmukhamedov, M. Andersen, B. A. Borlaug, and J. E. Møller. "Hemodynamic characteristics in significant symptomatic and asymptomatic primary mitral valve regurgitation at rest and during exercise". In: *Circulation. cardiovascular imaging* 11.2 (2018), e007171. DOI: 10.1161/CIRCIMAGING.117.007171.

[18] B. B. Bates, S. K. Rerych, and R. H. Jones. "Exercise techniques for radionuclide angiocardiography". In: *Journal of nuclear medicine technology* 6.4 (1978), pp. 199–201.

[19] A. M. Bavo, A. M. Pouch, J. Degroote, J. Vierendeels, J. H. Gorman, R. C. Gorman, and P. Segers. "Patient-specific cfd models for intraventricular flow analysis from 3d ultrasound imaging: comparison of three clinical cases". In: *Journal of biomechanics* 50 (2017), pp. 144–150. DOI: 10.1016/j.jbiomech.2016.11.039.

[20] R. I. Beaudry, T. J. Samuel, J. Wang, W. J. Tucker, M. J. Haykowsky, and M. D. Nelson. "Exercise cardiac magnetic resonance imaging: a feasibility study and meta-analysis". In: *American journal of physiology-regulatory, integrative and comparative physiology* 315.4 (2018), R638–R645.

[21] G. Bellanger, J. Darcourt, A.-C. Januel, and C. Cognard. "The reversed umbrella: displacement of a contour device into an mca aneurysm 18 months after treatment". In: *Journal of neurointerventional surgery* 16.2 (2024), pp. 213–215.

[22] L. Bennati, C. Vergara, V. Giambruno, I. Fumagalli, A. F. Corno, A. Quarteroni, G. Puppini, and G. B. Luciani. "An image-based computational fluid dynamics study of mitral regurgitation in presence of prolapse". In: *Cardiovascular engineering and technology* 14.3 (2023), pp. 457–475.

[23] P. Berg, S. Saalfeld, S. Voß, T. Redel, B. Preim, G. Janiga, and O. Beuing. "Does the dsa reconstruction kernel affect hemodynamic predictions in intracranial aneurysms? an analysis of geometry and blood flow variations". In: *Journal of neurointerventional surgery* 10.3 (2018), pp. 290–296.

[24] P. Berg, L. Radtke, S. Voß, S. Serowy, G. Janiga, B. Preim, O. Beuing, and S. Saalfeld. "3dra reconstruction of intracranial aneurysms–how does voxel size influences morphologic and hemodynamic parameters". In: *2018 40th annual international conference of the ieee engineering in medicine and biology society (embc)*. IEEE. 2018, pp. 1327–1330.

[25] P. Berg, S. Saalfeld, S. Voß, O. Beuing, and G. Janiga. "A review on the reliability of hemodynamic modeling in intracranial aneurysms: why computational fluid dynamics alone cannot solve the equation". In: *Neurosurgical focus* 47.1 (2019), E15.

[26] P. Berg, S. Voß, S. Saalfeld, G. Janiga, A. W. Bergersen, K. Valen-Sendstad, J. Bruening, L. Goubergrits, A. Spuler, N. M. Cancelliere, et al. "Multiple aneurysms anatomy challenge 2018 (MATCH): Phase I: segmentation". In: *Cardiovascular engineering and technology* 9.4 (2018), pp. 565–581.

[27] P. Berg et al. "The computational fluid dynamics rupture challenge 2013–phase ii: variability of hemodynamic simulations in two intracranial aneurysms". In: *Journal of biomechanical engineering* 137.12 (2015), p. 121008. DOI: 10.1115/1.4031794.

[28] P. Berg et al. "Multiple aneurysms anatomy challenge 2018 (match)-phase ii: rupture risk assessment". In: *International journal of computer assisted radiology and surgery* 14.10 (2019), pp. 1795–1804. DOI: 10.1007/s11548-019-01986-2.

[29] M. A. Bernstein. *Handbook of mri pulse sequences*. Amsterdam and Boston: Academic Press, 2004. ISBN: 9780120928613.

[30] M. Bertolini, G. Luraghi, I. Belicchi, F. Migliavacca, and G. Colombo. "Evaluation of segmentation accuracy and its impact on patient-specific cfd analysis". In: *International journal on interactive design and manufacturing (ijidem)* 16.2 (2022), pp. 545–556.

[31] P. Bhogal, I. Lylyk, J. Chudyk, N. Perez, C. Bleise, and P. Lylyk. "The contour—early human experience of a novel aneurysm occlusion device". In: *Clinical neuroradiology* 31 (2021), pp. 147–154.

[32] P. Bijlenga, R. Gondar, S. Schilling, S. Morel, S. Hirsch, J. Cuony, M.-V. Corniola, F. Perren, D. Rüfenacht, and K. Schaller. "Phases score for the management of intracranial aneurysm: a cross-sectional population-based retrospective study". In: *Stroke* 48.8 (2017), pp. 2105–2112. DOI: 10.1161/STROKEAHA.117.017391.

[33] A. Biondi, P. Primikiris, G. Vitale, and G. Charbonnier. "Endosaccular flow disruption with the contour neurovascular system: angiographic and clinical results in a single-center study of 60 unruptured intracranial aneurysms". In: *Journal of neurointerventional surgery* 15.9 (2023), pp. 838–843. DOI: 10.1136/jnis-2022-019271.

[34] C. Blum, S. Groß-Hardt, U. Steinseifer, and M. Neidlin. "An accelerated thrombosis model for computational fluid dynamics simulations in rotary blood pumps". In: *Cardiovascular engineering and technology* 13.4 (2022), pp. 638–649.

[35] H. E. Blum and D. Müller-Wieland, eds. *Klinische pathophysiologie*. 11., unveränderte Auflage. Stuttgart and New York: Georg Thieme Verlag, 2020. ISBN: 9783132435964.

[36] I. Borazjani, J. Westerdale, E. M. McMahon, P. K. Rajaraman, J. J. Heys, and M. Belohlavek. "Left ventricular flow analysis: recent advances in numerical methods and applications in cardiac ultrasound". In: *Computational and mathematical methods in medicine* 2013 (2013), p. 395081. DOI: 10.1155/2013/395081.

[37] P. Bouillot, O. Brina, B. M. Delattre, R. Ouared, A. Pellaton, H. Yilmaz, P. Machi, K.-O. Lovblad, M. Farhat, V. M. Pereira, et al. "Neurovascular stent artifacts in 3d-tof and 3d-pcmri: influence of stent design on flow measurement". In: *Magnetic resonance in medicine* 81.1 (2019), pp. 560–572.

[38] L. Boussel, V. Rayz, A. Martin, G. Acevedo-Bolton, M. T. Lawton, R. Higashida, W. S. Smith, W. L. Young, and D. Saloner. "Phase-contrast magnetic resonance imaging measurements in intracranial aneurysms in vivo of flow patterns, velocity fields, and wall shear stress: comparison with computational fluid dynamics". In: *Magnetic resonance in medicine: an official journal of the international society for magnetic resonance in medicine* 61.2 (2009), pp. 409–417.

[39] T. Bowker, P. Watton, P. Summers, J. Byrne, and Y. Ventikos. "Rest versus exercise hemodynamics for middle cerebral artery aneurysms: a computational study". In: *American journal of neuroradiology* 31.2 (2010), pp. 317–323.

[40] J. W. Brennan and M. L. Schwartz. "Unruptured intracranial aneurysms: appraisal of the literature and suggested recommendations for surgery, using evidence-based medicine criteria". In: *Neurosurgery* 47.6 (2000), pp. 1359–1372.

[41] F. Briganti, G. Leone, M. Marseglia, G. Mariniello, F. Caranci, A. Brunetti, and F. Maiuri. "Endovascular treatment of cerebral aneurysms using flow-diverter devices: a systematic review". In: *The neuroradiology journal* 28.4 (2015), pp. 365–375.

[42] M. C. Brindise and P. P. Vlachos. "Pulsatile pipe flow transition: flow waveform effects". In: *Physics of fluids* 30.1 (2018).

[43] M. C. Brindise and P. P. Vlachos. "Proper orthogonal decomposition truncation method for data denoising and order reduction". In: *Experiments in fluids* 58.4 (2017). DOI: 10.1007/s00348-017-2320-3.

[44] W. Brinjikji, H. Cloft, G. Lanzino, and D. Kallmes. "Comparison of 2d digital subtraction angiography and 3d rotational angiography in the evaluation of dome-to-neck ratio". In: *American journal of neuroradiology* 30.4 (2009), pp. 831–834.

[45] G. Byrne, F. Mut, and J. Cebral. "Quantifying the large-scale hemodynamics of intracranial aneurysms". In: *American journal of neuroradiology* 35.2 (2014), pp. 333–338.

[46] J. V. Byrne, R. Beltechi, J. A. Yarnold, J. Birks, and M. Kamran. "Early experience in the treatment of intra-cranial aneurysms by endovascular flow diversion: a multicentre prospective study". In: *Plos one* 5.9 (2010), e12492.

[47] H. S. Byun and K. Rhee. "Cfd modeling of blood flow following coil embolization of aneurysms". In: *Medical engineering & physics* 26.9 (2004), pp. 755–761.

[48] S. M. Cameron. "Theoretical description of piv measurement errors". In: *Acta geophysica* 70.5 (2022), pp. 2379–2387. DOI: 10.1007/s11600-022-00901-9.

[49] L. Campo-Deaño, M. S. N. Oliveira, and F. T. Pinho. "A review of computational hemodynamics in middle cerebral aneurysms and rheological models for blood flow". In: *Applied mechanics reviews* 67.3 (2015). DOI: 10.1115/1.4028946.

[50] M. Castro, C. M. Putman, and J. Cebral. "Computational fluid dynamics modeling of intracranial aneurysms: effects of parent artery segmentation on intra-aneurysmal hemodynamics". In: *American journal of neuroradiology* 27.8 (2006), pp. 1703–1709.

[51] N. Cavasin, U. A. Gava, S. Magrini, and E. Cagliari. "Treatment of a ruptured fetal-type posterior communicating aneurysm with a combined approach using the new contour neurovascular system". In: *Bmj case reports* 15.4 (2022). DOI: 10.1136/bcr-2021-248065.

[52] J. R. Cebral, F. Mut, J. Weir, and C. Putman. "Quantitative characterization of the hemodynamic environment in ruptured and unruptured brain aneurysms". In: *American journal of neuroradiology* 32.1 (2011), pp. 145–151. DOI: 10.3174/ajnr.A2419.

[53] J. R. Cebral, F. Mut, J. Weir, and C. M. Putman. "Association of hemodynamic characteristics and cerebral aneurysm rupture". In: *American journal of neuroradiology* 32.2 (2011), pp. 264–270. DOI: 10.3174/ajnr.A2274.

[54] J. Cebral, F. Mut, M. Raschi, E. Scrivano, R. Ceratto, P. Lylyk, and C. Putman. "Aneurysm rupture following treatment with flow-diverting stents: computational hemodynamics analysis of treatment". In: *American journal of neuroradiology* 32.1 (2011), pp. 27–33.

[55] J. R. Cebral, M. A. Castro, O. Soto, R. Löhner, and N. Alperin. "Blood-flow models of the Circle of Willis from magnetic resonance data". In: *Journal of engineering mathematics* 47.3 (2003), pp. 369–386.

[56] J. R. Cebral, R. S. Pergolizzi Jr, and C. M. Putman. "Computational fluid dynamics modeling of intracranial aneurysms:: qualitative comparison with cerebral angiography". In: *Academic radiology* 14.7 (2007), pp. 804–813.

[57] J. R. Cebral, M. Vazquez, D. M. Sforza, G. Houzeaux, S. Tateshima, E. Scrivano, C. Bleise, P. Lylyk, and C. M. Putman. "Analysis of hemodynamics and wall mechanics at sites of cerebral aneurysm rupture". In: *Journal of neurointerventional surgery* 7.7 (2015), pp. 530–536.

[58] J. R. Cebral, M. A. Castro, J. E. Burgess, R. S. Pergolizzi, M. J. Sheridan, and C. M. Putman. "Characterization of cerebral aneurysms for assessing risk of rupture by using patient-specific computational hemodynamics models". In: *American journal of neuroradiology* 26.10 (2005), pp. 2550–2559.

[59] M. D. Cheitlin et al. "Acc/aha/ase 2003 guideline update for the clinical application of echocardiography: summary article". In: *Journal of the american college of cardiology* 42.5 (2003), pp. 954–970. DOI: 10.1016/S0735-1097(03)01065-9.

[60] C. Chi, A. Abdelsamie, and D. Thévenin. "A directional ghost-cell immersed boundary method for incompressible flows". In: *Journal of computational physics* 404 (2020), p. 109122. DOI: 10.1016/j.jcp.2019.109122.

[61] V. K. Chivukula, L. Marsh, F. Chassagne, M. C. Barbour, C. M. Kelly, S. Levy, C. Geindreau, S. R. d. Roscoat, L. J. Kim, M. R. Levitt, et al. "Lagrangian trajectory simulation of platelets and synchrotron microtomography augment hemodynamic analysis of intracranial aneurysms treated with embolic coils". In: *Journal of biomechanical engineering* 143.7 (2021), p. 071002.

[62] C. Chnafa, O. Brina, V. Pereira, and D. Steinman. "Better than nothing: a rational approach for minimizing the impact of outflow strategy on cerebrovascular simulations". In: *American journal of neuroradiology* 39.2 (2018), pp. 337–343.

[63] C. Chnafa, P. Bouillot, O. Brina, B. Delattre, M. Vargas, K. Lovblad, V. Pereira, and D. Steinman. "Vessel calibre and flow splitting relationships at the internal carotid artery terminal bifurcation". In: *Physiological measurement* 38.11 (2017), p. 2044.

[64] D. Collia, L. Zovatto, G. Tonti, and G. Pedrizzetti. "Comparative analysis of right ventricle fluid dynamics". In: *Frontiers in bioengineering and biotechnology* 9 (2021), p. 667408. DOI: 10.3389/fbioe.2021.667408.

[65] S. Corporation. *Contour neurovascular system size. place. done.* https://www.stryker.com/de/en/neurovascular/products/contour-neurovascular-system.html, Accessed: 24.02.25. 2025.

[66] J. Cortese, J. Caroff, V. Chalumeau, S. Gallas, L. Ikka, J. Moret, F. Sabuzi, S. D. Popescu, A. Ozanne, L. Grimaldi, et al. "Determinants of cerebral aneurysm occlusion after embolization with the web device: a single-institution series of 215 cases with angiographic follow-up". In: *Journal of neurointerventional surgery* 15.5 (2023), pp. 446–451.

[67] R. J. Damiano, D. Ma, J. Xiang, A. H. Siddiqui, K. V. Snyder, and H. Meng. "Finite element modeling of endovascular coiling and flow diversion enables hemodynamic prediction of complex treatment strategies for intracranial aneurysm". In: *Journal of biomechanics* 48.12 (2015), pp. 3332–3340.

[68] N. N. Dange and J. M. Roy. “Initial experience with the contour device in the treatment of ruptured intracranial wide-necked bifurcation aneurysms: a single-operator, multicenter study”. In: *Neurology india* 70.5 (2022), pp. 2059–2064. DOI: 10.4103/0028-3886.359281.

[69] N. N. Dange and J. M. Roy. “Initial experience with the contour device in the treatment of ruptured intracranial wide-necked bifurcation aneurysms: a single-operator, multicenter study”. In: *Neurology india* 70.5 (2022), pp. 2059–2064.

[70] F. J. Detmer, B. J. Chung, F. Mut, M. Slawski, F. Hamzei-Sichani, C. Putman, C. Jiménez, and J. R. Cebral. “Development and internal validation of an aneurysm rupture probability model based on patient characteristics and aneurysm location, morphology, and hemodynamics”. In: *International journal of computer assisted radiology and surgery* 13.11 (2018), pp. 1767–1779. DOI: 10.1007/s11548-018-1837-0.

[71] S. Dhar, M. Tremmel, J. Mocco, M. Kim, J. Yamamoto, A. H. Siddiqui, L. N. Hopkins, and H. Meng. “Morphology parameters for intracranial aneurysm rupture risk assessment”. In: *Neurosurgery* 63.2 (2008), 185–96, discussion 196–7. DOI: 10.1227/01.NEU.0000316847.64140.81.

[72] F. Diana, M. de Dios Lascuevas, S. Peschillo, E. Raz, S. Yoshimura, M. Requena Ruiz, D. H. Morales, and A. Tomasello. “Intrasaccular flow disruptor-assisted coiling of intracranial aneurysms using the novel contour neurovascular systems and neqstent: a single-center safety and feasibility study”. In: *Brain sciences* 12.8 (2022). DOI: 10.3390/brainsci12080991.

[73] Y. Ding, D. Lewis, R. Kadirvel, D. Dai, and D. F. Kallmes. “The woven endobridge: a new aneurysm occlusion device”. In: *American journal of neuroradiology* 32.3 (2011), pp. 607–611.

[74] A. A. Dmytriw, M. M. Salem, V. X. D. Yang, T. Krings, V. M. Pereira, J. M. Moore, and A. J. Thomas. “Endosaccular flow disruption: a new frontier in endovascular aneurysm management”. In: *Neurosurgery* 86.2 (2020), pp. 170–181. DOI: 10.1093/neuros/nyz017.

[75] M. J. Durka, I. H. Wong, D. F. Kallmes, D. Pasalic, F. Mut, M. Jagani, P. J. Blanco, J. R. Cebral, and A. M. Robertson. “A data-driven approach for addressing the lack of flow waveform data in studies of cerebral arterial flow in older adults”. In: *Physiological measurement* 39.1 (2018), p. 015006. DOI: 10.1088/1361-6579/aa9f46.

[76] N. Etminan, H.-S. Chang, K. Hackenberg, N. K. De Rooij, M. D. Vergouwen, G. J. Rinkel, and A. Algra. “Worldwide incidence of aneurysmal subarachnoid hemorrhage according to region, time period, blood pressure, and smoking prevalence in the population: a systematic review and meta-analysis”. In: *Jama neurology* 76.5 (2019), pp. 588–597.

[77] D. Fabbri, Q. Long, S. Das, and M. Pinelli. “Computational modelling of emboli travel trajectories in cerebral arteries: influence of microembolic particle size and density”. In: *Biomechanics and modeling in mechanobiology* 13.2 (2014), pp. 289–302.

[78] F. Faletra, U. La Marchesina, R. Bragato, and A. Grimaldi. “Insufficienza mitralica”. In: *Italian heart journal. supplement : official journal of the italian federation of cardiology* 3.5 (2002), pp. 486–494.

[79] Félix Gallo-Pineda, Miriam Fernández-Gómez, Carlos Domínguez-Rodríguez, José Ignacio Gallego-León, Carlos Hidalgo-Barranco, Teresa Díaz-Martí, and Antonio Romance-García. “Evaluating efficacy and complications of contour intrasaccular device in cerebral aneurysm management: a multicenter analysis”. In: *World neurosurgery* (2024). DOI: 10.1016/j.wneu.2024.01.017.

[80] G. G. Ferguson. “Turbulence in human intracranial saccular aneurysms”. In: *Journal of neurosurgery* 33.5 (1970), pp. 485–497.

[81] J. H. Ferziger and M. Perić. *Computational methods for fluid dynamics*. 3rd, rev. ed. Berlin, Heidelberg, and New York: Springer, 2002. ISBN: 978-3-540-42074-3.

[82] D. Fiorella, A. S. Arthur, R. Chiacchierini, E. Emery, A. Molyneux, and L. Pierot. "How safe and effective are existing treatments for wide-necked bifurcation aneurysms? literature-based objective performance criteria for safety and effectiveness". In: *Journal of neurointerventional surgery* 9.12 (2017), pp. 1197–1201.

[83] M. D. Ford and U. Piomelli. "Exploring high frequency temporal fluctuations in the terminal aneurysm of the basilar bifurcation". In: *Journal of biomechanical engineering* 134 (2012).

[84] M. D. Ford, H. N. Nikolov, J. S. Milner, S. P. Lownie, E. M. DeMont, W. Kalata, F. Loth, D. W. Holdsworth, and D. A. Steinman. "Piv-measured versus cfd-predicted flow dynamics in anatomically realistic cerebral aneurysm models". In: *Journal of biomechanical engineering* 130.2 (2008), p. 021015. DOI: 10.1115/1.2900724.

[85] S. Frisken, N. Haouchine, R. Du, and A. J. Golby. "Using temporal and structural data to reconstruct 3d cerebral vasculature from a pair of 2d digital subtraction angiography sequences". In: *Computerized medical imaging and graphics : the official journal of the computerized medical imaging society* 99 (2022), p. 102076. DOI: 10.1016/j.compmedimag.2022.102076.

[86] J. Frösen, R. Tulamo, A. Paetau, E. Laaksamo, M. Korja, A. Laakso, M. Niemelä, and J. Hernesniemi. "Saccular intracranial aneurysm: pathology and mechanisms". In: *Acta neuropathologica* 123 (2012), pp. 773–786.

[87] A. Frydrychowicz, C. J. François, and P. A. Turski. "Four-dimensional phase contrast magnetic resonance angiography: potential clinical applications". In: *European journal of radiology* 80.1 (2011), pp. 24–35.

[88] M. Fujimoto, I. Lylyk, C. Bleise, P. Albiña, J. Chudyk, and P. Lylyk. "Long-term outcomes of the web device for treatment of wide-neck bifurcation aneurysms". In: *American journal of neuroradiology* 41.6 (2020), pp. 1031–1036.

[89] F. Gaidzik, S. Pathiraja, S. Saalfeld, D. Stucht, O. Speck, D. Thévenin, and G. Janiga. "Hemodynamic data assimilation in a subject-specific circle of willis geometry". In: *Clinical neuroradiology* 31 (2021), pp. 643–651.

[90] F. Gaidzik, M. Pravdivtseva, N. Larsen, O. Jansen, J.-B. Hövener, and P. Berg. "Luminal enhancement in intracranial aneurysms: fact or feature?—a quantitative multimodal flow analysis". In: *International journal of computer assisted radiology and surgery* 16.11 (2021), pp. 1999–2008. DOI: 10.1007/s11548-021-02486-y.

[91] F. Gärtner, T. Klintz, S. Peters, F. Bueno Neves, K. Mostafa, J. Mahnke, J. Hensler, C. Flüh, N. Larsen, and O. Jansen. "Intra-cranial aneurysm treatment with contour or web–a single center comparison of intervention times and learning curves". In: *Interventional neuroradiology* (2023), p. 15910199231179512.

[92] A. Geers, I. Larrabide, H. Morales, and A. Frangi. "Comparison of steady-state and transient blood flow simulations of intracranial aneurysms". In: *2010 annual international conference of the ieee engineering in medicine and biology*. IEEE. 2010, pp. 2622–2625.

[93] A. Geers, I. Larrabide, H. Morales, and A. Frangi. "Approximating hemodynamics of cerebral aneurysms with steady flow simulations". In: *Journal of biomechanics* 47.1 (2014), pp. 178–185.

[94] A. Geers, I. Larrabide, A. G. Radaelli, H. Bogunovic, M. Kim, H. G. Van Andel, C. Majoie, E. VanBavel, and A. Frangi. "Patient-specific computational hemodynamics of intracranial aneurysms from 3d rotational angiography and ct angiography: an in vivo reproducibility study". In: *American journal of neuroradiology* 32.3 (2011), pp. 581–586.

[95] M. Ghodrati, T. Khienwad, A. Maurer, F. Moscato, F. Zonta, H. Schima, and P. Aigner. "Validation of numerically simulated ventricular flow patterns during left ventricular assist device support". In: *The international journal of artificial organs* 44.1 (2021), pp. 30–38.

[96] S. Ghozy, B. I. Lashin, M. Elfil, C. Bilgin, H. Kobeissi, M. Shehata, R. Kadirvel, and D. F. Kallmes. "The safety and effectiveness of the contour neurovascular system for the treatment of wide-necked aneurysms: a systematic review and meta-analysis of early experience". In: *Interventional neuroradiology: journal of peritherapeutic neuroradiology, surgical procedures and related neurosciences* (2022), p. 15910199221139546. DOI: 10.1177/15910199221139546.

[97] S. Glaßer, P. Berg, M. Neugebauer, and B. Preim. "Reconstruction of 3d surface meshes for blood flow simulations of intracranial aneurysms". In: *Proceedings of the conference of the german society for computer and robotic assisted surgery*. 2015, pp. 163–168.

[98] R. Gnatowska, M. Sosnowski, and V. Uruba. "Cfd modelling and piv experimental validation of flow fields in urban environments". In: *E3s web of conferences* 14 (2017), p. 01034. DOI: 10.1051/e3sconf/20171401034.

[99] C. F. Gonzalez, Y. I. Cho, H. V. Ortega, and J. Moret. "Intracranial aneurysms: flow analysis of their origin and progression." In: *American journal of neuroradiology* 13.1 (1992), pp. 181–188.

[100] L. Goubergrits, F. Hellmeier, J. Bruening, A. Spuler, H.-C. Hege, S. Voss, G. Janiga, S. Saalfeld, O. Beuing, and P. Berg. "Multiple aneurysms anatomy challenge 2018 (MATCH): Uncertainty quantification of geometric rupture risk parameters". In: *Biomedical engineering online* 18.1 (2019), pp. 1–16.

[101] L. Goubergrits, J. Schaller, U. Kertzscher, T. Woelken, M. Ringelstein, and A. Spuler. "Hemodynamic impact of cerebral aneurysm endovascular treatment devices: coils and flow diverters". In: *Expert review of medical devices* 11.4 (2014), pp. 361–373.

[102] L. Goubergrits, K. Vellguth, L. Obermeier, A. Schlief, L. Tautz, J. Bruening, H. Lamecker, A. Szengel, O. Nemchyna, C. Knosalla, T. Kuehne, and N. Solowjowa. "Ct-based analysis of left ventricular hemodynamics using statistical shape modeling and computational fluid dynamics". In: *Frontiers in cardiovascular medicine* 9 (2022), p. 901902. DOI: 10.3389/fcvm.2022.901902.

[103] J. P. Greving, M. J. Wermer, R. D. Brown, A. Morita, S. Juvela, M. Yonekura, T. Ishibashi, J. C. Torner, T. Nakayama, G. J. Rinkel, et al. "Development of the phases score for prediction of risk of rupture of intracranial aneurysms: a pooled analysis of six prospective cohort studies". In: *The lancet neurology* 13.1 (2014), pp. 59–66.

[104] J. Grewal, R. B. McCully, G. C. Kane, C. Lam, and P. A. Pellikka. "Left ventricular function and exercise capacity". In: *Journal of the american medical association* 301.3 (2009), pp. 286–294.

[105] C. J. Griessenauer, S. Ghozy, A. Biondi, C. Hecker, F. Wodarg, T. Liebig, T. Patankar, S. Lamin, M. Martínez-Galdámez, C. Cognard, J. Fiehler, F. Dorn, A. A. Dmytriw, and M. Killer-Oberpfalzer. "Contour neurovascular system for endovascular embolization of cerebral aneurysms: a multicenter cohort study of 10 european neurovascular centers". In: *Journal of neurointerventional surgery* (2024). DOI: 10.1136/jnis-2023-021378.

[106] C. J. Griessenauer, M. Killer-Oberpfalzer, C. M. Beredjiklian, and M. Lunzer. "Microsurgical clipping after failed contour device embolization of an anterior communicating artery aneurysm: technical note". In: *Journal of neurological surgery. part a, central european neurosurgery* (2023). DOI: 10.1055/a-2103-7639.

[108] A. Günkan, L. Scarcia, M. Y. Ferreira, M. Vilardo, L. F. F. Paleare, J. E. Bocanegra-Becerra, M. E. Fouad, H. G. Maia, G. Semione, A. M. Alexandre, et al. "Safety and efficacy of the contour neurovascular system for treating intracranial aneurysms: a systematic review and meta-analysis". In: *Journal of neurointerventional surgery* (2024), Published Online First: 21 November 2024.

[109] T. Hagemeier, M. Börner, A. Bück, and E. Tsotsas. "A comparative study on optical techniques for the estimation of granular flow velocities". In: *Chemical engineering science* 131 (2015), pp. 63–75.

[110] W. D. Hall, J. W. Hurst, and H. K. Walker. *Clinical methods: the history, physical, and laboratory examinations*. 3. ed. Boston: Butterworths, 1990. ISBN: 040990077X.

[111] T. Hassan, M. Ezura, E. V. Timofeev, T. Tominaga, T. Saito, A. Takahashi, K. Takayama, and T. Yoshimoto. "Computational simulation of therapeutic parent artery occlusion to treat giant vertebrobasilar aneurysm". In: *American journal of neuroradiology* 25.1 (2004), pp. 63–68.

[112] T. Hassan, E. V. Timofeev, T. Saito, H. Shimizu, M. Ezura, T. Tominaga, A. Takahashi, and K. Takayama. "Computational replicas: anatomic reconstructions of cerebral vessels as volume numerical grids at three-dimensional angiography". In: *American journal of neuroradiology* 25.8 (2004), pp. 1356–1365.

[113] C. Hecker, E. Broussalis, J. A. R. Pfaff, S. Pikija, C. J. Griessenauer, and M. Killer-Oberpfalzer. "Comparison of the contour neurovascular system and woven endobridge device for treatment of wide-necked cerebral aneurysms at a bifurcation or sidewall". In: *Journal of neurosurgery* 139(2) (2023), pp. 563–572. DOI: 10.3171/2022.12.JNS222268.

[114] D. M. Heiferman, N. Goyal, V. Inoa, C. M. Nickele, and A. S. Arthur. "A new era in the treatment of wide necked bifurcation aneurysms: intrasaccular flow disruption". In: *Interventional neuroradiology: journal of peritherapeutic neuroradiology, surgical procedures and related neurosciences* (2022), pp. 31–36. DOI: 10.1177/15910199221094390.

[115] G. Hellstrom, W. Fischer-Colbrie, N. Wahlgren, and T. Jogestrand. "Carotid artery blood flow and middle cerebral artery blood flow velocity during physical exercise". In: *Journal of applied physiology* 81.1 (1996), pp. 413–418.

[116] M. Henningsson, S. Malik, R. Botnar, D. Castellanos, T. Hussain, and T. Leiner. "Black-blood contrast in cardiovascular mri". In: *Journal of magnetic resonance imaging* 55.1 (2022), pp. 61–80.

[117] P. G. Hewitt. "Bernoulli's principle". In: *The science teacher* 71.7 (2004), p. 51.

[118] J. E. Hippelheuser, A. Lauric, A. D. Cohen, and A. M. Malek. "Realistic non-newtonian viscosity modelling highlights hemodynamic differences between intracranial aneurysms with and without surface blebs". In: *Journal of biomechanics* 47.15 (2014), pp. 3695–3703.

[119] C. Hirsch. *Numerical computation of internal and external flows*. 2nd ed. Amsterdam: Elsevier/Butterworth-Heinemann, 2007. ISBN: 978-0-7506-6594-0.

[120] H. Hoffmann. "Violin. m-simple violin plot using matlab default kernel density estimation". In: *Inres (university of bonn), katzenburgweg* 5 (2015), p. 53115.

[121] L. S. Hong, M. A. H. M. Adib, M. S. Abdullah, and R. Hassan. "Qualitative and quantitative comparison of hemodynamics between mri measurement and cfd simulation on patient-specific cerebral aneurysm–a review". In: *Journal of advanced research in fluid mechanics and thermal sciences* 68.2 (2020), pp. 112–123.

[122] https://de.freepik.com/vektoren-kostenlos/. *Bild von macrovector auf freepik*. 2025.

[123] B. Hu, Z. Shi, U. J. Schoepf, A. Varga-Szemes, W. E. Few, and L. J. Zhang. "Computational fluid dynamics based hemodynamics in the management of intracranial aneurysms: state-of-the-art". In: *Chinese journal of academic radiology* 4.3 (2021), pp. 150–159. DOI: 10.1007/s42058-021-00081-3.

[124] F. Huang, G. Janiga, P. Berg, and S. A. Hosseini. "On flow fluctuations in ruptured and unruptured intracranial aneurysms: resolved numerical study". In: *Scientific reports* 14.1 (2024), p. 19658. DOI: 10.1038/s41598-024-70340-7.

[125] J. Hwang and H. J. Sung. "Wall-attached structures of velocity fluctuations in a turbulent boundary layer". In: *Journal of fluid mechanics* 856 (2018), pp. 958–983.

[126] H. Isoda, Y. Ohkura, T. Kosugi, M. Hirano, M. T. Alley, R. Bammer, N. J. Pelc, H. Namba, and H. Sakahara. "Comparison of hemodynamics of intracranial aneurysms between mr fluid dynamics using 3d cine phase-contrast mri and mr-based computational fluid dynamics". In: *Neuroradiology* 52 (2010), pp. 913–920.

[127] M. Ivantsits, L. Goubergrits, J.-M. Kuhnigk, M. Huellebrand, J. Bruening, T. Kossen, B. Pfahringer, J. Schaller, A. Spuler, T. Kuehne, et al. "Detection and analysis of cerebral aneurysms based on x-ray rotational angiography-the cada 2020 challenge". In: *Medical image analysis* 77 (2022), p. 102333.

[128] O. Izem, C. Maufrais, P. Obert, T. Rupp, I. Schuster, and S. Nottin. "Kinetics of left ventricular mechanics during transition from rest to exercise". In: *Medicine and science in sports and exercise* 51.9 (2019), pp. 1838–1844. DOI: 10.1249/MSS.0000000000002005.

[129] P. Jagtiani, G. S. Sioutas, J. Vivanco-Suarez, J.-K. Burkhardt, and V. M. Srinivasan. "An updated meta-analysis on the safety and effectiveness of the contour neurovascular system". In: *Interventional neuroradiology: journal of peritherapeutic neuroradiology, surgical procedures and related neurosciences* (2024), p. 15910199231226280. DOI: 10.1177/15910199231226280.

[130] K. Jain, J. Jiang, C. Strother, and K.-.-A. Mardal. "Transitional hemodynamics in intracranial aneurysms — comparative velocity investigations with high resolution lattice boltzmann simulations, normal resolution ansys simulations, and mr imaging". In: *Medical physics* 43.11 (2016), pp. 6186–6198. DOI: 10.1118/1.4964793.

[131] K. Jain, S. Roller, and K.-A. Mardal. "Transitional flow in intracranial aneurysms–a space and time refinement study below the kolmogorov scales using lattice boltzmann method". In: *Computers & fluids* 127 (2016), pp. 36–46.

[132] G. Janiga, P. Berg, S. Sugiyama, K. Kono, and D. Steinman. "The computational fluid dynamics rupture challenge 2013—Phase I: prediction of rupture status in intracranial aneurysms". In: *American journal of neuroradiology* 36.3 (2015), pp. 530–536.

[133] G. Janiga, P. Berg, O. Beuing, M. Neugebauer, R. Gasteiger, B. Preim, G. Rose, M. Skalej, and D. Thévenin. "Recommendations for accurate numerical blood flow simulations of stented intracranial aneurysms". In: *Biomedizinische technik/biomedical engineering* 58.3 (2013), pp. 303–314. DOI: 10.1515/bmt-2012-0119.

[134] G. Janiga, C. Rössl, M. Skalej, and D. Thévenin. "Realistic virtual intracranial stenting and computational fluid dynamics for treatment analysis". In: *Journal of biomechanics* 46.1 (2013), pp. 7–12.

[135] I. Jansen, J. Schneiders, W. Potters, P. Van Ooij, R. Van Den Berg, E. Van Bavel, H. Marquering, and C. Majoie. "Generalized versus patient-specific inflow boundary conditions in computational fluid dynamics simulations of cerebral aneurysmal hemodynamics". In: *American journal of neuroradiology* 35.8 (2014), pp. 1543–1548.

[136] W. Jeans. "The development and use of digital subtraction angiography". In: *The british journal of radiology* 63.747 (1990), pp. 161–168.

[137] J. Jiang and C. Strother. "Computational fluid dynamics simulations of intracranial aneurysms at varying heart rates: a "patient-specific" study". In: *Journal of biomechanical engineering* 131(9) (2009), p. 091001. DOI: 10.1115/1.3127251.

[138] Y. Jiang, G. Lu, L. Ge, R. Zou, G. Li, H. Wan, X. Leng, J. Xiang, and X. Zhang. "Hemodynamic comparison of treatment strategies for intracranial vertebral artery fusiform aneurysms". In: *Frontiers in neurology* (2022). DOI: 10.3389/fneur.2022.927135.

[139] C. Kabbasch, L. Goertz, E. Siebert, M. Herzberg, J. Borggrefe, A. Mpotsaris, F. Dorn, and T. Liebig. "Comparison of web embolization and coiling in unruptured intracranial aneurysms: safety and efficacy based on a propensity score analysis". In: *World neurosurgery* 126 (2019), e937–e943. DOI: 10.1016/j.wneu.2019.03.016.

[141] M. O. Khan, K. Valen-Sendstad, and D. A. Steinman. "Cerebral aneurysm blood flow simulations: there's solver settings and then there's solver settings." In: *Journal of biomechanics* 61 (2017), pp. 280–280.

[142] M. O. Khan, V. Toro Arana, M. Najafi, D. E. MacDonald, T. Natarajan, K. Valen-Sendstad, and D. A. Steinman. "On the prevalence of flow instabilities from high-fidelity computational fluid dynamics of intracranial bifurcation aneurysms". In: *Journal of biomechanics* 127 (2021), p. 110683. DOI: 10.1016/j.jbiomech.2021.110683.

[143] M. O. Khan, C. Chnafa, D. Gallo, F. Molinari, U. Morbiducci, D. A. Steinman, and K. Valen-Sendstad. "On the quantification and visualization of transient periodic instabilities in pulsatile flows". In: *Journal of biomechanics* 52 (2017), pp. 179–182.

[144] K. M. Khanafer, J. L. Bull, G. R. Upchurch, and R. Berguer. "Turbulence significantly increases pressure and fluid shear stress in an aortic aneurysm model under resting and exercise flow conditions". In: *Annals of vascular surgery* 21.1 (2007), pp. 67–74. DOI: 10.1016/j.avsg.2006.10.009.

[145] J. Kim, G. Hwang, B.-T. Kim, S. Q. Park, J. S. Oh, S. P. Ban, O.-K. Kwon, and J. Chung. "Safety and efficacy of flow diverter therapy for unruptured intracranial aneurysm compared to traditional endovascular strategy : a multi-center, randomized, open-label trial". eng. In: *Journal of korean neurosurgical society* 65.6 (2022), pp. 772–778. DOI: 10.3340/jkns.2022.0043.

[146] T. Kim, C. W. Oh, J. S. Bang, S. P. Ban, S. U. Lee, Y. D. Kim, and O.-K. Kwon. "Higher oscillatory shear index is related to aneurysm recanalization after coil embolization in posterior communicating artery aneurysms". In: *Acta neurochirurgica* 163 (2021), pp. 2327–2337.

[147] F. von Knobelsdorff-Brenkenhoff, M. A. Dieringer, K. Fuchs, F. Hezel, T. Niendorf, and J. Schulz-Menger. "Isometric handgrip exercise during cardiovascular magnetic resonance imaging: set-up and cardiovascular effects". In: *Journal of magnetic resonance imaging* 37.6 (2013), pp. 1342–1350.

[148] J. L. Koep, B. Bond, C. E. Taylor, A. R. Barker, S. L. Ruediger, F. K. Pizzey, J. S. Coombes, and T. G. Bailey. "The relationships between age, sex, and exercise intensity on cerebral artery hemodynamics during isometric handgrip exercise". In: *American journal of physiology-regulatory, integrative and comparative physiology* 328.1 (2025), R1–R20.

[159] H. Kortman, S. B. T. van Rooij, U. Mutlu, I. Boukrab, W. J. van Rooij, B. van der Pol, B. Burhani, and J. P. P. Peluso. "Web treatment of ruptured intracranial aneurysms: long-term follow-up of a single-center cohort of 100 patients". In: *American journal of neuroradiology* 44.1 (2023), pp. 60–64. DOI: 10.3174/ajnr.A7748.

[160] F. W. Kremkau. *Diagnostic ultrasound: principles and practice*. 6th ed. London: W.B. Saunders, 2001. ISBN: 072169330X.

[161] T. Krings, D. M. Mandell, T.-R. Kiehl, S. Geibprasert, M. Tymianski, H. Alvarez, K. G. terBrugge, and F.-J. Hans. "Intracranial aneurysms: from vessel wall pathology to therapeutic approach". In: *Nature reviews. neurology* 7.10 (2011), pp. 547–559. DOI: 10.1038/nrneurol.2011.136.

[162] Kristian Valen-Sendstad, Kent-André Mardal, and David A. Steinman. "High-resolution cfd detects high-frequency velocity fluctuations in bifurcation, but not sidewall, aneurysms". In: *Journal of biomechanics* 46.2 (2013), pp. 402–407. DOI: 10.1016/j.jbiomech.2012.10.042.

[163] Z. Kulcsár, L. Augsburger, P. Reymond, V. M. Pereira, S. Hirsch, A. S. Mallik, J. Millar, S. G. Wetzel, I. Wanke, and D. A. Rüfenacht. "Flow diversion treatment: intra-aneurismal blood flow velocity and wss reduction are parameters to predict aneurysm thrombosis". In: *Acta neurochirurgica* 154 (2012), pp. 1827–1834.

[164] Z. Kulcsár, U. Ernemann, S. G. Wetzel, A. Bock, S. Goericke, V. Panagiotopoulos, M. Forsting, D. A. Ruefenacht, and I. Wanke. "High-profile flow diverter (silk) implantation in the basilar artery: efficacy in the treatment of aneurysms and the role of the perforators". In: *Stroke* 41.8 (2010), pp. 1690–1696.

[165] I. Larrabide, M. Kim, L. Augsburger, M. C. Villa-Uriol, D. Rüfenacht, and A. F. Frangi. "Fast virtual deployment of self-expandable stents: method and in vitro evaluation for intracranial aneurysmal stenting". In: *Medical image analysis* 16.3 (2012), pp. 721–730.

[166] D. Larsson, J. H. Spuhler, S. Petersson, T. Nordenfur, M. Colarieti-Tosti, J. Hoffman, R. Winter, and M. Larsson. "Patient-specific left ventricular flow simulations from transthoracic echocardiography: robustness evaluation and validation against ultrasound doppler and magnetic resonance imaging". In: *Ieee transactions on medical imaging* 36.11 (2017), pp. 2261–2275. DOI: 10.1109/TMI.2017.2718218.

[167] H. Le, P. Moin, and J. Kim. "Direct numerical simulation of turbulent flow over a backward-facing step". In: *Journal of fluid mechanics* 330 (1997), pp. 349–374.

[168] K. S. Lee, J. J. Zhang, V. Nguyen, J. Han, J. N. Johnson, R. Kirollos, and M. Teo. "The evolution of intracranial aneurysm treatment techniques and future directions". In: *Neurosurgical review* 45.1 (2022), pp. 1–25.

[169] Leibniz Supercomputing Centre. *Supermuc-ng: gauss centre for supercomputing.* URL: www.gauss-centre.eu.

[170] B. Li, T. Liu, J. Liu, Y. Liu, B. Cao, X. Zhao, W. Wang, M. Shi, L. Zhang, K. Xu, et al. "Reliability of using generic flow conditions to quantify aneurysmal haemodynamics: a comparison against simulations incorporating boundary conditions measured in vivo". In: *Computer methods and programs in biomedicine* 225 (2022), p. 107034.

[171] W. Li, S. Wang, Z. Tian, W. Zhu, Y. Zhang, Y. Zhang, Y. Wang, K. Wang, X. Yang, and J. Liu. "Discrimination of intracranial aneurysm rupture status: patient-specific inflow boundary may not be a must-have condition in hemodynamic simulations". In: *Neuroradiology* 62 (2020), pp. 1485–1495.

[172] F. Liang, X. Liu, R. Yamaguchi, and H. Liu. "Sensitivity of flow patterns in aneurysms on the anterior communicating artery to anatomic variations of the cerebral arterial network". In: *Journal of biomechanics* 49.15 (2016), pp. 3731–3740.

[173] L. Liang, D. A. Steinman, O. Brina, C. Chnafa, N. M. Cancelliere, and V. M. Pereira. "Towards the clinical utility of cfd for assessment of intracranial aneurysm rupture–a systematic review and novel parameter-ranking tool". In: *Journal of neurointerventional surgery* 11.2 (2019), pp. 153–158.

[174] T. Liebig, M. Killer-Oberpfalzer, G. Gal, P. Schramm, A. Berlis, F. Dorn, O. Jansen, J. Fiehler, and F. Wodarg. "The safety and effectiveness of the contour neurovascular system (contour) for the treatment of bifurcation aneurysms: the cerus study". In: *Neurosurgery* 90.3 (2022), pp. 270–277. DOI: 10.1227/NEU.0000000000001783.

[175] F. Linn, G. Rinkel, A. Algra, and J. Van Gijn. "Incidence of subarachnoid hemorrhage: role of region, year, and rate of computed tomography: a meta-analysis". In: *Stroke* 27.4 (1996), pp. 625–629.

[176] H. Liu, L. Lan, J. Abrigo, H. L. Ip, Y. Soo, D. Zheng, K. S. Wong, D. Wang, L. Shi, T. W. Leung, et al. "Comparison of newtonian and non-newtonian fluid models in blood flow simulation in patients with intracranial arterial stenosis". In: *Frontiers in physiology* 12 (2021), p. 718540.

[177] J. Liu, F. Cao, N. Zhenmei, Y. Guo, Y. Li, D. Yuan, W. Jiang, and J. Yan. "Flow-diverter stents in intracranial aneurysm treatment: impact on covered cerebral artery branches". In: *International journal of surgery* 110.1 (2024), pp. 53–65.

[178] G. Lu, L. Huang, X. L. Zhang, S. Z. Wang, Y. Hong, Z. Hu, and D. Y. Geng. "Influence of hemodynamic factors on rupture of intracranial aneurysms: patient-specific 3d mirror aneurysms model computational fluid dynamics simulation". In: *American journal of neuroradiology* 32.7 (2011), pp. 1255–1261. DOI: 10.3174/ajnr.A2461.

[179] B. Lubicz, L. Collignon, G. Raphaeli, J.-P. Pruvo, M. Bruneau, O. De Witte, and X. Leclerc. "Flow-diverter stent for the endovascular treatment of intracranial aneurysms: a prospective study in 29 patients with 34 aneurysms". In: *Stroke* 41.10 (2010), pp. 2247–2253.

[180] N. Lv, C. Wang, C. Karmonik, Y. Fang, J. Xu, Y. Yu, W. Cao, J. Liu, and Q. Huang. "Morphological and hemodynamic discriminators for rupture status in posterior communicating artery aneurysms". In: *Plos one* 11.2 (2016), e0149906. DOI: 10.1371/journal.pone.0149906.

[181] M. Lyu, R. Torii, C. Liang, T. W. Peach, P. Bhogal, L. Makalanda, Q. Li, Y. Ventikos, and D. Chen. "Treatment for middle cerebral artery bifurcation aneurysms: in silico comparison of the novel contour device and conventional flow-diverters". In: *Biomechanics and modeling in mechanobiology* (2024), pp. 1–12.

[182] D. Ma, G. F. Dargush, S. K. Natarajan, E. I. Levy, A. H. Siddiqui, and H. Meng. "Computer modeling of deployment and mechanical expansion of neurovascular flow diverter in patient-specific intracranial aneurysms". In: *Journal of biomechanics* 45.13 (2012), pp. 2256–2263.

[183] Z. Ma, Y. Zhuang, X. Long, B. Yu, J. Li, Y. Yang, and Y. Yu. "Modeling and evaluation of biomechanics and hemodynamic based on patient-specific small intracranial aneurysm using fluid-structure interaction". In: *Computer methods and programs in biomedicine* 244 (2024), p. 107963.

[184] S. Madhavan and E. M. C. Kemmerling. "The effect of inlet and outlet boundary conditions in image-based cfd modeling of aortic flow". In: *Biomedical engineering online* 17 (2018), pp. 1–20.

[185] J. Madjidyar, M. Pravdivtseva, J. Hensler, O. Jansen, N. Larsen, and F. Wodarg. "Non-invasive follow-up for intracranial aneurysms treated with contour neurovascular system—comparison of digital subtraction angiography (dsa) to magnetic resonance imaging (mri) and spectral computed tomography angiography (cta) in vitro". In: *Interventional neuroradiology* (2024), p. 15910199241277907.

[186] S. Maimon, L. Gonen, E. Nossek, I. Strauss, R. Levite, and Z. Ram. "Treatment of intracranial aneurysms with the silk flow diverter: 2 years' experience with 28 patients at a single center". In: *Acta neurochirurgica* 154 (2012), pp. 979–987.

[187] S. Makino, K. Shimano, S. Shiratori, H. Nagano, and H. Ujiie. "Influence of different outflow boundary conditions on hemodynamic analysis of cerebral aneurysm". In: *Journal of biorheology* 37.1 (2023), pp. 21–34.

[188] D. Mantilla, A. Berod, A. F. Ortiz, D. D. Vera, F. Nicoud, and V. Costalat. "Heterogeneous model to evaluate cfd in intracranial bifurcation aneurysms treated with the web device to predict angiographic outcome". In: *Interventional neuroradiology* (2023), p. 15910199231152514.

[189] D. Mantilla, C. A. Ferreira-Prada, M. Galvis, O. Vargas, C. Valenzuela-Santos, P. Canci, M. Ochoa, F. Nicoud, and V. Costalat. "Clinical impact of sim & size® simulation software in the treatment of patients with cerebral aneurysms with flow-diverter pipeline stents". In: *Interventional neuroradiology* 29.1 (2023), pp. 47–55.

[190] E. B. Maramkandam et al. "Review of cfd based simulations to study the hemodynamics of cerebral aneurysms". In: *Journal of the indian institute of science* 104.1 (2024), pp. 77–110. DOI: 10.1007/s41745-024-00431-x.

[191] J. R. Mascitelli. "Management of wide-neck aneurysms in 2024: how does one make the best treatment decision when there are so many good options?" In: *Journal of neurointerventional surgery* 16.5 (2024), pp. 433–434.

[192] S. A. Matulevicius, A. Rohatgi, S. R. Das, A. L. Price, A. DeLuna, and S. C. Reimold. "Appropriate use and clinical impact of transthoracic echocardiography". In: *Journal of the american medical association internal medicine* 173.17 (2013), pp. 1600–1607. DOI: 10.1001/jamainternmed.2013.8972.

[193] W. McComb. "Theory of turbulence". In: *Reports on progress in physics* 58.10 (1995), p. 1117.

[194] MediSys. "Mr ergometer pedal - medication free, load adjusted patient activation during mr scans". In: *Hiv medicine* (accessed at January 26th, 2025). DOI: http://www.medisys.net.au/product/mr-ergometer-pedal/.

[195] V. Meschini, F. Viola, and R. Verzicco. "Heart rate effects on the ventricular hemodynamics and mitral valve kinematics". In: *Computers & fluids* 197 (2020), p. 104359.

[196] A. P. Mitsos, N. M. Kakalis, Y. P. Ventikos, and J. V. Byrne. "Haemodynamic simulation of aneurysm coiling in an anatomically accurate computational fluid dynamics model". In: *Neuroradiology* 50 (2008), pp. 341–347.

[197] J. P. Mohr. *Stroke: pathophysiology, diagnosis, and management*. 5th ed. Philadelphia, PA: Elsevier/Saunders, 2011. ISBN: 9781416054788.

[198] A. J. Molyneux, J. Birks, A. Clarke, M. Sneade, and R. S. Kerr. "The durability of endovascular coiling versus neurosurgical clipping of ruptured cerebral aneurysms: 18 year follow-up of the uk cohort of the international subarachnoid aneurysm trial (isat)". In: *The lancet* 385.9969 (2015), pp. 691–697.

[199] K. Moncion, E. Y. Allison, B. K. Al-Khazraji, M. J. MacDonald, M. Roig, and A. Tang. "What are the effects of acute exercise and exercise training on cerebrovascular hemodynamics following stroke? a systematic review and meta-analysis". In: *Journal of applied physiology* 132.6 (2022), pp. 1379–1393.

[200] H. G. Morales, I. Larrabide, A. J. Geers, M. L. Aguilar, and A. F. Frangi. "Newtonian and non-newtonian blood flow in coiled cerebral aneurysms". In: *Journal of biomechanics* 46.13 (2013), pp. 2158–2164.

[201] H. G. Morales, I. Larrabide, A. J. Geers, L. San Román, J. Blasco, J. M. Macho, and A. F. Frangi. "A virtual coiling technique for image-based aneurysm models by dynamic path planning". In: *Ieee transactions on medical imaging* 32.1 (2012), pp. 119–129.

[202] R. D. Moser, J. Kim, and N. N. Mansour. "Direct numerical simulation of turbulent channel flow up to reτ= 590". In: *Physics of fluids* 11.4 (1999), pp. 943–945.

[203] K. Mostafa, F. Bueno Neves, F. Gärtner, S. Peters, J. Hensler, N. Larsen, T. Klintz, J. Mahnke, C. Flüh, and O. Jansen. "Contour device implantation for treatment of intracranial aneurysms in the basilar tip". In: *Interventional neuroradiology* (2023), Advance online publication. DOI: https://doi.org/10.1177/15910199231219018.

[204] F. Al-Mufti, E. R. Cohen, K. Amuluru, V. Patel, M. El-Ghanem, R. Nuoman, N. Majmundar, N. S. Dangayach, and P. M. Meyers. "Bailout strategies and complications associated with the use of flow-diverting stents for treating intracranial aneurysms". In: *Interventional neurology* 8.1 (2020), pp. 38–54. DOI: 10.1159/000489016.

[205] C. D. Murray. "The physiological principle of minimum work: i. The vascular system and the cost of blood volume". In: *Proceedings of the national academy of sciences* 12.3 (1926), pp. 207–214.

[206] F. Mut, S. Appanaboyina, and J. R. Cebral. "Simulation of stent deployment in patient-specific cerebral aneurysm models for their hemodynamics analysis". In: *Summer bioengineering conference*. Vol. 43215. American Society of Mechanical Engineers. 2008, pp. 267–268.

[207] F. Mut, R. Löhner, A. Chien, S. Tateshima, F. Viñuela, C. Putman, and J. Cebral. "Computational hemodynamics framework for the analysis of cerebral aneurysms". In: *International journal for numerical methods in biomedical engineering* 27.6 (2011), pp. 822–839. DOI: 10.1002/cnm.1424.

[208] F. Nabi, A. Malaty, and D. J. Shah. "Stress cardiac magnetic resonance". In: *Current opinion in cardiology* 26.5 (2011), pp. 385–391.

[209] T. Nagai and T. Anzai. "Nyha functional classification and aha/acc stages for heart failure management". In: *Nihon rinsho. japanese journal of clinical medicine* 74 Suppl 6 (2016), pp. 340–344.

[210] B. V. Nahed, M. Bydon, A. K. Ozturk, K. Bilguvar, F. Bayrakli, and M. Gunel. "Genetics of intracranial aneurysms". In: *Neurosurgery* 60.2 (2007), 213–25, discussion 225–6. DOI: 10.1227/01.NEU.0000249270.18698.BB.

[211] M. Najafi, N. M. Cancelliere, O. Brina, P. Bouillot, M. I. Vargas, B. M. Delattre, V. M. Pereira, and D. A. Steinman. "How patient-specific do internal carotid artery inflow rates need to be for computational fluid dynamics of cerebral aneurysms?" In: *Journal of neurointerventional surgery* 13.5 (2021), pp. 459–464.

[212] P. Nakaji, L. Rangel-Castilla, E. I. Levy, R. F. Spetzler, and A. H. Siddiqui. *Decision making in neurovascular disease*. Thieme Medical Publishers Incorporated, 2018. ISBN: 9781684200573.

[213] K. S. Nayak, Y. Lim, A. E. Campbell-Washburn, and J. Steeden. "Real-time magnetic resonance imaging". In: *Journal of magnetic resonance imaging* 55.1 (2022), pp. 81–99. DOI: 10.1002/jmri.27411.

[214] M. Neidlin. "Moving mesh". In: *Github* (accessed on 1 June 2022). DOI: https://github.com/mneidlin/movingmesh.

[215] M. Neidlin, M. Büsen, C. Brockmann, M. Wiesmann, S. J. Sonntag, U. Steinseifer, and T. A. Kaufmann. "A numerical framework to investigate hemodynamics during endovascular mechanical recanalization in acute stroke". In: *International journal for numerical methods in biomedical engineering* 32.4 (2016), e02748.

[216] V.-T. Nguyen, S. N. Wibowo, Y. an Leow, H.-H. Nguyen, Z. Liang, and H. L. Leo. "A patient-specific computational fluid dynamic model for hemodynamic analysis of left ventricle diastolic dysfunctions". In: *Cardiovascular engineering and technology* 6.4 (2015), pp. 412–429. DOI: 10.1007/s13239-015-0244-8.

[217] R. A. Niezen, J. Doornbos, E. E. van der Wall, and A. de Roos. "Measurement of aortic and pulmonary flow with mri at rest and during physical exercise". In: *Journal of computer assisted tomography* 22.2 (1998), pp. 194–201.

[218] L. Obermeier, K. Vellguth, A. Schlief, L. Tautz, J. Bruening, C. Knosalla, T. Kuehne, N. Solowjowa, and L. Goubergrits. "Ct-based simulation of left ventricular hemodynamics: a pilot study in mitral regurgitation and left ventricle aneurysm patients". In: *Frontiers in cardiovascular medicine* 9 (2022), p. 828556. DOI: 10.3389/fcvm.2022.828556.

[219] J. Ognard, M. Abdelrady, and J.-C. Gentric. "Flow diverter stents". In: *Endovascular surgery of cerebral aneurysms*. Ed. by X. Lv. Singapore: Springer Nature Singapore, 2022, pp. 103–138. ISBN: 978-981-16-7102-9. DOI: 10.1007/978-981-16-7102-9_9.

[220] S. Ogoh, K. Sato, K. Okazaki, T. Miyamoto, A. Hirasawa, K. Morimoto, and M. Shibasaki. "Blood flow distribution during heat stress: cerebral and systemic blood flow". In: *Journal of cerebral blood flow & metabolism* 33.12 (2013), pp. 1915–1920.

[221] M. Olufsen, H. Tran, and J. Ottesen. "Modeling cerebral blood flow control during posture change from sitting to standing". In: *Cardiovascular engineering: an international journal* 4 (2004), pp. 47–58.

[222] T. Otani, S. Ii, M. Hirata, and S. Wada. "Computational study of the non-newtonian effect of blood on flow stagnation in a coiled cerebral aneurysm". In: *Nihon reoroji gakkaishi* 45.5 (2017), pp. 243–249.

[223] R. Ouared, I. Larrabide, O. Brina, P. Bouillot, G. Erceg, H. Yilmaz, K.-O. Lovblad, and V. M. Pereira. "Computational fluid dynamics analysis of flow reduction induced by flow-diverting stents in intracranial aneurysms: a patient-unspecific hemodynamics change perspective". In: *Journal of neurointerventional surgery* 8.12 (2016), pp. 1288–1293.

[224] C. Özcan, Ö. Kocatürk, C. Işlak, and C. Öztürk. "Integrated particle image velocimetry and fluid–structure interaction analysis for patient-specific abdominal aortic aneurysm studies". In: *Biomedical engineering online* 22.1 (2023), p. 113.

[225] P. Pagano, L. Paiusan, S. Soize, and L. Pierot. "Intracranial aneurysm treatment with intrasaccular flow disruption: comparison of web-21 and web-17 systems". In: *Journal of neurointerventional surgery* 14.9 (2022), pp. 904–909.

[226] A. S. Pearlman, T. Ryan, M. H. Picard, and P. S. Douglas. "Evolving trends in the use of echocardiography: a study of medicare beneficiaries". In: *Journal of the american college of cardiology* 49.23 (2007), pp. 2283–2291. DOI: 10.1016/j.jacc.2007.02.048.

[227] V. Pereira, O. Brina, A. M. Gonzales, A. Narata, P. Bijlenga, K. Schaller, K. Lovblad, and R. Ouared. "Evaluation of the influence of inlet boundary conditions on computational fluid dynamics for intracranial aneurysms: a virtual experiment". In: *Journal of biomechanics* 46.9 (2013), pp. 1531–1539.

[228] L. Pierot. "Flow diverter stents in the treatment of intracranial aneurysms: where are we?" In: *Journal of neuroradiology* 38.1 (2011), pp. 40–46.

[229] L. Pierot, A.-C. Januel, H. Raoult, C. Papagiannaki, K. Kadziolka, D. Herbreteau, J.-Y. Gauvrit, and C. Cognard. "Abstract 106: intra-aneurysmal flow disruption: a new approach for the endovascular treatment of intracranial aneurysms. preliminary clinical experience". In: *Stroke* 44.suppl_1 (2013). DOI: 10.1161/str.44.suppl-1.A106.

[230] L. Pierot, I. Szikora, X. Barreau, M. Holtmannspoetter, L. Spelle, J. Klisch, D. Herbreteau, V. Costalat, J. Fiehler, A.-C. Januel, et al. "Aneurysm treatment with the woven endobridge (web) device in the combined population of two prospective, multicenter series: 5-year follow-up". In: *Journal of neurointerventional surgery* 15.6 (2023), pp. 552–557.

[231] L. Pierot and A. K. Wakhloo. "Endovascular treatment of intracranial aneurysms: current status". In: *Stroke* 44.7 (2013), pp. 2046–2054. DOI: 10.1161/STROKEAHA.113.000733.

[232] C. Poelma, P. N. Watton, and Y. Ventikos. "Transitional flow in aneurysms and the computation of haemodynamic parameters". In: *Journal of the royal society, interface* 12.105 (2015). DOI: 10.1098/rsif.2014.1394.

[233] M. S. Pravdivtseva, F. Gaidzik, P. Berg, C. Hoffman, L. A. Rivera-Rivera, R. Medero, L. Bodart, A. Roldan-Alzate, M. A. Speidel, K. M. Johnson, et al. "Pseudo-enhancement in intracranial aneurysms on black-blood mri: effects of flow rate, spatial resolution, and additional flow suppression". In: *Journal of magnetic resonance imaging* 54.3 (2021), pp. 888–901.

[234] M. S. Pravdivtseva, F. Gaidzik, P. Berg, P. Ulloa, N. Larsen, O. Jansen, J.-B. Hövener, and M. Salehi Ravesh. "Influence of spatial resolution and compressed sense acceleration factor on flow quantification with 4d flow mri at 3 tesla". In: *Tomography* 8.1 (2022), pp. 457–478.

[236] M. S. Pravdivtseva, E. Peschke, T. Lindner, F. Wodarg, J. Hensler, D. Gabbert, I. Voges, P. Berg, A. J. Barker, O. Jansen, et al. "3d-printed, patient-specific intracranial aneurysm models: from clinical data to flow experiments with endovascular devices". In: *Medical physics* 48.4 (2021), pp. 1469–1484.

[237] M. S. Pravdivtseva, A. N. Pravdivtsev, S. Peters, J. Hensler, N. Larsen, J.-B. Hövener, O. Jansen, and F. Wodarg. "The effect of the size of the new contour neurovascular device for altering intraaneurysmal flow". In: *Interventional neuroradiology: journal of peritherapeutic neuroradiology, surgical procedures and related neurosciences* (2023), p. 15910199221145985. DOI: 10.1177/15910199221145985.

[238] T. Puiseux, A. Sewonu, O. Meyrignac, H. Rousseau, F. Nicoud, S. Mendez, and R. Moreno. "Reconciling pc-mri and cfd: an in-vitro study". In: *Nmr in biomedicine* 32.5 (2019), e4063.

[239] E. Qaja and P. Theetha Kariyanna. *Statpearls: carotid artery surgery*. Treasure Island (FL), 2025.

[240] A. Quaini, S. Canic, G. Guidoboni, R. Glowinski, S. R. Igo, C. J. Hartley, W. A. Zoghbi, and S. H. Little. "A three-dimensional computational fluid dynamics model of regurgitant mitral valve flow: validation against in vitro standards and 3d color doppler methods". In: *Cardiovascular engineering and technology* 2 (2011), pp. 77–89.

[241] A. Quattrocchi, G. Garufi, G. Gugliandolo, C. De Marchis, D. Collufio, S. M. Cardali, and N. Donato. "Handgrip strength in health applications: a review of the measurement methodologies and influencing factors". In: *Sensors* 24.16 (2024), p. 5100.

[242] A. Radomi, L. Goertz, R. Forbrig, M. Pflaeging, C. Kabbasch, and T. Liebig. "Safety and efficacy of the contour neurovascular system for intracranial aneurysm treatment: a retrospective analysis of 76 patients". In: *Journal of neurosurgery* (2024), pp. 1–9. DOI: 10.3171/2024.5.JNS232852.

[243] H. Rajabzadeh-Oghaz, P. van Ooij, S. S. Veeturi, V. M. Tutino, J. J. Zwanenburg, and H. Meng. "Inter-patient variations in flow boundary conditions at middle cerebral artery from 7t pc-mri and influence on computational fluid dynamics of intracranial aneurysms". In: *Computers in biology and medicine* 120 (2020), p. 103759.

[244] M. Ramachandran, R. Retarekar, R. E. Harbaugh, D. Hasan, B. Policeni, R. Rosenwasser, C. Ogilvy, and M. L. Raghavan. "Sensitivity of quantified intracranial aneurysm geometry to imaging modality". In: *Cardiovascular engineering and technology* 4 (2013), pp. 75–86.

[245] M. Raschi, F. Mut, G. Byrne, C. M. Putman, S. Tateshima, F. Viñuela, T. Tanoue, K. Tanishita, and J. R. Cebral. "Cfd and piv analysis of hemodynamics in a growing intracranial aneurysm". In: *International journal for numerical methods in biomedical engineering* 28.2 (2012), pp. 214–228. DOI: 10.1002/cnm.1459.

[246] V. L. Rayz, L. Boussel, G. Acevedo-Bolton, A. J. Martin, W. L. Young, M. T. Lawton, R. Higashida, and D. Saloner. "Numerical simulations of flow in cerebral aneurysms: comparison of cfd results and in vivo mri measurements". In: *Journal of biomechanical engineering* 130.5 (2008), p. 051011. DOI: 10.1115/1.2970056.

[247] V. L. Rayz and A. A. Cohen-Gadol. "Hemodynamics of cerebral aneurysms: connecting medical imaging and biomechanical analysis". In: *Annual review of biomedical engineering* 22.1 (2020), pp. 231–256.

[248] Y. Ren, Q. Chen, and Z. Y. Li. "A 3D numerical study of the collateral capacity of the Circle of Willis with anatomical variation in the posterior circulation". In: *Biomedical engineering online* 14 (Suppl 1 2015), S11.

[249] S. K. Rerych, P. M. Scholz, G. E. Newman, D. C. Sabiston Jr, and R. H. Jones. "Cardiac function at rest and during exercise in normals and in patients with coronary heart disease: evaluation by radionuclide angiocardiography". In: *Annals of surgery* 187.5 (1978), p. 449.

[250] M. Rezaeitaleshmahalleh, Z. Lyu, N. Mu, and J. Jiang. "Using convolutional neural network-based segmentation for image-based computational fluid dynamics simulations of brain aneurysms: initial experience in automated model creation". In: *Journal of mechanics in medicine and biology* 23.4 (2023).

[251] A. J. Ringer. *Intracranial aneurysms*. London: Academic Press, An imprint of Elsevier, 2018. ISBN: 978-0-12-811740-8.

[252] A. Robertson and P. Watton. "Computational fluid dynamics in aneurysm research: critical reflections, future directions". In: *American journal of neuroradiology* 33.6 (2012), pp. 992–995.

[253] C. Roloff and P. Berg. "Effect of flow diverter stent malposition on intracranial aneurysm hemodynamics—an experimental framework using stereoscopic particle image velocimetry". In: *Plos one* 17.3 (2022), e0264688.

[254] C. Roloff, D. Stucht, O. Beuing, and P. Berg. "Comparison of intracranial aneurysm flow quantification techniques: standard piv vs stereoscopic piv vs tomographic piv vs phase-contrast mri vs cfd". In: *Journal of neurointerventional surgery* 11.3 (2019), pp. 275–282. DOI: 10.1136/neurintsurg-2018-013921.

[255] B. Romner, M. Olsson, B. Ljunggren, S. Holtås, H. Säveland, L. Brandt, and B. Persson. "Magnetic resonance imaging and aneurysm clips. magnetic properties and image artifacts". In: *Journal of neurosurgery* 70.3 (1989), pp. 426–431. DOI: 10.3171/jns.1989.70.3.0426.

[256] S. Saalfeld, P. Berg, A. Niemann, M. Luz, B. Preim, and O. Beuing. "Semiautomatic neck curve reconstruction for intracranial aneurysm rupture risk assessment based on morphological parameters". In: *International journal of computer assisted radiology and surgery* 13.11 (2018), pp. 1781–1793. DOI: 10.1007/s11548-018-1848-x.

[259] S. Saalfeld, S. Voß, O. Beuing, B. Preim, and P. Berg. "Flow-splitting-based computation of outlet boundary conditions for improved cerebrovascular simulation in multiple intracranial aneurysms". In: *International journal of computer assisted radiology and surgery* 14.10 (2019), pp. 1805–1813. DOI: 10.1007/s11548-019-02036-7.

[260] Safoora Karimi, Mahsa Dabagh, Paritosh Vasava, Mitra Dadvar, Bahram Dabir, and Payman Jalali. "Effect of rheological models on the hemodynamics within human aorta: cfd study on ct image-based geometry". In: *Journal of non-newtonian fluid mechanics* 207 (2014), pp. 42–52. DOI: 10.1016/j.jnnfm.2014.03.007.

[261] T. Sano, F. Ishida, M. Tsuji, K. Furukawa, S. Shimosaka, and H. Suzuki. "Hemodynamic differences between ruptured and unruptured cerebral aneurysms simultaneously existing in the same location: 2 case reports and proposal of a novel parameter oscillatory velocity index". In: *World neurosurgery* 98 (2017), 868–e5.

[262] K. M. Saqr, S. Rashad, S. Tupin, K. Niizuma, T. Hassan, T. Tominaga, and M. Ohta. "What does computational fluid dynamics tell us about intracranial aneurysms? a meta-analysis and critical review". In: *Journal of cerebral blood flow and metabolism* 40.5 (2020), pp. 1021–1039. DOI: 10.1177/0271678X19854640.

[263] A. Sarrami-Foroushani, M. N. Esfahany, H. S. Rad, K. Firouznia, M. Shakiba, and H. Ghanaati. "Effects of variations of flow and heart rate on intra-aneurysmal hemodynamics in a ruptured internal carotid artery aneurysm during exercise". In: *Iranian journal of radiology* 13.1 (2016).

[264] K. Sato and T. Sadamoto. "Different blood flow responses to dynamic exercise between internal carotid and vertebral arteries in women". In: *Journal of applied physiology* 109.3 (2010), pp. 864–869.

[265] D. Schanz, S. Gesemann, and A. Schröder. "Shake-the-box: lagrangian particle tracking at high particle image densities". In: *Experiments in fluids* 57.5 (2016). DOI: 10.1007/s00348-016-2157-1.

[266] N. Schineis. "10 fakten über das menschliche herz". In: *Https://www.kardiologe-bayreuth.de/herz-fakten/* (2022).

[267] R. F. Schmidt and F. Lang. *Physiologie des menschen: mit pathophysiologie*. 30., neu bearbeitete und aktualisierte Aufl. Springer-Lehrbuch. Berlin, Heidelberg: Springer Medizin Verlag Heidelberg, 2007. ISBN: 978-3-540-32908-4. DOI: 10.1007/978-3-540-32910-7.

[268] J. Schneiders, H. Marquering, L. Antiga, R. Van den Berg, E. VanBavel, and C. Majoie. "Intracranial aneurysm neck size overestimation with 3d rotational angiography: the impact on intra-aneurysmal hemodynamics simulated with computational fluid dynamics". In: *American journal of neuroradiology* 34.1 (2013), pp. 121–128.

[269] W. Schröder. *Fluidmechanik*. 3., korrigierte Auflage. Vol. 7. Aachener Beiträge zur Strömungsmechanik. Aachen: Wissenschaftsverlag Mainz, 2014.

[270] A. Schulz, H. Mittelmeier, L. Wagenhofer, S. J. Backhaus, T. Lange, R. Evertz, S. Kutty, J. T. Kowallick, G. Hasenfuß, and A. Schuster. "Assessment of the cardiac output at rest and during exercise stress using real-time cardiovascular magnetic resonance imaging in hfpef-patients". In: *The international journal of cardiovascular imaging* 40.4 (2024), pp. 853–862.

[271] B. Seibert, R. P. Tummala, R. Chow, A. Faridar, S. A. Mousavi, and A. A. Divani. "Intracranial aneurysms: review of current treatment options and outcomes". eng. In: *Frontiers in neurology* 2 (2011), p. 45. DOI: 10.3389/fneur.2011.00045. eprint: 21779274.

[272] D. Sekhane and K. Mansour. "Heart rate effects on intracranial aneurysm hemodynamic". In: *Dynamical systems theory and applications*. Springer, 2021, pp. 471–489.

[273] Y. Sen, Y. Qian, A. Avolio, and M. Morgan. "Image segmentation methods for intracranial aneurysm haemodynamic research". In: *Journal of biomechanics* 47.5 (2014), pp. 1014–1019.

[274] R. S. Seymour, Q. Hu, and E. P. Snelling. "Blood flow rate and wall shear stress in seven major cephalic arteries of humans". In: *Journal of anatomy* 236.3 (2020), pp. 522–530.

[275] D. M. Sforza, C. M. Putman, and J. R. Cebral. "Hemodynamics of cerebral aneurysms". In: *Annual review of fluid mechanics* 41 (2009), pp. 91–107. DOI: 10.1146/annurev.fluid.40.111406.102126.

[276] B. Sheng, D. Wu, J. Yuan, S. Xu, Z. Li, J. Dong, N. Lai, and X. Fang. "Hemodynamic characteristics associated with paraclinoid aneurysm recurrence in patients after embolization". In: *Frontiers in neurology* 10 (2019), p. 429. DOI: 10.3389/fneur.2019.00429.

[277] M. Shojima, A. Morita, T. Kimura, M. Oshima, T. Kin, and N. Saito. "Computational fluid dynamic simulation of a giant basilar tip aneurysm with eventual rupture following hunterian ligation". In: *World neurosurg* 24 (2013).

[278] S. Sindeev, P. G. Arnold, S. Frolov, S. Prothmann, D. Liepsch, A. Balasso, P. Berg, S. Kaczmarz, and J. S. Kirschke. "Phase-contrast mri versus numerical simulation to quantify hemodynamical changes in cerebral aneurysms after flow diverter treatment". In: *Plos one* 13.1 (2018), e0190696.

[279] L. Sirovich. "Chaotic dynamics of coherent structures". In: *Physica d: nonlinear phenomena* 37.1-3 (1989), pp. 126–145. DOI: 10.1016/0167-2789(89)90123-1.

[280] S. Soldozy, P. Norat, M. Elsarrag, A. Chatrath, J. S. Costello, J. D. Sokolowski, P. Tvrdik, M. Y. S. Kalani, and M. S. Park. "The biophysical role of hemodynamics in the pathogenesis of cerebral aneurysm formation and rupture". In: *Neurosurgical focus* 47.1 (2019), E11. DOI: 10.3171/2019.4.FOCUS19232.

[283] D. A. Steinman, Y. Hoi, P. Fahy, L. Morris, M. T. Walsh, N. Aristokleous, A. S. Anayiotos, Y. Papaharilaou, A. Arzani, S. C. Shadden, et al. "Variability of computational fluid dynamics solutions for pressure and flow in a giant aneurysm: the asme 2012 summer bioengineering conference cfd challenge". In: *Journal of biomechanical engineering* 135.2 (2013), p. 021016.

[284] E. J. Stöhr, J. González-Alonso, I. Bezodis, and R. Shave. "Left ventricular energetics: new insight into the plasticity of regional contributions at rest and during exercise". In: *American journal of physiology. heart and circulatory physiology* 306 (2013). DOI: 10.1152/ajpheart.00938.2012.

[285] D. Stucht, K. A. Danishad, P. Schulze, F. Godenschweger, M. Zaitsev, and O. Speck. "Highest resolution in vivo human brain mri using prospective motion correction". In: *Plos one* 10.7 (2015), e0133921.

[286] T. Sugimoto, F. Bandera, G. Generati, E. Alfonzetti, M. Barletta, M. Losito, V. Labate, M. Rovida, M. Caracciolo, C. Pappone, G. Ciconte, and M. Guazzi. "Left atrial dynamics during exercise in mitral regurgitation of primary and secondary origin: pathophysiological insights by exercise echocardiography combined with gas exchange analysis". In: *Cardiovascular imaging* 13.1 Pt 1 (2020), pp. 25–40. DOI: 10.1016/j.jcmg.2018.12.031.

[287] I. D. Šutalo, A. V. Bui, S. Ahmed, K. Liffman, and R. Manasseh. "Modeling of flow through the Circle of Willis and cerebral vasculature to assess the effects of changes in the peripheral small cerebral vasculature on the inflows". In: *Engineering applications of computational fluid mechanics* 8 (4 Jan. 2014), pp. 609–622.

[288] B. T. Tang, C. P. Cheng, M. T. Draney, N. M. Wilson, P. S. Tsao, R. J. Herfkens, and C. A. Taylor. "Abdominal aortic hemodynamics in young healthy adults at rest and during lower limb exercise: quantification using image-based computer modeling". In: *American journal of physiology-heart and circulatory physiology* 291.2 (2006), H668–H676.

[289] C. Tang, R. Ruan, B. Pan, M. Xu, J. Huang, Z. Xiong, and Z. Zhang. "The relationship between autoimmune disorders and intracranial aneurysms in east asian and european populations: a bidirectional and multivariable two-sample mendelian randomization study". In: *Frontiers in neurology* 15 (2024), p. 1412114. ISSN: 1664-2295. DOI: 10.3389/fneur.2024.1412114.

[290] Z. Tian, J. Liu, Y. Zhang, Y. Zhang, X. Zhang, H. Zhang, M. Yang, X. Yang, and K. Wang. "Risk factors of angiographic recurrence after endovascular coil embolization of intracranial saccular aneurysms: a retrospective study using a multicenter database". In: *Frontiers in neurology* 11 (2020), p. 1026. DOI: 10.3389/fneur.2020.01026.

[291] K. M. Timmins, I. C. van der Schaaf, E. Bennink, Y. M. Ruigrok, X. An, M. Baumgartner, P. Bourdon, R. De Feo, T. Di Noto, F. Dubost, et al. "Comparing methods of detecting and segmenting unruptured intracranial aneurysms on tof-mras: the adam challenge". In: *Neuroimage* 238 (2021), p. 118216.

[292] C. Trenti, M. Ziegler, N. Bjarnegaerd, T. Ebbers, M. Lindenberger, P. Dyverfeldt, et al. "Wall shear stress and relative residence time as potential risk factors for abdominal aortic aneurysms in males: a 4d flow cardiovascular magnetic resonance case control study". In: *Journal of cardiovascular magnetic resonance* 24.1 (2022), p. 18.

[293] Z. G. Turi. "Mitral valve disease". In: *Circulation* 109.6 (2004), e38–e41.

[294] K. Valen-Sendstad and D. A. Steinman. "Mind the gap: impact of computational fluid dynamics solution strategy on prediction of intracranial aneurysm hemodynamics and rupture status indicators". In: *American journal of neuroradiology* 35.3 (2014), pp. 536–543. DOI: 10.3174/ajnr.A3793.

[295] K. Valen-Sendstad, A. W. Bergersen, Y. Shimogonya, L. Goubergrits, J. Bruening, J. Pallares, S. Cito, S. Piskin, K. Pekkan, A. J. Geers, et al. "Real-world variability in the prediction of intracranial aneurysm wall shear stress: the 2015 international aneurysm cfd challenge". In: *Cardiovascular engineering and technology* 9 (2018), pp. 544–564.

[296] K. Valen-Sendstad, K.-A. Mardal, M. Mortensen, B. A. P. Reif, and H. P. Langtangen. "Direct numerical simulation of transitional flow in a patient-specific intracranial aneurysm". In: *Journal of biomechanics* 44.16 (2011), pp. 2826–2832.

[297] K. Valen-Sendstad, K.-A. Mardal, and D. A. Steinman. "High-resolution cfd detects high-frequency velocity fluctuations in bifurcation, but not sidewall, aneurysms". In: *Journal of biomechanics* 46.2 (2013), pp. 402–407.

[298] K. Valen-Sendstad, M. Piccinelli, R. KrishnankuttyRema, and D. A. Steinman. "Estimation of inlet flow rates for image-based aneurysm cfd models: where and how to begin?" In: *Annals of biomedical engineering* 43 (2015), pp. 1422–1431.

[299] K. Valen-Sendstad, M. Piccinelli, and D. A. Steinman. "High-resolution computational fluid dynamics detects flow instabilities in the carotid siphon: implications for aneurysm initiation and rupture?" In: *Journal of biomechanics* 47.12 (2014), pp. 3210–3216.

[300] L. T. van der Kamp et al. "Risk of rupture after intracranial aneurysm growth". In: *Journal of the american medical association neurology* 78.10 (2021), pp. 1228–1235. ISSN: 2168-6149. DOI: 10.1001/jamaneurol.2021.2915.

[301] C. Vega, J. V. Kwoon, and S. D. Lavine. "Intracranial aneurysms: current evidence and clinical practice". In: *American family physician* 66.4 (2002), pp. 601–608. ISSN: 0002-838X.

[302] Venkat Keshav Chivukula, Michael R. Levitt, Alicia Clark, Michael C. Barbour, Kurt Sansom, Luke Johnson, Cory M. Kelly, Christian Geindreau, Sabine Rolland du Roscoat, Louis J. Kim, and Alberto Aliseda. "Reconstructing patient-specific cerebral aneurysm vasculature for in vitro investigations and treatment efficacy assessments". In: *Journal of clinical neuroscience* 61 (2019), pp. 153–159. ISSN: 0967-5868. DOI: 10.1016/j.jocn.2018.10.103.

[303] T. J. Vogl, E. J. Rummeny, W. Reith, and J. O. Balzer, eds. *Diagnostische und interventionelle radiologie*. Berlin: Springer, 2011. ISBN: 9783540876687. DOI: 10.1007/978-3-540-87668-7.

[304] D. Voilliot and P. Lancellotti. "Exercise testing and stress imaging in mitral valve disease". In: *Current treatment options in cardiovascular medicine* 19.3 (2017), p. 17. DOI: 10.1007/s11936-017-0516-8.

[305] S. Voß. "Unsicherheit in der hämodynamischen charakterisierung intrakranieller aneurysmen". PhD thesis. University of Magdeburg, 2022.

[306] S. Voß, O. Beuing, G. Janiga, and P. Berg. "Multiple aneurysms anatomy challenge 2018 (MATCH)—Phase Ib: effect of morphology on hemodynamics". In: *Plos one* 14.5 (2019), e0216813.

[307] A. Wagner, M. Cortsen, J. Hauerberg, B. Romner, and M. P. Wagner. "Treatment of intracranial aneurysms. reconstruction of the parent artery with flow-diverting (silk) stent". In: *Neuroradiology* 54 (2012), pp. 709–718.

[308] N. Al-Wakeel, J. F. Fernandes, A. Amiri, H. Siniawski, L. Goubergrits, F. Berger, and T. Kuehne. "Hemodynamic and energetic aspects of the left ventricle in patients with mitral regurgitation before and after mitral valve surgery". In: *Journal of magnetic resonance imaging* 42.6 (2015), pp. 1705–1712. DOI: 10.1002/jmri.24926.

[309] A. K. Wakhloo, J. Mandell, M. J. Gounis, C. Brooks, I. Linfante, J. Winer, and J. P. Weaver. "Stent-assisted reconstructive endovascular repair of cranial fusiform atherosclerotic and dissecting aneurysms: long-term clinical and angiographic follow-up". In: *Stroke* 39.12 (2008), pp. 3288–3296.

[310] H. Wan, L. Ge, L. Huang, Y. Jiang, X. Leng, X. Feng, J. Xiang, and X. Zhang. "Sidewall aneurysm geometry as a predictor of rupture risk due to associated abnormal hemodynamics". In: *Frontiers in neurology* 10 (2019), p. 841. DOI: 10.3389/fneur.2019.00841.

[311] M. Waqas, K. Vakharia, R. H. Dossani, G. B. Rajah, M. K. Tso, A. D. Gong, K. Rho, H. H. Rai, K. V. Snyder, E. I. Levy, A. H. Siddiqui, and J. M. Davies. "Transradial access for flow diversion of intracranial aneurysms: case series". In: *Interventional neuroradiology: journal of peritherapeutic neuroradiology, surgical procedures and related neurosciences* 27.1 (2021), pp. 68–74. DOI: 10.1177/1591019920938961.

[312] B. Widder and M. Görtler. *Doppler- und duplexsonographie der hirnversorgenden arterien*. 6th ed. Berlin: Springer, 2004. ISBN: 9783540022367.

[313] D. Wilcox. "Turbulence modeling for cfd. la cañada flintridge, california: dcw industries". In: *Inc. la canada* (1994).

[314] S. R. Wilson, C. Withers, S. Wilson, W. Charboneau, et al. "Diagnostic ultrasound". In: *Philadephia: elsevier mosby publisher* 853 (2005), p. 863.

[315] F. Wodarg, Y. Ozpeynirci, J. Hensler, O. Jansen, and T. Liebig. "Contour-assisted coiling with jailed microcatheter may result in better occlusion (cocojambo) in wide-necked intracranial aneurysms: proof of principle and immediate angiographic results". In: *Interventional neuroradiology: journal of peritherapeutic neuroradiology, surgical procedures and related neurosciences* 29.1 (2023), pp. 79–87. DOI: 10.1177/15910199211069782.

[316] J. Wong, R. Chabiniok, S. M. Tibby, K. Pushparajah, E. Sammut, D. Celermajer, D. Giese, T. Hussain, G. F. Greil, T. Schaeffter, et al. "Exploring kinetic energy as a new marker of cardiac function in the single ventricle circulation". In: *Journal of applied physiology* 125.3 (2018), pp. 889–900.

[317] J. Xiang, D. Ma, K. V. Snyder, E. I. Levy, A. H. Siddiqui, and H. Meng. "Increasing flow diversion for cerebral aneurysm treatment using a single flow diverter". In: *Neurosurgery* 75.3 (2014), pp. 286–294.

[318] J. Xiang, S. K. Natarajan, M. Tremmel, D. Ma, J. Mocco, L. N. Hopkins, A. H. Siddiqui, E. I. Levy, and H. Meng. "Hemodynamic-morphologic discriminants for intracranial aneurysm rupture". eng. In: *Stroke* 42.1 (2011), pp. 144–152. DOI: 10.1161/STROKEAHA.110.592923.

[319] J. Xiang, M. Tremmel, J. Kolega, E. I. Levy, S. K. Natarajan, and H. Meng. "Newtonian viscosity model could overestimate wall shear stress in intracranial aneurysm domes and underestimate rupture risk". In: *Journal of neurointerventional surgery* 4.5 (2012), pp. 351–357.

[320] D. Xu and M. Avila. "The effect of pulsation frequency on transition in pulsatile pipe flow". In: *Journal of fluid mechanics* 857 (2018), pp. 937–951.

[321] D. Xu, S. Warnecke, B. Song, X. Ma, and B. Hof. "Transition to turbulence in pulsating pipe flow". In: *Journal of fluid mechanics* 831 (2017), pp. 418–432. DOI: 10.1017/jfm.2017.620.

[322] F. Xu and S. Kenjereš. "Numerical simulations of flow patterns in the human left ventricle model with a novel dynamic mesh morphing approach based on radial basis function". In: *Computers in biology and medicine* 130 (2021), p. 104184.

[323] L. Xu, L. Gu, and H. Liu. "Exploring potential association between flow instability and rupture in patients with matched-pairs of ruptured-unruptured intracranial aneurysms". In: *Biomedical engineering online* 15.Suppl 2 (2016), p. 166. DOI: 10.1186/s12938-016-0277-8.

[324] L. Xu, F. Liang, L. Gu, and H. Liu. "Flow instability detected in ruptured versus unruptured cerebral aneurysms at the internal carotid artery". In: *Journal of biomechanics* 72 (2018), pp. 187–199. DOI: 10.1016/j.jbiomech.2018.03.014.

[325] Z. Xu, Y.-N. Rui, J. P. Hagan, and D. H. Kim. "Intracranial aneurysms: pathology, genetics, and molecular mechanisms". In: *Neuromolecular medicine* 21.4 (2019), pp. 325–343. DOI: 10.1007/s12017-019-08537-7.

[326] Yang, Z.: Yu, H., P. Huang, R. Schwieterman, and B. Ludwig. "Computational fluid dynamics simulation of intracranial aneurysms – comparing size and shape". In: *Journal of coastal life medicine* (2015). DOI: 10.12980/JCLM.3.201514JCLM-2015-0004.

[327] S. G. Yazdi, P. Geoghegan, P. Docherty, M. Jermy, and A. Khanafer. "A review of arterial phantom fabrication methods for flow measurement using piv techniques". In: *Annals of biomedical engineering* 46 (2018), pp. 1697–1721.

[328] J. Zhang, P. Zhang, K. H. Fraser, B. P. Griffith, and Z. J. Wu. "Comparison and experimental validation of fluid dynamic numerical models for a clinical ventricular assist device". In: *Artificial organs* 37.4 (2013), pp. 380–389.

[329] Y. Zhang, O. S. E. Nateras, Q. Peng, C. A. Rosende, and T. Q. Duong. "Blood flow mri of the human retina/choroid during rest and isometric exercise". In: *Investigative ophthalmology & visual science* 53.7 (2012), pp. 4299–4305.

[330] J. Zhao, Y. Farhatnia, D. M. Kalaskar, Y. Zhang, P. E. Bulter, and A. M. Seifalian. "The influence of porosity on the hemocompatibility of polyhedral oligomeric silsesquioxane poly (caprolactone-urea) urethane". In: *The international journal of biochemistry & cell biology* 68 (2015), pp. 176–186.

[331] J. Zhao, D. Kalaskar, Y. Farhatnia, X. Bai, P. E Bulter, and A. M Seifalian. "Intracranial stents past, present and the future trend: stents made with nano-particle or nanocomposite biomaterials". In: *Current medicinal chemistry* 21.37 (2014), pp. 4290–4299.

[332] J. Zhao, H. Lin, R. Summers, M. Yang, B. G. Cousins, and J. Tsui. "Current treatment strategies for intracranial aneurysms: an overview". In: *Angiology* 69.1 (2018), pp. 17–30. DOI: 10.1177/0003319717700503.

[333] M. Zhao, F. T. Charbel, N. Alperin, F. Loth, and M. Clark. "Improved phase-contrast flow quantification by three-dimensional vessel localization". In: *Magnetic resonance imaging* 18.6 (2000), pp. 697–706.

[334] G. Zhou, Y. Zhu, Y. Yin, M. Su, and M. Li. "Association of wall shear stress with intracranial aneurysm rupture: systematic review and meta-analysis". In: *Scientific reports* 7 (1 July 2017), p. 5331.

[335] G. Zhu, Q. Yuan, J. Yang, and J. H. Yeo. "The role of the circle of willis in internal carotid artery stenosis and anatomical variations: a computational study based on a patient-specific three-dimensional model". In: *Biomedical engineering online* 14 (2015), pp. 1–19.

List of own Publications

Journal articles

[107] A. Grünwald, **J. Korte**, N. Wilmanns, C. Winkler, K. Linden, U. Herberg, S. Groß-Hardt, U. Steinseifer, and M. Neidlin. "Intraventricular flow simulations in singular right ventricles reveal deteriorated washout and low vortex formation". In: *Cardiovascular engineering and technology* (2021), pp. 1–9. DOI: 10.1007/s13239-021-00598-9.

[149] **Korte, J.**, F. Gaidzik, N. Larsen, E. Schütz, T. Damm, F. Wodarg, J.-B. Hövener, O. Jansen, G. Janiga, P. Berg, et al. "In vitro and in silico assessment of flow modulation after deploying the contour neurovascular system in intracranial aneurysm models". In: *Journal of neurointerventional surgery* 16.8 (2024), pp. 815–823.

[150] **Korte, J.**, F. Gaidzik, S. Saalfeld, G. Janiga, and P. Berg. "Image-based hemodynamic simulations for intracranial aneurysms: the impact of complex vasculature". In: *International journal of computer assisted radiology and surgery* 19.4 (2024), pp. 687–697.

[152] **Korte, J.**, E. S. Klopp, and P. Berg. "Multi-dimensional modeling of cerebral hemodynamics: a systematic review". In: *Bioengineering* 11.1 (2024), p. 72.

[155] **Korte, J.**, L. M. Marsh, S. Saalfeld, D. Behme, A. Aliseda, and P. Berg. "Fusiform versus saccular intracranial aneurysms—hemodynamic evaluation of the pre-aneurysmal, pathological, and post-interventional state". In: *Journal of clinical medicine* 13.2 (2024).

[156] **Korte, J.**, L. Obermeier, K. Vellguth, F. Barbieri, F. Hellmeier, P. Berg, and L. Goubergrits. "Inter-model and inter-modality analysis of left ventricular hemodynamics: comparative study of two cfd approaches based on echocardiography and magnetic resonance imaging". In: *Gamm-mitteilungen* 47.1 (2024), e2023 70 004.

[157] **Korte, J.**, T. Rauwolf, J.-N. Thiel, A. Mitrasch, P. Groschopp, M. Neidlin, A. Schmeißer, R. Braun-Dullaeus, and P. Berg. "Hemodynamic assessment of the pathological left ventricle function under rest and exercise conditions". In: *Fluids* 8.2 (2023), p. 71.

[158] **Korte, J.**, S. Voß, G. Janiga, O. Beuing, D. Behme, S. Saalfeld, and P. Berg. "Is accurate lumen segmentation more important than outlet boundary condition in image-based blood flow simulations for intracranial aneurysms?" In: *Cardiovascular engineering and technology* 14.5 (2023), pp. 617–630. ISSN: 1869-4098. DOI: 10.1007/s13239-023-00675-1.

[258] S. Saalfeld, J. Stahl, **J. Korte**, L. M. Miller Marsh, B. Preim, O. Beuing, Y. Cherednychenko, D. Behme, and P. Berg. "Can endovascular treatment of fusiform intracranial aneurysms restore the healthy hemodynamic environment?–a virtual pilot study". In: *Frontiers in neurology* 12 (2022), p. 771694.

[281] L. Spitz, **J. Korte**, F. Gaidzik, N. Larsen, B. Preim, and S. Saalfeld. "Assessment of intracranial aneurysm neck deformation after contour deployment". In: *International journal of computer assisted radiology and surgery* (2024). ISSN: 1861-6429. DOI: 10.1007/s11548-024-03189-w.

Conference articles

[140] B. A. D. T. E. Khader, J. J. Kolliyil, **J. Korte**, N. S. Shirdade, E. W. Church, and M. C. Brindise. "Evaluating high frequency fluctuations and its effect on hemodynamics at varying heart rates in intracranial aneurysms via 4d ptv". In: *Proceedings of the international symposium on the application of laser and imaging techniques to fluid mechanics* 21 (2024), pp. 1–21. DOI: 10.55037/lxlaser.21st.202.

[151] **Korte, J.**, P. Groschopp, and P. Berg. "Resolution-based comparative analysis of 4d-phase-contrast magnetic resonance images and hemodynamic simulations of the aortic arch". In: *Current directions in biomedical engineering*. Vol. 9. 1. De Gruyter. 2023, pp. 650–653.

[153] **Korte, J.**, L. Marsh, F. Gaidzik, M. Pravdivtseva, N. Larsen, and P. Berg. "Correlation of black blood mri with image-based blood flow simulations in intracranial aneurysms". In: *Current directions in biomedical engineering* 7.2 (2021), pp. 895–898.

[154] **Korte, J.**, L. Marsh, M. Pravdivtseva, F. Gaidzik, N. Larsen, G. Janiga, and P. Berg. "Can black blood mri predict hemodynamics in intracranial aneurysms? - an analysis of in-vitro signal intensity and cfd". eng. In: *Proceedings in conference on modelling fluid flow cmff'22* 18.1 (2022), pp. 246–252.

[235] M. S. Pravdivtseva, **J. Korte**, F. Gaidzik, P. Berg, F. Wodarg, J.-B. Hövener, O. Jansen, and N. Larsen. "3d-printed aneurysm models for studying endovascular treatment efficacy". In: *Transactions on additive manufacturing meets medicine* 6.S1 (2024), pp. 1852–1852.

[257] S. Saalfeld, M. Mirzaie, S. Fatehpur, **J. Korte**, and P. Berg. "Image-based blood flow analysis of popliteal artery aneurysms – an interdisciplinary pilot study". In: *Current directions in biomedical engineering* 7.2 (2021), pp. 891–894. DOI: 10.1515/cdbme-2021-2227.

[282] L. Spitz, J. Schmidt, **J. Korte**, P. Berg, D. Behme, B. Neyazi, B. Preim, and S. Saalfeld. "Morphologic and hemodynamic analysis of intracranial mirror aneurysms". In: *Current directions in biomedical engineering*. Vol. 10. 2. De Gruyter. 2024, pp. 87–90.

Conference contribution

M. Laurel, **J. Korte**, F. Gaidzik, M. S. Pravdivtseva, N. Larsen, A. Aliseda, P. Berg: Black Blood MRI within Intracranial Aneurysms: Can Eulerian and Lagrangian Characteristics of the Flow Elucidate Signal Intensity?. In: 74th Annual Meeting of the Division of Fluid Dynamics, Phoenix, USA, 2021

J. Korte, F. Gaidzik, T. Weiß, S. Saalfeld, P. Berg: Advanced flow-splitting for image-based hemodynamic simulations in neurovascular diseases. In: 47th Annual European Society of Artificial Organs Congress, Virtual Conference, 2021

F. Gaidzik, M. S. Pravdivtseva, **J. Korte**, N. Larsen, S. Saalfeld, P. Berg: Focal enhancement in intracranial aneurysms – effects of local hemodynamics on black blood mri signals. In: Summer Biomechanics Bioengineering Biotransport, Virtual Conference, 2021

D. Behme, S. Voß, **J. Korte**, M. Thormann, A. Mpotsaris, S. Saalfeld, G. Janiga, P. Berg: E-069 Discrimination between stable and unstable intracranial aneurysms using image-based blood flow simulations. In: Journal of NeuroInterventional Surgery Poster Abstract, 2021

J. Korte, L. Marsh, F. Gaidzik,M. S. Pravdivtseva, N. Larsen, P. Berg: Correlations between black blood MRI and hemodynamics in intracranial aneurysms. In: 5th conference on "Image-Guided Interventions", Magdeburg, Germany, 2021

J. Korte, L. Marsh, S. Saalfeld, J. Stahl, D. Behme, P. Berg: Fusiform vs. Saccular intracranial aneurysms: image-based blood flow simulations can help to understand formation and treatment effects. In: Summer Biomechanics Bioengineering Biotransport, Maryland, USA, 2022

M. S. Pravdivtseva, F. Wodarg, **J. Korte**, P. Berg, J.-B. Hövener, O. Jansen, N. Larsen: Quantification and visualization of aneurysm treatment outcome with signal enhancement on Black Blood MRI. In: 2022 Joint Annual Meeting ISMRM-ESMRMB & ISMRT 31st Annual Meeting, London, United Kingdom, 2022

J. Korte, T. Rauwolf, P. Groschopp, J.-N. Thiel, A. Schmeißer, R. Braun-Dullaeus, P. Berg: Numerical analysis of patient-specific LV function with mitral valve insufficiency using a moving mesh method: The effect of exercise and rest onto the heart washout. In: 48th Annual European Society of Artificial Organs Congress, Krems, Austria, 2022

M. S. Pravdivtseva, A. N. Pravdivtsev, **J. Korte**, F. Gaidzik, P. Berg, S. Peters, J. Hensler, N. Larsen, J.B. Hövener, O. Jansen, F. Wodarg: Effect of the contour neurovascular device on the flow in 3d printed patient-based aneurysm models. In: 48th Annual European Society of Artificial Organs Congress, Krems, Austria, 2022

J. Korte, M. S. Pravdivtseva, F. Gaidzik, F. Wodarg, N. Larsen, P. Berg: A virtual pipeline to assess hemodynamics within intracranial aneurysms treated with a novel contour neurovascular device. In: 57. Jahrestagung der Deutschen Gesellschaft für Neuroradiologie e.V., Kassel, Germany, 2022

M. Neidlin, A. Grünwald, **J. Korte** , N. Wilmanns, C. Winkler, S. Gross-Hardt, U. Steinseifer, K. Linden, U. Herberg: Intraventricular Flow Dynamics in Single Right Ventricle Patients with Real-Time Echocardiography and Computational Modeling Provide Additional Insight into Cardiac Function. In: The Thoracic and Cardiovascular Surgeon, Virtual Conference, 2022

J. Korte, A. Abdelsamie, B. A.-D. T. El-Khader, M. Brindise, P. Berg: Hemodynamic Fluctuations in Patient-Specific Intracranial Aneurysms: An In-Vitro and In-Silico Study. In: 76th Annual Meeting of the Division of Fluid Dynamics, Washington DC, USA, 2023

J. Korte, L. Obermeier, L. Goubergrits, P. Berg: Inter-model and inter-modality analysis of left ventricular hemodynamics: comparative study of CFD approaches, echocardiographic and MRI data. In: 49th Annual European Society of Artificial Organs Congress, Bergamo, Italy, 2023

J. Korte, F. Gaidzik, N. Larsen, E. Schütz, T. Damm, F. Wodarg, J.-B. Hövener, O. Jansen, G. Janiga, P. Berg, M. S. Pravdivtseva: In-silico analysis to assess the efficacy of the Contour Neurovascular System. In: 58. Jahrestagung der Deutschen Gesellschaft für Neuroradiologie e.V., Kassel, Germany, 2023

J. Korte, S. Voß, G. Janiga, O. Beuing, D. Behme, S. Saalfeld, P. Berg: Comparative analysis of the impact of lumen segmentation and outlet boundary condition in image-based blood flow simulations for intracranial aneurysms. In: 6th conference on "Image-Guided Interventions", Mannheim, Germany, 2023

B. A.-D. El-Khader, **J. Korte**, N. S Shirdade, P. Berg, M. C. Brindise: Evaluating high frequency fluctuations and its effect on hemodynamics at varying heart rates in intracranial

aneurysms via 4D PTV. In: 21st International Symposium on Applications of Laser and Imaging Techniques to Fluid Mechanics, Lisbon, Portugal, 2024

I. Spitz, **J. Korte**, F. Gaidzik, N. Larsen, B. Preim, S. Saalfeld: Deformation analysis of intracranial aneurysm neck curves after Contour deployment. In: 59. Jahrestagung der Deutschen Gesellschaft für Neuroradiologie e.V., Kassel, Germany, 2024

J. Korte, F. Gaidzik, I. Spitz, D. Behme, M. S. Pravdivtseva, N. Larsen, P. Berg: Hemodynamic longitudinal analysis of the efficacy of the contour neurovascular system based on in vivo data. In: 50th Annual European Society of Artificial Organs Congress, Aachen, Germany, 2024

P. Berg, J. Stahl, **J. Korte**, D. Behme, A. Alaraj, S. Saalfeld: Multimodal imaging for the patient-specific assessment of neurovascular hemodynamics. In: 50th Annual European Society of Artificial Organs Congress, Aachen, Germany, 2024

J. Stahl, **J. Korte**, F. Gaidzik, M. Pravdivtseva, L. Stone McGuire, S. Saalfeld, D. Behme, N. Larsen, A. Alaraj, P. Berg: Can black blood MRI indicate unstable neurovascular pathologies? A hemodynamic analysis of wall and intraluminal enhancement. In: The 19th international symposium on Biomechanics in Vascular Biology and Cardiovascular Disease, Rotterdam, Netherlands, 2024

J. Korte, B. A.-D. El-Khader, A. Abdelsamie, M. Brindise, P. Berg: Assessing high-frequency fluctuations in intracranial aneurysms using direct numerical simulation, conventional computational fluid dynamics and particle tracking velocimetry. In: 77th Annual Meeting of the Division of Fluid Dynamics, Salt Lake City, USA, 2024

M. S. Pravdivtseva, H. Toraman, **J. Korte**, F. Gaidzik, P. Berg, L. Bautz, F. Wodarg, J.-B. Hövener, O. Jansen, N. Larsen: BB MRI for monitoring aneurysm treatment – a novel biomarker?. In: The International Society for Magnetic Resonance in Medicine, Toronto, Canada, 2023

Planned to be published content of dissertation

Part of Chapter 4	Abdelsamie, A., El-Khader, B., Shirdade, N., Church, E. W., Brindise, M. C., Berg, P. Resolving High Frequency Fluctuations in Cerebral Aneurysm Hemodynamics: The Critical Role of High-Fidelity Simulations and Heart Rate Effects. Submitted in: Computer Methods and Programs in Biomedicine.
Part of Chapter 5	Gaidzik, F., Spitz, I., Behme, D., Pravdivtseva, M., Larsen, N., Saalfeld, S. & Berg, P. Analysis of Contour Neurovascular System Analysis of the treatment effect of the Contour Neurovascular System in intracranial aneurysms: larger neck coverage area is associated with longitudinal flow reduction. Under review in: Computers in Biology and Medicine.